Research paper #1

ARTICLE

OPEN

Check for updates

The ALPK1/TIFA/NF-κB axis links a bacterial carcinogen to R-loop-induced replication stress

Michael Bauer[1,11], Zuzana Nascakova[2,3,11], Anca-Irina Mihai [1,11], Phil F. Cheng [4], Mitchell P. Levesque[4], Simon Lampart[1], Robert Hurwitz[5], Lennart Pfannkuch[5], Jana Dobrovolna[2], Melanie Jacobs[6], Sina Bartfeld[6], Anders Dohlman[7], Xiling Shen [7], Alevtina A. Gall[8], Nina R. Salama[8], Antonia Töpfer[9], Achim Weber [1,9,10], Thomas F. Meyer[5], Pavel Janscak [1,2,10,12✉] & Anne Müller [1,10,12✉]

Exposure of gastric epithelial cells to the bacterial carcinogen *Helicobacter pylori* causes DNA double strand breaks. Here, we show that *H. pylori*-induced DNA damage occurs co-transcriptionally in S-phase cells that activate NF-κB signaling upon innate immune recognition of the lipopolysaccharide biosynthetic intermediate β-ADP-heptose by the ALPK1/TIFA signaling pathway. DNA damage depends on the bi-functional RfaE enzyme and the Cag pathogenicity island of *H. pylori*, is accompanied by replication fork stalling and can be observed also in primary cells derived from gastric organoids. Importantly, *H. pylori*-induced replication stress and DNA damage depend on the presence of co-transcriptional RNA/DNA hybrids (R-loops) that form in infected cells during S-phase as a consequence of β-ADP-heptose/ ALPK1/TIFA/NF-κB signaling. *H. pylori* resides in close proximity to S-phase cells in the gastric mucosa of gastritis patients. Taken together, our results link bacterial infection and NF-κB-driven innate immune responses to R-loop-dependent replication stress and DNA damage.

[1] Institute of Molecular Cancer Research, University of Zurich, 8057 Zurich, Switzerland. [2] Institute of Molecular Genetics, Academy of Sciences of the Czech Republic, 142 20 Prague, Czech Republic. [3] Faculty of Science, Charles University in Prague, 128 00 Prague, Czech Republic. [4] Department of Dermatology, University Hospital Zurich, Zurich, Switzerland. [5] Max Planck Institute for Infection Biology, Department of Molecular Biology, 10117 Berlin, Germany. [6] Research Center for Infectious Diseases, Institute for Molecular Infection Biology, University of Würzburg, 97080 Würzburg, Germany. [7] Biomedical Engineering, Duke University, Durham, NC, USA. [8] Division of Human Biology, Fred Hutchinson Cancer Research Center, Seattle, WA, USA. [9] Department of Pathology and Molecular Pathology, University Hospital Zurich and University of Zurich, Zurich, Switzerland. [10] Comprehensive Cancer Center Zurich, Zurich, Switzerland. [11] These authors contributed equally: Michael Bauer, Zuzana Nascakova, Anca-Irina Mihai. [12] These authors jointly supervised this work: Pavel Janscak, Anne Müller. ✉email: pjanscak@imcr.uzh.ch; mueller@imcr.uzh.ch

Observational studies in humans first described a link between infection with the human gastric pathogen *Helicobacter pylori* and gastric cancer in the early 1990's[1,2]. This discovery led to the categorization of *H. pylori* as a class I (highest class) carcinogen by the World Health Organization in 1994. A causal link between *H. pylori* infection and gastric adenocarcinoma was later confirmed in experimental models using Mongolian gerbils[3] and inbred mouse strains[4,5], especially in settings of hypergastrinemia[6] or a high salt diet[7]. Gastric *H. pylori*-induced carcinogenesis is preceded by a series of precursor lesions that manifest as chronic inflammation, atrophy, intestinal metaplasia, and dysplasia[8]. The *H. pylori* type IV secretion system (T4SS), which is encoded by the Cag pathogenicity island (Cag-PAI), and its T4SS-translocated effector CagA have been described as major risk factors of gastric cancer and its precursor lesions in observational studies in humans[9] and in experimental models[10,11]. As a consequence of a large body of evidence implicating *H. pylori* in gastric carcinogenesis, screening programs using upper gastrointestinal tract endoscopy are now in place in countries with a particularly high gastric cancer burden, such as South Korea or Japan. These programs have allowed for early detection of gastric cancer and have reduced mortality from this disease[12]. Eradication therapy targeting *H. pylori* is efficacious at reducing gastric cancer risk, especially if it is applied in patients with non-atrophic or atrophic gastritis but without evidence of metaplasia[13]. A recent study has shown that even patients with early gastric cancers that are limited to the gastric mucosa or submucosa can benefit from eradication therapy, as they show a lower risk of progressing to metachronous gastric cancer than non-eradicated controls[14].

We and others have demonstrated in several independent studies that *H. pylori* induces DNA double-strand breaks (DNA DSBs) in gastric epithelial cells in vitro and in vivo[15–17]. DNA DSB induction in *H. pylori*-exposed cells depends on a functional T4SS[16–18] and preferentially occurs in transcribed regions of the genome[17]. Whereas translocation of the only described protein substrate of the T4SS, CagA, does not contribute to DNA DSB induction, the depletion of NF-κB subunits strongly reduces DNA DSB formation, suggesting that *H. pylori*-induced DNA damage is driven by active transcription of NF-κB target genes, which in turn is Cag-PAI-dependent[18]. Interestingly, a reduction in the level of *H. pylori*-induced DSBs is also observed upon depletion of the nucleotide excision repair endonucleases XPG and XPF[18] that have been shown to cleave co-transcriptional RNA/DNA hybrids, termed R-loops[19,20].

The earliest immune response to *H. pylori* is initiated by gastric epithelial cells, to which *H. pylori* adheres tightly in vitro and in vivo. Gastric epithelial cells sense *H. pylori* through a recently described innate immune defense pathway that is comprised of a sensor, the alpha-kinase 1 (ALPK1), and a signaling adaptor, the tumor necrosis factor receptor-associated factor (TRAF)-interacting protein with forkhead-associated domain (TIFA), which together initiate T4SS-dependent NF-κB signaling[21–24]. The pathway is activated upon T4SS-dependent delivery of either D-glycero-beta-D-manno-heptose 1,7-bisphosphate (HBP) or ADP-beta-D-manno-heptose (β-ADP-heptose) into the host cell[21–24]; both molecules are metabolic precursors of lipopolysaccharide (LPS) biosynthesis. The binding of β-ADP-heptose, and possibly of β-ADP-heptose 7-P (generated in the host cell from HBP), to ALPK1 stimulates its kinase domain to phosphorylate and activate TIFA[24,25], which forms large complexes (TIFAsomes) that also include interactors such as TRAF2[22]. *H. pylori* mutants that lack the ability to produce HBP or β-ADP-heptose are incapable of activating the ALPK1/TIFA pathway[22,23]; conversely, the extracellular addition of β-ADP-heptose alone is sufficient to activate NF-κB signaling in

an ALPK1/TIFA-dependent manner[24]. Other Gram-negative pathogens are sensed via the same pathway; these include *Salmonella typhimurium*, *Shigella flexneri*[26], *Yersinia pseudotuberculosis*[25] as well as *Neisseria meningitidis* and *Neisseria gonorrhoeae*, for which the pathway was first described[27]. In the case of all these pathogens, the activation of the ALPK1/TIFA signaling axis lead to NF-κB activation and the subsequent production of pro-inflammatory cytokines and chemokines, of which the most often investigated example was IL-8.

As DNA damage induced by *H. pylori* is dependent on NF-κB activation, and NF-κB activation is now known to be triggered by the ADP-heptose/ALPK1/TIFA axis, we set out here to investigate a possible link between the two processes and to elucidate in detail the molecular mechanism of *H. pylori*-induced DNA damage.

Results

H. pylori induces ALPK1/TIFA/NF-κB-dependent DNA damage. To investigate whether the β-ADP-heptose/ALPK1/TIFA signaling axis is involved in *H. pylori*-induced DNA damage, we took advantage of AGS gastric epithelial cells that were either proficient or deficient for ALPK1 and TIFA expression due to genetic ablation of the respective loci by CRISPR/Cas9 technology[21]. Cells were infected with wild-type *H. pylori* and were subjected to immunofluorescence microscopy to quantify 53BP1 and γH2AX foci, which identify sites of DNA DSBs. In wild-type AGS cells, *H. pylori* exposure induced multiplicity-of-infection (MOI)-dependent DNA damage, which could be observed as early as 6 h post infection (Fig. 1a, b, Supplementary Data 1 and 2). The genetic ablation of *ALPK1* or *TIFA* in AGS cells strongly reduced DNA DSBs as judged by quantification of 53BP1/γH2AX foci (Fig. 1a, b). DNA damage was limited to cells in S-phase, which were identified by PCNA staining (Fig. 1b, Supplementary Fig. 1a, Supplementary Data 2 and 3) and was also observed with a second strain of *H. pylori* (Supplementary Fig. 1b). Plotting the signal intensities of PCNA over DAPI, which readily separates cells in G1, S, and G2/M phases of the cell cycle, confirmed that cells with five and more 53BP1 foci are typically in S-phase (Fig. 1c). To rule out that off-target effects of genome-editing by CRISPR led to the reduction in 53BP1 foci, we took advantage of a second, independently generated ALPK1-deficient AGS line published previously[22] and of *TIFA*-deficient AGS cells that had been complemented by transduction with a lentivirus containing the complete TIFA coding sequence[21]. In these complemented cells, TIFA expression is driven by the lentiviral MND promoter and completely restores IL-8 production upon co-culture with *H. pylori*[21]. When subjected to *H. pylori* exposure followed by 53BP1 staining and the quantification of 53BP1 foci, the second *ALPK1*-deficient cell line phenocopied the effects of the first one (Supplementary Fig. 1c); TIFA-complemented cells exhibited an almost complete restoration of 53BP1 foci formation, whereas the baseline levels (uninfected condition) were unchanged (Supplementary Fig. 1c). These results indicate that the resistance of *ALPK1*- or *TIFA*-deficient AGS cells to *H. pylori*-induced DNA damage is indeed due to *TIFA* ablation and not off-target effects of CRISPR.

A second readout of DNA damage, for which extracted nuclear DNA was separated by pulsed-field gel electrophoresis, confirmed that wild-type AGS cells sustain more DNA DSBs upon *H. pylori* exposure than their ALPK1- or TIFA-deficient counterparts (Fig. 1d, e, Supplementary Data 4). The differential induction of DNA damage as observed in both readouts was mirrored by differential IL-8 production, which, as published previously[21–23], was strongly dependent on ALPK1 and TIFA also in our experiments (Fig. 1f). As the activation of ALPK1/TIFA results in
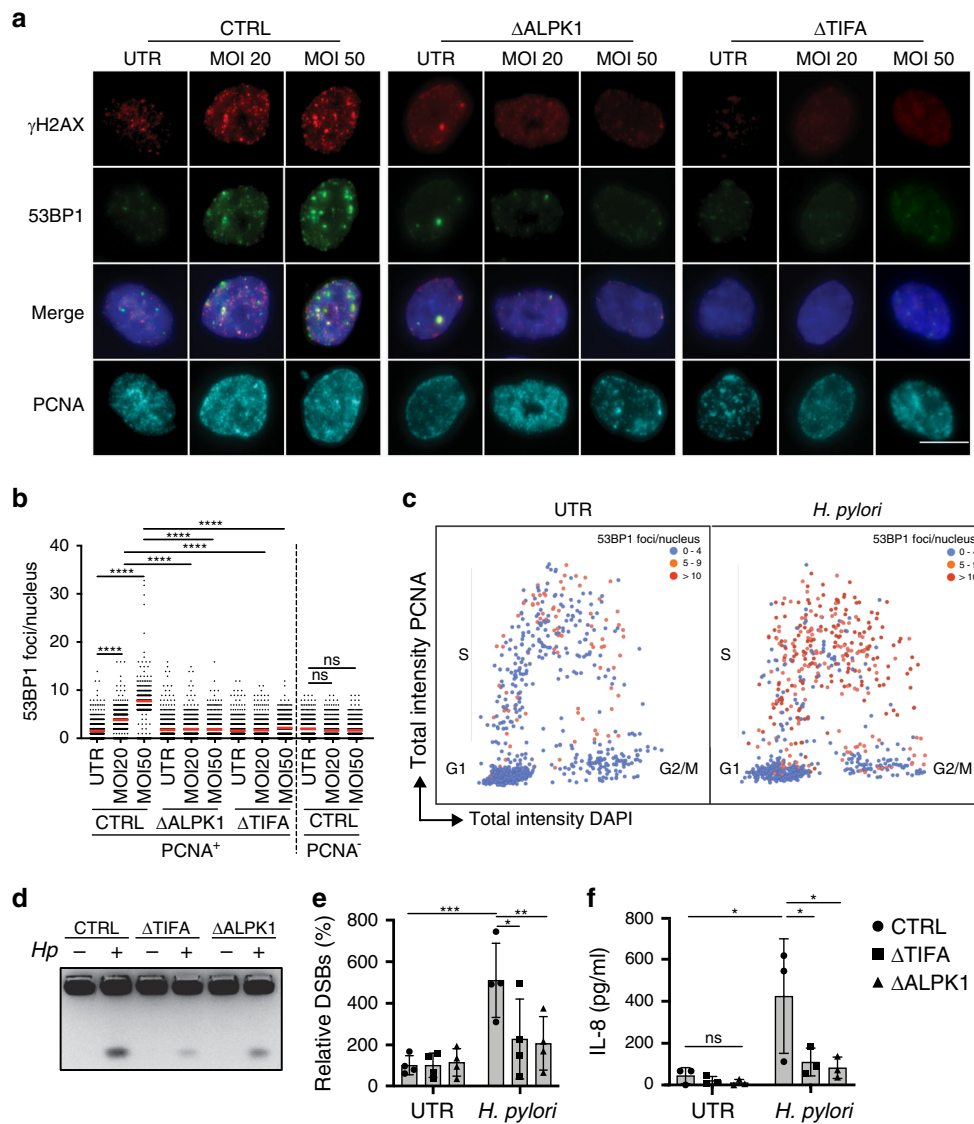
Fig. 1 *H. pylori* induces DNA DSBs in gastric epithelial cells that depend on ALPK1/TIFA signaling and occur in S-phase. a–c Wild-type (CTRL), ALPK1-deficient (ΔALPK1), and TIFA-deficient (ΔTIFA) AGS cells were infected for 6 h with *H. pylori* strain P12 at multiplicities of infection (MOIs) of 20 and 50 (or left untreated, UTR) and subjected to immunofluorescence staining for phosphorylated H2AX (γH2AX), 53BP1 and PCNA. DAPI was used to stain nuclei. Representative images are shown in **a** for one PCNA-positive cell per condition, alongside scatter dot plots of the number of 53BP1 foci per nucleus of >553 and up to 650 cells per condition for PCNA+ and PCNA− cells of the indicated genotypes in **b**. Data in **b** are pooled from three independent experiments. Red lines indicate medians. In **c**, the PCNA and DAPI signal intensities of ~600 uninfected and as many *H. pylori*-infected (MOI 50) wild-type cells were plotted to visualize cell cycle phase (G1, S, G2/M). The color code indicates the number of 53BP1 foci/nucleus. Scale bar in **a**, 10 μm. **d–f** Wild-type (CTRL), ALPK1-deficient (ΔALPK1), and TIFA-deficient (ΔTIFA) AGS cells were infected for 6 h as described above and subjected to PFGE. A representative gel is shown in **d** alongside the quantification of three gels in **e**. Fragmented DNA was normalized to the intact DNA retained in the slot, and to the uninfected control condition, which was set as 100%. IL-8 secretion as assessed by ELISA is shown in **f**. In **e** and **f**, data are represented as mean +/− SEM of four independent experiments. In **f**, data are represented as mean +/− SEM of three independent experiments. *P*-values were calculated by one-way ANOVA with Dunn's multiple comparisons correction. ns, not significant; *$p < 0.05$, **$p < 0.01$, ***$p < 0.005$, ****$p < 0.0001$.

NF-κB activation, we asked whether the inhibition of NF-κB activation, or generally the inhibition of transcription, would prevent *H. pylori*-induced DNA damage. Indeed, the exposure of cells to an irreversible inhibitor of IKK-α, BAY 11-7082, which prevents phosphorylation of IκBα and the translocation of NF-κB to the nucleus, was as efficient as *ALPK1* or *TIFA* deletion in abrogating the formation of 53BP1 foci in S-phase cells upon *H. pylori* infection (Fig. 2a, b, Supplementary Fig. 2a). Application of the transcription inhibitor triptolide, a natural product extracted from the Chinese plant *Tripterygium wilfordii* that is known to block RNA polymerase II activity[28], had similar effects on DNA damage induction by *H. pylori* as NF-κB inhibition (Fig. 2a, b).

Interestingly, application of the canonical NF-κB activator TNF-α did not result in DNA damage (Fig. 2a, b), even at concentrations that trigger IL-8 secretion at levels comparable to those induced by *H. pylori* infection (Fig. 2c). The consequences of *H. pylori* infection on genomic integrity were comparable in magnitude to DNA damage induced by the topoisomerase inhibitor camptothecin (CPT), the effects of which were however not limited to S-phase cells (Fig. 2a, b, Supplementary Fig. 2a). All results combined indicate that activation of the ALPK1/TIFA/NF-κB signaling axis by *H. pylori* triggers DNA damage in target cells that appears to be specific to this pathway of NF-κB activation, and that requires active transcription and occurs predominantly
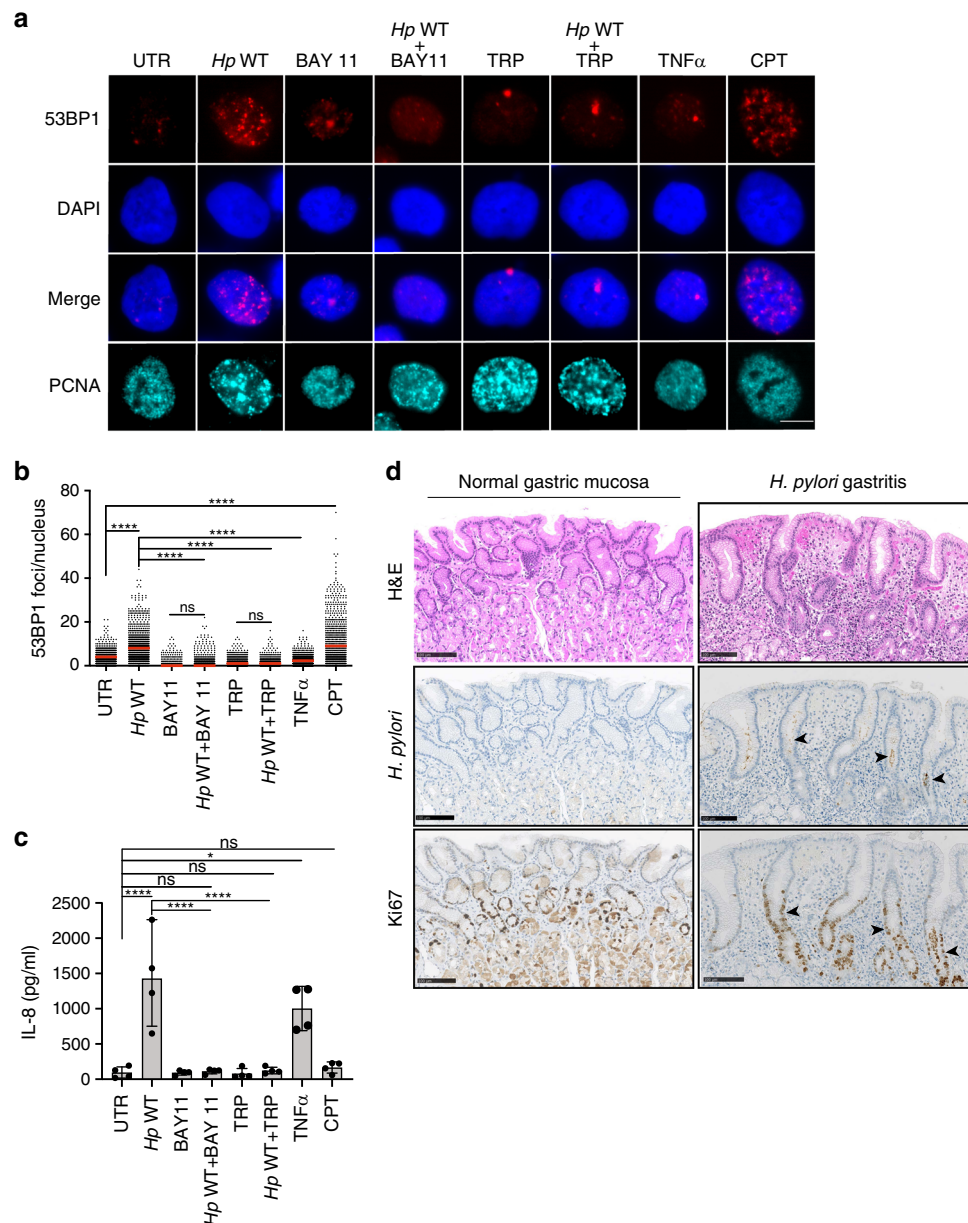
Fig. 2 *H. pylori*-induced DNA DSBs require active transcription and NF-κB activation. a–c Wild-type AGS cells were infected for 6 h with *H. pylori* P12 at an MOI of 50 in the presence or absence of the NF-κB inhibitor BAY 11-7082 and the transcription inhibitor triptolide (1 μM and 100 nM final concentration, respectively), or treated with 10 nM TNF-α or 100 nM camptothecin (CPT) for 6 h, and subjected to immunofluorescence staining for 53BP1 and PCNA. Representative images are shown in **a** (scale bar, 10 μm) alongside scatter dot plots of >430 and up to 954 cells per condition in **b**. IL-8 secretion as assessed by ELISA is shown in **c**. Data in **b** and **c** are pooled from four independent experiments. Red lines indicate medians. Data in **c** are represented as mean + SEM of three independent experiments. *P*-values were calculated by one-way ANOVA with Dunn's multiple comparisons correction in **b** and by two-way ANOVA with Tukey's multiple comparisons correction in **c**. ns, not significant; *$p < 0.05$, ****$p < 0.0001$. **d** Immunohistochemical analysis of *H. pylori* staining relative to Ki67+ cells in the gastric mucosa of patients presenting with (right panels) or without gastritis (left panels); six patients with gastritis and three control patients were stained with very similar results. Hematoxylin and eosin (H&E)-stained sections are shown as well. Scale bars, 100 μm. Arrows point to areas where *H. pylori* resides in close proximity to proliferating cells.

in actively replicating (S-phase) cells. As NF-κB activation and the resulting production of reactive oxygen species (ROS), through mechanisms involving inducible nitric oxide synthase (iNOS) and other inflammatory enzymes, have been implicated in *H. pylori*-induced DNA damage[29], we addressed this possibility experimentally using the antioxidant *N*-acetyl-cysteine. We found that *H. pylori* induces ROS, as judged by their flow cytometric detection and quantification (Supplementary Fig. 2b, Supplementary Data 5). However, co-culturing AGS cells with *H. pylori* in the presence of *N*-acetyl-cysteine—at concentrations that

completely abrogated ROS production—failed to reduce the DNA damage as judged by 53BP1 foci formation (Supplementary Fig. 2b–d). This result argues against a major contribution of ROS to *H. pylori*-induced DNA damage in this setting.

To address whether *H. pylori* indeed resides in close proximity to actively replicating cells in the human gastric mucosa, we selected biopsies from six cases of *H. pylori*-associated gastritis and three cases of normal (uninfected) gastric mucosa for immunohistochemical analysis of *H. pylori* and of the proliferation marker Ki67. We indeed found numerous examples of

regions where *H. pylori* could be detected in close proximity to Ki67^{+} cells in gastric glands; gastric glands typically exhibited more Ki67^{+} cells than glands of uninfected controls (Fig. 2d). These data indicate that areas of hyperproliferation are readily detectable in the *H. pylori*-infected gastric mucosa, and *H. pylori* resides in close proximity to proliferating cells.

H. pylori LPS biosynthetic intermediates induce DNA damage. We next set out to assess which bacterial determinants are required for DNA damage induction in addition to the above-mentioned Cag-PAI/T4SS identified earlier[16–18]. The gene *rfaE* (*hldE*; HP0858) of *H. pylori* encodes a bifunctional enzyme with kinase as well as ADP transferase activity, forms a contiguous operon with *gmhA*, *gmhB*, and *rfaD*, and is involved in the synthesis of both HBP and ADP-heptose as intermediate metabolites of LPS biosynthesis[23]. To examine whether *rfaE* is required for DNA damage induction by *H. pylori*, we infected AGS cells with the wild-type *H. pylori* strain P12 or its *rfaE* and Cag-PAI mutants. The *rfaE* mutant induced less DNA damage as determined by 53BP1 immunofluorescence microscopy than the wild-type parental strain, and its phenotype resembled that of the Cag-PAI mutant (Fig. 3a, b). Both mutants failed to induce IL-8 production by AGS cells (Fig. 3c); in contrast, the ability of the *rfaE* mutant to deliver CagA and to thereby induce cell elongation and scattering was not compromised (Supplementary Fig. 3a). The reduced DNA damage associated with *rfaE* mutant infection could be confirmed using pulsed-field gel electrophoresis (Fig. 3d, e, Supplementary Data 6) and phenocopied what was previously published for the Cag-PAI mutant[18]. As the product of RfaE activity, β-ADP-heptose, has recently been shown to enter host cells and activate ALPK1[24,25], we synthesized the α- and β-anomers of ADP-heptose and determined the consequences of their addition to AGS cells on genomic integrity. The β-anomer, but not the α-anomer, induced DNA damage—as judged by 53BP1 formation—as well as IL-8 secretion in a ALPK1/TIFA-dependent manner (Fig. 3f, g, Supplementary Fig. 3b); which was also confirmed by PFGE of fragmented DNA (Supplementary Fig. 3c, d, Supplementary Data 7). As in the context of live *H. pylori* infection, DNA damage upon β-ADP-heptose exposure was limited to PCNA^{+} cells (Fig. 3f, Supplementary Fig. 3b, e). The defect of the *rfaE* mutant could not be rescued by addition of TNF-α (Supplementary Fig. 3f). The combined results indicate that *rfaE* activity is required, and its product β-ADP-heptose is sufficient, to induce the ALPK1/TIFA-dependent DNA damage observed upon live *H. pylori* infection of cultured gastric epithelial cells.

We next asked whether the findings could be recapitulated in a gastric organoid model. Gastric organoids were grown from two donors undergoing bariatric surgery[30] and were subsequently transformed into 2D cultures as previously described[31]. Infection of primary cells from gastric organoids with wild-type bacteria, but not the *rfaE* or Cag-PAI mutants, resulted in the production and secretion of IL-8 into the culture supernatant (Supplementary Fig. 3g). Exposure of the cells to the β- but not the α-anomer of ADP-heptose elicited a similar IL-8 response as the wild-type *H. pylori* infection (Supplementary Fig. 3g). Importantly, wild-type, but not mutant bacteria-induced 53BP1 foci as judged by immunofluorescence microscopy; as in AGS cells, this increase in 53BP1 focus formation was restricted to S-phase cells identified by PCNA foci (Fig. 3h, i, Supplementary Fig. 3h). The addition of β- but not α-ADP-heptose phenocopied the effect of *H. pylori* infection with respect to 53BP1 focus formation (Fig. 3h, i, Supplementary Fig. 3h). The results from gastric organoid-derived primary cells confirm that DNA damage occurs upon *H. pylori* exposure also in this more physiological setting, is specific

to S-phase, depends on the *H. pylori* enzyme *rfaE* and the Cag-PAI, and can be elicited by the addition of the ALPK1 ligand β-ADP-heptose.

β-ADP-heptose/ALPK1/TIFA signaling induces replication stress. Physical obstacles such as active transcription complexes or DNA secondary structures are known to cause the slowing or arrest of replication fork progression, a condition commonly referred to as DNA replication stress[32]. To investigate whether the DNA damage induced by *H. pylori* infection is linked to replication stress, we employed a DNA fiber assay that exploits the ability of eukaryotic cells to incorporate halogenated pyrimidine nucleoside analogs into replicating DNA and provides a powerful tool to monitor genome-wide replication perturbations at single-molecule resolution[33]. Ongoing replication events were sequentially labeled with two thymidine analogs—chlorodeoxyuridine (CldU) and iododeoxyuridine (IdU)—and individual two-color labeled DNA tracts were visualized on stretched DNA fibers by immunofluorescence microscopy (Fig. 4a, b). We found that *H. pylori* infection led to slowing of replication fork progression in wild-type AGS cells as judged by measuring the lengths of CldU tracts (Fig. 4b, c) and also by plotting replication fork speeds (Supplementary Fig. 4a) that were calculated based on the assumption that 1 μm of fiber corresponds to 2.59 kb[34]. As replication fork slowing and shorter tracts can, in this assay, result from two scenarios, i.e., either a slower overall DNA polymerization rate or increased frequency of fork stalling[35], we analyzed the fates of two (sister) replication forks emanating in opposite directions from the same origin. To this end, we calculated the ratio of the lengths of CldU tracts of sister replication forks (length of the shorter tract divided by the length of longer tract); in uninfected cells, the ratio was ~1, indicating that sister forks traveled at similar speed. In *H. pylori*-infected AGS cells, the ratio dropped to ~0.6, indicating fork asymmetry and selective slowing/stalling of one fork only (Supplementary Fig. 4b). Replication fork slowing was not only observed upon *H. pylori* infection, but also upon treatment of AGS cells with the β- but not the α-anomer of ADP-heptose (Fig. 4b, c, Supplementary Fig. 4a). AGS cells lacking ALPK1 or TIFA expression were resistant to replication fork slowing in this assay, both in the setting of live infection and of exposure to β-ADP-heptose (Fig. 4b, c, Supplementary Fig. 4a). Complementation of TIFA-deficient AGS cells by TIFA overexpression from the lentiviral MND promoter rescued the effects of live *H. pylori* infection on fiber shortening (Supplementary Fig. 4c). The effect size of *H. pylori* infection on replication fork progression was comparable to the effects of the topoisomerase inhibitor camptothecin[36], and to the effects of the G quadruplex DNA (G4) ligand pyridostatin, a well-known inducer of both DNA damage and genome instability[37], which served as our positive controls (Fig. 4d). The slowing of replication forks upon *H. pylori* infection was dependent on RfaE and the Cag-PAI, as both null mutants failed to cause CldU tract shortening (Fig. 4e, f). TNF-α exposure did not cause CldU tract shortening (Fig. 4e, f), and also failed to rescue the phenotype of the RfaE mutant (Supplementary Fig. 4d). Exposure of infected cells to the NF-κB inhibitor BAY 11-7082 or to the transcription inhibitor triptolide rescued *H. pylori*-induced fork slowing (Fig. 4e, f). In contrast, treatment with the antioxidant *N*-acetyl-cysteine did not prevent fork slowing (Supplementary Fig. 4d). The combined results suggest that active transcription driven by NF-κB as a consequence of β-ADP-heptose delivery and ALPK1/TIFA signaling is a prerequisite of replication fork slowing in *H. pylori*-infected cells; in contrast, ROS produced by infected cells do not contribute to DNA damage or replication stress.
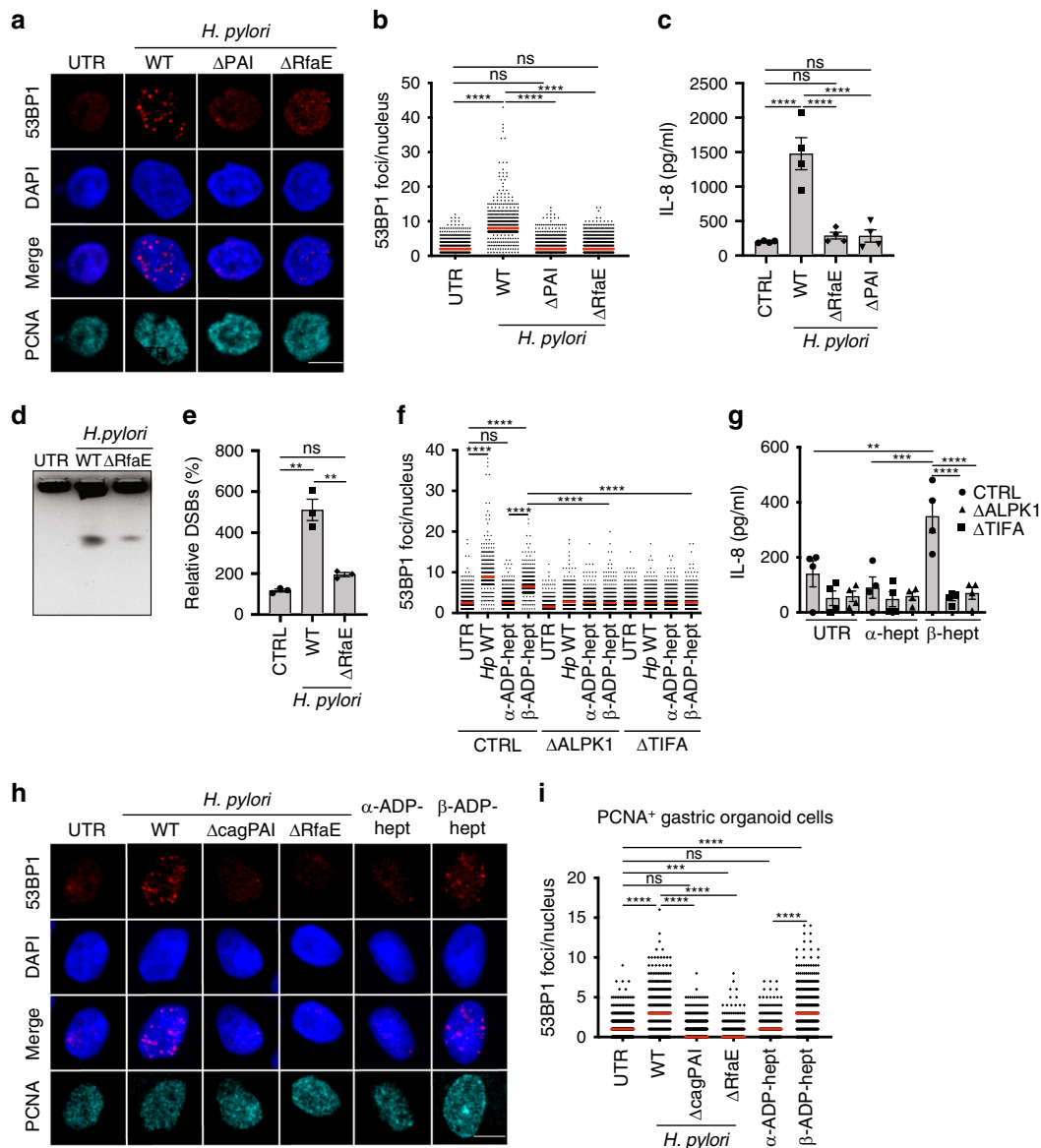
Fig. 3 The bifunctional RfaE enzyme is required, and its product β-ADP-heptose is sufficient for the induction of DNA DSBs. a–c AGS cells were infected for 6 h with *H. pylori* P12 or its isogenic RfaE and Cag-PAI mutants at an MOI of 50 and subjected to immunofluorescence staining for 53BP1 and PCNA as well as DAPI. Representative images are shown in **a** alongside scatter dot plots of >730 and up to 1655 cells per condition in **b**. IL-8 secretion as assessed by ELISA is shown in **c**. Data in **b** and **c** are pooled from four independent experiments. Red lines indicate medians. Data in **c** are represented as mean +/− SEM of four independent experiments. Scale bar in **a**, 10 μm. **d, e** AGS cells were infected for 6 h as described above and subjected to PFGE. A representative gel is shown in **d** alongside the quantification of three gels (independent experiments) in **e**. Fragmented DNA was normalized to the intact DNA retained in the slot, and to the uninfected control condition, which was set as 100%. Data are presented as mean values +/− SEM. **f, g** Wild-type (CTRL), ALPK1-deficient (ΔALPK1), and TIFA-deficient (ΔTIFA) AGS cells were exposed to α- or β-ADP-heptose at 0.5 μM final concentration for 6 h and subjected to immunofluorescence staining for 53BP1 and PCNA as well as DAPI. Scatter dot plots of >579 and up to 706 cells per condition are shown in **f**, with red lines indicating medians. IL-8 secretion as assessed by ELISA is shown in **g**. Data in **f** and **g** are pooled from four independent experiments. *P*-values were calculated by one-way ANOVA with Dunn's multiple comparisons correction. Data in **g** are presented as mean values +/− SEM. Scale bar, 10 μm. **h, i** Gastric organoids were transferred to 2D cultures and infected with the indicated strains of *H. pylori* P12 (MOI of 50) or exposed to α- or β-ADP-heptose at 0.5 μM final concentration for 6 h. Cells were subjected to immunofluorescence staining for 53BP1 and PCNA as well as DAPI. Representative images are shown in **h** of 53BP1 foci (scale bar, 10 μm), alongside scatter dot plots of >298 and up to 603 cells per condition for PCNA⁺ cells (in **i**). Data in **i** are pooled from two independent experiments with cells derived from two different donors. Red lines indicate medians. *P*-values were calculated by one-way ANOVA with Dunn's multiple comparisons correction. ns, not significant; **$p < 0.01$, ***$p < 0.005$, ****$p < 0.0001$.

R-loop formation is required for replication stress. Active replication and transcription that co-occur in the same regions of the genome can result in replication stress and DNA damage if both machineries collide. Replication fork stalling at sites of these conflicts is caused by the formation of co-transcriptional R-loops[38–40]. To address whether R-loop formation is the cause of

DNA damage and replication stress induced by *H. pylori*, we used a cell line that conditionally expresses human RNase H1[41], an enzyme that cleaves the RNA strand in RNA/DNA hybrids and thereby eliminates R-loops. This cell line is derived from U2OS osteosarcoma cells that have previously been shown to be susceptible to *H. pylori*-induced DNA damage[15,18] and that are
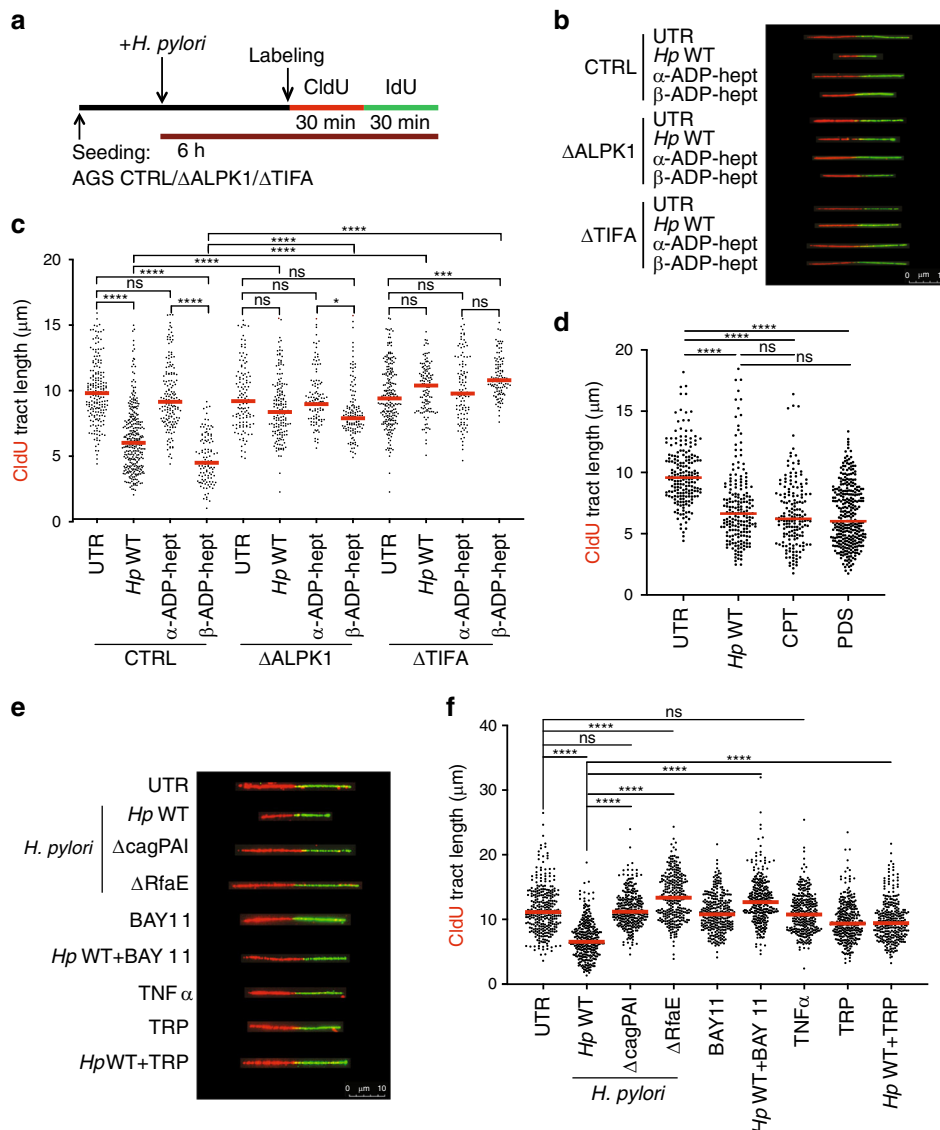
Fig. 4 *H. pylori* induces DNA replication stress in host cells. a Schematic representation of the protocol used for the quantification of the length of newly synthesized DNA tracts (fibers). **b, c** Wild-type (CTRL), ALPK1-deficient (ΔALPK1), and TIFA-deficient (ΔTIFA) AGS cells were either infected for 6 h with *H. pylori* strain P12 (MOI of 50) or treated with 0.5 μM α- or β-ADP-heptose and then labeled sequentially with CldU and IdU as shown in **a**. Representative DNA fibers are shown in **b** and scatter dot plots of CldU tract length (in μm) are shown in **c** for the indicated conditions. At least 106 and up to 318 fibers were analyzed per condition. Data in **c** are pooled from two independent experiments. **d** Wild-type AGS cells were either infected for 6 h with *H. pylori* strain P12 (MOI of 50) or treated with 100 nM camptothecin (CPT) or 10 μM pyridostatin (PDS) for 6 h and then labeled sequentially with CldU and IdU as shown in **a**. At least 200 fibers were analyzed per condition. Data in d are pooled from two independent experiments. **e, f** AGS cells were infected for 6 h with either the wild-type *H. pylori* strain P12 or its isogenic RfaE and Cag-PAI mutants (MOI of 50) and/or treated with the NF-κB inhibitor BAY 11-7082 (1 μM), the transcription inhibitor triptolide (100 nM), or TNF-α (10 nM) and labeled sequentially with CldU and IdU during the last 60 min of infection as shown in **a**. Representative DNA fibers are shown in **e** and scatter dot plots of CldU tract length (in μm) are shown in **f** for the indicated conditions. At least 141 and up to 213 fibers were analyzed per condition. Data in **f** are pooled from two independent experiments. Red lines indicate medians throughout. *P*-values were calculated throughout by one-way ANOVA with Dunn's multiple comparisons correction. ns, not significant; *$p < 0.05$, ****$p < 0.0001$.

commonly used in DNA damage research. Exposure of U2OS cells to wild-type *H. pylori* for six hours induced the formation of 53BP1 foci that increased with the MOI and were specific to S-phase, and were comparable in extent to those observed in AGS cells (Fig. 5a, b, left panels −DOX, Supplementary Fig. 5a, b). This DNA damage phenotype was accompanied by replication fork slowing as determined by DNA fiber assay (Fig. 5c, d, Supplementary Fig. 5c). As observed for AGS cells, replication fork slowing in *H. pylori*-infected U2OS cells was dependent on a functional Cag-PAI and RfaE, and could be completely reversed

by blocking transcription with the inhibitor triptolide or the NF-κB inhibitor BAY 11-7082 (Supplementary Fig. 5d, e). Both DNA damage in S-phase cells and replication stress could be induced also in U2OS cells by the addition of β- but not α-ADP-heptose (Fig. 5e–h, upper and left panels, −DOX, Supplementary Fig. 5f). Importantly, the induction of RNase H1 expression by doxycycline abrogated both 53BP1 foci formation (Fig. 5a, b, right panels, +DOX) and replication fork slowing (Fig. 5c, d, lower and right panels, +DOX, Supplementary Fig. 5c) upon *H. pylori* infection, and also upon β-ADP-heptose treatment (Fig. 5e–h).
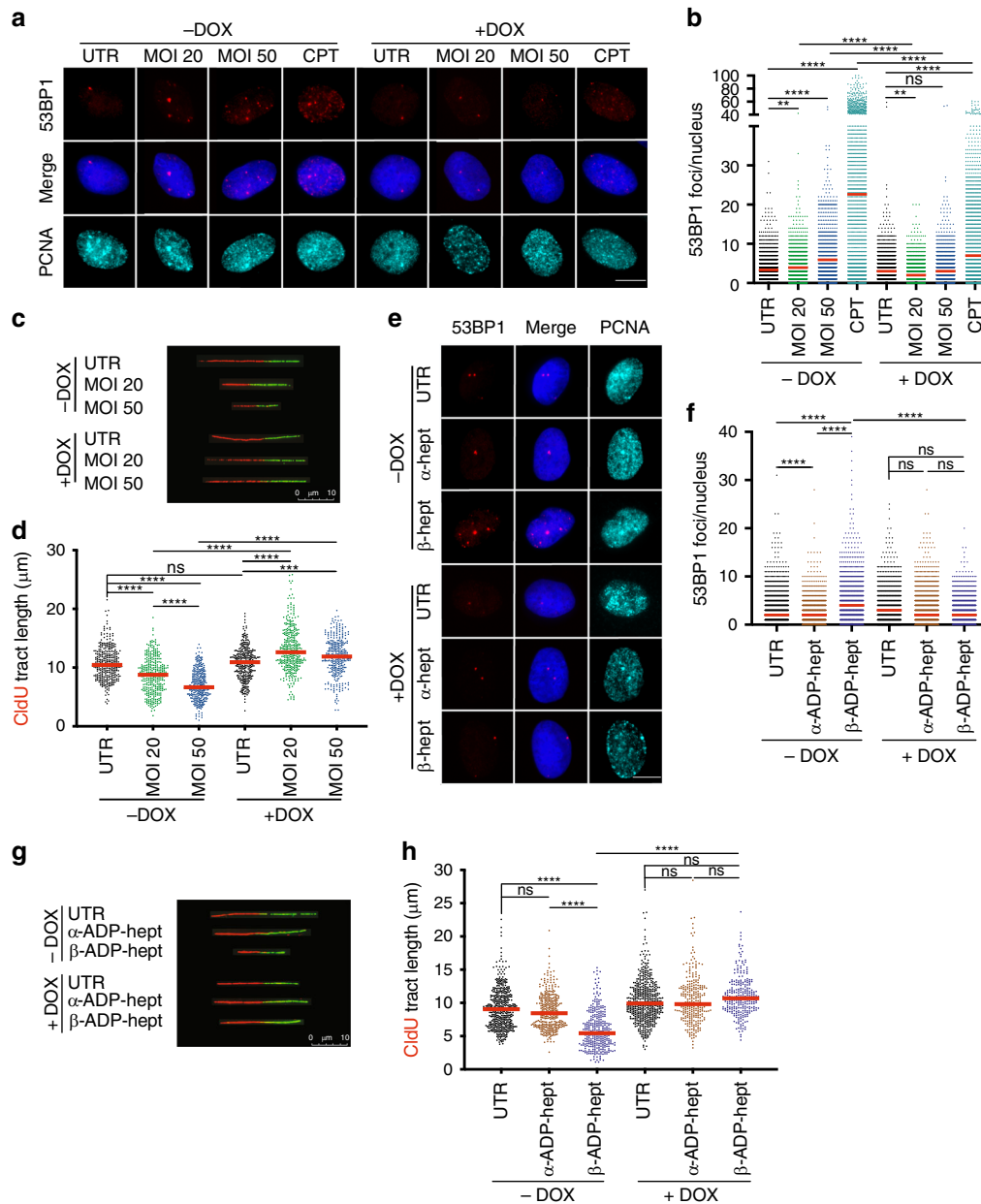
Fig. 5 *H. pylori*-induced DNA damage and replication stress is prevented by overexpression of RNase H1. a, **b** U2OS cells were either infected for 6 h with *H. pylori* P12 (MOI of 20 or 50), or treated with 100 nM camptothecin (CPT), and were treated or not with doxycycline (−/+ DOX) to induce the expression of RNase H1. Cells were subjected to immunofluorescence staining for 53BP1 and PCNA as well as DAPI. Representative images are shown in **a** alongside scatter dot plots of >1382 and up to 1752 cells per condition in **b**. Data in **b** are pooled from three independent experiments. **c**, **d** U2OS cells were infected as described in **a**, **b** and additionally labeled sequentially with CIdU and IdU as shown in Fig. 4a for the assessment of replication tract length. Representative DNA fibers are shown in **c** and scatter dot plots of CIdU tract length (in μm) are shown in **d** for the indicated conditions. At least 100 and up to 500 fibers were analyzed per condition. Data in **d** are pooled from three independent experiments. **e**, **f** U2OS cells were exposed to α- or β-ADP-heptose at 0.5 μM final concentration for 6 h and treated or not with doxycycline (−/+ DOX) to induce the expression of RNase H1. Cells were subjected to immunofluorescence staining for 53BP1 and PCNA as well as DAPI. Representative images are shown in **e** alongside scatter dot plots of >1500 and up to 1752 cells per condition in **f**. Data in **f** are pooled from three independent experiments. Scale bar in **a** and **e**, 10 μm. **g**, **h** U2OS cells were exposed to α- or β-ADP-heptose at 0.5 μM final concentration for 6 h, treated or not with doxycycline (−/+ DOX) to induce the expression of RNase H1, and additionally labeled sequentially with CIdU and IdU for the assessment of DNA fiber tract length. Representative DNA fibers are shown in **g** and scatter dot plots of CIdU tract length (in μm) are shown in **h** for the indicated conditions. At least 299 and up to 514 fibers were analyzed per condition. Data in **h** are pooled from three independent experiments. Red lines indicate medians throughout. In **b**, **d**, **f**, and **h**, −DOX and +DOX samples of the same condition are color-coded to facilitate comparisons. *P*-values were calculated by one-way ANOVA with Dunn's multiple comparisons correction. ns, not significant; ****p < 0.01, ******p < 0.005, *******p < 0.0001.

The analysis of sister forks emanating from the same origin showed that not only the slowing of fork progression, but also the fork asymmetry associated with *H. pylori* infection, could be reversed by induction of RNase H1 (Supplementary Fig. 5g, h). The combined results implicate R-loops, processed by RNase H1, in DNA damage and replication stress induced by *H. pylori*.

R-loops form in a Cag-PAI-, RfaE-, and NF-κB-dependent manner. The dependence of DNA damage and replication stress on R-loops prompted us to examine these structures in more detail, and to address the prerequisites of their formation. To this end, we used a cell line in the U2OS background that inducibly expresses a GFP-tagged RNase H1 harboring a point mutation (D210N) in its nuclease active site (RNase H1^{D210N}/GFP)[41], rendering it enzymatically inactive. Such inactive RNase H1 molecules bind their target structures but fail to resolve them; RNase H1^{D210N}/GFP foci forming in this cell line thus report the presence of R-loops. The addition of doxycycline to these reporter cells and concomitant *H. pylori* infection led to the appearance of on average 10–20 (and up to 80) RNase H1^{D210N}/GFP foci per cell that were not seen without doxycycline and that were clearly dependent on the MOI (Fig. 6a, b, Supplementary Fig. 6a). The extent of R-loop formation upon infection was comparable to that induced by the topoisomerase inhibitor camptothecin (Fig. 6a, b), a known inducer of R-loops[19]. RNase H1^{D210N}/GFP foci did not co-localize with sites of DNA damage (i.e., 53BP1 foci; Fig. 6a). Treatment of the reporter cells with β-ADP-heptose, but not the α-anomer, also resulted in R-loop formation (Fig. 6c, d) with a similar effect size as observed for live *H. pylori* infection or camptothecin treatment. Importantly, induction of expression of the catalytically inactive mutant of RNase H1 failed to resolve *H. pylori*- or β-ADP-heptose-induced DNA damage as assessed by the quantification of 53BP1 foci (Fig. 6a, c, e), indicating that the reduced DNA damage observed in settings of wild-type RNase H1 overexpression indeed results from its enzymatic activity. R-loop formation upon *H. pylori* infection was also abrogated by inhibition of transcription with triptolide, and by inhibition of NF-κB activation (Fig. 6f, g); the same treatments also blocked the formation of DNA damage in U2OS cells (Fig. 6f, h), as shown above for AGS cells (Fig. 2). The *rfaE* and Cag-PAI mutants of *H. pylori* failed to induce RNase H1^{D210N}/GFP foci (Fig. 6f, g). Infection-induced RNase H1^{D210N}/GFP foci were highly specific for PCNA$^+$ S-phase cells and were not observed in PCNA$^-$ cells (Fig. 6a–h, Supplementary Fig. 6b, c). Interestingly, the induction of RNase H1^{D210N}/GFP foci and of DNA damage correlated strongly with the level of incorporation of 5-fluorouracil (Supplementary Fig. 6d), which was also strongly dependent on *rfaE*, the Cag-PAI and NF-κB, and which we used as an indicator of RNA synthesis. Staining of infected cells with an antibody specifically recognizing RNA/DNA hybrids (clone S9.6) confirmed that infection with wild-type *H. pylori*, but not its *rfaE* and Cag-PAI mutants, induces R-loops not only in U2OS cells as shown with the reporter cell line, but also in AGS cells (Supplementary Fig. 6e, f). Taken together, the results suggest that the active transcription (of NF-κB target genes) that is induced by *H. pylori* in an β-ADP-heptose/ALPK1/TIFA-dependent manner leads to R-loop formation in actively replicating cells, possibly at sites where the transcription and replication machineries collide.

H. pylori-infected cells show evidence of genotoxicity. Our experimental data from two human cell lines as well as primary gastric cells are consistent with the hypothesis that transcription/replication conflicts generate substantial DNA damage during *H. pylori* infection. Such widespread DNA damage, especially if inadequately repaired, results in the subsequent accumulation of

mutations and an associated high risk of malignant transformation. As *H. pylori* is tightly associated with gastric carcinogenesis both epidemiologically and in various animal models, we investigated possible links between DNA damage, mutational burden, and gastric carcinogenesis. We first examined whether we would find evidence for *H. pylori*-associated genotoxicity in AGS cells by using the well-established cytokinesis-block micronucleus assay, a simple and sensitive procedure for reading out chromosome damage. AGS cells were treated, either already before or only during infection, with cytochalasin B, an inhibitor of the mitotic spindle that prevents cytokinesis. Cells that had completed one division were identified by their binucleated appearance, and the presence of small DAPI-stained fragments (micronuclei) that are indicative of chromosome breaks or intact mis-segregated chromosomes was quantified. We found up to three micronuclei per *H. pylori*-infected AGS cell, and substantially more infected cells exhibited evidence of micronuclei formation than control cells (Fig. 7a, b). The RfaE mutant failed to induce micronuclei (Fig. 7a, b), suggesting that *H. pylori* induces genotoxicity in an RfaE-dependent manner. The extent of genotoxicity induced by *H. pylori* would be expected to result in checkpoint activation, a DNA damage response and apoptosis. However, infected cells did not undergo apoptosis (Fig. 7c, d) and checkpoint activation— readout as phosphorylation of the DNA damage sensor ATM and its target KAP1— is very weak upon *H. pylori* infection relative to other DNA damaging agents such as camptothecin (Supplementary Fig. 7a, b, Supplementary Data 8–12). We conclude from these data that the DNA damage induced by *H. pylori*, despite causing chromosome breaks and mis-segregated chromosomes, fails to induce a DNA damage response or apoptosis.

Higher mutational burden in H. pylori-associated gastric cancer. We next asked whether gastric cancer genomic data would possibly provide circumstantial evidence for the presence of *H. pylori* as a driving force of malignant transformation. To this end, we used the non-human transcript and genomic information that is present in publicly accessible multi-omics (RNA-sequencing, whole-genome sequencing, and whole-exome sequencing) datasets of gastric cancer, which had been generated as part of the Cancer Genome Atlas (TCGA) project, to annotate gastric cancer samples with their *H. pylori* status. We had access to multi-omics datasets for 291 tumors from treatment-naive gastric cancer patients that had previously been subjected to array-based somatic copy number analysis, whole-exome sequencing, and array-based DNA methylation profiling, and that had resulted in the description of four major genetically defined subtypes of gastric cancer[42]. These subtypes were EBV-positive gastric cancer (characterized by the presence of EBV genes and transcripts, a very low mutational burden and *PIK3CA* mutations), microsatellite-instable gastric cancer (high mutational burden, MSI high), chromosomally instable gastric cancer (with large numbers of copy number variations and a high mutational burden, and ubiquitous TP53 mutations) and genomically stable gastric cancer (low mutational burden, diffuse type by histology, early-onset, *RHOA* and *ARHGAP6/26* somatic genomic alterations)[42]. We were able to recapitulate the stratification of the 291 patients into these subtypes (Fig. 7e). We found evidence of *H. pylori* presence in all four subtypes, with 1/3 to 1/2 of patients of each subtype exhibiting evidence of *H. pylori* transcripts or genomic DNA in either their tumor and/or adjacent tissue (Fig. 7e). When comparing the tumor mutational burden of the four subtypes, we found that tumors from patients with evidence of *H. pylori* infection (in either tumor and/or adjacent tissue) of the most common MSI and CIN subtypes had a higher mutational burden than those without *H. pylori*
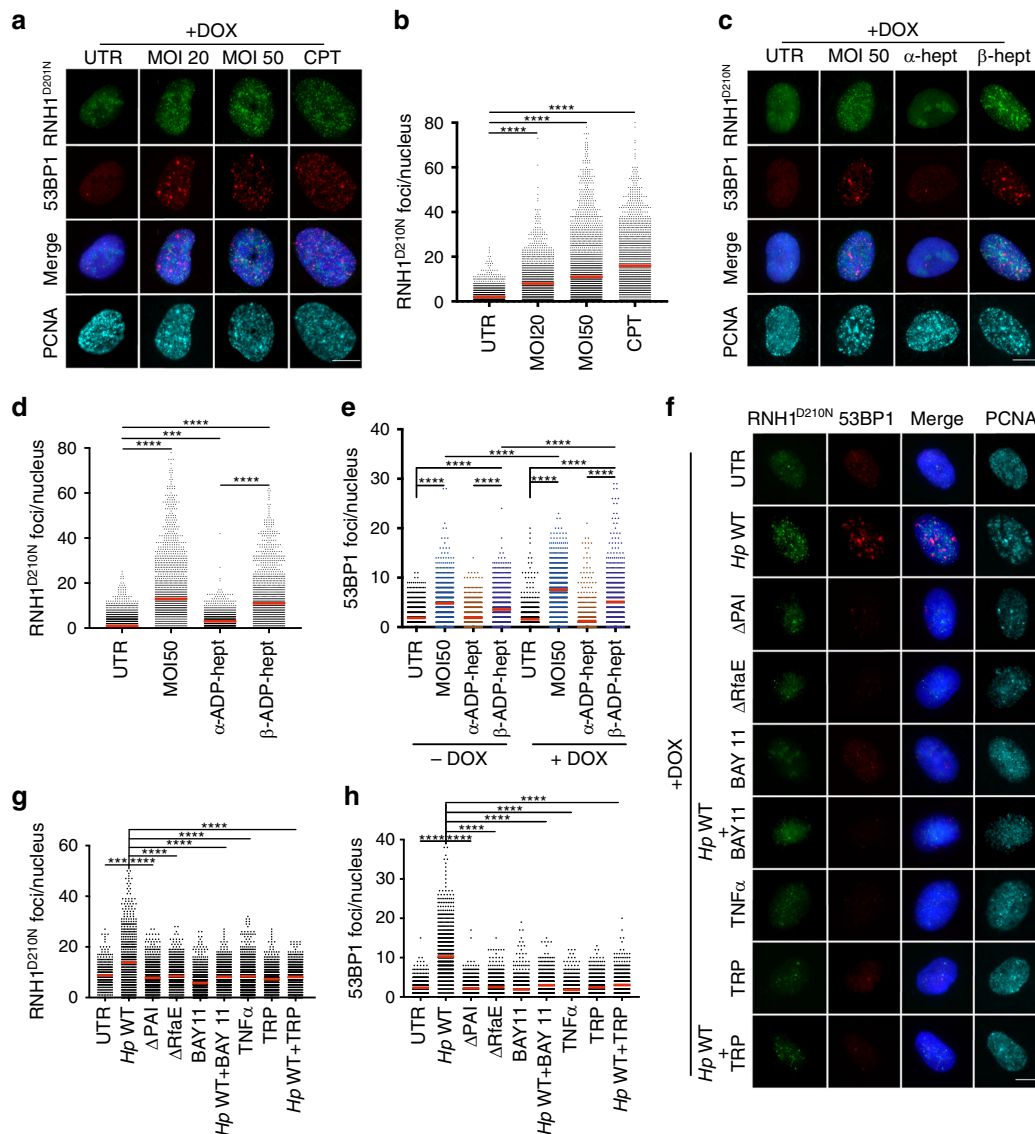
Fig. 6 *H. pylori* induces R-loop formation that depends on NF-κB and active transcription. a, b U2OS cells were either infected for 6 h with *H. pylori* P12 (MOI of 20 or 50), or treated with 100 nM camptothecin (CPT), and were treated or not with doxycycline (−/+ DOX) to induce the expression of a (D210N) mutant version of RNase H1 fused to GFP (RNH1^{D210N}). Cells were subjected to immunofluorescence staining for 53BP1 and PCNA as well as DAPI. Representative images are shown in RNH1^{D210N}/GFP foci and 53BP1 foci, alongside scatter dot plots of RNH1^{D210N}/GFP foci of >1468 and up to 1661 cells per condition in **b**; the −DOX panel shows lack of background signal in the GFP channel in the absence of RNH1^{D210N}/GFP expression. Data in **b** are pooled from three independent experiments. **c, d** U2OS cells were infected with *H. pylori* (MOI of 50) or exposed to α- or β-ADP-heptose at 0.5 μM final concentration for 6 h and treated or not with doxycycline (−/+ DOX) to induce the expression of RNH1^{D210N}/GFP. Cells were subjected to immunofluorescence staining for 53BP1 and PCNA as well as DAPI. Representative images are shown in **c** of RNH1^{D210N}/GFP foci and 53BP1 foci, alongside scatter dot plots of RNH1^{D210N}/GFP foci of >1326 and up to 1565 cells per condition in **d**. Data in **d** are pooled from three independent experiments. **e** Scatter dot plots showing 53BP1 foci of >1000 and up to 3000 cells per condition of the U2OS cells shown in **a** and **c**, and their counterparts not treated with doxycycline. **f–h** U2OS cells were infected with the indicated strains of *H. pylori* (MOI of 50) and/or exposed to the NF-κB inhibitor BAY 11-7082 (1 μM) or triptolide (100 nM) and treated with doxycycline to induce the expression of RNH1^{D210N}/GFP. Cells were subjected to immunofluorescence staining for 53BP1 and PCNA as well as DAPI. Representative images are shown in **f** of RNH1^{D210N}/GFP foci and 53BP1 foci, alongside scatter dot plots of RNH1^{D210N}/GFP foci of >405 and up to 868 cells per condition in **g**, and of 53BP1 foci of >691 and up to 1042 cells per condition in **h**. Data in **g** and **h** are pooled from three independent experiments. Red lines indicate medians throughout. *P*-values were calculated by one-way ANOVA with Dunn's multiple comparisons correction. ns, not significant; ***$p < 0.005$, ****$p < 0.0001$. Scale bars, 10 μm.

infection: within the CIN subtype, which with 136 samples was the most common of the four gastric cancer subtypes in the TCGA dataset, 57 *H. pylori*-infected patients had on average $2 +/− 1.5$ mutations per megabase, whereas this number was $1.54 +/− 0.98$ in the 79 *H. pylori*-negative patients ($p = 0.052$ as determined by student's *T*-test). Within the MSI subtype, the figures were $20 +/− 16$ for 23 *H. pylori*-positive vs. $16 +/− 7$ for

33 *H. pylori*-negative patients, but the difference was not statistically significant ($p = 0.2$). A total of 232 genes were differentially affected by mutations as a function of *H. pylori* infection across all 291 samples (Supplementary Data 13, Fig. 7e).

We also looked specifically for mutations and copy number variations (CNVs) in genes involved in R-loop prevention and processing, with the idea that mutations in such genes might
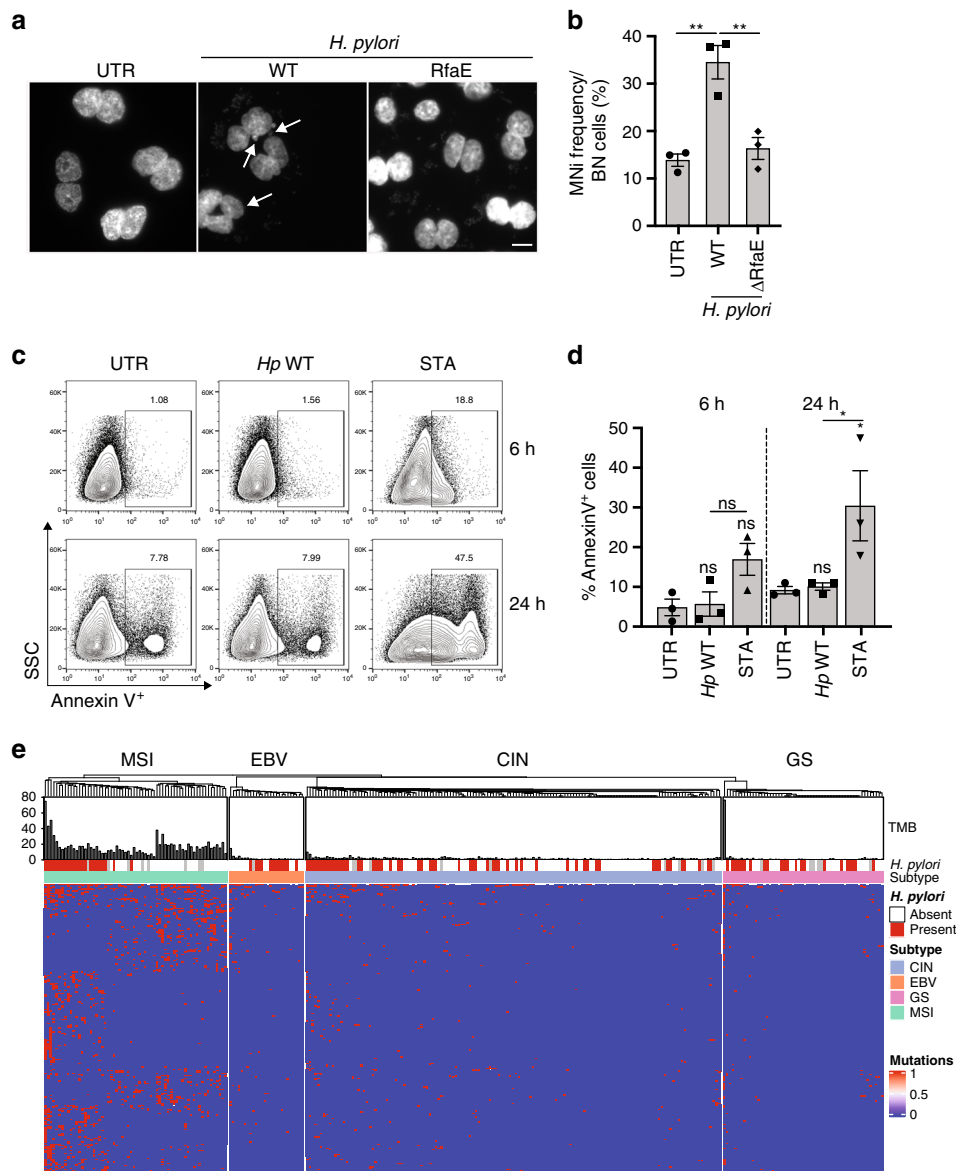
Fig. 7 *H. pylori* induces micronuclei but not apoptosis in gastric epithelial cells and its presence is associated with specific mutational patterns in gastric cancer. a, **b** Micronuclei formation as quantified in binucleated AGS cells that had been subjected to cytochalasin B treatment to prevent cytokinesis, and had additionally been infected for 16 h with the indicated WT or *RfaE* mutant strains of *H. pylori*. Representative images are shown in **a**; arrows point to micronuclei. Frequencies of binucleated (BN) cells with micronuclei are quantified in **b** and pooled from three independent experiments. Data are presented as mean values $+/-$ SEM. *P*-values were calculated by one-way ANOVA with Dunn's multiple comparisons correction. Scale bar represents 15 µm. **c**, **d** Annexin V staining for apoptosis of AGS cells infected with WT *H. pylori*, or treated with 5 µm staurosporine (STA) for 6 or 24 h. Representative FACS plots are shown in **c**, and the quantification of Annexin V-positive cells of three independent experiments is shown in **d**. Data are presented as mean values $+/-$ SEM. *P*-values were calculated by two-way ANOVA with Tukey's multiple comparisons correction. **e** Mutational signature of *H. pylori* in gastric cancer as determined on 291 gastric cancer samples available through the Cancer Genome Atlas (TCGA). The *H. pylori* status was annotated based on the presence of at least one unambiguous *H. pylori*-specific read detected in the transcriptome, whole genome or exome of either the tumor or adjacent tissue of a total of 267 among the 291 patients. The gastric cancer subtype was assigned based on the previous description[42] of CNVs, presence of EBV transcripts, methylation of signature genes and microsatellite instability; the color code on the right indicates the four subtypes chromosomally instable (CIN), microsatellite instable (MSI), EBV-positive (EBV), and genomically stable (GS). The heatmap shows the 232 genes found to be differentially mutated between *H. pylori*-positive and -negative cases (*p* < 0.05 as determined by Student's *t*-test); the majority of differentially mutated genes are found in the MSI subtype. Genes are listed in Supplementary Table 1. ns, not significant; **p* < 0.05, ***p* < 0.01.

predispose to gastric carcinogenesis. We plotted the mutations and CNVs in 18 genes with functions in R-loop prevention or processing relative to seven known gastric cancer driver genes, i.e., *CDH1*, *APC*, *TP53*, *ARID1A*, *PIK3CA*, *KRAS*, and *ERBB2*, and relative to the mutational burden per megabase. The 18 genes with R-loop metabolism-related functions were selected based on literature searches: we focused on the RNA/DNA helicases *AQR*,

SETX, and *DHX9* involved in R-loop unwinding[19,43,44], the DNA helicase *PIF1* known to prevent the accumulation of R-loops at tRNA genes[45], the DNA topoisomerase *TOP3B*, which also prevents accumulation of R-loops[46], the endonuclease *RNASEH2* which, like RNase H1 cleaves the RNA strand in RNA/DNA hybrids[47], the splicing factor *SRSF1*, known to prevent R-loop formation[48], *THOC1* and *THOC2*, components of the

THO/TREX complex involved in mRNA export and R-loop prevention[49], the THO/TREX complex associated histone deacetylase *SIN3A*[50], and the six components of the TREX-2 complex that, with *BRCA2*, is also associated with mRNA export and R-loop prevention[51]. Several of these genes were recurrently (in up to 36% of gastric cancer cases) affected by CNVs and/or missense or frameshift mutations, with the most recurrently affected genes belonging to the TREX-2 complex (*ENY2, MCM3AP, SEM1, CETN3*) or having RNA/DNA helicase or endonuclease activity (*SETX, AQR, DHX9, RNASEH2*) (Supplementary Fig. 7c). Mutations in R-loop metabolism genes were largely predicted to be damaging mutations, and—not unexpectedly—were mostly detected in the microsatellite-instable subtype of gastric cancer that exhibited the highest overall mutational burden; CNVs affecting R-loop genes were mostly detected in the chromosomally instable subtype (Supplementary Fig. 7c). In conclusion, the mutational landscape of gastric cancer provides circumstantial evidence for the hypothesis that *H. pylori* infection favors chromosomal instability, and that the inactivation of genes encoding helicases, RNases and other factors involved in R-loop prevention or processing may be an early event in gastric carcinogenesis, predisposing *H. pylori*-infected cells to aberrant R-loop accumulation and its potentially deleterious consequences.

Discussion

It is now widely accepted that Gram-negative bacteria are sensed by epithelial cells via their production of LPS biosynthetic intermediates, which bind directly to ALPK1 to induce downstream TIFA/NF-κB signaling. The mechanisms through which LPS intermediates such as HBP and β-ADP-heptose reach the host cell cytosol likely differ across bacterial species and, in the case of *H. pylori*, appear to involve a functional T4SS[21–23]. Our data corroborate this notion, as the loss of a key enzyme (RfaE) involved in HBP and β-ADP-heptose synthesis phenocopies the loss of the T4SS-encoding Cag-PAI of *H. pylori* in all DNA-damage-related settings examined here. Other functions of the Cag-PAI, such as the delivery of the only known T4SS protein substrate CagA, are unaffected by RfaE deficiency. We and others have reported previously that the DNA damage induced by *H. pylori* in its epithelial target cells is dependent on a functional T4SS[16–18], and is largely restricted to transcribed regions of the genome[17]. These earlier observations are consistent with the model emerging from the current findings, where co-occurring active replication and transcription in S-phase cells leads to R-loop formation, which is followed by the processing of both the RNA and the DNA strands of the RNA/DNA hybrid by dedicated enzymes (Supplementary Fig. 8). The nucleolytic processing of DNA in such structures is in turn sensed by DNA repair factors such as 53BP1 and can be readily visualized and quantified by pulsed-field gel electrophoresis and immunofluorescence microscopy.

NF-κB has emerged in the course of our studies as the dominant transcription factor driving the early, ALPK1/TIFA-dependent response to *H. pylori*. The increase in incorporation of 5-FU —which served as our readout of de novo RNA synthesis— due to *H. pylori* infection was almost completely blocked not only by a general inhibitor of RNA-Pol II, but also by a highly specific inhibitor of NF-κB nuclear translocation. The same treatments prevented R-loop formation, replication fork slowing, and DNA damage. NF-κB was initially established as a key molecular link between inflammation and cancer[52] by two seminal studies showing that NF-κB has tumor-promoting properties in settings of inflammation-associated cancers of the colon and the liver[53,54]. NF-κB promotes carcinogenesis in such particularly susceptible organs through both tumor-cell-intrinsic and -extrinsic mechanisms (recently reviewed in ref. [52]). NF-κB on

the one hand acts directly in tumor cells by promoting the production of reactive oxygen and nitrogen species, which induce DNA damage and oncogenic mutations[55] and by promoting cell survival through the activation of anti-apoptotic genes such as BCL-X$_L$ and BCL-2[56,57]. On the other hand, NF-κB activation in various cell types of the tumor microenvironment, especially myeloid cells and cancer-associated fibroblasts, promotes tumor growth and dissemination through the production of cytokines (with TNF-α and IL-6 being the best-understood pro-tumorigenic NF-κB targets), chemokines, and pro-angiogenic factors[58]. Our data additionally implicate NF-κB activation in genomic instability through co-transcriptional R-loop formation that is associated with replication stress and DNA damage. Not every pathway to NF-κB activation is equally prone to R-loop induction and DNA damage; we have extensively tested TNF-α, which activates IKK and NF-kB via the TRADD, TRAF2, NIK signaling axis[59] and bypasses ALPK1 and TIFA, and never found evidence of R-loops or DNA damage in this setting. TNF-α also fails to synergize with the non-genotoxic *RfaE* mutant to induce DNA damage. These results indicate that NF-κB signaling is required, but not sufficient, to induce DNA damage in actively transcribing/ replicating cells.

Two scenarios are conceivable that are not easily distinguished experimentally but would both explain R-loop formation in the context of *H. pylori*-induced NF-κB activation. As shown by multiple laboratories in various models systems—ranging from bacteria, to yeast, to mammalian cells—R-loops may either form as a consequence of head-on collisions between a replication fork and transcription bubble as proposed previously, or alternatively, may form in highly transcribed regions of the genome, where they cause pausing of RNA-Pol II, which in turn blocks the progression of oncoming replication forks[38,60–63]. Irrespective of the sequence of events, we find that R-loop accumulation upon *H. pylori* exposure promotes S-phase-specific DNA damage, as overexpression of RNase H1 reduces DNA damage and abrogates replication stress. Both suppressive effects of RNase H1 require its enzymatic activity as they are not observed with a catalytically dead version of the enzyme. R-loops have been linked not only to DNA damage, genomic instability, and chromosomal rearrangements, but also to oncogenesis[51,61,64–66]. Increased transcriptional activity resulting from oncogene activation is known to promote R-loop accumulation and replication stress. This has been well documented for HRAS^{V12} overexpression, which through elevated expression of the general transcription factor TATA-box binding protein leads to increased RNA synthesis, R-loop accumulation, replication fork slowing, and DNA damage[66]. In breast cancer cells, R-loops accumulate and drive DNA damage in heavily transcribed estrogen-induced genes, and translocations and structural variants are found in genes induced by estrogen signaling[67]. In the scenarios described by these two studies, the transcriptional landscape of cancer cells appears to dictate where DNA damage occurs through R-loop formation. Future studies integrating data from ChIP-seq-based surveys (for example, by pull-down of R-loop-associated DNA with the RNA/ DNA hybrid-specific antibody S9.6) with transcriptional profiling and mutational data for gastric cancer and its precursor lesions will reveal whether certain heavily transcribed (NF-κB-regulated) loci are particularly prone to R-loop-dependent DNA damage and mutagenesis.

Several molecular mechanisms have been implicated in R-loop-induced DNA damage. On the one hand, persistent RNA/DNA hybrids may compromise DNA repair by blocking access of DNA repair factors to DNA DSBs[68], or by reducing the efficiency of DNA end resection, which determines whether repair proceeds via homologous recombination or non-homologous end joining[69]. An alternative mechanism that has been proposed to link R-loops to DNA damage posits that nucleotide excision repair

(NER) enzymes XPG and XPF cut the DNA in the RNA/DNA hybrid, producing a single-strand gap that is converted into a DSB by replication or additional strand breaks[19]. Having shown previously that the depletion of XPF or XPG reduces DNA DSBs upon *H. pylori* infection[18], our combined data are consistent with a model where the processing of R-loops by NER factors, rather than compromised DNA repair in the face of R-loops, link R-loop formation to DNA damage (Supplementary Fig. 8).

The physiological prevention and/or processing of R-loops requires a number of factors (RNA processing and splicing factors, helicases and nucleases), some of which were found in this study to be recurrently mutated or subject to copy number losses in gastric cancer. In particular, the genes encoding RNase H2 and the RNA/DNA helicase Aquarius (*AQR*), and genes encoding the components of the TREX-2 mRNA export complex—all known to be involved in R-loop processing or prevention[45,51,60,70] were recurrently subjected to CNVs or mutated in gastric cancer, and especially in the microsatellite instable and chromosomally instable subtypes of the disease. In agreement with the hypothesis that *H. pylori*-induced DNA damage causes genotoxicity and predisposes to mutagenesis, we find more mutations, and different mutation patterns, in gastric cancer samples of patients with evidence of *H. pylori* presence at the time of diagnosis. As the diagnosis of *H. pylori* presence in non-human sequences of gastric cancer and adjacent tissue is prone to false-negative (not so much false-positive) results, the differences observed in the mutational burden need to be interpreted with caution; this is especially true because *H. pylori* disappears from its gastric niche as intestinal metaplasia and other gastric cancer precursor lesions form. We propose that inactivating mutations or copy number losses in genes involved in the prevention or elimination of R-loops are early events in gastric cancer that predispose hyper-proliferating cells to *H. pylori*-induced R-loop accumulation and DNA damage. Immunohistochemical staining of consecutive sections for proliferating cells and for *H. pylori* suggests that live bacteria may indeed come in direct contact with replicating cells in gastric corpus glands of gastritis patients. In summary, we propose here a mechanism of transcription-associated R-loop formation linked to DNA damage that may connect innate immunity to DNA damage, and bacterial infection to carcinogenesis.

Methods

Cell culture, bacterial strains, and infection conditions. Wild-type AGS cells (ATCC CRL 1739, a human gastric adenocarcinoma cell line) and AGS cells subjected to TIFA and ALPK1 deletion by CRISPR, and to TIFA complementation with the wild-type *TIFA* gene[21,22] were grown in RPMI supplemented with 10% fetal calf serum (FCS), 100 U/ml penicillin, and 100 μg/ml streptomycin. U2OS (ATCC HTB96, a human osteosarcoma cell line) T-Rex cell lines carrying pAIO vectors for the expression of RNase H1/GFP or RNase H1[D210N]/GFP were cultivated in Dulbecco's modified Eagle's medium (DMEM) supplemented with 10% FCS (Tet-free approved), 100 U/ml penicillin, and 100 μg/ml streptomycin, 50 μg/ml hygromycin B and 1 μg/ml puromycin. Doxycycline (1 ng/ml) was added for 24 h to induce the expression of recombinant RNase H1 and to downregulate the endogenous RNH1 expression. BAY 11-7082 and triptolide were purchased from Sigma-Aldrich. *H. pylori* was grown on solid medium on horse blood agar containing 4% Columbia agar base (Oxoid; Basingstoke), 5% defibrinated horse blood (HemoStatLabs), 0.2% β-cyclodextrin, 5 μg/ml trimethoprim, 8 μg/ml amphotericin B, 10 μg/ml vancomycin, 5 μg/ml cefsulodin, and 2.5 U/ml poly-myxin B sulfate (all from Sigma-Aldrich) at 37 °C for 2 days under microaerophilic conditions. For liquid culture, *H. pylori* was grown in Brucella broth (Difco) containing 10% FBS (Life Technologies) with shaking in a microaerobic atmosphere at 37 °C. Bacterial numbers were determined by measuring the optical density at 600 nm, and bacteria were added to cells at an MOI of 20 or 50 for 6 h. The following strains of *H. pylori* were used: G27[71], P12 wild-type, P12ΔPAI[72], and P12ΔRfaE[22]. All *H. pylori* liquid cultures were routinely assessed by light microscopy for contamination, morphology, and motility prior to use in infections.

Two-dimensional gastric organoid culture and *H. pylori* infection. Human tissues were obtained from patients of the University Clinic, Wuerzburg. This study

was approved by the ethical committee of the University of Wuerzburg's University Clinic (approval 37/16). Gastric organoids were initiated from tissues[30] and for infection in 2D, were sheared to single cells and seeded in coated μ-slide coverslips (IBIDI, 8 Well, Cat. No. 80826) in antibiotic-free culture medium: Advanced Dulbecco's modified Eagle medium (DMEM)/F12 supplemented with 10 mmol/L HEPES, GlutaMAX, 1× B27, 1 mmol/L N-acetylcysteine, 50 ng/mL epidermal growth factor (EGF) (all from Invitrogen, Waltham, MA), 10% noggin-conditioned medium, 10% R-spondin1-conditioned medium, 50% Wnt-conditioned medium, 200 ng/mL fibroblast growth factor (FGF)10 (Peprotech, Hamburg, Germany), 1 nmol/L gastrin (Tocris, Bristol, UK), and 2 mmol/L transforming growth factor (TGF)βi (A-83-01; Tocris). After seeding, 10 mmol/L rho-associated coiled-coil forming protein serine/threoninekinase (RHOK) (Y-27632; Sigma-Aldrich) was added. The medium was refreshed every 2–3 days. Liquid cultures of *H. pylori* were prepared as described above. Cells were infected on day 7 or 8 at 50% confluency with an MOI of 50 or treated with α-ADP-heptose and β-ADP-heptose, respectively, at a final concentration of 0.5 μM for 6 h. Supernatants were collected for ELISA. Cells were subjected to immunofluorescence microscopy.

Cytokinesis-block micronuclei assay. Cells were grown on autoclaved coverslips and supplemented with 2 μg/ml Cytochalasin B prior to infection with *Helicobacter pylori* (P12 wild-type, P12ΔRfaE) for 12 h. Cells were washed three times with 1× PBS and then fixed with 4% paraformaldehyde for 15 min at RT. After washing three times with 1× PBS cells were stained with 1 μg/ml DAPI diluted in distilled water for 5 min at RT. Coverslips were mounted with Fluoromount-G mounting medium (Invitrogen, 00-4958-02). Images were acquired with a Leica DM6B fluorescent microscope. In each experiment micronuclei of at least 100 binucleated cells were counted per condition.

Flow cytometric quantification of apoptosis and reactive oxygen species formation. For quantification of reactive oxygen species, AGS cells were stained with 25 μM 2′,7′-dichlorofluorescein diacetate (DCFDA, Abcam, ab113851) and infected with *Helicobacter pylori* or treated with 50 μM Tert-Butyl Hydrogen Peroxide (TBHP, Abcam, ab113851) for 6 h. Cells were harvested, resuspended in 1× PBS/1%BSA and subjected to flow cytometry. Apoptosis was quantified by Annexin V staining. Cells were infected with *Helicobacter pylori* or treated with 5 μM Staurosporin for 6 or 24 h. After harvesting cells were stained with PE-Cy7-labeled Annexin V (BioLegend, Cat No. 559934) diluted in 1x Annexin V Binding buffer (BD Bioscience, Cat No 640950) for 15 min at RT in the dark. Data were acquired on a CyAn ADP (Beckman Coulter) flow cytometer and analyzed with the FlowJo software (TreeStar).

5-Fluorouridine incorporation and staining. Cells grown on coverslips were infected with *Helicobacter pylori* or treated as described above and pulse-labeled with 1 mM 5-Fluorouridine (F5130, Sigma-Aldrich) for the last 30 min of the experiment. After incubation, cells were washed with PBS, pre-extracted with pre-extraction buffer (25 mM Hepes-NaOH, pH 7.7, 50 mM NaCl, 1 mM EDTA, 3 mM MgCl₂, 0.3 M sucrose, 0.5% Triton X-100) for 5 min on ice and fixed with 4% formaldehyde (F8775, Sigma-Aldrich) in PBS for 15 min (in the dark, room temperature), washed with PBS and fixed with ice-cold methanol for 20 min (in the dark, −20 °C). After fixation, coverslips were washed with PBS and blocked with 1% BSA in PBS for 10 min and then stained with mouse monoclonal anti-BrdU antibody (clone BU-33, which recognizes 5-Fluorouridine, B2531, Sigma-Aldrich) in 1% BSA in PBS and with polyclonal rabbit anti-PCNA antibody (ab18197, Abcam) for 120 min. After washing with PBS, coverslips were incubated with Alexa Fluor 568-conjugated secondary antibody (Invitrogen, a11031), AF647 goat anti-rabbit (Invitrogen, a21245) in 1% BSA in PBS, counterstained with DAPI and mounted using Fluoromount-G mounting media (Invitrogen). Images were captured on Olympus IX83 microscope equipped with ScanR imaging platform using 40×/0.9 NA dry objective. For analysis images were submitted to ScanR Analysis software based on signal intensity for FU. Nuclei were identified based on the DAPI signal. Approximately 1000 cells were measured per condition.

Immunofluorescence microscopy. Cells grown on autoclaved coverslips were infected with *Helicobacter pylori* or treated as described above for 6 h. After the infection/treatment, cells were washed three times with 1× PBS and then permeabilized for 5 min with pre-extraction solution (25 mM Hepes, pH 7.7; 50 mM NaCl; 1 mM EDTA; 3 mM MgCl2; 300 mM sucrose, 0.5% Triton X-100) on ice. After a brief wash with 1× PBS, cells were fixed with 4% paraformaldehyde for 15 min at RT in the dark. For PCNA immunofluorescence, after fixation with paraformaldehyde, cells were washed three times with 1× PBS and then fixed with ice-cold methanol for 20 min at −20 °C. After fixation, cells were washed three times with 1× PBS and blocked in 1% BSA/1× PBS for 20 min at RT. Coverslips were then incubated with appropriate primary antibodies diluted in 1% BSA/1× PBS for 90 min at RT in dark. The following antibodies and dilutions were used: anti-phospho Histone H2A.X (Ser139) mouse monoclonal (Millipore, 05-636-AF647, 1:300), anti-53BP1 rabbit polyclonal (Santa Cruz, sc-33760, 1:300), and anti-PCNA Mouse monoclonal (Santa Cruz, sc56, 1:250). Coverslips were washed three times with 1× PBS and then incubated with secondary antibodies diluted in 1% BSA/1× PBS for 30 min at RT in dark. Secondary antibodies and dilutions were

Alexa Fluor 488 Goat Anti-Rabbit IgG (Life Technologies, A11034, 1:400), Alexa Fluor 568 Goat Anti-Rabbit (Life Technologies, A11036, 1:400), Alexa Fluor 568 Goat Anti-Mouse (Life Technologies, A11031, 1:400), Alexa Fluor 647 Goat Anti-Rabbit (Life Technologies, A21245, 1:400), and Alexa Fluor 647 Goat Anti-Mouse (Invitrogen, A21235, 1:400). After three washes with 1× PBS, coverslips were stained with 1 μg/ml DAPI diluted in distilled water for 2 min at RT in dark. Coverslips were mounted with Fluoromount-G mounting medium (Invitrogen, 00-4958-02). Images were acquired with a Leica DM6B fluorescent microscope or Leica SP8 inverted confocal microscope. For the analysis of phosphorylated H2AX signal and 53BP1 foci, automated image acquisition was performed on a IX83 microscope (Olympus) equipped with ScanR imaging platform using a 40×/0.9 NA objective. The analysis of acquired images was performed using ScanR Analysis software. For the analysis of RNH1-GFP foci, images were acquired using GE IN Cell Analyzer 2500HS with a 40×/1.15 NA water-immersion objective and the analysis was performed using CellProfiler 3.1.5[73]. Nuclei were identified based on the DAPI signal and the parameters of interest were analyzed for each nuclear object using modules of the ScanR Analysis software or CellProfiler 3.1.5.

Pulsed-field gel electrophoresis (PFGE). For PFGE, cells were harvested, embedded in 1.5% agarose plugs (5×10^5 cells/plug), digested in lysis buffer (100 mM EDTA, 1% (w/v) sodium lauryl sarcosyne, 0.2% (w/v) sodium deoxycholate, 1 mg/ml proteinase K) at 37 °C for 48 h and washed in TE (20 mM Tris-HCl (pH 8.0), 50 mM EDTA). Electrophoresis was performed for 23 h at 14 °C in 0.9% (w/v) pulsed-field-certified agarose (Bio-Rad) containing Tris-borate/EDTA buffer according to the conditions described in ref. [74] and adapted to a Bio-Rad CHEF DR III apparatus. Gels were stained with ethidium bromide and imaged on an Alpha Innotech Imager. Two images were taken of each gel with 8 and 100 ms exposure time, respectively. For quantification, the signal intensity of the fragmented DNA (which has migrated into the gel and formed a distinct band) after 100 ms exposure time was normalized to the signal intensity of intact DNA (retained in the loading pocket) of the same sample at 8 ms exposure.

DNA fiber assay. For the analysis of DNA fiber length, cells were sequentially pulse-labeled with 30 mM CldU (Sigma-Aldrich) and 250 mM IdU (European Pharmacopoeia) for 30 min each. The cells were collected and resuspended in PBS at 2.5×10^5 cells per ml. The labeled cells were diluted 1:1 (v/v) with unlabeled cells, and 3 μl of cells were mixed with 7 μl of lysis buffer (200 mM Tris-HCl (pH 7.5), 50 mM EDTA, and 0.5% (w/v) SDS) on a glass slide. After 9 min, the slides were tilted to 15–45°, and the resulting DNA spreads were air-dried and fixed in methanol/acetic acid (3:1) solution overnight at 4°. The DNA fibers were denatured with 2.5 M HCl for 60 min, washed several times with PBS to neutralize the pH, and blocked with 0.1% Tween 20 in 2% BSA/PBS for 40 min. The newly replicated CldU and IdU tracks were labeled for 2.5 h in the dark, at room temperature, with anti-BrdU antibodies recognizing CldU (rat, Abcamab6326, 1:500) and IdU (mouse, BD 347580 B44, 1:100), followed by 1 h incubation with secondary antibodies at room temperature in the dark: anti-mouse Alexa Fluor 488 (1:300, A11001, Invitrogen) and anti-rat Cy3 (1:150, 712-166-153, Jackson ImmunoResearchLaboratories). Fibers were visualized on a Leica DMI 6000 inverted microscope using an HCX Plan APO DIC 63x oil objective (1.4–0.6 NA) and analyzed using Fiji[75]. At least 100 fibers were analyzed per replicate condition. Fork speed in kb/min was calculated by multiplying the measured length in μm with a conversion factor of 2.59 kb/μm and dividing by the duration of the labeling pulse[34].

Immunohistochemistry. Consecutive gastric formalin-fixed and paraffin-embedded sections from six patients presenting with *H. pylori*-associated gastritis and three patients with normal gastric mucosa were either stained with hematoxylin and eosin (H&E) or pretreated with CC1 buffer (Ventana Roche) for 16 min at 100 °C prior to staining with either Ki67 rabbit monoclonal antibody (clone 30-9, Ventana Roche) or with anti-*H. pylori* polyclonal rabbit antibody (B0471, Dako) for 30 min at 36 °C. Immunohistochemical staining and detection were performed using the BenchMark Ultra system (Ventana Roche) and OptiView DAB IHC Detection kit (Roche). Slides were scanned using the Hamamatsu Nanozoomer HAT scanner and analyzed using NDP.view version 2. The study was approved by the Cantonal Ethics Committee of Zurich (KEK).

Western blotting. AGS cells were infected with *H. pylori* or treated as described above for 6 h. Cells were harvested and lysed using 50 μl RIPA buffer (Sigma-Aldrich, Cat. No. R0278-50ML) supplemented with 1× complete protease inhibitor cocktail (Roche). Protein concentrations were determined using Bradford assay (Bio-Rad, Cat No. 5000002) and equal amounts were separated by SDS/PAGE (10% gel) followed by transfer onto nitrocellulose membranes (GE Healthcare Life Sciences, Cat No. 10600023). Membranes were incubated with antibodies against β-Actin (CST, 3700), p-KAP1 (S824) (Abcam, ab70369), and p-ATM (Abcam, ab81292).

TCGA data analysis and annotation of *H. pylori* status. TCGA stomach adenocarcinoma mutation and copy number data were downloaded with the R package TCGAbiolinks[76]. Copy number thresholds were taken from the TCGA

CNV pipeline (−0.3 for loss and 0.3 for gain). Molecular subtyping was performed based on a previous publication[42]. The Oncoprint-like plot was generated using the R package ComplexHeatmap[77]. Damaging mutations were defined by having a "deleterious" annotation from SIFT and "damaging" annotation from PolyPhen. To annotate stomach adenocarcinoma (STAD) samples from TCGA with *H. pylori* status, we acquired whole-genome (WGS), whole-exome (WXS), and transcriptome (RNA-seq) sequencing data from TCGA via the application programming interface (API) of the National Cancer Institute's (NCI) Genomic Data Commons (GDC). Raw sequencing data in bam format were screened for *H. pylori* and other microbiota using the PathSeq pipeline[78], which is available through the Broad Institute's Genome Analysis Toolkit (GATK v4.0.3). The PathSeq analysis was performed using prebuilt human and microbial reference genomes from the PathSeq resource bundle, available through the Broad Institute's Genome Sequence Archive (GSA) FTP server. All sequencing data were analyzed using a local high-performance computing cluster. *H. pylori* status of a sample was determined by having at least 1 unambiguous read in either WGS or RNAseq from the tumor tissue or either WGS, WES, or RNAseq from normal adjacent tissue.

Statistics. All statistical analysis was performed using Graph Pad prism 5.0 software. One-way ANOVA was used for statistical comparisons of groups of unequal sizes, followed by Dunn's multiple comparisons correction. Two-way ANOVA with Tukey's multiple comparisons correction was used wherever group sizes were identical. *P*-values are indicated as follows: *, <0.05; **, <0.01; ***, <0.005; ****, <0.001.

Reporting summary. Further information on research design is available in the Nature Research Reporting Summary linked to this article.

Data availability

The source data underlying Figs. 1–7 and Supplementary Figs. 1–7 are provided as source data files (Supplementary Data 1–13). All the other data supporting the findings of this study are available within the article and its Supplementary Information files. A Reporting Summary for this article is available as a Supplementary Information file. Access to TCGA gastric cancer data is available through the link: https://gdc.cancer.gov/about-data/publications/stad_2014.

References

1. Nomura, A. et al. *Helicobacter pylori* infection and gastric carcinoma among Japanese Americans in Hawaii. *N. Engl. J. Med.* **325**, 1132–1136 (1991).
2. Parsonnet, J. et al. *Helicobacter pylori* infection and the risk of gastric carcinoma. *N. Engl. J. Med.* **325**, 1127–1131 (1991).
3. Watanabe, T., Tada, M., Nagai, H., Sasaki, S. & Nakao, M. *Helicobacter pylori* infection induces gastric cancer in mongolian gerbils. *Gastroenterology* **115**, 642–648 (1998).
4. Lee, C. W. et al. *Helicobacter pylori* eradication prevents progression of gastric cancer in hypergastrinemic INS-GAS mice. *Cancer Res.* **68**, 3540–3548 (2008).
5. Fox, J. G. et al. *Helicobacter pylori*-associated gastric cancer in INS-GAS mice is gender specific. *Cancer Res.* **63**, 942–950 (2003).
6. Wang, T. C. et al. Synergistic interaction between hypergastrinemia and *Helicobacter* infection in a mouse model of gastric cancer. *Gastroenterology* **118**, 36–47 (2000).
7. Fox, J. G. et al. High-salt diet induces gastric epithelial hyperplasia and parietal cell loss, and enhances *Helicobacter pylori* colonization in C57BL/6 mice. *Cancer Res.* **59**, 4823–4828 (1999).
8. Fox, J. G. & Wang, T. C. Inflammation, atrophy, and gastric cancer. *J. Clin. Investig.* **117**, 60–69 (2007).
9. Huang, J. Q., Zheng, G. F., Sumanac, K., Irvine, E. J. & Hunt, R. H. Meta-analysis of the relationship between cagA seropositivity and gastric cancer. *Gastroenterology* **125**, 1636–1644 (2003).
10. Rieder, G., Merchant, J. L. & Haas, R. *Helicobacter pylori* cag-type IV secretion system facilitates corpus colonization to induce precancerous conditions in Mongolian gerbils. *Gastroenterology* **128**, 1229–1242 (2005).
11. Arnold, I. C. et al. Tolerance rather than immunity protects from *Helicobacter pylori*-induced gastric preneoplasia. *Gastroenterology* **140**, 199–209 (2011).
12. Jun, J. K. et al. Effectiveness of the Korean National Cancer Screening Program in reducing gastric cancer mortality. *Gastroenterology* **152**, 1319–1328 e1317 (2017).
13. Rokkas, T., Rokka, A. & Portincasa, P. A systematic review and meta-analysis of the role of *Helicobacter pylori* eradication in preventing gastric cancer. *Ann. Gastroenterol.* **30**, 414–423 (2017).

14. Choi, I. J., Kim, Y. I. & Park, B. *Helicobacter pylori* and prevention of gastric cancer. *N. Engl. J. Med.* **378**, 2244–2245 (2018).

15. Toller, I. M. et al. Carcinogenic bacterial pathogen *Helicobacter pylori* triggers DNA double-strand breaks and a DNA damage response in its host cells. *Proc. Natl Acad. Sci. USA* **108**, 14944–14949 (2011).

16. Hanada, K. et al. *Helicobacter pylori* infection introduces DNA double-strand breaks in host cells. *Infect. Immun.* **82**, 4182–4189 (2014).

17. Koeppel, M., Garcia-Alcalde, F., Glowinski, F., Schlaermann, P. & Meyer, T. F. *Helicobacter pylori* infection causes characteristic DNA damage patterns in human cells. *Cell Rep.* **11**, 1703–1713 (2015).

18. Hartung, M. L. et al. *H. pylori*-induced DNA strand breaks are introduced by nucleotide excision repair endonucleases and promote NF-kappaB target gene expression. *Cell Rep.* **13**, 70–79 (2015).

19. Sollier, J. et al. Transcription-coupled nucleotide excision repair factors promote R-loop-induced genome instability. *Mol. Cell* **56**, 777–785 (2014).

20. Sollier, J. & Cimprich, K. A. Breaking bad: R-loops and genome integrity. *Trends Cell Biol.* **25**, 514–522 (2015).

21. Gall, A., Gaudet, R. G., Gray-Owen, S. D. & Salama, N. R. TIFA signaling in gastric epithelial cells initiates the *cag* type 4 secretion system-dependent innate immune response to *Helicobacter pylori* infection. *mBio* **8**, https://doi.org/10.1128/mBio.01168-17 (2017).

22. Zimmermann, S. et al. ALPK1- and TIFA-dependent innate immune response triggered by the *Helicobacter pylori* type iv secretion system. *Cell Rep.* **20**, 2384–2395 (2017).

23. Stein, S. C. et al. *Helicobacter pylori* modulates host cell responses by CagT4SS-dependent translocation of an intermediate metabolite of LPS inner core heptose biosynthesis. *PLoS Pathog.* **13**, e1006514 (2017).

24. Pfannkuch, L. et al. ADP heptose, a novel pathogen-associated molecular pattern identified in *Helicobacter pylori*. *FASEB J.* **33**, 9087–9099 (2019).

25. Zhou, P. et al. Alpha-kinase 1 is a cytosolic innate immune receptor for bacterial ADP-heptose. *Nature* **561**, 122–126 (2018).

26. Milivojevic, M. et al. ALPK1 controls TIFA/TRAF6-dependent innate immunity against heptose-1,7-bisphosphate of gram-negative bacteria. *PLoS Pathog.* **13**, e1006224 (2017).

27. Gaudet, R. G. et al. INNATE IMMUNITY. Cytosolic detection of the bacterial metabolite HBP activates TIFA-dependent innate immunity. *Science* **348**, 1251–1255 (2015).

28. Vispe, S. et al. Triptolide is an inhibitor of RNA polymerase I and II-dependent transcription leading predominantly to down-regulation of short-lived mRNA. *Mol. Cancer Ther.* **8**, 2780–2790 (2009).

29. Kidane, D. Molecular Mechanisms of *H. pylori*-induced DNA double-strand breaks. *Int. J. Mol. Sci.* **19**, 2891 (2018).

30. Bartfeld, S. et al. In vitro expansion of human gastric epithelial stem cells and their responses to bacterial infection. *Gastroenterology* **148**, 126–136 (2015).

31. Bartfeld, S. & Clevers, H. Organoids as model for infectious diseases: culture of human and murine stomach organoids and microinjection of *Helicobacter pylori*. *JoVE* **105**, e53359 (2015).

32. Zeman, M. K. & Cimprich, K. A. Causes and consequences of replication stress. *Nat. Cell Biol.* **16**, 2–9 (2014).

33. Vindigni, A. & Lopes, M. Combining electron microscopy with single molecule DNA fiber approaches to study DNA replication dynamics. *Biophys. Chem.* **225**, 3–9 (2017).

34. Jackson, D. A. & Pombo, A. Replicon clusters are stable units of chromosome structure: evidence that nuclear organization contributes to the efficient activation and propagation of S phase in human cells. *J. Cell Biol.* **140**, 1285–1295 (1998).

35. Nieminuszczy, J., Schwab, R. A. & Niedzwiedz, W. The DNA fibre technique —tracking helicases at work. *Methods* **108**, 92–98 (2016).

36. Ray Chaudhuri, A. et al. Topoisomerase I poisoning results in PARP-mediated replication fork reversal. *Nat. Struct. Mol. Biol.* **19**, 417–423 (2012).

37. Rodriguez, R. et al. Small-molecule-induced DNA damage identifies alternative DNA structures in human genes. *Nat. Chem. Biol.* **8**, 301–310 (2012).

38. Crossley, M. P., Bocek, M. & Cimprich, K. A. R-loops as cellular regulators and genomic threats. *Mol. Cell* **73**, 398–411 (2019).

39. Aguilera, A. & Garcia-Muse, T. R loops: from transcription byproducts to threats to genome stability. *Mol. Cell* **46**, 115–124 (2012).

40. Garcia-Muse, T. & Aguilera, A. R loops: from physiological to pathological roles. *Cell* **179**, 604–618 (2019).

41. Teloni, F. et al. Efficient pre-mRNA cleavage prevents replication-stress-associated genome instability. *Mol. Cell* **73**, 670–683 (2019).

42. Bass, A. J. et al. Comprehensive molecular characterization of gastric adenocarcinoma. *Nature* **513**, 202–209 (2014).

43. Skourti-Stathaki, K., Proudfoot, N. J. & Gromak, N. Human senataxin resolves RNA/DNA hybrids formed at transcriptional pause sites to promote Xrn2-dependent termination. *Mol. Cell* **42**, 794–805 (2011).

44. Cristini, A., Groh, M., Kristiansen, M. S. & Gromak, N. RNA/DNA hybrid interactome identifies DXH9 as a molecular player in transcriptional

45. termination and R-loop-associated DNA damage. *Cell Rep.* **23**, 1891–1905 (2018).

45. Tran, P. L. T. et al. PIF1 family DNA helicases suppress R-loop mediated genome instability at tRNA genes. *Nat. Commun.* **8**, 15025 (2017).

46. Yang, Y. et al. Arginine methylation facilitates the recruitment of TOP3B to chromatin to prevent R loop accumulation. *Mol. Cell* **53**, 484–497 (2014).

47. Zimmer, A. D. & Koshland, D. Differential roles of the RNases H in preventing chromosome instability. *Proc. Natl Acad. Sci. USA* **113**, 12220–12225 (2016).

48. Li, X. & Manley, J. L. Inactivation of the SR protein splicing factor ASF/SF2 results in genomic instability. *Cell* **122**, 365–378 (2005).

49. Dominguez-Sanchez, M. S., Barroso, S., Gomez-Gonzalez, B., Luna, R. & Aguilera, A. Genome instability and transcription elongation impairment in human cells depleted of THO/TREX. *PLoS Genet.* **7**, e1002386 (2011).

50. Salas-Armenteros, I. et al. Human THO-Sin3A interaction reveals new mechanisms to prevent R-loops that cause genome instability. *EMBO J.* **36**, 3532–3547 (2017).

51. Bhatia, V. et al. BRCA2 prevents R-loop accumulation and associates with TREX-2 mRNA export factor PCID2. *Nature* **511**, 362–365 (2014).

52. Taniguchi, K. & Karin, M. NF-kappaB, inflammation, immunity and cancer: coming of age. *Nat. Rev. Immunol.* **18**, 309–324 (2018).

53. Greten, F. R. et al. IKKbeta links inflammation and tumorigenesis in a mouse model of colitis-associated cancer. *Cell* **118**, 285–296 (2004).

54. Pikarsky, E. et al. NF-kappaB functions as a tumour promoter in inflammation-associated cancer. *Nature* **431**, 461–466 (2004).

55. Grivennikov, S. I., Greten, F. R. & Karin, M. Immunity, inflammation, and cancer. *Cell* **140**, 883–899 (2010).

56. Luo, J. L., Kamata, H. & Karin, M. IKK/NF-kappaB signaling: balancing life and death–a new approach to cancer therapy. *J. Clin. Investig.* **115**, 2625–2632 (2005).

57. Grivennikov, S. et al. IL-6 and Stat3 are required for survival of intestinal epithelial cells and development of colitis-associated cancer. *Cancer Cell* **15**, 103–113 (2009).

58. Taniguchi, K. & Karin, M. IL-6 and related cytokines as the critical lynchpins between inflammation and cancer. *Semin Immunol.* **26**, 54–74 (2014).

59. Hayden, M. S. & Ghosh, S. Regulation of NF-kappaB by TNF family cytokines. *Semin. Immunol.* **26**, 253–266 (2014).

60. Allison, D. F. & Wang, G. G. R-loops: formation, function, and relevance to cell stress. *Cell Stress* **3**, 38–46 (2019).

61. Garcia-Rubio, M. L. et al. The fanconi anemia pathway protects genome integrity from R-loops. *PLoS Genet.* **11**, e1005674 (2015).

62. Lang, K. S. et al. Replication-transcription conflicts generate R-loops that orchestrate bacterial stress survival and pathogenesis. *Cell* **170**, 787–799 (2017).

63. Herrera-Moyano, E., Mergui, X., Garcia-Rubio, M. L., Barroso, S. & Aguilera, A. The yeast and human FACT chromatin-reorganizing complexes solve R-loop-mediated transcription-replication conflicts. *Genes Dev.* **28**, 735–748 (2014).

64. Schwab, R. A. et al. The fanconi anemia pathway maintains genome stability by coordinating replication and transcription. *Mol. Cell* **60**, 351–361 (2015).

65. Helmrich, A., Ballarino, M. & Tora, L. Collisions between replication and transcription complexes cause common fragile site instability at the longest human genes. *Mol. Cell* **44**, 966–977 (2011).

66. Kotsantis, P. et al. Increased global transcription activity as a mechanism of replication stress in cancer. *Nat. Commun.* **7**, 13087 (2016).

67. Stork, C. T. et al. Co-transcriptional R-loops are the main cause of estrogen-induced DNA damage. *eLife* **5**, e17548 (2016).

68. Aguilera, A. & Gomez-Gonzalez, B. DNA-RNA hybrids: the risks of DNA breakage during transcription. *Nat. Struct. Mol. Biol.* **24**, 439–443 (2017).

69. Costantino, L. & Koshland, D. Genome-wide map of R-loop-induced damage reveals how a subset of R-loops contributes to genomic instability. *Mol. Cell* **71**, 487–497 e483 (2018).

70. Sakasai, R. et al. Aquarius is required for proper CtIP expression and homologous recombination repair. *Sci. Rep.* **7**, 13808 (2017).

71. Censini, S. et al. *cag*, a pathogenicity island of *Helicobacter pylori*, encodes type I-specific and disease-associated virulence factors. *Proc. Natl Acad. Sci. USA* **93**, 14648–14653 (1996).

72. Gorrell, R. J. et al. A novel NOD1- and CagA-independent pathway of interleukin-8 induction mediated by the *Helicobacter pylori* type IV secretion system. *Cell Microbiol.* **15**, 554–570 (2013).

73. Carpenter, A. E. et al. CellProfiler: image analysis software for identifying and quantifying cell phenotypes. *Genome Biol.* **7**, R100 (2006).

74. Hanada, K. et al. The structure-specific endonuclease Mus81 contributes toreplication restart by generating double-strand DNA breaks. *Nat. Struct. Mol. Biol.* **14**, 1096e1104 (2007).

75. Schindelin, J. et al. Fiji: an open-source platform for biological-image analysis. *Nat. Methods* **9**, 676–682 (2012).

76. Colaprico, A. et al. TCGAbiolinks: an R/Bioconductor package for integrative analysis of TCGA data. *Nucleic Acids Res.* **44**, e71 (2016).
77. Gu, Z., Eils, R. & Schlesner, M. Complex heatmaps reveal patterns and correlations in multidimensional genomic data. *Bioinformatics* **32**, 2847–2849 (2016).
78. Kostic, A. D. et al. PathSeq: software to identify or discover microbes by deep sequencing of human tissue. *Nat. Biotechnol.* **29**, 393–396 (2011).

Acknowledgements

Author contributions

M.B., Z.N., A.M., and S.L. performed experiments and analyzed the data. M.J. and S.B. planned and performed gastric organoid experiments together with M.B.; A.G., N.R.S., R.H., M.S., L.P., J.D., and T.F.M. provided critical reagents, cell lines, and bacterial mutants. J.D. supervised. Z.N., A.T., and A.W. contributed human gastritis samples and performed IHC experiments. P.F.C. performed TCGA data analysis with input from M.P.L. and A.W. A.D. and X.S. annotated TCGA data with the *H. pylori* status. P.J. and A.M. conceived the study, analyzed the data, and wrote the manuscript.

Competing interests

The authors declare no competing interests.

Additional information

Supplementary information is available for this paper at https://doi.org/10.1038/s41467-020-18857-z.

Correspondence and requests for materials should be addressed to P.J. or A.M.

Peer review information *Nature Communications* thanks the anonymous reviewers for their contribution to the peer review of this work. Peer reviewer reports are available.

Reprints and permission information is available at http://www.nature.com/reprints

Publisher's note Springer Nature remains neutral with regard to jurisdictional claims in published maps and institutional affiliations.
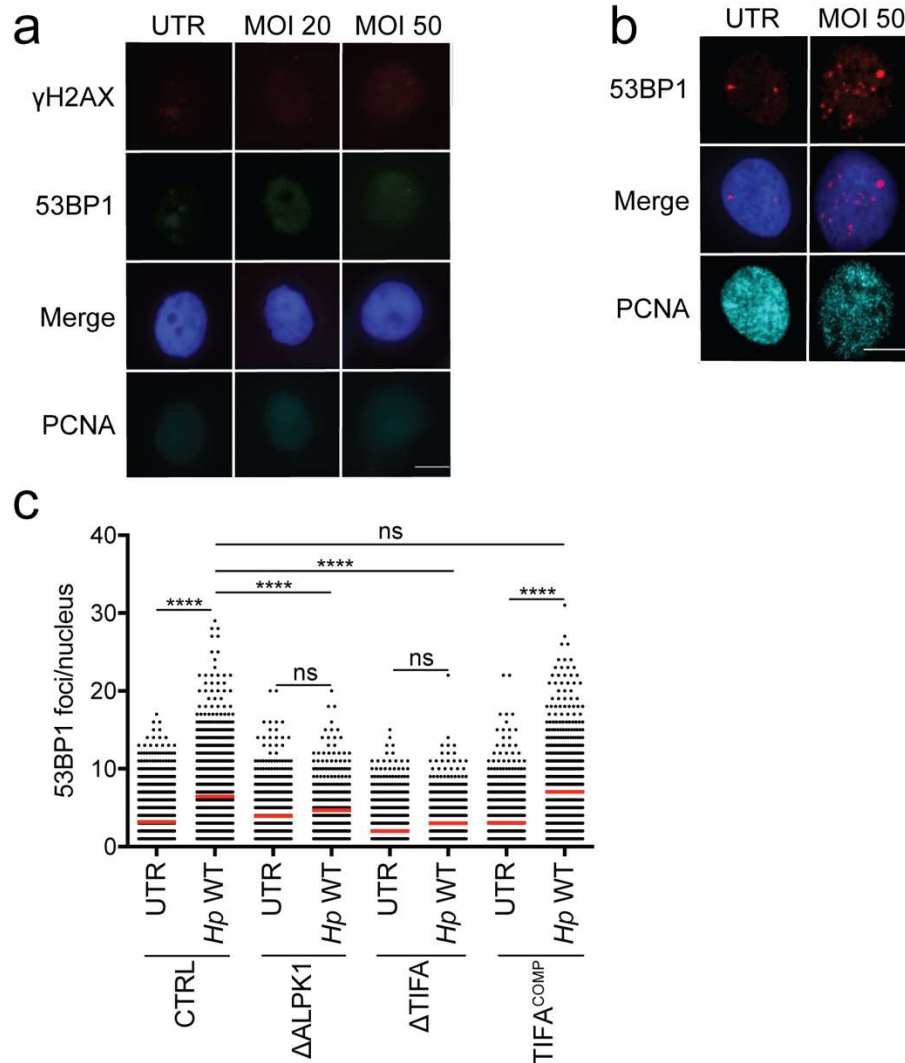
The ALPK1/TIFA/NF-κB axis links a bacterial carcinogen to R-loop-induced replication stress

Bauer/Nascakova/Mihai et al., Nature Communications 2020

Supplementary Information

Supplementary Figures 1-8

Supplementary Fig. 1. ***H. pylori*** **induces DNA DSBs in gastric epithelial cells that depend on a functional ALPK1/TIFA signaling axis and occur in S-phase. a** Wild type AGS cells were infected for 6 hours with *H. pylori* strain P12 at MOIs of 20 and 50 and subjected to immunofluorescence staining for phosphorylated H2AX (γH2AX), 53BP1 and PCNA as well as DAPI. Images of PCNA⁻ cells are representative of three independently conducted experiments. **b** Wild type AGS cells were infected for 6 hours with *H. pylori* strain G27 at MOI 50 and stained for 53BP1 and PCNA as well as DAPI. Images of PCNA⁺ cells are representative of three independently conducted experiments. Scale bar in a and b, 10 μm. **c** The indicated mutant cell lines in the AGS background were infected for 6 hours with *H. pylori* strain P12 at MOI 50 and subjected to immunofluorescence staining for phosphorylated H2AX (γH2AX), 53BP1 and PCNA as well as DAPI. Scatter dot plots of >811 and up to 2424 PCNA-positive cells per condition are shown. Data are pooled from three independent experiments. P-values in c were calculated by one-way ANOVA with Dunn's multiple comparisons correction; ns, not significant; ****p < 0.0001. Note that the ALPK1 ko cell line shown here was generated independently of the one shown in Figure 1.
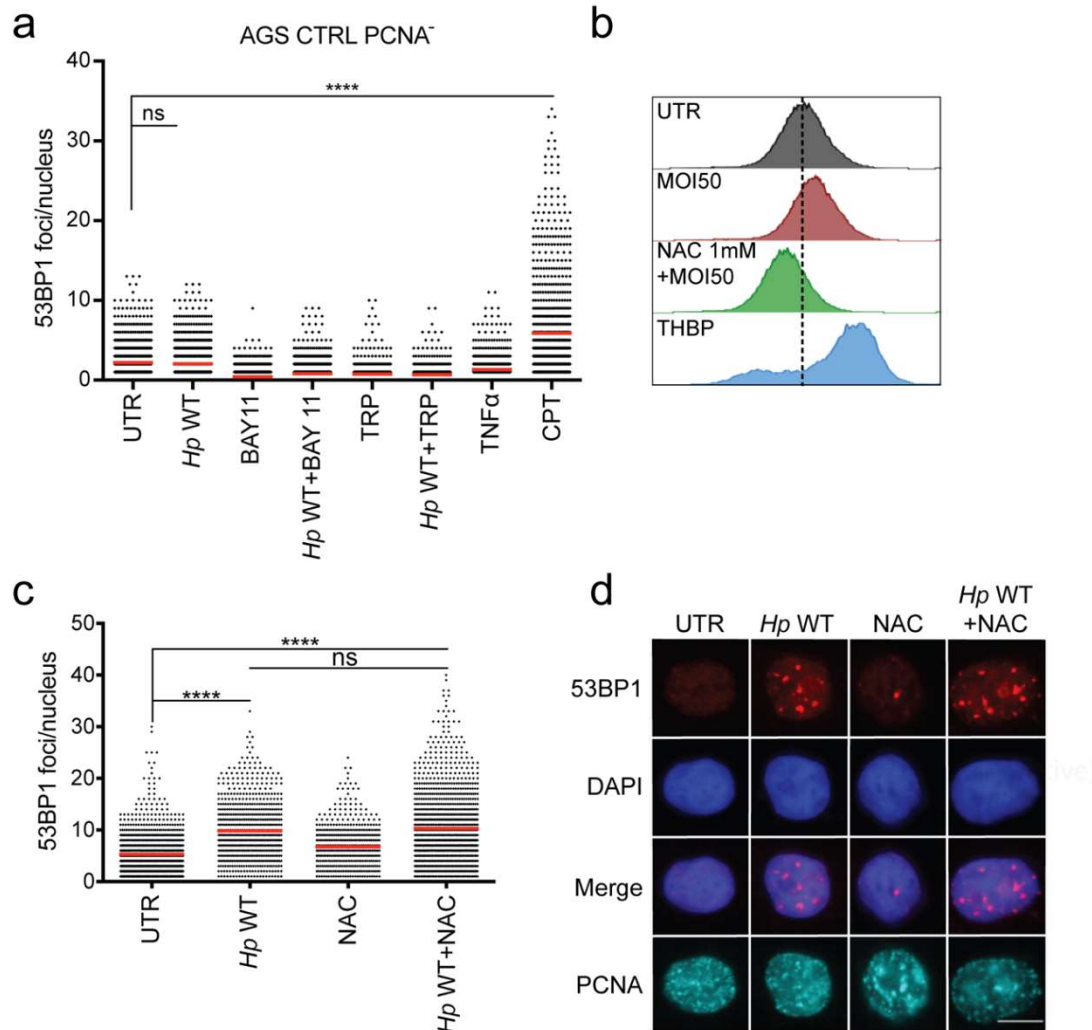
Supplementary Fig. 2. *H. pylori*-induced DNA DSBs are specific to S-phase cells and not caused by reactive oxygen species. a AGS cells were infected for 6 hours with *H. pylori* P12 at an MOI of 50 in the presence or absence of the NF-κB inhibitor BAY 11-7082 and the transcription inhibitor triptolide (1 μM and 100 nM final concentration, respectively), or were treated with 10 nM TNF-α or 100 nM camptothecin (CPT) for 6 hours, and subjected to immunofluorescence staining for 53BP1 and PCNA as well as DAPI. Scatter dot plots of >422 and up to 903 PCNA-negative cells per condition are shown. Data are pooled from three independent experiments. **b-d** AGS cells were infected for 6 hours with *H. pylori* P12 at an MOI of 50 in the presence or absence of N-acetyl-cysteine (NAC) at 1 mM final concentration. ROS formation as detected by flow cytometry of DCFDA-stained (FITC) cells is shown in b (treatment with 50 μM Tert-Butyl Hydrogen Peroxide -TBHP- for 6 hours served as positive control) and scatter dot plots of >895 and up to 1110 PCNA-positive cells per condition are shown in c alongside representative images in d (scale bar 10 μm). Data in c are pooled from three independent experiments. P-values in a and c were calculated by one-way ANOVA with Dunn's multiple comparisons correction; ns, not significant; ****$p < 0.0001$.
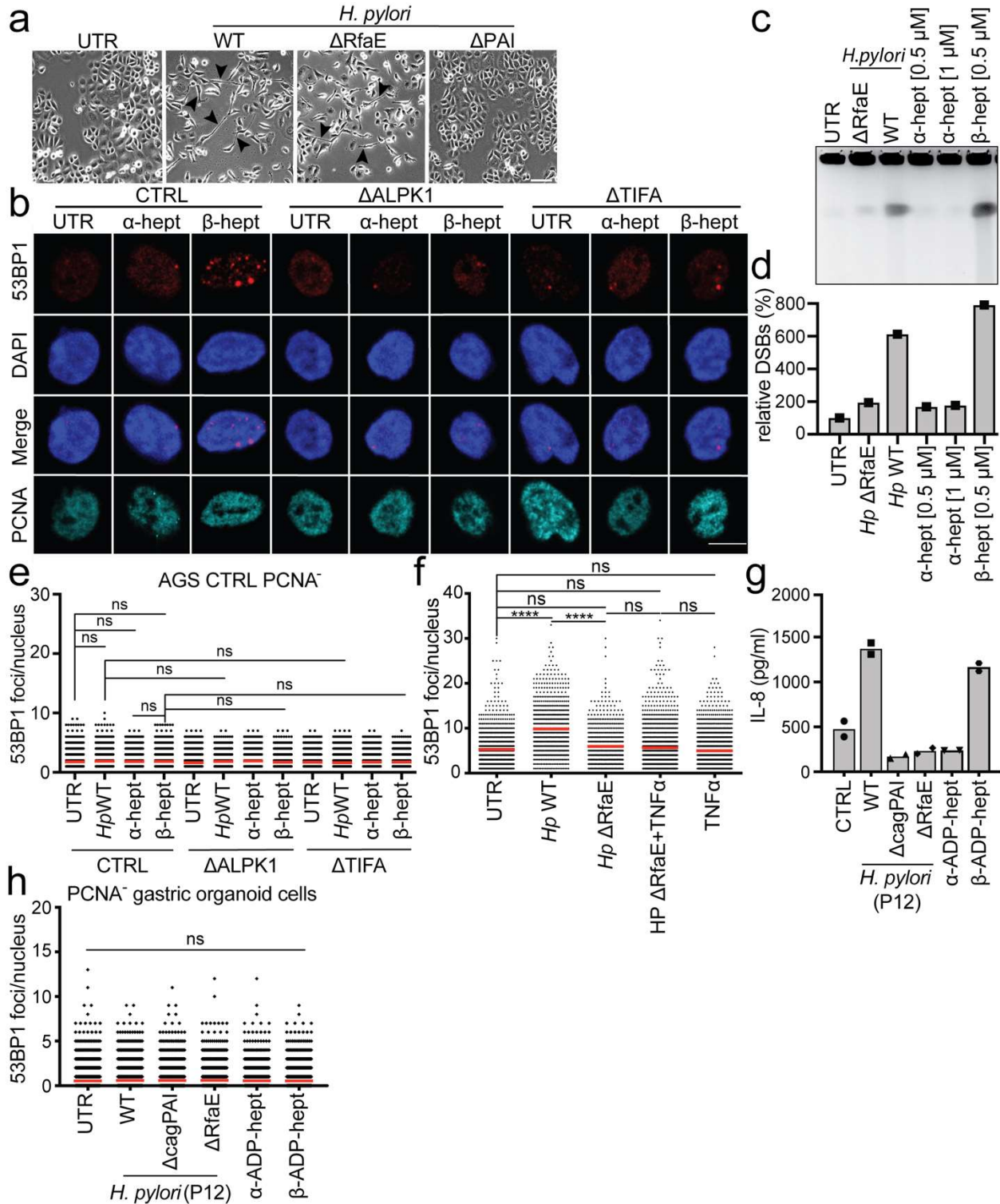
Supplementary Fig. 3. ADP-heptose-induced DNA DSBs are ALPK1- and TIFA-dependent and specific to S-phase cells as determined in cultured primary and transformed gastric epithelial cells. a AGS cells were infected for 6 hours with *H. pylori* P12 or its isogenic RfaE and Cag-PAI mutants at an MOI of 50 and examined by light microscopy for cell elongation and scattering as an indicator of CagA delivery. Arrows point to characteristic elongated cells. Images are representative of three independently

conducted experiments. Scale bar, 100 μm. **b** Wild type (CTRL), ALPK1-deficient (ΔALPK1) and TIFA-deficient (ΔTIFA) AGS cells were exposed to α- or β-ADP-heptose at 0.5 μM final concentration for 6 hours and subjected to immunofluorescence staining for 53BP1 and PCNA as well as DAPI. Images are representative of three independent experiments. Scale bar, 10 μm. **c,d** AGS cells were infected for 6 hours with *H. pylori* P12 or its isogenic RfaE mutant at an MOI of 50, or exposed to α- or β-ADP-heptose at the indicated final concentration for 6 hours and subjected to pulsed-field gel electrophoresis. The scan of the gel is shown in c alongside its quantification in d. **e** Wild type (CTRL), ALPK1-deficient (ΔALPK1) and TIFA-deficient (ΔTIFA) AGS cells were either infected for 6 hours with *H. pylori* P12 or exposed to α- or β-ADP-heptose at 0.5 μM final concentration for 6 hours and subjected to immunofluorescence staining for 53BP1 and PCNA as well as DAPI. Scatter dot plots of >793 and up to 1081 PCNA-negative cells per condition are shown. Data are pooled from three independent experiments. Red lines in e indicate medians. **f** AGS cells were infected for 6 hours with *H. pylori* P12 or its isogenic RfaE mutant at an MOI of 50, and/or treated with 10 nM TNF-α, and subjected to immunofluorescence staining for 53BP1 and PCNA as well as DAPI. Scatter dot plots of >604 and up to 1508 PCNA-positive cells per condition are shown. Data are pooled from three independent experiments. **g,h** Gastric organoids were transferred to 2D cultures and infected with the indicated strains of *H. pylori* P12 (MOI of 50) or exposed to α- or β-ADP-heptose at 0.5 μM final concentration for 6 hours. Supernatants were subjected to IL-8 ELISA and cells were subjected to immunofluorescence staining for 53BP1 and PCNA, as well as DAPI. IL-8 secretion is shown in g, and scatter dot plots of >1888 and up to 2760 PCNA-negative cells per condition are shown in h. Data in g and h are pooled from two independent experiments with cells derived from two different donors. Red lines indicate medians. P-values in e, f and h were calculated by one-way ANOVA with Dunn's multiple comparisons correction; ns, not significant; ****$p < 0.0001$. A statistical analysis of the two replicates per condition in g was not possible.
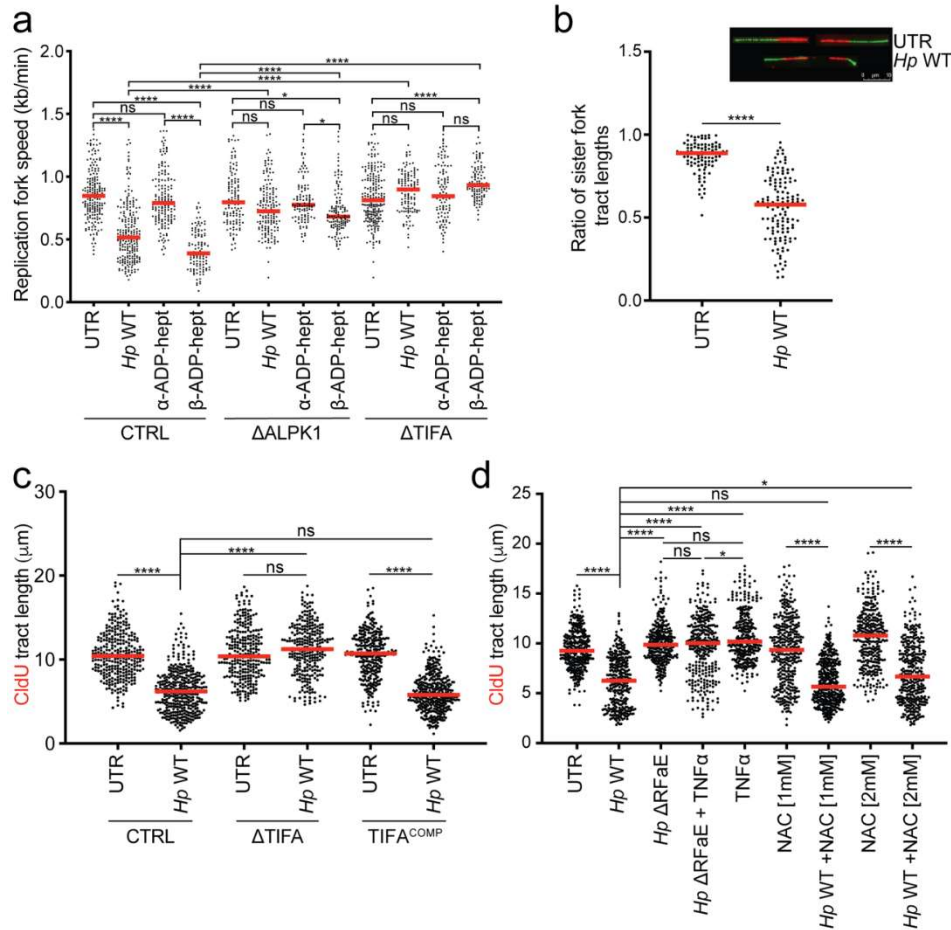
Supplementary Fig. 4. *H. pylori*-induced replication stress is RfaE-, ALPK1- and TIFA-dependent, but independent of reactive oxygen species. a Wild type (CTRL), ALPK1-deficient (ΔALPK1) and TIFA-deficient (ΔTIFA) AGS cells were either infected for 6 hours with *H. pylori* strain P12 (MOI of 50) or treated with 0.5 μM α- or β-ADP-heptose and then labeled sequentially with CIdU and IdU as shown in Figure 4a. Scatter dot plots of replication fork speed (in bp/min) were calculated based on the assumption that 1 μm of DNA fiber corresponds to 2.59 kb. At least 106 and up to 318 fibers were analyzed per condition as described in the legend to Figure 4c. Data in a are pooled from two independent experiments. **b** Sister fork asymmetry as determined by calculating ratios of CIdU tract lengths of DNA fibers generated from AGS cells that had been infected or not for 6 hours with *H. pylori* strain P12 (MOI of 50). CIdU/CIdU ratios were calculated by dividing the length of the shorter tract by the length of longer tract. At least 100 and up to 133 fibers were analyzed per condition. Data are pooled from two independent experiments. The inset shows representative sister forks of the two indicated conditions. **c** The indicated wild type and mutant cell lines in the AGS background were infected for 6 hours with *H. pylori* strain P12 at MOI 50 and subjected to the quantification of the length of newly synthesized DNA tracts. At least 281 and up to 386 fibers were analyzed per condition. Data are pooled from three independent experiments. **d** AGS cells were infected for 6 hours with *H. pylori* P12 or its isogenic RfaE mutant at an MOI of 50, and/or treated with 10 nM TNF-α; N-acetyl-cysteine (NAC) was added where indicated at 1 or 2mM final concentration. Cells were subjected to the quantification of the length of newly synthesized DNA tracts. Data in d are pooled from three independent experiments and at least 308 up to 380 fibers were analyzed per condition. Red lines indicate medians throughout. P-values in a-d were calculated by one-way ANOVA with Dunn's multiple comparisons correction; ns, not significant; *$p < 0.05$, ****$p < 0.0001$.

6
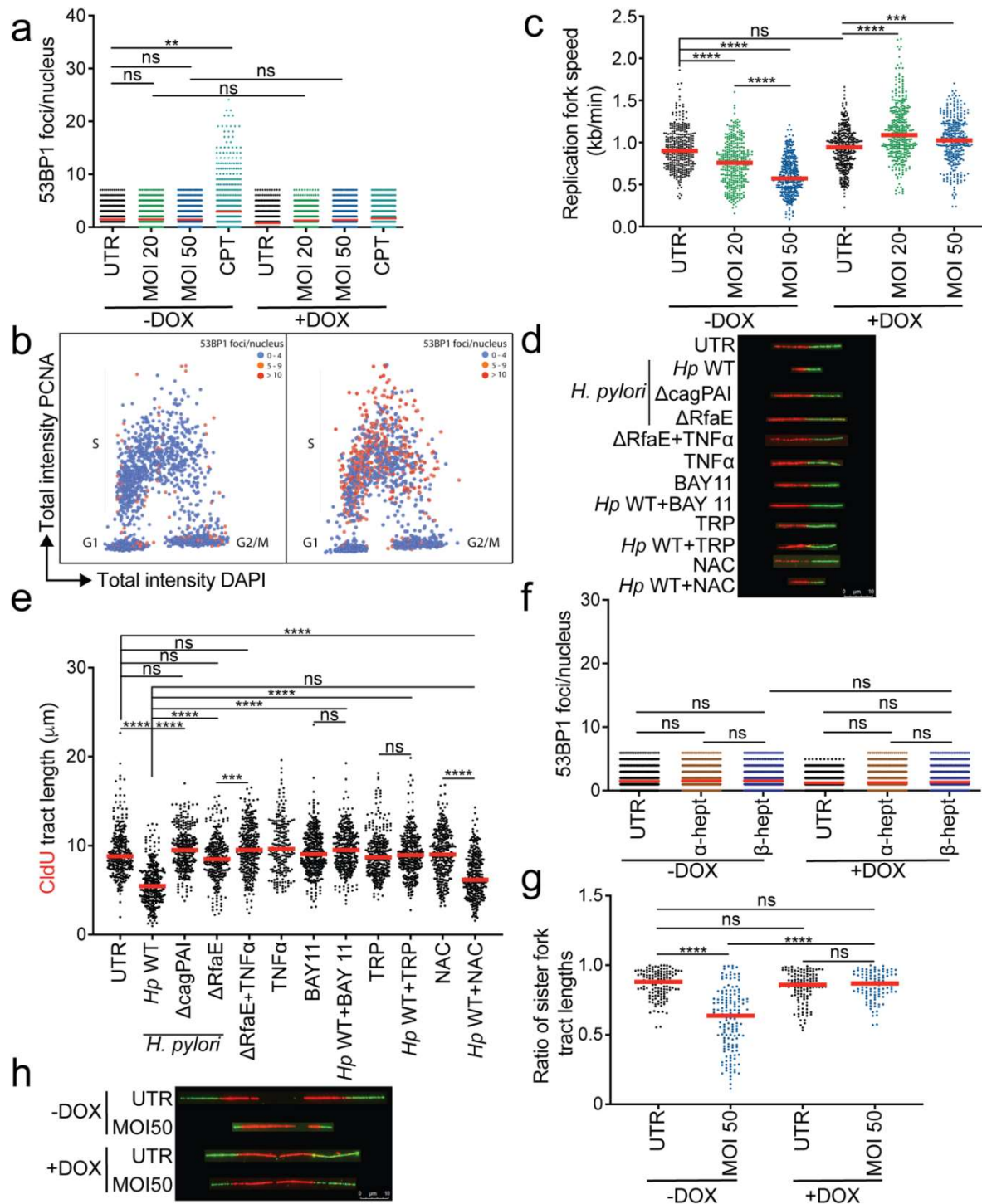
Supplementary Fig. 5. *H. pylori* infection induces R-loop-mediated replication stress in U2OS cells. a U2OS cells were either infected for 6 hours with *H. pylori* P12 (MOI of 20 or 50), or treated with 100 nM camptothecin (CPT), and were treated or not with doxycycline (-/+ DOX) to induce the expression of RNase H1. Cells were subjected to immunofluorescence staining for 53BP1 and PCNA as well as DAPI. Scatter dot plots of >500 and up to 800 PCNA-negative cells per condition are shown. Data are pooled from three independent experiments. **b** U2OS cells were infected for 6 hours with *H. pylori* P12 (MOI of 50) and subjected to immunofluorescence staining for 53BP1 and PCNA as well as DAPI. The PCNA and DAPI

signal intensities of ~800 uninfected and as many *H. pylori*-infected cells were plotted to visualize cell cycle phase (G1, S, G2/M). The color code indicates the number of 53BP1 foci/nucleus. **c** U2OS cells were infected and treated with doxycycline as described in a and additionally labeled sequentially with CIdU and IdU as shown in Fig. 4a for the assessment of DNA fiber tract length. Scatter dot plots of replication fork speed (in bp/min), as calculated based on the assumption that 1 μm of DNA fiber corresponds to 2.59 kb. At least 100 and up to 500 fibers were analyzed per condition. Data in c are pooled from three independent experiments. **d,e** Wild type U2OS cells were infected with the indicated strains of *H. pylori* (MOI of 50) and/or exposed to the NF-κB inhibitor BAY 11-7082 (1 μM) or triptolide (100 nM), or TNF-α (10 nM), and additionally labeled sequentially with CIdU and IdU for the assessment of replication tract length. Representative DNA fibers are shown in d and scatter dot plots of CIdU tract length (in μm) are shown in e for the indicated conditions. At least 200 and up to 500 fibers were analyzed per condition. Data in e are pooled from three independent experiments. **f** U2OS cells were exposed to α- or β-ADP-heptose at 0.5 μM final concentration for 6 hours, and were treated or not with doxycycline (-/+ DOX) to induce the expression of RNase H1. Cells were subjected to immunofluorescence staining for 53BP1 and PCNA as well as DAPI. Scatter dot plots of >500 and up to 800 PCNA-negative cells per condition are shown. Data are pooled from three independent experiments. **g,h** Sister fork asymmetry as determined by calculating ratios of CIdU tract lengths of DNA fibers generated from U2OS cells that had been infected or not for 6 hours with *H. pylori* strain P12 (MOI of 50) and treated or not with doxycycline. CIdU/CIdU ratios were calculated by dividing the length of the shorter tract by the length of longer tract. At least 102 and up to 155 fibers were analyzed per condition. Data in g are pooled from two independent experiments. Representative fibers are shown in h. Red lines indicate medians throughout. P-values in a, c, e, f and g were calculated by one-way ANOVA with Dunn's multiple comparisons correction; ns, not significant; **p < 0.01, ***p < 0.005, ****p < 0.0001..
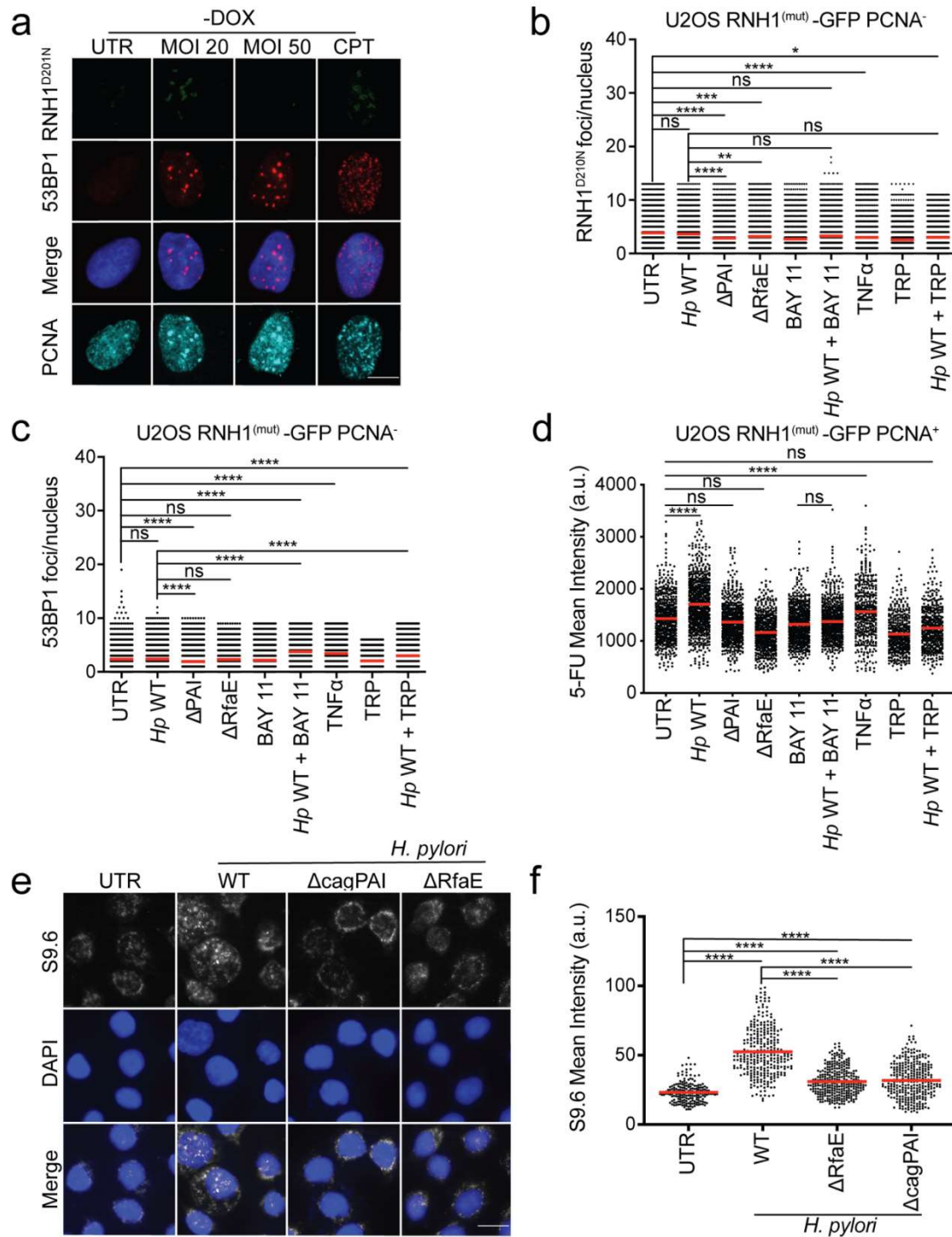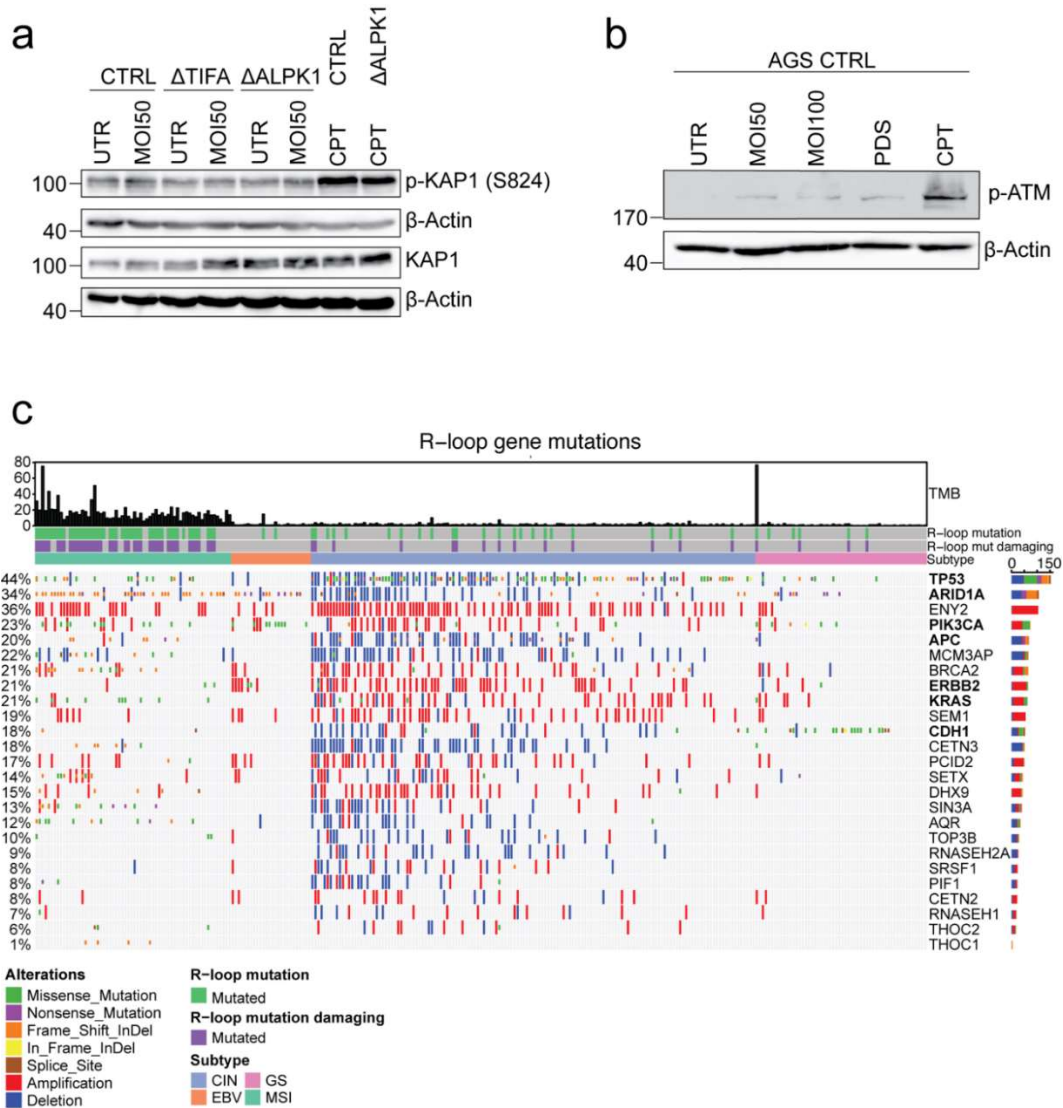
Supplementary Fig. 6. *H. pylori* infection induces R-loops in S-phase cells in an RfaE- and NF-kB-dependent manner. a U2OS cells were either infected for 6 hours with *H. pylori* P12 (MOI of 20 or 50), or treated with 100 nM camptothecin (CPT), and were treated or not with doxycycline (-/+ DOX) to induce the expression of a (D210N) mutant version of RNase H1 fused to GFP (RNH1^{D210N}). Cells were subjected to immunofluorescence staining for 53BP1 and PCNA as well as DAPI. Representative images are shown of the untreated (-DOX) condition, of RNH1^{D210N}/GFP foci and 53BP1 foci of a PCNA-positive cell each; images are representative of three independent experiments. Scale bar, 10 μm. **b,c** U2OS cells were infected

with the indicated strains of *H. pylori* (MOI of 50) and/or exposed to the NF-κB inhibitor BAY 11-7082 (1 μM) or triptolide (100 nM), or TNF-α (10 nM) and treated with doxycycline to induce the expression of RNH1^{D210N}/GFP. Cells were subjected to immunofluorescence staining for 53BP1 and PCNA as well as DAPI. Scatter dot plots of RNH1^{D210N}/GFP foci of >889 and up to 981 PCNA$^-$ cells per condition are shown in b, and of 53BP1 foci of >931 and up to 1029 cells per condition in c. Data in b and c are pooled from three independent experiments. **d** U2OS cells were treated as described above, and additionally exposed to 1 μM 5-FU for the last hour of a 6-hour infection experiment. 5-FU mean fluorescence intensity was quantified by microscopy. A minimum of 436 and up to 748 cells were analyzed per condition. Representative data from one experiment of two is shown. **e,f** AGS cells were infected with the indicated strains of *H. pylori* (MOI of 50) for 6 hours and subjected to immunofluorescence staining for RNA/DNA hybrids (clone S9.6) and DAPI. Representative images are shown in e (scale bar 15 μm) and quantitative data from one representative experiment of two independently conducted ones is shown in f. At least 190 and up to 305 cells were analyzed per condition. Red lines indicate medians throughout. P-values in b, c, d and f were calculated by one-way ANOVA with Dunn's multiple comparisons correction; ns, not significant; $*p < 0.05$, $**p < 0.01$, $***p < 0.005$, $****p < 0.0001$.

a

CTRL ΔTIFA ΔALPK1 CTRL ΔALPK1

UTR MOI50 UTR MOI50 UTR MOI50 CPT CPT

100 — p-KAP1 (S824)
40 — β-Actin
100 — KAP1
40 — β-Actin

b

AGS CTRL

UTR MOI50 MOI100 PDS CPT

p-ATM
170 —
40 — β-Actin

c

R−loop gene mutations

TMB

R−loop mutation
R−loop mut damaging
Subtype

0   150

44% TP53
34% ARID1A
36% ENY2
23% PIK3CA
20% APC
22% MCM3AP
21% BRCA2
21% ERBB2
21% KRAS
19% SEM1
18% CDH1
18% CETN3
17% PCID2
14% SETX
15% DHX9
13% SIN3A
12% AQR
10% TOP3B
9% RNASEH2A
8% SRSF1
8% PIF1
8% CETN2
7% RNASEH1
6% THOC2
1% THOC1

Alterations
Missense_Mutation
Nonsense_Mutation
Frame_Shift_InDel
In_Frame_InDel
Splice_Site
Amplification
Deletion

R−loop mutation
Mutated

R-loop mutation damaging
Mutated

Subtype
CIN GS
EBV MSI

Supplementary Fig. 7. *H. pylori* induces DNA damage without an associated DNA damage response, and factors involved in R-loop metabolism are recurrently mutated in gastric cancer. a The indicated wild type and mutant cell lines in the AGS background were infected for 6 hours with *H. pylori* strain P12 at MOI 50 or treated with 100 nM camptothecin (CPT). Extracts were subjected to Western blotting using the indicated antibodies for total and phosphorylated KAP-1; β-actin was used as loading control. **b** AGS cells were infected for 6 hours with *H. pylori* strain P12 at MOI 50 or 100 or treated with 100 nM camptothecin (CPT) or 10 μm pyridostatin (PDS). Extracts were subjected to Western blotting using the indicated antibodies for phosphorylated ATM, with β-actin serving as loading control. Blots in a and b are representative of three independently conducted experiments. **c** The mutational landscape of gastric cancer with relation to genes involved in R-loop metabolism. 227 tumors from treatment-naïve gastric cancer patients that had previously been subjected to array-based somatic copy number analysis, whole-exome sequencing and array-based DNA methylation profiling as part of the Cancer Genome Atlas (TCGA) project were screened for mutations and copy number variations in 18 R-loop metabolism genes, which are plotted alongside the seven known gastric cancer driver genes *CDH1, APC, TP53, ARID1A, PIK3CA, KRAS* and *ERBB2* (shown in bold)*,* and along with the mutational burden per megabase (TMB). The color codes indicate the four subtypes of gastric cancer, and the types of genetic alterations as well as the presence of (any, or damaging only) mutations in R-loop metabolism genes (in green and purple).

11
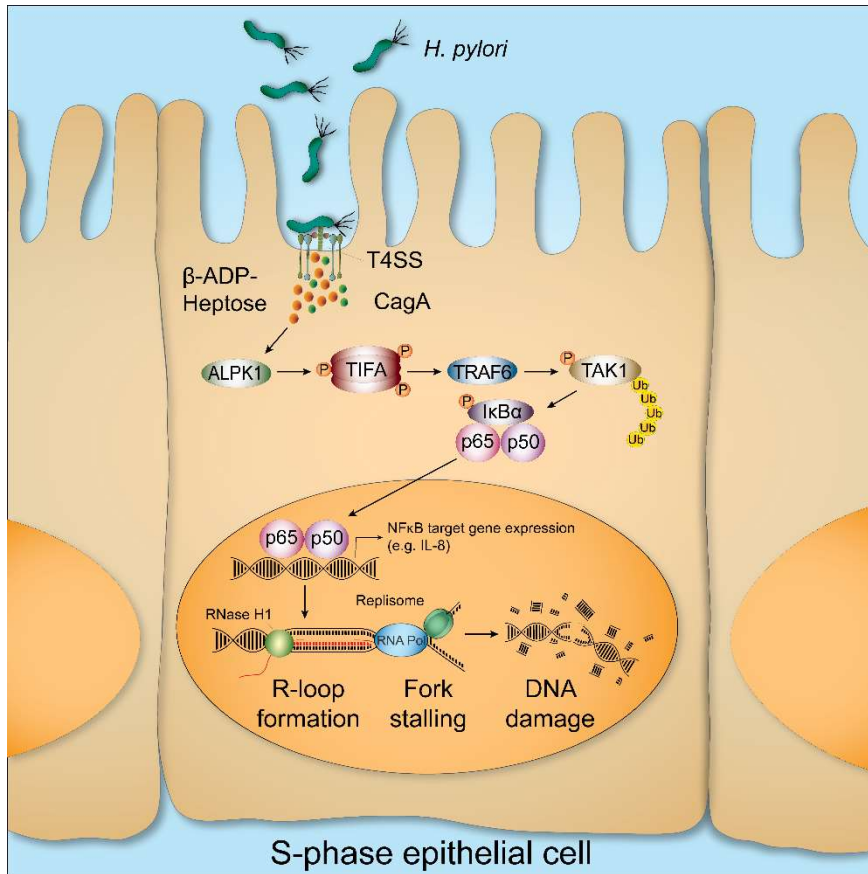
Supplementary Fig. 8. Schematic representation of *H. pylori*-induced R-loop formation and DNA damage. Upon attachment of *H. pylori* to gastric epithelial cells, the bacteria translocate ADP-heptose, HBP and/or other LPS biosynthetic intermediates into the cytoplasm of their target cells through the activity of the Cag-PAI-encoded T4SS. This process activates ALPK1, which phosphorylates TIFA and leads to the activation of TIFAsomes which, through activation of TAK1 kinase activity, promote IκBα degradation and the translocation of NF-κB to the nucleus. If NF-κB activation occurs in S-phase cells, active transcription machinery may collide with replication forks head-on, which may result in R-loop formation and replication fork stalling. Unless resolved promptly by dedicated enzymes including RNase H1, R-loop formation and the resulting replication stress may lead to DNA damage that manifests as DNA DSBs.

Research paper #2

Fork Cleavage-Religation Cycle and Active Transcription Mediate Replication Restart after Fork Stalling at Co-transcriptional R-Loops

Graphical Abstract
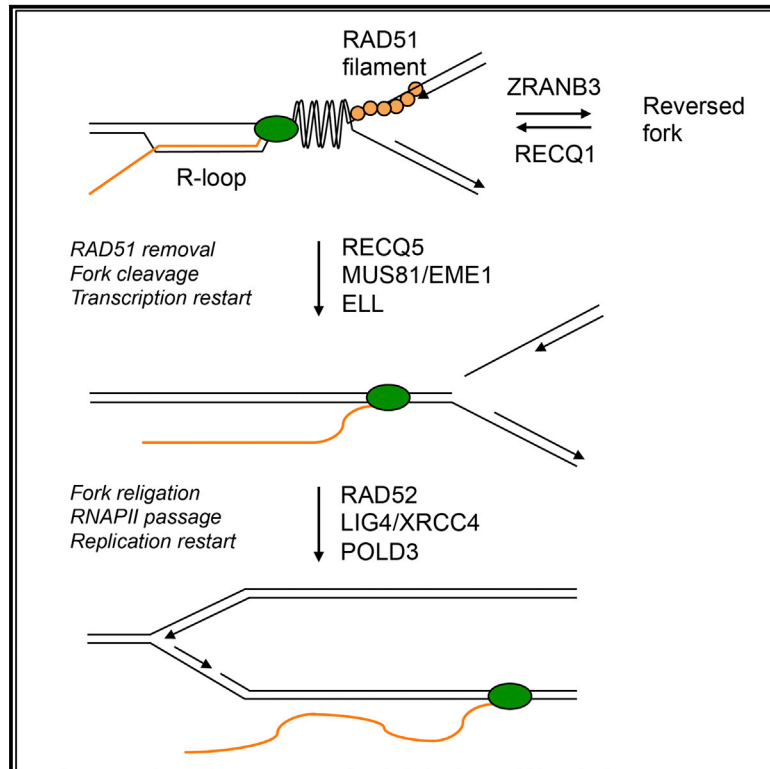
Authors

Nagaraja Chappidi,
Zuzana Nascakova,
Barbora Boleslavska, ...,
Antonio Porro, Massimo Lopes,
Pavel Janscak

Correspondence

pjanscak@imcr.uzh.ch

In Brief

Transcription-replication conflicts associated with the formation of R-loops represent a major cause of replication stress. Chappidi et al. reveal that replication forks blocked by co-transcriptional R-loops can be restarted by fork cleavage and religation linked to transcription restart.

Highlights

- R-loop-induced fork stalling is followed by MUS81-dependent replication restart

- RECQ5 mediates the switch from fork stalling to restart by suppressing fork reversal

- Restart of R-loop-stalled forks is mediated by fork cleavage and religation

- Restart of R-loop-stalled forks requires reactivation of transcription

CellPress

Fork Cleavage-Religation Cycle and Active Transcription Mediate Replication Restart after Fork Stalling at Co-transcriptional R-Loops

Nagaraja Chappidi,[1] Zuzana Nascakova,[2] Barbora Boleslavska,[2] Ralph Zellweger,[1] Esin Isik,[1] Martin Andrs,[2] Shruti Menon,[1] Jana Dobrovolna,[2] Chiara Balbo Pogliano,[3] Joao Matos,[3] Antonio Porro,[1] Massimo Lopes,[1] and Pavel Janscak[1,2,4,*]

[1]Institute of Molecular Cancer Research, University of Zurich, Winterthurerstrasse 190, 8057 Zurich, Switzerland
[2]Institute of Molecular Genetics of the Czech Academy of Sciences, Videnska 1083, 142 20 Prague, Czech Republic
[3]Institute of Biochemistry, ETH Zurich, Otto-Stern-Weg 3, 8093 Zurich, Switzerland
[4]Lead Contact
*Correspondence: pjanscak@imcr.uzh.ch
https://doi.org/10.1016/j.molcel.2019.10.026

SUMMARY

Formation of co-transcriptional R-loops underlies replication fork stalling upon head-on transcription-replication encounters. Here, we demonstrate that RAD51-dependent replication fork reversal induced by R-loops is followed by the restart of semiconservative DNA replication mediated by RECQ1 and RECQ5 helicases, MUS81/EME1 endonuclease, RAD52 strand-annealing factor, the DNA ligase IV (LIG4)/XRCC4 complex, and the non-catalytic subunit of DNA polymerase δ, POLD3. RECQ5 disrupts RAD51 filaments assembled on stalled forks after RECQ1-mediated reverse branch migration, preventing a new round of fork reversal and facilitating fork cleavage by MUS81/EME1. MUS81-dependent DNA breaks accumulate in cells lacking RAD52 or LIG4 upon induction of R-loop formation, suggesting that RAD52 acts in concert with LIG4/XRCC4 to catalyze fork religation, thereby mediating replication restart. The resumption of DNA synthesis after R-loop-associated fork stalling also requires active transcription, the restoration of which depends on MUS81, RAD52, LIG4, and the transcription elongation factor ELL. These findings provide mechanistic insights into transcription-replication conflict resolution.

INTRODUCTION

During genome duplication, DNA replication forks frequently encounter various obstacles, including active transcription complexes, that can halt their progression (Zeman and Cimprich, 2014). Transcription-replication conflicts (TRCs) can occur in both co-directional and head-on orientation, with the latter scenario having a much stronger deleterious effect on replication fork progression and genomic integrity than the former (Hamperl et al., 2017; Prado and Aguilera, 2005). The frequency of head-on TRCs can be enhanced by the deregulation of origin firing (Hamperl et al., 2017), which occurs upon the activation of oncogenes (Jones et al., 2013; Macheret and Halazonetis, 2018). Accumulating evidence suggests that TRCs represent a major source of genomic instability in precancerous lesions and cancer cells (Gaillard et al., 2015; Macheret and Halazonetis, 2018).

Head-on TRCs promote the formation of co-transcriptional R-loops that act as a potent block to replication fork progression (Hamperl et al., 2017; Lang et al., 2017). These structures are generated by the invasion of the nascent transcript into the DNA duplex behind the RNA polymerase (RNAP) complex, leading to the formation of an RNA:DNA hybrid between the transcript and the template DNA strand, with the non-transcribed strand being extruded as a single-stranded DNA (ssDNA) loop (Hamperl and Cimprich, 2014). The formation of R-loops is facilitated by negative DNA supercoiling generated behind the elongating RNAP complex and occurs preferentially in the transcriptional units containing a high density of Gs in the non-template strand (Hamperl and Cimprich, 2014). Evidence suggests that G-quadruplex (G4) structures formed in the non-template DNA strand promote R-loop extension and stability (De Magis et al., 2019; Duquette et al., 2004; Hamperl and Cimprich, 2014). Importantly, R-loops, but not normal transcription complexes, induce DNA breaks during conflicts with replication forks (Hamperl et al., 2017), suggesting that R-loop formation is a major cause of replication stalling induced by head-on transcription.

Although much is known about the strategies that cells evolved to prevent TRCs or to remove R-loops (García-Muse and Aguilera, 2016; Hamperl and Cimprich, 2014, 2016), understanding whether and how a replication fork blocked by an R-loop can restart DNA synthesis remains elusive. Recent studies have shown that S-phase progression in cells undergoing oncogene-induced replication stress requires proteins involved in the restarting of stalled replication forks, namely MUS81 endonuclease, SLX4 scaffold protein, RAD52 strand-annealing protein, and the non-catalytic subunit of DNA polymerase δ, POLD3 (Costantino et al., 2014; Regairaz et al., 2011; Sotiriou et al., 2016). These proteins are also required for mitotic DNA synthesis (MiDAS), a process that occurs at
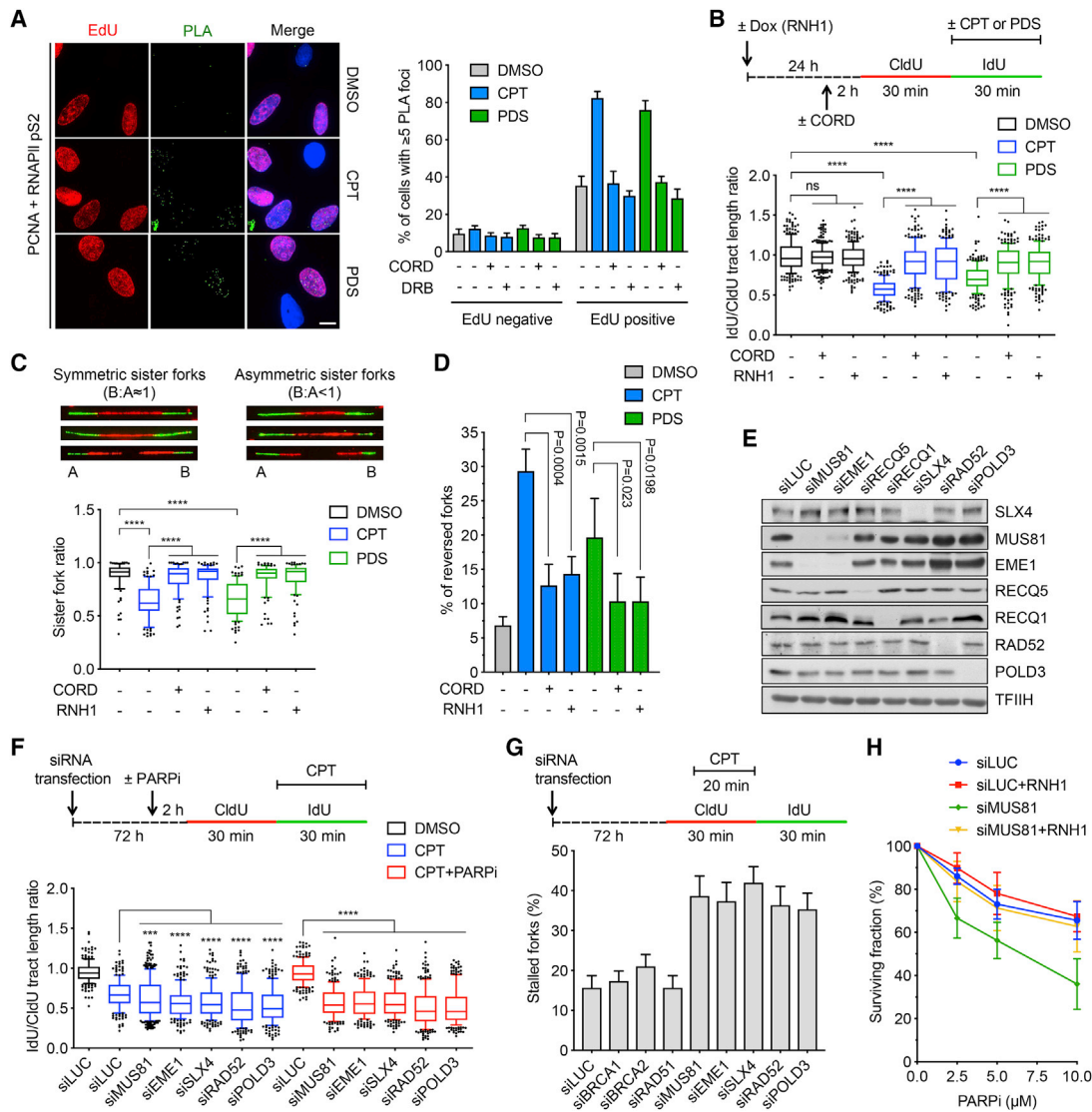
Figure 1. Replication Fork Stalling Induced by Co-transcriptional R-Loops Is Followed by Replication Restart via the SLX4-MUS81-RAD52-POLD3 Axis

(A) Co-localization of PCNA and elongating RNA polymerase II (RNAPII pS2) in S phase nuclei of U2OS cells after 1 h of treatment with camptothecin (CPT; 100 nM) or pyridostatin (PDS; 10 μM), as determined by proximity ligation assay (PLA) and EdU-pulse labeling. Representative images (left panel) and quantification of the percentage (right panel) of EdU[+] and EdU^{−} cells with ≥5 PLA foci per nucleus are shown. EdU (10 μM) was added 10 min before CPT/PDS treatment. Where indicated, cordycepin (CORD; 50 μM) or DRB (100 μM) were added 2 h before CPT/PDS treatment. Data represent the means ± SDs, n = 3. Scale bar, 10 μm.

(B) Effect of RNase H1 (RNH1) overexpression and transcription inhibition on replication fork slowing induced by CPT (100 nM) or PDS (10 μM) in U2OS T-REx/RNH1-GFP cells. Top panel: experimental workflow of DNA fiber assays. Bottom panel: boxplot of values of the IdU:CldU tract length ratio obtained for indicated conditions (n ≥ 200, whiskers: 10th–90th percentiles). RNH1 expression was induced with doxycycline (Dox). ns, not significant; ***p < 0.001; ****p < 0.0001 (Mann-Whitney test).

(C) PDS and CPT induce sister fork asymmetry in a manner dependent on R-loop formation. Top panel: representative images of symmetric and asymmetric replication tracts of sister forks identified on DNA fibers in (B). Bottom panel: boxplot of the values of the sister fork IdU tract length ratio measured for the indicated conditions (n ≥ 100, whiskers: 10th–90th percentiles). ns, not significant; ***p < 0.001; ****p < 0.0001 (Mann-Whitney test).

(D) Effect of transcription inhibition and RNH1 overexpression on the frequency of reversed replication forks in U2OS T-REx/RNH1-GFP cells treated with CPT (100 nM) or PDS (10 μM) for 1 h. RNH1 expression was induced by the addition of Dox at 24 h before treatment. CORD (50 μM) was added 2 h before treatment. Data represent the means ± SDs, n = 3. p values: paired t test.

(E) Western blot analysis of the extracts of U2OS cells transfected with indicated siRNAs.

(F) Effect of the depletion of MUS81, EME1, SLX4, RAD52, and POLD3, respectively, on the rescue of CPT-induced replication fork slowing by PARP inhibition (PARPi) with 10 μM olaparib. Top panel: experimental workflow of DNA fiber assays. Bottom panel: boxplot of values of the IdU:CldU tract length ratio obtained for indicated conditions (n ≥ 200, whiskers: 10th–90th percentiles). ns, not significant; ***p < 0.001; ****p < 0.0001 (Mann-Whitney test).

(legend continued on next page)

under-replicated common fragile sites (CFSs) upon replication stress to prevent chromosome breakage during cell division (Bhowmick et al., 2016; Minocherhomji et al., 2015). Given that R-loop formation underlies oncogene-induced replication stress and causes CFS instability (Helmrich et al., 2011; Jones et al., 2013), it is likely that MUS81, SLX4, RAD52, and POLD3 constitute a pathway that promotes replication fork progression through regions of active transcription.

Here, we provide evidence that replication forks stalled by co-transcriptional R-loops can resume DNA synthesis via a multi-step process involving cleavage of the stalled fork by SLX4-associated MUS81-EME1 endonuclease and subsequent fork religation catalyzed by RAD52 and the DNA ligase IV (LIG4)/XRCC4 complex. Our results also suggest that this fork cleavage-religation cycle allows the stalled transcription complexes to restart RNA synthesis, leading to TRC resolution without the need for their disruption.

RESULTS

Replication Fork Reversal Induced by Co-transcriptional R-Loops Is Followed by Replication Restart via the SLX4-MUS81-RAD52-POLD3 Axis

To induce R-loop-mediated TRCs, we sought to treat human U2OS cells with drugs that promote R-loop formation, namely the DNA topoisomerase I inhibitor camptothecin (CPT) and the G4-DNA-binding ligand pyridostatin (PDS) (De Magis et al., 2019; Sollier et al., 2014). We observed that CPT and PDS induced the formation of the nuclear foci of a GFP-tagged and catalytically inactive form of RNase H1 (Figure S1A), indicating the presence of RNA:DNA hybrids (Nguyen et al., 2017). This was confirmed by immunofluorescence staining with the S9.6 antibody, which specifically recognizes RNA:DNA hybrids (Figure S1B). Using the proximity ligation assay (PLA), we found that the exposure of cells to CPT or PDS increased S phase-specific co-localization of elongating RNA polymerase II (RNAPII) with the replisome component proliferating cell nuclear antigen (PCNA) and with FANCD2 (Figures 1A and S1C–S1E), which binds to stalled forks (Lossaint et al., 2013). Co-localization signals were significantly reduced upon transcription inhibition with cordycepin or 5,6-dichloro-benzimidazole 1-β-ᴅ-ribofuranoside (DRB) (Figures 1A and S1C–S1E), suggesting that CPT and PDS induce transcription-replication interference. Of note, using a cell-based plasmid system with control over the direction and timing of replication and transcription, the PLA signals between PCNA and RNAPII have been detected upon the induction of head-on but not co-directional TRCs (Hamperl et al., 2017). To directly assess the impact of CPT- and PDS-induced R-loops on replication fork progression, cells were pulsed with 5-chloro-2′-deoxyuridine (CldU), followed by treatment with the R-loop-inducing drug and concomitant labeling of the replication tracts

with 5-iodo-2′-deoxyuridine (IdU) (Figure 1B). We observed that IdU tracts of individual forks were shorter than CldU tracts under these conditions (Figures 1B, S1F, and S1G). Moreover, the lengths of the replication tracts of the sister replication forks displayed a marked asymmetry upon CPT or PDS treatment (Figure 1C), which is indicative of replication fork stalling (Tuduri et al., 2009). These replication fork slowing and sister fork asymmetry phenotypes could be almost completely rescued by the inhibition of transcription or by the overexpression of wild-type RNase H1 (Figures 1B, 1C, and S1F–S1H), which eliminates R-loops (Tuduri et al., 2009). Thus, it appears that co-transcriptional R-loops induced by CPT or PDS act in cis to block replication fork progression. It is possible that fork slowing extends also to forks that are not directly challenged by these structures via recently reported and yet elusive ATR-mediated signaling (Mutreja et al., 2018).

CPT-induced replication fork slowing is associated with RAD51-mediated fork reversal, a DNA transaction that prevents the breakage of stalled forks (Ray Chaudhuri et al., 2012; Zellweger et al., 2015). We found that the frequency of reversed forks was significantly increased not only in CPT-treated but also in PDS-treated cells as compared to mock-treated cells (Figures 1D and S2A; Table S1A). The inhibition of transcription or the overexpression of RNase H1 suppressed fork reversal in these cells (Figure 1D). Moreover, both CPT- and PDS-induced fork slowing was rescued by RAD51 depletion (Figure S2B), which blocks fork reversal (Zellweger et al., 2015). These results suggest that R-loop-induced replication fork stalling is associated with RAD51-mediated fork reversal.

CPT-induced fork reversal is followed by poly (ADP-ribose) polymerase (PARP)-regulated replication restart, which is dependent on RECQ1 DNA helicase (Berti et al., 2013). We thought to test whether this process requires the factors that are implicated in the restart of stalled forks at CFSs in early mitosis (Bhowmick et al., 2016; Minocherhomji et al., 2015), as replication stalling at these loci is likely to be a consequence of R-loop-mediated TRCs (Helmrich et al., 2011). We found that the depletion of either of these proteins, namely MUS81, EME1, SLX4, RAD52, and POLD3, enhanced the inhibitory effect of CPT on replication fork progression in U2OS cells and abolished its rescue by PARP inhibition or RAD51 depletion (Figures 1E, 1F, S2C, S2E, and S2F). Similar results were obtained if cells were treated with PDS (Figures S2C–S2F). Moreover, MUS81 depletion markedly enhanced sister fork asymmetry in both CPT- and PDS-treated cells and prevented the rescue of this phenotype by PARP inhibition (Figure S2G). To prove that the SLX4-MUS81-RAD52-POLD3 pathway operates in cells that are capable of fork reversal, CPT or PDS was added to cells during the first pulse labeling with CldU, followed by IdU labeling in drug-free medium. This allowed us to monitor persistent fork stalling by measuring the percentage of CldU tracts without an

---

(G) Effect of the depletion of the indicated proteins on replication restart following the treatment of U2OS cells with 100 nM CPT. Top panel: experimental workflow of DNA fiber assays. Bottom panel: quantification of the replication fork stalling events. The data represent the percentage of active replicons (CldU labeled) that fail to resume DNA synthesis (not IdU labeled) 30 min after the removal of CPT. Data represent the means ± SDs, n = 3.

(H) RNH1 overexpression rescues the hypersensitivity of MUS81-depleted U2OS T-REx/RNH1-GFP cells to PARPi. Dox was added 24 h before PARPi treatment. Data represent the means ± SDs, n = 3.

See also Figures S1 and S2.

IdU tract (Figure S2H). We found that cells depleted of MUS81, SLX4, EME1, RAD52, or POLD3 displayed a marked increase in the frequency of stalled forks 30 min after CPT or PDS treatment as compared to mock-depleted cells, suggesting a replication restart defect (Figures 1G and S2I). The resumption of DNA synthesis after CPT or PDS removal was also compromised by the addition of a RAD52 inhibitor (Figure S2K). However, depletion of RAD51, BRCA1 or BRCA2, or RAD51 inhibition did not impair the resumption of DNA synthesis following the exposure of cells to CPT or PDS (Figures 1G and S2I–S2K), excluding a primary role of the homologous recombination machinery in this process. We also observed that cells depleted of MUS81 displayed hypersensitivity to olaparib, which was rescued by the overexpression of wild-type RNase H1 (Figure 1H). The latter suggests that fork reversal and the following replication restart via the MUS81 pathway collectively promote cell survival upon R-loop-mediated TRCs. Along this line, we found that RNase H1 overexpression could also rescue the hypersensitivity of MUS81-depleted cells to CPT and PDS (Figure S2L).

Taken together, these data support a model wherein R-loop-stalled replication forks, initially stabilized by RAD51-mediated fork reversal, are subsequently channeled into a replication restart pathway mediated by SLX4, MUS81/EME1, RAD52, and POLD3.

RECQ5 Mediates the Switch from R-Loop-Induced Fork Stalling to Replication Restart by Disrupting RAD51 Filaments

MiDAS is promoted by RECQ5 helicase, which disrupts RAD51 filaments on stalled replication forks at CFSs to facilitate fork cleavage by MUS81/EME1 (Di Marco et al., 2017). This prompted us to test whether RECQ5 is also required for the restart of replication forks stalled by R-loops during S phase. Using U2OS cells, we found that RECQ5 depletion compromised the rescue of CPT- and PDS-induced replication fork slowing by PARP inhibition as well as replication restart after CPT or PDS treatment (Figures 2A and S3A–S3C). In contrast, RECQ5 was dispensable for the rescue of CPT- and PDS-induced replication fork slowing by RAD51 depletion (Figures 2A and S3A). Similar results were obtained if cells were depleted of RECQ1 (Figures 2A and S3A–S3C), which eliminates the regressed arm of reversed forks by promoting reverse branch migration (Berti et al., 2013). RECQ5, but not RECQ1, was required for the rescue of CPT- and PDS-induced replication fork slowing by the depletion of ZRANB3 (Figures 2A, S3A, and S3B), a DNA translocase that mediates fork reversal (Vujanovic et al., 2017). These data not only confirm that RECQ1 promotes replication restart by converting reversed forks to the original three-way structure but they also provide evidence that RECQ5 eliminates the RAD51 filaments assembled on stalled forks before fork reversal. Consistently, the depletion of RECQ5 and the depletion of the subunits of the MUS81 endonuclease complex increased the frequency of fork reversal events both in untreated and CPT-treated cells (Figure 2B; Table S1B). Moreover, cells expressing RECQ5 mutants that are defective in disrupting RAD51 filaments, namely RECQ5K58R and RECQ5F666A (Di Marco et al., 2017), displayed an elevated frequency of reversed forks and a defect in replication restart upon CPT treatment (Figures

2C–2E; Table S1C). These data suggest that RECQ1 and RECQ5 regulate the balance between replication fork reversal and restart at sites of R-loop-mediated TRCs.

RECQ5-Assisted Cleavage of R-Loop-Stalled Forks by MUS81 Endonuclease Triggers Replication Restart

The inhibition of PARP activity in CPT-treated cells not only restores normal rates of replication fork progression but it also leads to the accumulation of DNA double-strand breaks (DSBs) (Ray Chaudhuri et al., 2012). By pulsed-field gel electrophoresis (PFGE), we observed that PARP inhibition stimulated DNA breakage in both CPT- and PDS-treated U2OS cells (Figure 3A). Upon CPT or PDS treatment, PARP inhibition also enhanced the formation of 53BP1 foci (a DSB marker) in the nuclei of S phase cells (Figures S4A and S4B). DNA breakage and 53BP1 focus formation under these conditions could be suppressed by the inhibition of DNA replication or transcription or by the overexpression of RNase H1 (Figures 3A and S4B), suggesting that DSBs form as a consequence of R-loop-mediated TRCs and may represent an intermediate in the replication restart process. In support of this notion, we found that depletion of MUS81 endonuclease reduced DNA breakage and the formation of S phase-specific 53BP1 foci in CPT- and PDS-treated cells upon PARP inhibition (Figures 3B, S4C, and S4D). Moreover, these phenotypes were suppressed by the depletion of SLX4 (Figures 3B, S4C, and S4D), which binds and activates MUS81/EME1 for replication fork cleavage on the leading arm (Wyatt et al., 2017). A small interfering RNA (siRNA)-resistant wild-type MUS81 cDNA, but not a catalytically inactive version (D338A/D339A), could restore DSB formation and efficient DNA synthesis in MUS81 siRNA-transfected cells treated with CPT or PDS upon PARP inhibition (Figures 3C, 3D, and S4E), confirming that the restart of R-loop-stalled forks requires MUS81 endonuclease activity. MUS81 interacts with SLX4 through a conserved motif, called the SAP domain, which is located at the C terminus of SLX4 (Kim et al., 2013). Consistently, we found that PARP inhibition did not rescue CPT- and PDS-induced replication fork slowing in an FANCP patient-derived (SLX4 deficiency) cell line complemented with SLX4 ΔSAP cDNA (Kim et al., 2013; Figure 3E). Moreover, these cells did not accumulate DSBs upon CPT treatment as did cells complemented with wild-type SLX4 cDNA (Figure S4F).

To further prove that MUS81 endonuclease acts at sites of R-loop-mediated TRCs during S phase, we analyzed the nuclear distribution of MUS81 in U2OS cells exposed to CPT or PDS. We found that both CPT and PDS stimulated the formation of MUS81 nuclear foci that co-localized with FANCD2 foci (Figure 3F), suggesting that MUS81 accumulates at stalled replication forks. The formation of MUS81 and FANCD2 foci in CPT- or PDS-treated cells was impaired by transcription inhibition or by RNase H1 overexpression (Figures 3G and S4G), implying dependence on R-loop-mediated TRCs. Moreover, MUS81 focus formation in CPT-treated U2OS cells was impaired by SLX4 depletion (Figures 3H and S4H), suggesting that MUS81 recruitment to stalled replication forks is mediated by SLX4. The depletion of EME1 also abrogated MUS81 focus formation in CPT-treated cells (Figures 3H and S4H), confirming that
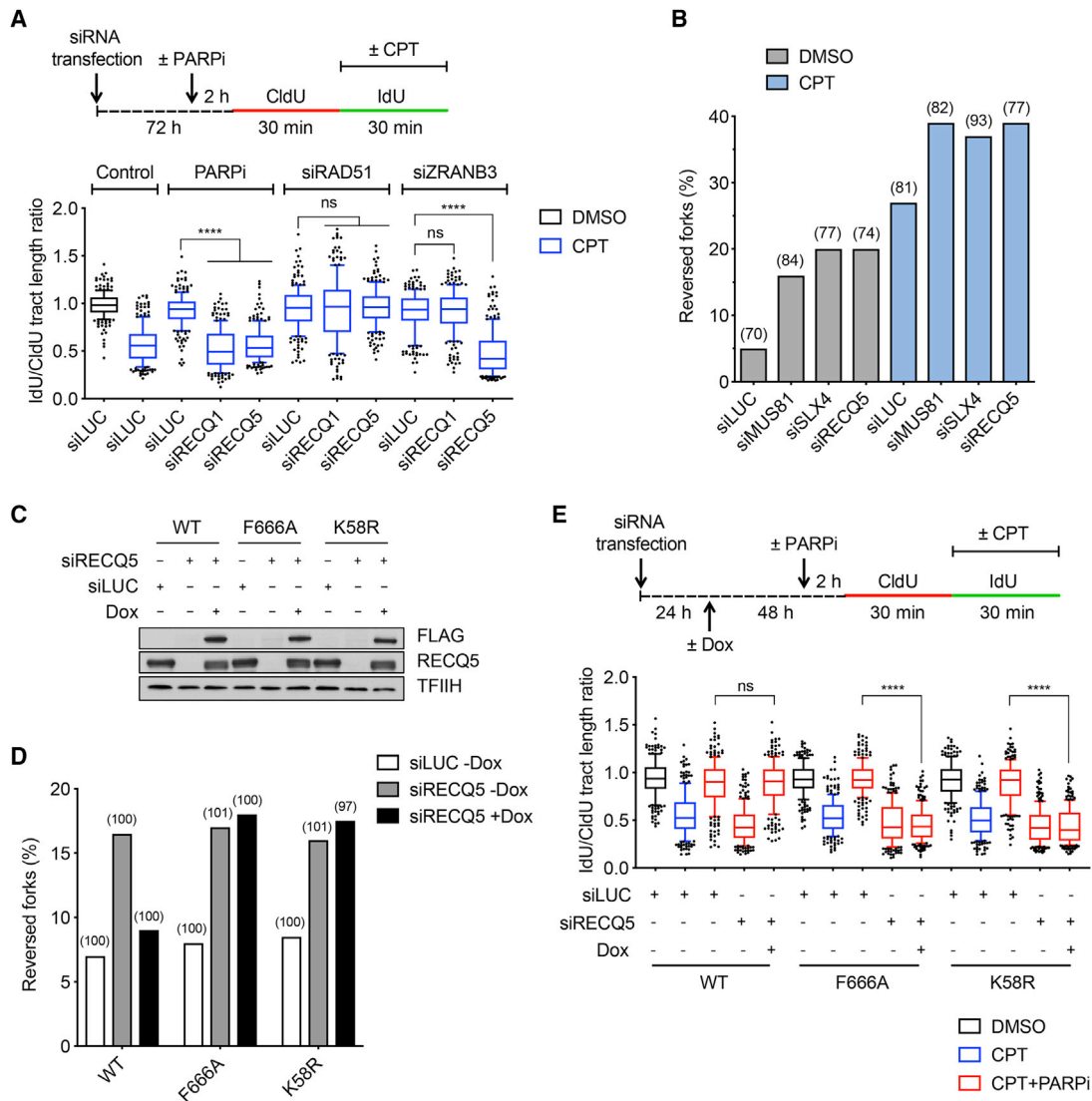
Figure 2. RECQ5 Helicase Mediates the Switch from Fork Stalling to Replication Restart by Disrupting RAD51 Filaments

(A) Effects of the depletion of RECQ1 or RECQ5 on the rescue of CPT-induced replication fork slowing in U2OS cells by PARPi and RAD51 or ZRANB3 depletion, respectively. Top panel: experimental workflow of DNA fiber assays. Bottom panel: boxplot of the values of the IdU:CldU tract length ratio obtained for the indicated conditions (n ≥ 200, whiskers: 10th–90th percentiles). ns, not significant; ****p < 0.0001 (Mann-Whitney test).

(B) Frequency of the reversed replication forks in U2OS cells transfected with indicated siRNAs. Where indicated, cells were treated with 100 nM CPT for 1 h. The numbers in brackets indicate the number of analyzed molecules. Similar results were obtained in an independent experiment (Table S1B).

(C) Western blot analysis of extracts of U2OS T-REx cells harboring wild-type (WT), K58R, or F666A forms of the siRNA-resistant RECQ5-FLAG fusion gene controlled by a Dox-inducible promoter. Twenty-four hours after the transfection of the indicated siRNAs, Dox or DMSO was added for a further 48 h, as indicated.

(D) Frequency of spontaneous replication fork reversal in cells in (C). The numbers in brackets indicate the number of analyzed molecules. Similar results were obtained in an independent experiment (Table S1C).

(E) Effect of PARPi on CPT-induced replication fork slowing in cells in (C). Top panel: experimental workflow of DNA fiber assays. Bottom panel: boxplot of the values of the IdU:CldU tract length ratio obtained for indicated conditions (n ≥ 200, whiskers: 10th–90th percentiles). ns, not significant; ****p < 0.0001 (Mann-Whitney test).

See also Figure S3.

MUS81 acts at R-loop-stalled forks as part of the MUS81/EME1 heterodimer.

Finally, we investigated whether MUS81-mediated cleavage of R-loop-stalled forks requires RECQ5 DNA helicase. We found that RECQ5 depletion reduced DNA breakage in U2OS cells treated with CPT or PDS upon PARP inhibition (Figures 3B, S4C, and S4D). This defect in RECQ5-depleted cells could be rescued by the expression of an siRNA-resistant variant of wild-type RECQ5, but not by the expression of RECQ5 mutants that cannot disrupt RAD51 filaments (Figures S4I and S4J).
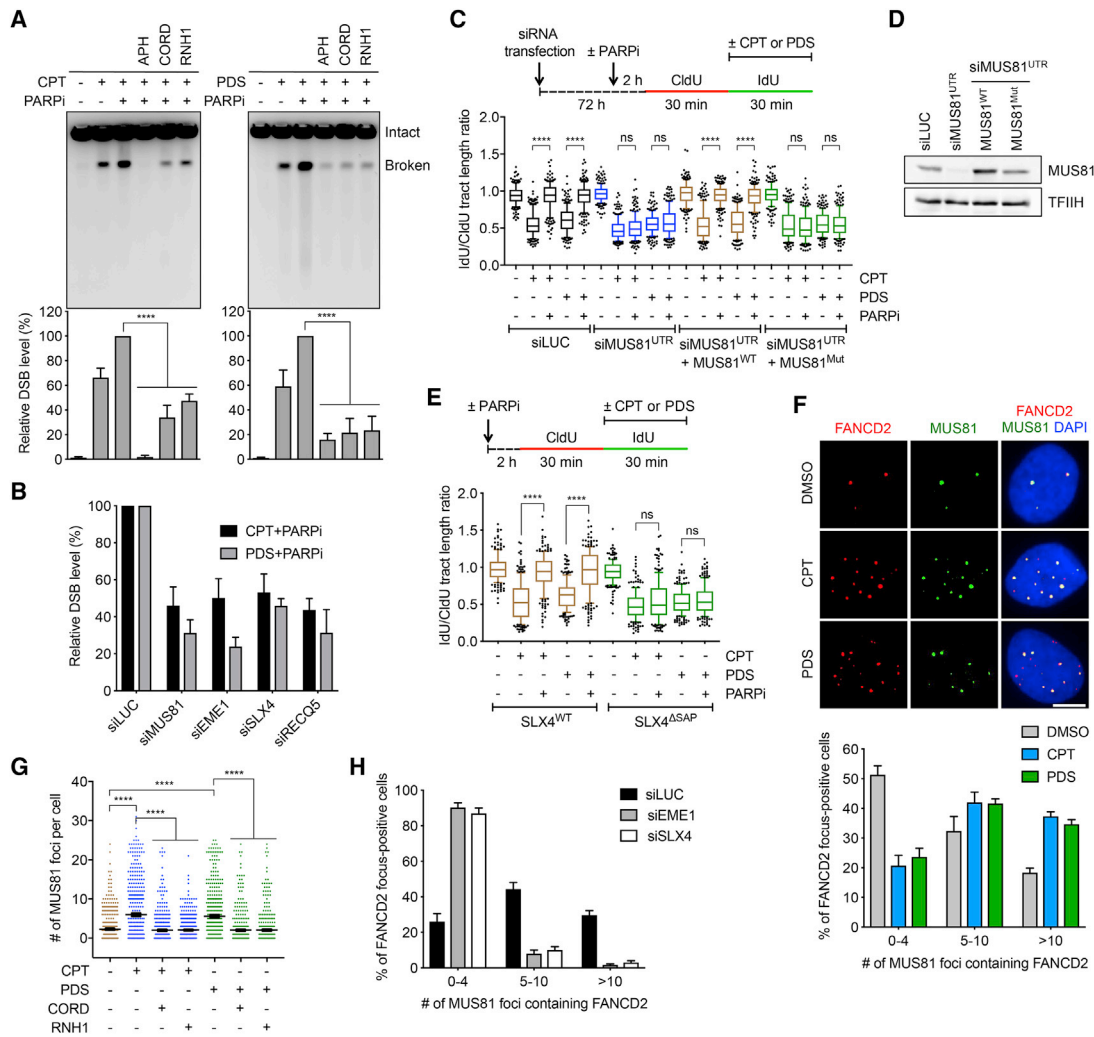
Figure 3. Restart of R-Loop-Stalled Forks Requires Fork Cleavage by MUS81 Endonuclease

(A) Genomic DNA breakage stimulated by PARPi in CPT- and PDS-treated U2OS T-REx/RNH1-GFP depends on DNA replication, transcription, and R-loop formation. Cells were treated with CPT (1 μM) or PDS (20 μM) for 5 h. Olaparib (PARPi; 10 μM), CORD (50 μM), and APH (5 μM), respectively, were added 2 h before CPT/PDS treatment. DNA breakage was monitored by pulsed-field gel electrophoresis (top panels) and quantified using ImageJ software (bottom panels). Data were normalized and represent the means ± SDs, n = 3. ****p < 0.0001 (unpaired t test). DSB, double-strand break.

(B) Effect of the depletion of the indicated proteins on the level of DNA breakage in U2OS cells treated for 5 h with 1 μM CPT (black bars) or 20 μM PDS (gray bars) in the presence of PARPi. Genomic DNA was analyzed as in (A). Data represent the means ± SDs, n = 4.

(C) The PARPi-mediated rescue of CPT- and PDS-induced replication fork slowing in U2OS cells requires MUS81 endonuclease activity. Top panel: experimental workflow of DNA fiber assays with U2OS cells stably transfected with WT *MUS81* or *MUS81(D338A/D339A)* (MUS81^{Mut}) cDNA constructs. Endogenous MUS81 was depleted with siRNA targeting MUS81 3′ UTR (siMUS81^{UTR}). Bottom panel: boxplot of the values of the IdU:CldU tract length ratio obtained for the indicated conditions (n ≥ 200, whiskers: 10th–90th percentiles). ns, not significant; ****p < 0.0001 (Mann-Whitney test).

(D) Western blot analysis of the extract of cells in (C).

(E) Effect of CPT (100 nM) and PDS (10 μM) on replication fork progression in RA3331/E6E7/hTERT fibroblasts, complemented with either SLX4 WT or SLX4 ΔSAP cDNAs, before and after PARPi. Top panel: experimental workflow of DNA fiber assays. Bottom panel: boxplot of the values of the IdU:CldU tract length ratio obtained for the indicated conditions (n ≥ 200, whiskers: 10th–90th percentiles). ns, not significant; ****p < 0.0001 (Mann-Whitney test).

(F) Representative immunofluorescence images (top panel) and quantification (bottom panel) of MUS81 foci (green) colocalizing with FANCD2 foci (red) in U2OS cell nuclei (DAPI, blue) before and after treatment with CPT (100 nM) or PDS (10 μM) for 1 h. Data represent the means ± SDs, n = 3. Scale bar, 10 μm.

(G) Effects of RNase H1 (RNH1) overexpression and transcription inhibition on the formation of MUS81 foci in U2OS T-REx/RNH1-GFP cells treated with CPT (100 nM) or PDS (10 μM) for 1 h. RNH1-GFP expression was induced 24 h before CPT/PDS treatment. CORD (50 μM) was added 2 h before the addition of CPT or PDS. Horizontal lines represent the means ± SEMs (n ≥ 300). ns, not significant; ****p < 0.0001 (Mann-Whitney test).

(H) Effects of SLX4 and EME1 depletions on the formation of FANCD2^{+} MUS81 foci in U2OS cells treated with CPT for 1 h. Data represent the means ± SDs, n = 3. See also Figure S4.

A + APH + RO3306 → G2 phase arrest (16 h) → + EdU + Colcemid → Metaphase spread 'click' reaction (1 h release)

B

DAPI EdU

Single focus | Twin foci | Complex

C

n=700

% of EdU incorporation events — Single, Twin, Complex

D

siRNA transfection → PARPi / ± CPT / ± HU

CldU (30 min) / IdU (30 min) / 5 h / 72 h

IdU/CldU tract length ratio

ns | ns | ****

siLUC, siBRCA2, siRAD51 (DMSO, CPT, CPT/HU, HU)
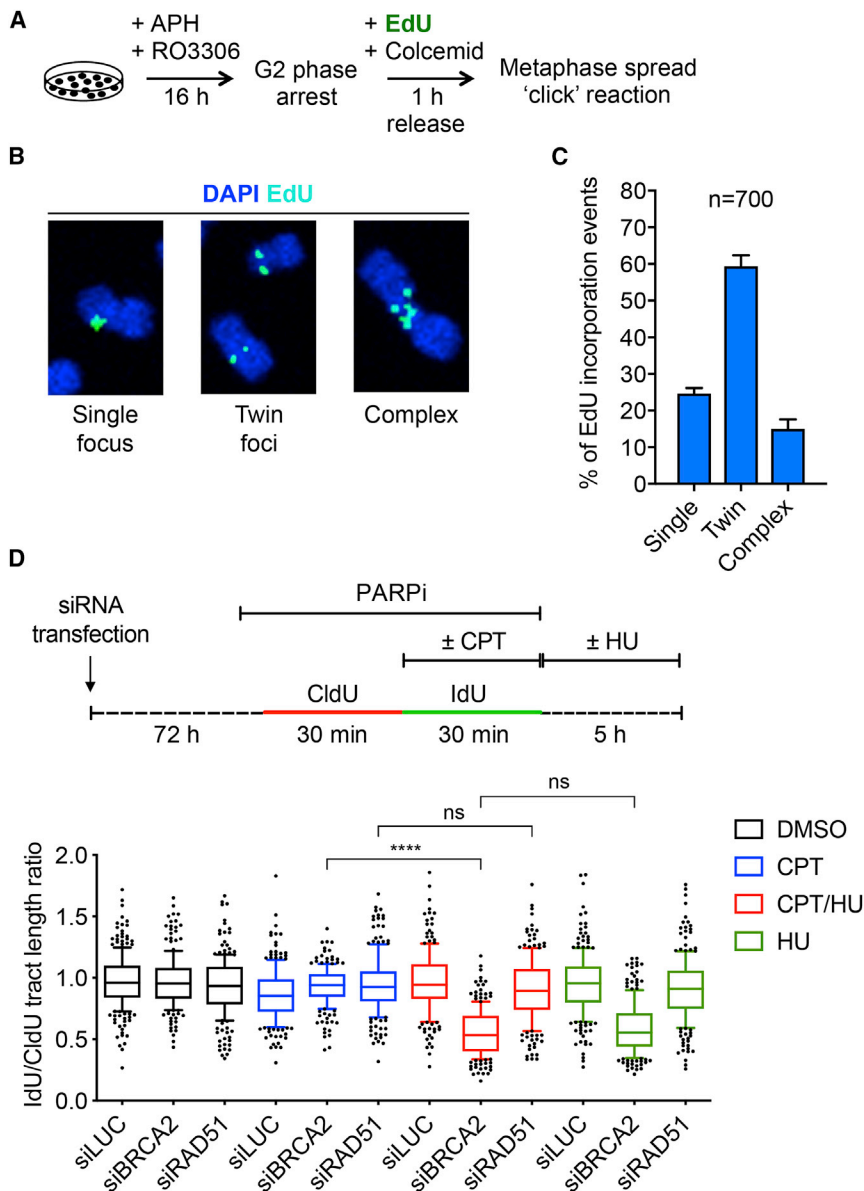
□ DMSO
□ CPT
□ CPT/HU
□ HU

Figure 4. Restart of Semiconservative DNA Replication Following R-Loop-Mediated Fork Stalling

(A–C) Experimental workflow (A), representative images (B), and quantification (C) of EdU incorporation patterns (cyan) on isolated metaphase chromosomes (DAPI, blue) of U2OS cells following replication stress induced by a low dose of APH (+APH; 0.4 µM). Twin EdU foci (one on each sister chromatid) indicate semiconservative DNA replication.

(D) Nascent DNA strands generated in the presence of CPT and PARPi are degraded upon replication arrest by hydroxyurea (HU) in BRCA2-depleted U2OS cells. Top panel: experimental workflow of DNA fiber assays. Cells were cultured in the presence of olaparib (PARPi; 10 µM) during DNA fiber labeling. Where indicated, cells were treated with CPT (100 nM) during IdU labeling and/or with HU (4 mM) for 5 h after IdU labeling. Bottom panel: boxplot of the values of the IdU:CldU tract length ratio for mock (siLUC)-, BRCA2-, and RAD51-depleted cells treated as indicated (n ≥ 200, whiskers: 10th–90th percentiles). ns, not significant; ****p < 0.0001 (Mann-Whitney test). See also Figure S5.

These data support the proposal that RECQ5 eliminates RAD51 filaments on R-loop-stalled forks to facilitate fork cleavage by MUS81/EME1 endonuclease, which triggers replication restart.

Restart of Semiconservative DNA Replication Following R-Loop-Mediated Fork Stalling

The identification of POLD3 as a factor required for replication stress-induced DNA synthesis was interpreted as the involvement of break-induced replication (BIR) (Costantino et al., 2014; Minocherhomji et al., 2015), in which newly synthesized DNA strands segregate with the broken chromatid (Donnianni and Symington, 2013). However, by analyzing 5-ethynyl-2′-deoxyuridine (EdU) incorporation patterns on metaphase chromosome spreads, we found that aphidicolin (APH)-induced MiDAS predominantly occurred on both sister chromatids in a variety of cell lines (Figures 4A–4C and S5A–S5E), which is indicative of a semiconservative mode of DNA replication. MiDAS and the concomitant formation of DAPI⁻ gaps on metaphase chromosomes were suppressed upon the overexpression of RNase H1 (Figures S5F and S5G), confirming that it is mainly caused by R-loops. Thus, we next assessed whether the DNA synthesis initiated at R-loop-stalled forks during S phase also occurs in a semiconservative manner. It is known that replication arrest induced by hydroxyurea (HU) triggers the MRE11-dependent degradation of nascent DNA strands in BRCA2-defective cells (Schlacher et al., 2011). As this phenomenon requires replication fork reversal (Mijic et al., 2017), we reasoned that it could be used as an indication of semiconservative DNA replication. We therefore tested by DNA fiber assay whether the nascent DNA strands generated in BRCA2-depleted U2OS cells upon CPT treatment are sensitive to nucleolytic resection if the replication process is blocked by HU. Specifically, replication tracts in these cells were sequentially pulse labeled by CldU and IdU, with CPT being present during the IdU labeling. Olaparib was added 2 h before DNA fiber labeling to boost replication restart and block fork degradation during CPT treatment (Mijic et al., 2017). This was followed by HU treatment for 5 h (Figure 4D). The same assay was also performed with RAD51-depleted cells. We found that, upon HU treatment, IdU tracts were shortened in BRCA2-depleted cells, but not in RAD51-depleted cells (Figure 4D). This shortening of IdU tracts in BRCA2-depleted cells was prevented by the addition of the MRE11 inhibitor mirin (Figure S5H), indicating that it

results from the resection of reversed forks (Mijic et al., 2017). The extent of HU-induced nascent strand degradation in BRCA2-depleted cells pretreated with CPT and olaparib was comparable to that measured in cells treated with HU only (Figure 4D), excluding the possibility that nascent strand degradation occurred only at the forks that were not impaired by R-loops. Essentially the same results were obtained if CPT was substituted with PDS (Figures S5H and S5I). Of note, the nucleolytic degradation of nascent DNA strands could also occur during BIR if HU-induced replication arrest resulted in D-loop disruption. In this scenario, IdU tract shortening should be detectable in both BRCA2- and RAD51-depleted cells (Figure S5J). However, this was not observed in our experiments (Figures 4D and S5I). Therefore, our data strongly suggest that replication fork stalling at R-loops is followed by the restart of semiconservative DNA replication.

Restart of R-Loop-Stalled Forks Requires a Concerted Action of RAD52 and LIG4 after Fork Cleavage by MUS81

We considered the possibility that the restoration of replication forks after endonucleolytic cleavage by MUS81/EME1 occurred via RAD52-mediated reannealing of the parental DNA strands. In this case, replication restart would require a DNA ligase capable of sealing the nick in the leading strand template. To test this hypothesis, we depleted U2OS cells of either DNA ligase III (LIG3) or LIG4 and evaluated whether the absence of these proteins impairs the restart of CPT- and PDS-stalled forks. Using a DNA fiber assay, we found that the depletion of LIG4, but not LIG3, enhanced the inhibitory effect of CPT and PDS on replication fork progression and prevented its rescue by PARP inhibition (Figures 5A, 5B, and S6A). The depletion of LIG4 also impaired the resumption of DNA synthesis after the removal of CPT or PDS (Figure 5C). Essentially the same phenotypes were observed upon the depletion of XRCC4 (Figures 5A–5C and S6A), which forms a complex with LIG4 and stimulates its activity (Grawunder et al., 1997). On the contrary, the depletion of KU70 did not significantly affect the restart of CPT- and PDS-stalled forks (Figures 5A–5C and S6A), suggesting that the LIG4/XRCC4 complex operates in the replication restart process independently of the non-homologous end-joining (NHEJ) machinery. We also found that LIG4 and XRCC4, but not LIG3 and KU70, were required for MiDAS in U2OS cells exposed to a low dose of APH (Figures 5D and S6B). Similar results were obtained with MRC5 fibroblasts (Figures S6B and S6C). Consistently, LIG4 or XRCC4 deficiency decreased the number of DAPI⁻ gaps on the metaphase chromosomes of APH-treated cells and increased the formation of 53BP1 nuclear bodies in G1 cells (Figures S6D–S6F).

To assess whether the restart of R-loop-stalled forks depends on the catalytic activity of LIG4, we used human telomerase reverse transcriptase (hTERT)-immortalized fibroblasts derived from an LIG4 syndrome patient (411BR) carrying a hypomorphic homozygous mutation (R278H) in the catalytic domain of LIG4, which reduces the adenylation and ligation activities of the enzyme to 5%–10% of the wild type (Girard et al., 2004; O'Driscoll et al., 2001). The 411BR patient also carried two additional amino acid substitutions (A3V + T9I) at the N terminus of LIG4 (A3V + T9I) that further reduce the polyadenylation and ligation

activity of the R278H mutant without affecting LIG4 protein levels or the interaction with XRCC4 (Cottarel et al., 2013; Girard et al., 2004; O'Driscoll et al., 2001). We found that PARP inhibition did not rescue CPT- and PDS-induced replication fork slowing in 411BR cells (Figure 5E). However, PARP inhibition did prevent CPT- and PDS-induced replication fork slowing in hTERT-immortalized control human fibroblasts 1BR (Figure 5E). These data suggest that the DNA-ligase activity of the LIG4/XRCC4 complex is required for replication restart after R-loop-mediated fork stalling.

In agreement with a model implicating RAD52 and the LIG4/XRCC4 heterodimer in the religation of MUS81-cleaved replication forks at sites of R-loop-mediated fork stalling, we found that U2OS cells depleted of RAD52 or LIG4 displayed elevated levels of MUS81-dependent DSBs upon treatment with CPT as compared to mock-depleted cells (Figure 5F). Moreover, the depletion of LIG4 or RAD52 conferred R-loop-dependent hypersensitivity to PARP inhibition in U2OS cells, to an extent similar to that caused by MUS81 depletion (Figures S6G and S6H). Upon PARP inhibition, both LIG4- and RAD52-depleted cells also displayed increased sensitivity to CPT and PDS as compared to mock-depleted cells, which could be rescued by RNase H1 overexpression (Figures S6I–S6K). The depletion of LIG4 or RAD52 did not increase the sensitivity of MUS81-knockout HeLa cells to PARP inhibition, although the lack of these proteins decreased the survival of wild-type HeLa cells upon PARP inhibition (Figures 5G and S6L). These data suggest that LIG4 and RAD52 act epistatically with MUS81 to counteract the lethal effects of R-loop-mediated TRCs.

Restart of R-Loop-Stalled Forks Requires Reactivation of Transcription

If R-loop-forming transcription complexes persisted ahead of restarting replication forks, then they would hinder replication fork progression, preventing TRC resolution. We therefore considered the possibility that the restart of R-loop-stalled forks is preceded by transcription reactivation that occurs after fork cleavage by MUS81/EME1. To test this hypothesis, we evaluated the effect of transcription elongation inhibitors cordycepin and DRB on the restart of CPT- and PDS-stalled forks measured by DNA fiber assay (Figure S2H). Cordycepin and DRB were added after the removal of the R-loop-inducing drugs, to be present only during the replication restart process (Figure 6A). We found that 30 min after CPT or PDS exposure, cells incubated in the presence of transcription elongation inhibitors exhibited a significantly higher percentage of stalled forks as compared to mock-treated cells (Figure 6A), reaching the levels detected in cells lacking the proteins of the MUS81 pathway (Figures 1G and S2I). Cordycepin and DRB also inhibited MiDAS induced by APH (Figure S7A). These data suggest that the restart of R-loop-stalled forks requires active transcription.

To further explore our hypothesis, we quantified by 5-ethynyl uridine (EU) labeling nascent RNA transcripts at the end and after treatment of MUS81-depleted U2OS cells with CPT or PDS for 30 min. We found that CPT and PDS inhibited nascent RNA transcript production in both mock- and MUS81-depleted cells (Figures 6B and S7B–S7F). Nascent RNA transcript production was significantly restored in control cells 30 min after the removal of
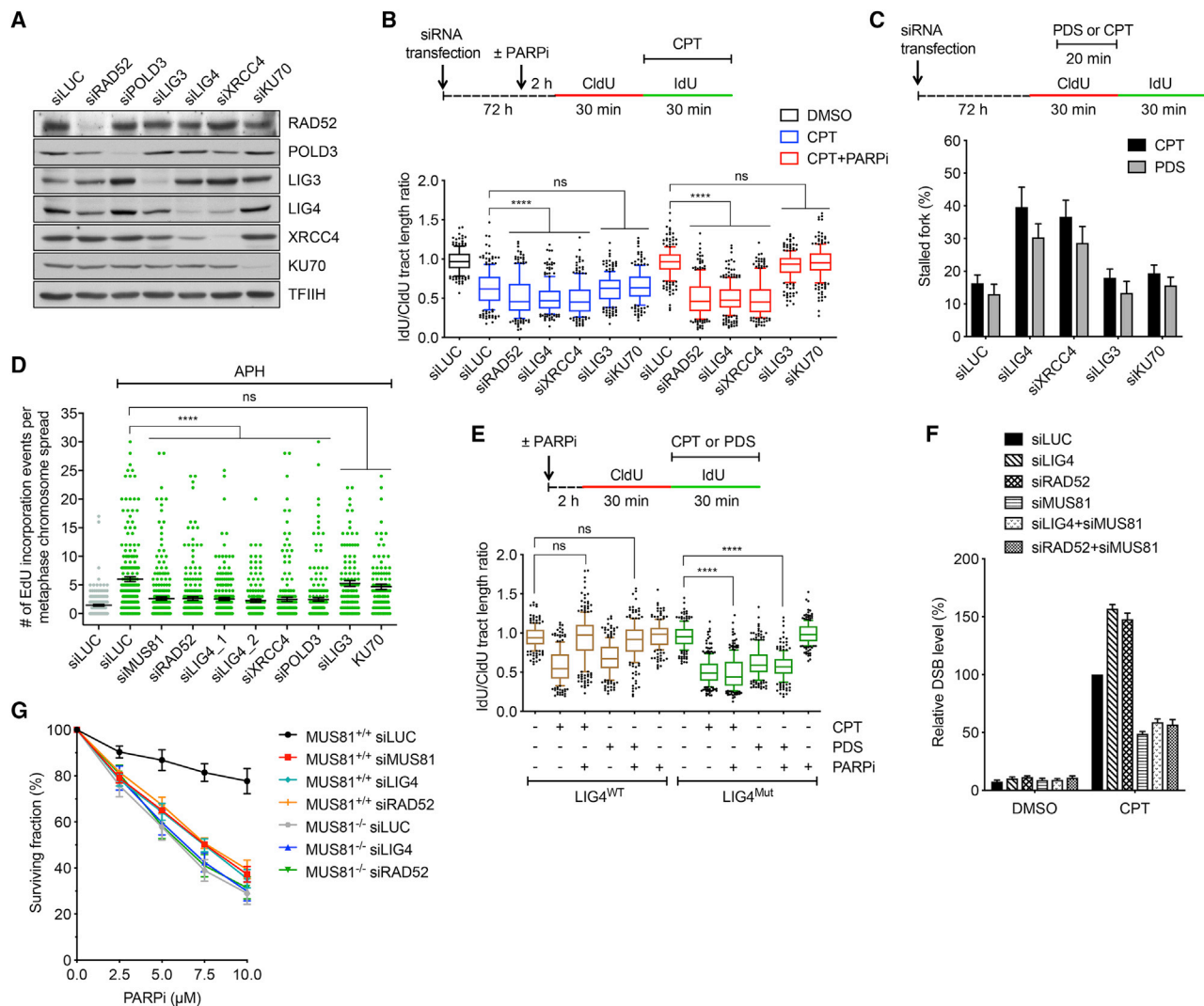
Figure 5. Restart of R-Loop-Stalled Forks Depends on the Catalytic Activity of the LIG4/XRCC4 Complex

(A) Western blot analysis of the extracts of U2OS cells transfected with indicated siRNAs.

(B) Effect of the depletion of the indicated proteins on replication fork progression in U2OS cells upon treatment with 100 nM CPT, and on the rescue of CPT-induced replication fork slowing by PARPi (10 μM olaparib). Top panel: experimental workflow of DNA fiber assays. Bottom panel: boxplot of the values of the IdU:CldU tract length ratio obtained for the indicated conditions (n ≥ 200, whiskers: 10th–90th percentiles). ns, not significant; ****p < 0.0001 (Mann-Whitney test).

(C) Effect of depletion of the indicated proteins on replication restart following the exposure of U2OS cells to CPT (100 nM) or PDS (10 μM). Top panel: experimental workflow of DNA fiber assays. Bottom panel: quantification of replication fork stalling events performed as in Figure 1G. Data represent the means ± SDs, n = 3.

(D) LIG4/XRCC4 is required for mitotic DNA synthesis (MiDAS) in U2OS cells. MiDAS assay was performed as depicted in Figure S6B. The data points represent the number of EdU incorporation events per metaphase spread (n ≥ 150). Horizontal lines represent the means ± SEMs. ns, not significant; ****p < 0.0001 (Mann-Whitney test).

(E) Effect of CPT and PDS on replication fork progression in human fibroblasts expressing WT (LIG4^WT, 1BR) or catalytically inactive (LIG4^MUT, 411 BR) forms of LIG4, with or without PARPi. DNA fiber assays were performed as in Figure 3E.

(F) The levels of spontaneous (DMSO) and CPT-induced DNA breakage in U2OS cells depleted for the indicated proteins. Cells were treated with 1 μM CPT for 5 h. Genomic DNA was analyzed as in Figure 3A. Data represent the means ± SDs, n = 4.

(G) Effect of the depletion of LIG4 and RAD52 on the sensitivity of WT and MUS81 knockout (KO) HeLa Kyoto cells to PARPi, as determined by clonogenic assay. Data represent the means ± SDs, n = 3.
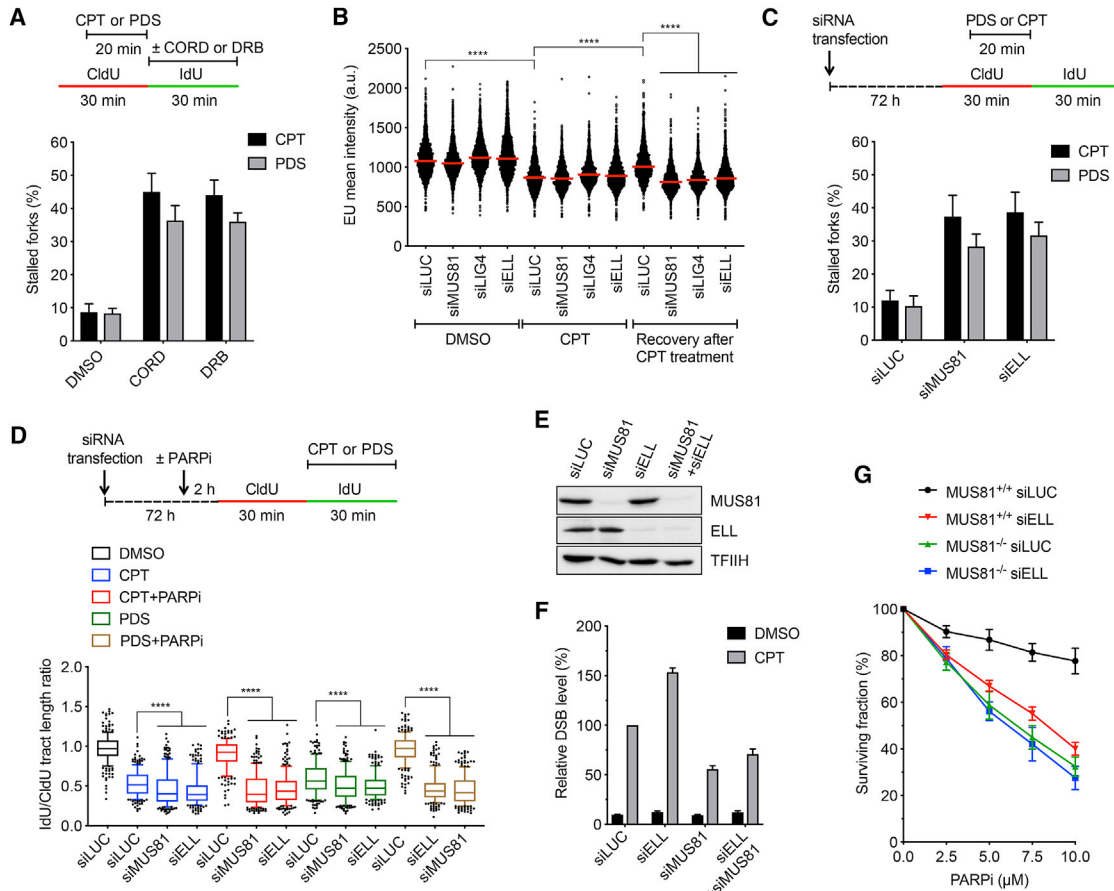
Also see Figure S6.

Figure 6. Restart of R-Loop-Stalled Forks Requires Reactivation of Transcription

(A) Effect of DRB (100 μM) and CORD (50 μM) on replication restart following the treatment of U2OS cells with 100 nM CPT or 10 μM PDS. Top panel: experimental workflow of DNA fiber assays. Bottom panel: quantification of replication fork stalling events performed as in Figure 1G. Data represent the means ± SDs, n = 3.

(B) Depletion of MUS81, LIG4, or ELL impairs the resumption of transcription following the exposure of U2OS cells to CPT. Nascent RNA strand production was quantified using 5-ethynyl uridine (EU; 1 mM) labeling during a 30-min treatment of cells with 100 nM CPT (or DMSO, control) and during a subsequent 30-min chase with CPT-free medium. The data represent the mean intensity of the EU signal in the nucleus. Horizontal lines represent median (n > 1,800). ****p < 0.0001 (Mann-Whitney test).

(C) Effect of ELL depletion on replication restart following the treatment of U2OS cells with CPT (100 nM) or PDS (10 μM). Replication restart was quantified as in (A).

(D) Effect of ELL depletion on replication fork progression in U2OS cells upon treatment with 100 nM CPT or 10 μM PDS, and on the rescue of CPT- or PDS-induced replication fork slowing by PARPi (10 μM olaparib). Top panel: experimental workflow of DNA fiber assay. Bottom panel: boxplot of the values of the IdU:CldU tract length obtained for the indicated conditions (n ≥ 200, whiskers: 10th–90th percentiles). ns, not significant; ****p < 0.0001 (Mann-Whitney test).

(E) Western blot analysis of the extracts of U2OS cells transfected with indicated siRNAs.

(F) The levels of spontaneous (DMSO) and CPT-induced DNA breakage in U2OS cells depleted for the indicated proteins. Cells were treated with 1 μM CPT for 5 h. Genomic DNA was analyzed as in Figure 3A. Data represent the means ± SDs, n = 3.

(G) Effect of ELL depletion on the sensitivity of WT and MUS81 KO HeLa Kyoto cells to PARPi as determined by clonogenic assay. Data represent the means ± SDs, n = 3.

See also Figure S7.

the R-loop-inducing drugs, but not in cells lacking MUS81 (Figures 6B, S7B, and S7D–S7F). The restoration of active transcription during the recovery from CPT or PDS treatment was also impaired in cells depleted of LIG4 or RAD52, but not in cells depleted of POLD3 (Figures 6B and S7D–S7F). Moreover, the resumption of RNA synthesis following the removal of CPT or PDS was impaired by RAD52 inhibitor (Figures S7B and S7G). MUS81, RAD52, and LIG4 depletion did not significantly affect

transcription in unchallenged cells (Figures 6B and S7D–S7F). These results suggest that the DNA transactions mediated by MUS81, RAD52, and LIG4, but not the restart of DNA synthesis, promote the resumption of active transcription at sites of R-loop-mediated TRCs.

Transcription restart after the removal of transcription-blocking DNA lesions by the nucleotide excision repair machinery requires the eleven-nineteen lysine-rich leukemia (ELL) protein, a
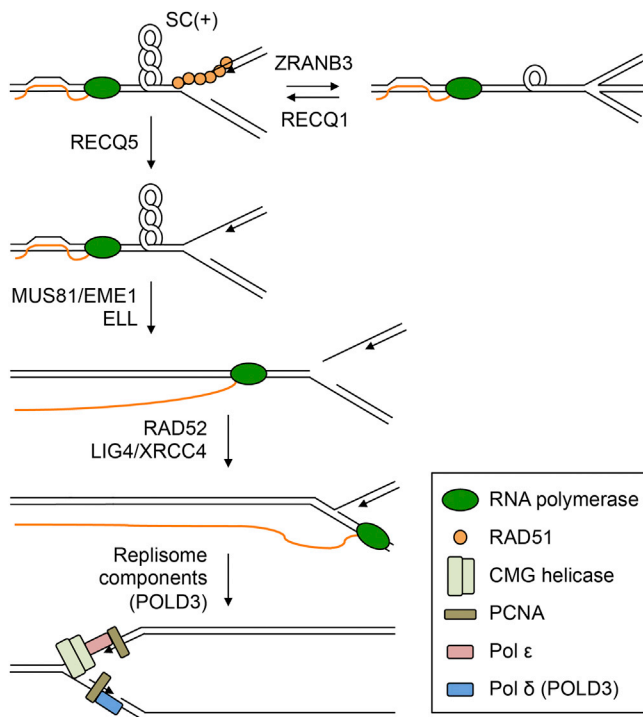
Figure 7. Model for the Resolution of R-Loop-Mediated TRCs

The blockage of replication fork progression by an oncoming transcription complex results from the buildup of positive supercoiling within the intervening DNA region and the formation of an R-loop. Replication fork stalling leads to the assembly of RAD51 filament at the fork junction, which promotes fork reversal in conjunction with the DNA translocase ZRANB3. RECQ1 DNA helicase counteracts replication fork reversal to promote replication restart. In this pathway, RECQ5 DNA helicase disrupts the RAD51 filament on the stalled fork to facilitate fork cleavage by MUS81/EME1 endonuclease. This relieves the topological barrier in the DNA template, allowing ELL-mediated transcription restart. After re-annealing of the parental strands by RAD52 and sealing the nick in the parental duplex by the LIG4/XRCC4 complex, the re-activated transcription complex bypasses the replication-stalling site. This is followed by the POLD3-mediated restart of semiconservative DNA replication. It is assumed that after fork stalling, the replicative helicase CMG traverses the fork junction onto dsDNA via its ssDNA gate (not shown). After fork religation, CMG translocates back onto ssDNA to nucleate a functional replisome.

component of the little elongation complex (LEC), which is recruited to damaged chromatin through its interaction with the CDK7 subunit of transcription factor II H (TFIIH) (Mourgues et al., 2013). We therefore sought to explore the possibility that ELL acts on the stalled transcription complexes at sites of TRCs to mediate the reactivation of RNA synthesis, thus allowing replication restart. Consistently, using EU pulse labeling, we found that ELL depletion impaired transcription recovery after the treatment of U2OS cells with CPT or PDS to an extent comparable to that observed in MUS81-depleted cells (Figures 6B and S7D). ELL depletion also abolished the PARP-regulated restart of CPT- and PDS-stalled replication forks (Figures 6C–6E and S7H). Moreover, U2OS cells depleted of ELL displayed elevated levels of MUS81-dependent DSBs upon CPT treatment as compared to mock-depleted cells (Figures 6E, 6F, and S7I). Finally, compared to mock-depleted cells, cells lacking ELL dis-

played increased sensitivity to olaparib, CPT, and PDS, which could be rescued by RNase H1 overexpression (Figures S7J–S7L). The hypersensitivity of MUS81-knockout HeLa cells to olaparib was not increased by ELL depletion (Figures 6G and S7M), suggesting that ELL and MUS81 act in a common pathway to mediate TRC resolution.

DISCUSSION

Recent studies have suggested that the impairment of replication fork progression by head-on transcription complexes is caused by the formation of co-transcriptional R-loops (Hamperl et al., 2017; Lang et al., 2017). Here, we show that R-loop-induced replication fork stalling is an active process involving replication fork reversal, and is followed by replication fork restart, which is mediated by the SLX4-MUS81/EME1-RAD52-LIG4/XRCC4-POLD3 axis. Moreover, we demonstrate that the switch from fork stalling to replication restart is mediated by the RecQ DNA helicases RECQ1 and RECQ5. Our data suggest that RECQ1 converts reversed forks to the original three-way structure, while RECQ5 disrupts RAD51 nucleoprotein filaments assembled on stalled forks in advance of a new round of fork reversal, thereby generating suitable substrates for MUS81/EME1 endonuclease (Figure 7). We propose that replication restart at sites of R-loop-associated fork stalling is mediated by RECQ5-assisted cleavage of the leading arm of the stalled fork by MUS81/EME1, followed by fork religation with the LIG4/XRCC4 complex after RAD52-mediated reannealing of the parental DNA strands (Figure 7). This is consistent with the observed accumulation of MUS81-dependent DNA breaks in cells lacking RAD52 or LIG4 upon the induction of R-loop formation with CPT (Figure 5F). Moreover, we have found that LIG4 and RAD52 act epistatically with MUS81 to suppress the R-loop-mediated toxicity of PARP inhibition (Figure 5G), which activates RECQ1 to counteract fork reversal (Berti et al., 2013). Of note, although the Ku heterodimer is known to transiently associate with single-ended DSBs generated at stalled forks in CPT-treated cells (Chanut et al., 2016), we found that it was not required for MUS81-initiated replication restart. Thus, our study implicates a specific function for LIG4/XRCC4 in replication fork restart that goes beyond its canonical role in NHEJ. It is possible that the DNA synapsis step in this process relies solely on the single-strand annealing activity of RAD52 (Figure 7).

We propose that replication fork cleavage by MUS81/EME1 is required to relieve the torsional stress generated in DNA by converging transcription and replication machineries (Figure 7), which halts their progression and probably triggers R-loop formation (García-Muse and Aguilera, 2016; Hamperl et al., 2017). This would allow the reactivation of RNA synthesis, eliminating the obstacle to replication fork progression. Along this line, we found that MUS81 depletion impaired transcription recovery after the treatment of cells with R-loop-inducing drugs (Figures 6B and S7D–S7F). Moreover, the MUS81-initiated restart of R-loop-stalled forks was impaired upon the depletion of the transcription elongation factor ELL or upon the addition of transcription elongation inhibitors (Figures 6A and 6C). Transcription recovery following the induction of R-loop-mediated TRCs also required LIG4 and RAD52, but not POLD3 (Figures 6B and S7B–S7G).

This suggests that the passage of transcription complexes across the replication-stalling site occurs after fork religation, eliminating the gap on the lagging strand that could block transcription (Figure 7). Thus, the fork cleavage-religation cycle would ensure the movement of the replication machinery through oppositely transcribed DNA regions without disrupting the transcription complexes. This would be particularly relevant for the longest human genes where TRCs occur during each transcription round because it takes longer than one cell cycle (Helmrich et al., 2011).

The question arises regarding the fate of the replisome upon a TRC. A recent study has shown the Cdc45-MCM-GINS (CMG) helicase harbors an ssDNA gate, which enables the complex to traverse forked junctions onto double-stranded DNA (dsDNA), when uncoupled from DNA polymerase (Wasserman et al., 2019). Moreover, CMG undergoes rapid diffusion on dsDNA and can transition back onto ssDNA to nucleate a functional replisome (Wasserman et al., 2019). Thus, it is tempting to speculate that this ssDNA gating process may help preserve CMG on dsDNA during the initial steps of the TRC resolution process. After fork religation, CMG would traverse back onto the leading arm of the fork to enable fork bypass by the transcription complex and subsequent reassembly of the replisome.

We show that MiDAS, the prophase-specific DNA-repair synthesis induced by mild replication stress at CFSs (Minocherhomji et al., 2015), depends on R-loop formation and requires the same set of factors as the restart of R-loop-stalled replication forks in S phase. However, the notable difference between the processing of stalled replication forks in S phase and in early mitosis is that the binding of MUS81 to SLX4, which is essential for MUS81/EME1 recruitment to replication stalling sites (Minocherhomji et al., 2015; Figure 3H), is enhanced upon entry to mitosis through cyclin-dependent kinase 1 (CDK1)-mediated phosphorylation of the SAP domain of SLX4 that binds MUS81 (Duda et al., 2016; Wyatt et al., 2013). As a result, MUS81 is markedly enriched on CFSs in mitotic prophase (Di Marco et al., 2017; Minocherhomji et al., 2015). We propose that this phosphorylation-driven enhancement of MUS81/SLX4 complex formation serves to ensure that all persistent replication intermediates are resolved before the onset of anaphase.

Previous studies have postulated that MUS81-initiated restart of DNA synthesis at stalled replication forks occurs by BIR, which is a conservative form of DNA replication (Costantino et al., 2014; Minocherhomji et al., 2015; Sotiriou et al., 2016). We show here that the nascent DNA strands generated during MiDAS segregate, in the majority of MiDAS events, with both sister chromatids, which is indicative of a semiconservative mode of DNA replication. Moreover, we demonstrate that the nascent DNA strands synthesized after replication restart at R-loops in S phase are sensitive to HU-induced resection in BRCA2-deficient cells. As this process is initiated from reversed forks (Mijic et al., 2017), our data suggest that the MUS81 pathway initiates semiconservative DNA replication, at least after replication fork stalling by R-loops. Studies in yeast have shown that the BIR-mediated restart of collapsed replication forks is largely dependent upon the Rad51 recombinase, which mediates BIR initiation by catalyzing D-loop formation (Mayle et al., 2015). However, the human RAD51 and its loader BRCA2 are not required for MiDAS

and the restart of R-loop-stalled forks in S phase (Bhowmick et al., 2016; Figures 1G and S2I). Instead, RAD51 restrains replication restart by promoting fork reversal (Zellweger et al., 2015). Thus, we conclude that RAD51-dependent BIR does not play a major role in the restart of DNA synthesis at sites of R-loop-mediated TRCs.

STAR★METHODS

Detailed methods are provided in the online version of this paper and include the following:

- KEY RESOURCES TABLE
- LEAD CONTACT AND MATERIALS AVAILABILITY
- EXPERIMENTAL MODEL AND SUBJECT DETAILS
- METHOD DETAILS
  - Cell culture
  - CRISPR/Cas9-mediated generation of MUS81 knockout cells
  - Small-interfering RNA transfections
  - Clonogenic assay
  - Preparation cell extracts and western blot analysis
  - Immunofluorescence assays
  - Detection of RNA:DNA hybrids with S9.6 antibody
  - *In situ* proximity ligation assay
  - Analysis of metaphase chromosome spreads and MiDAS assay
  - DNA fiber spreading assay
  - Quantification of nascent RNA production by 5-ethynyl uridine labeling
  - Electron microscopy
  - Pulsed-field gel electrophoresis
- QUANTIFICATION AND STATISTICAL ANALYSIS
- DATA AND CODE AVAILABILITY

AUTHOR CONTRIBUTIONS

P.J. and N.C. conceived the overall experimental design; M.L. and A.P. aided in the experimental design; N.C. performed the majority of the experiments; Z.N., S.M., and J.D. performed the R-loop analyses; B.B. performed a part of the EU-labeling experiments; R.Z. aided in the electron microscopy analyses; E.I. and M.A. performed a part of the DNA fiber experiments; C.B.P.

and J.M. prepared the *MUS81* knockout HeLa Kyoto cells; P.J. and N.C. wrote the paper; M.L. and A.P. revised and modified the paper.

DECLARATION OF INTERESTS

The authors declare no competing interests.

REFERENCES

Berti, M., Ray Chaudhuri, A., Thangavel, S., Gomathinayagam, S., Kenig, S., Vujanovic, M., Odreman, F., Glatter, T., Graziano, S., Mendoza-Maldonado, R., et al. (2013). Human RECQ1 promotes restart of replication forks reversed by DNA topoisomerase I inhibition. Nat. Struct. Mol. Biol. *20*, 347–354.

Bhowmick, R., Minocherhomji, S., and Hickson, I.D. (2016). RAD52 Facilitates Mitotic DNA Synthesis Following Replication Stress. Mol. Cell *64*, 1117–1126.

Chanut, P., Britton, S., Coates, J., Jackson, S.P., and Calsou, P. (2016). Coordinated nuclease activities counteract Ku at single-ended DNA double-strand breaks. Nat. Commun. *7*, 12889.

Costantino, L., Sotiriou, S.K., Rantala, J.K., Magin, S., Mladenov, E., Helleday, T., Haber, J.E., Iliakis, G., Kallioniemi, O.P., and Halazonetis, T.D. (2014). Break-induced replication repair of damaged forks induces genomic duplications in human cells. Science *343*, 88–91.

Cottarel, J., Frit, P., Bombarde, O., Salles, B., Négrel, A., Bernard, S., Jeggo, P.A., Lieber, M.R., Modesti, M., and Calsou, P. (2013). A noncatalytic function of the ligation complex during nonhomologous end joining. J. Cell Biol. *200*, 173–186.

De Magis, A., Manzo, S.G., Russo, M., Marinello, J., Morigi, R., Sordet, O., and Capranico, G. (2019). DNA damage and genome instability by G-quadruplex ligands are mediated by R loops in human cancer cells. Proc. Natl. Acad. Sci. USA *116*, 816–825.

Di Marco, S., Hasanova, Z., Kanagaraj, R., Chappidi, N., Altmannova, V., Menon, S., Sedlackova, H., Langhoff, J., Surendranath, K., Hühn, D., et al. (2017). RECQ5 Helicase Cooperates with MUS81 Endonuclease in Processing Stalled Replication Forks at Common Fragile Sites during Mitosis. Mol. Cell *66*, 658–671.e8.

Donnianni, R.A., and Symington, L.S. (2013). Break-induced replication occurs by conservative DNA synthesis. Proc. Natl. Acad. Sci. USA *110*, 13475–13480.

Duda, H., Arter, M., Gloggnitzer, J., Teloni, F., Wild, P., Blanco, M.G., Altmeyer, M., and Matos, J. (2016). A Mechanism for Controlled Breakage of Under-replicated Chromosomes during Mitosis. Dev. Cell *39*, 740–755.

Duquette, M.L., Handa, P., Vincent, J.A., Taylor, A.F., and Maizels, N. (2004). Intracellular transcription of G-rich DNAs induces formation of G-loops, novel structures containing G4 DNA. Genes Dev. *18*, 1618–1629.

Gaillard, H., García-Muse, T., and Aguilera, A. (2015). Replication stress and cancer. Nat. Rev. Cancer *15*, 276–289.

García-Muse, T., and Aguilera, A. (2016). Transcription-replication conflicts: how they occur and how they are resolved. Nat. Rev. Mol. Cell Biol. *17*, 553–563.

Girard, P.M., Kysela, B., Härer, C.J., Doherty, A.J., and Jeggo, P.A. (2004). Analysis of DNA ligase IV mutations found in LIG4 syndrome patients: the impact of two linked polymorphisms. Hum. Mol. Genet. *13*, 2369–2376.

Grawunder, U., Wilm, M., Wu, X., Kulesza, P., Wilson, T.E., Mann, M., and Lieber, M.R. (1997). Activity of DNA ligase IV stimulated by complex formation with XRCC4 protein in mammalian cells. Nature *388*, 492–495.

Hamperl, S., and Cimprich, K.A. (2014). The contribution of co-transcriptional RNA:DNA hybrid structures to DNA damage and genome instability. DNA Repair (Amst.) *19*, 84–94.

Hamperl, S., and Cimprich, K.A. (2016). Conflict Resolution in the Genome: How Transcription and Replication Make It Work. Cell *167*, 1455–1467.

Hamperl, S., Bocek, M.J., Saldivar, J.C., Swigut, T., and Cimprich, K.A. (2017). Transcription-Replication Conflict Orientation Modulates R-Loop Levels and Activates Distinct DNA Damage Responses. Cell *170*, 774–786.e19.

Helmrich, A., Ballarino, M., and Tora, L. (2011). Collisions between replication and transcription complexes cause common fragile site instability at the longest human genes. Mol. Cell *44*, 966–977.

Jones, R.M., Mortusewicz, O., Afzal, I., Lorvellec, M., García, P., Helleday, T., and Petermann, E. (2013). Increased replication initiation and conflicts with transcription underlie Cyclin E-induced replication stress. Oncogene *32*, 3744–3753.

Kim, Y., Spitz, G.S., Veturi, U., Lach, F.P., Auerbach, A.D., and Smogorzewska, A. (2013). Regulation of multiple DNA repair pathways by the Fanconi anemia protein SLX4. Blood *121*, 54–63.

Lang, K.S., Hall, A.N., Merrikh, C.N., Ragheb, M., Tabakh, H., Pollock, A.J., Woodward, J.J., Dreifus, J.E., and Merrikh, H. (2017). Replication-Transcription Conflicts Generate R-Loops that Orchestrate Bacterial Stress Survival and Pathogenesis. Cell *170*, 787–799.e18.

Lossaint, G., Larroque, M., Ribeyre, C., Bec, N., Larroque, C., Décaillet, C., Gari, K., and Constantinou, A. (2013). FANCD2 binds MCM proteins and controls replisome function upon activation of s phase checkpoint signaling. Mol. Cell *51*, 678–690.

Macheret, M., and Halazonetis, T.D. (2018). Intragenic origins due to short G1 phases underlie oncogene-induced DNA replication stress. Nature *555*, 112–116.

Mayle, R., Campbell, I.M., Beck, C.R., Yu, Y., Wilson, M., Shaw, C.A., Bjergbaek, L., Lupski, J.R., and Ira, G. (2015). DNA REPAIR. Mus81 and converging forks limit the mutagenicity of replication fork breakage. Science *349*, 742–747.

Mijic, S., Zellweger, R., Chappidi, N., Berti, M., Jacobs, K., Mutreja, K., Ursich, S., Ray Chaudhuri, A., Nussenzweig, A., Janscak, P., and Lopes, M. (2017). Replication fork reversal triggers fork degradation in BRCA2-defective cells. Nat. Commun. *8*, 859.

Minocherhomji, S., Ying, S., Bjerregaard, V.A., Bursomanno, S., Aleliunaite, A., Wu, W., Mankouri, H.W., Shen, H., Liu, Y., and Hickson, I.D. (2015). Replication stress activates DNA repair synthesis in mitosis. Nature *528*, 286–290.

Mourgues, S., Gautier, V., Lagarou, A., Bordier, C., Mourcet, A., Slingerland, J., Kaddoum, L., Coin, F., Vermeulen, W., Gonzales de Peredo, A., et al. (2013). ELL, a novel TFIIH partner, is involved in transcription restart after DNA repair. Proc. Natl. Acad. Sci. USA *110*, 17927–17932.

Mutreja, K., Krietsch, J., Hess, J., Ursich, S., Berti, M., Roessler, F.K., Zellweger, R., Patra, M., Gasser, G., and Lopes, M. (2018). ATR-Mediated Global Fork Slowing and Reversal Assist Fork Traverse and Prevent Chromosomal Breakage at DNA Interstrand Cross-Links. Cell Rep. *24*, 2629–2642.e5.

Nguyen, H.D., Yadav, T., Giri, S., Saez, B., Graubert, T.A., and Zou, L. (2017). Functions of Replication Protein A as a Sensor of R Loops and a Regulator of RNaseH1. Mol. Cell *65*, 832–847.e4.

O'Driscoll, M., Cerosaletti, K.M., Girard, P.M., Dai, Y., Stumm, M., Kysela, B., Hirsch, B., Gennery, A., Palmer, S.E., Seidel, J., et al. (2001). DNA ligase IV mutations identified in patients exhibiting developmental delay and immunodeficiency. Mol. Cell *8*, 1175–1185.

Prado, F., and Aguilera, A. (2005). Impairment of replication fork progression mediates RNA polII transcription-associated recombination. EMBO J. *24*, 1267–1276.

Ray Chaudhuri, A., Hashimoto, Y., Herrador, R., Neelsen, K.J., Fachinetti, D., Bermejo, R., Cocito, A., Costanzo, V., and Lopes, M. (2012). Topoisomerase I poisoning results in PARP-mediated replication fork reversal. Nat. Struct. Mol. Biol. *19*, 417–423.

Regairaz, M., Zhang, Y.W., Fu, H., Agama, K.K., Tata, N., Agrawal, S., Aladjem, M.I., and Pommier, Y. (2011). Mus81-mediated DNA cleavage resolves replication forks stalled by topoisomerase I-DNA complexes. J. Cell Biol. *195*, 739–749.

Schlacher, K., Christ, N., Siaud, N., Egashira, A., Wu, H., and Jasin, M. (2011). Double-strand break repair-independent role for BRCA2 in blocking stalled replication fork degradation by MRE11. Cell 145, 529–542.

Sollier, J., Stork, C.T., García-Rubio, M.L., Paulsen, R.D., Aguilera, A., and Cimprich, K.A. (2014). Transcription-coupled nucleotide excision repair factors promote R-loop-induced genome instability. Mol. Cell 56, 777–785.

Sotiriou, S.K., Kamileri, I., Lugli, N., Evangelou, K., Da-Ré, C., Huber, F., Padayachy, L., Tardy, S., Nicati, N.L., Barriot, S., et al. (2016). Mammalian RAD52 Functions in Break-Induced Replication Repair of Collapsed DNA Replication Forks. Mol. Cell 64, 1127–1134.

Teloni, F., Michelena, J., Lezaja, A., Kilic, S., Ambrosi, C., Menon, S., Dobrovolna, J., Imhof, R., Janscak, P., Baubec, T., and Altmeyer, M. (2019). Efficient Pre-mRNA Cleavage Prevents Replication-Stress-Associated Genome Instability. Mol. Cell 73, 670–683.e12.

Tuduri, S., Crabbé, L., Conti, C., Tourrière, H., Holtgreve-Grez, H., Jauch, A., Pantesco, V., De Vos, J., Thomas, A., Theillet, C., et al. (2009). Topoisomerase I suppresses genomic instability by preventing interference between replication and transcription. Nat. Cell Biol. 11, 1315–1324.

Urban, V., Dobrovolna, J., Hühn, D., Fryzelkova, J., Bartek, J., and Janscak, P. (2016). RECQ5 helicase promotes resolution of conflicts between replication and transcription in human cells. J. Cell Biol. 214, 401–415.

Vujanovic, M., Krietsch, J., Raso, M.C., Terraneo, N., Zellweger, R., Schmid, J.A., Taglialatela, A., Huang, J.W., Holland, C.L., Zwicky, K., et al. (2017). Replication Fork Slowing and Reversal upon DNA Damage Require PCNA Polyubiquitination and ZRANB3 DNA Translocase Activity. Mol. Cell 67, 882–890.e5.

Wasserman, M.R., Schauer, G.D., O'Donnell, M.E., and Liu, S. (2019). Replication Fork Activation Is Enabled by a Single-Stranded DNA Gate in CMG Helicase. Cell 178, 600–611.e16.

Wyatt, H.D., Sarbajna, S., Matos, J., and West, S.C. (2013). Coordinated actions of SLX1-SLX4 and MUS81-EME1 for Holliday junction resolution in human cells. Mol. Cell 52, 234–247.

Wyatt, H.D., Laister, R.C., Martin, S.R., Arrowsmith, C.H., and West, S.C. (2017). The SMX DNA Repair Tri-nuclease. Mol. Cell 65, 848–860.e11.

Zellweger, R., Dalcher, D., Mutreja, K., Berti, M., Schmid, J.A., Herrador, R., Vindigni, A., and Lopes, M. (2015). Rad51-mediated replication fork reversal is a global response to genotoxic treatments in human cells. J. Cell Biol. 208, 563–579.

Zeman, M.K., and Cimprich, K.A. (2014). Causes and consequences of replication stress. Nat. Cell Biol. 16, 2–9.

STAR★METHODS

KEY RESOURCES TABLE

REAGENT or RESOURCE	SOURCE	IDENTIFIER
Antibodies		
Mouse monoclonal anti-FLAG M2	Sigma-Aldrich	Cat# F1804; RRID: AB_262044
Mouse monoclonal anti-BRCA1 (D-9)	Santa Cruz Biotechnology	Cat# sc-6954; RRID: AB_626761
Mouse monoclonal anti-MUS81 Clone MTA30 2G10/3	Sigma-Aldrich	Cat# M1445; RRID: AB_532259
Mouse monoclonal anti-MUS81 (MTA30 2G103)	Santa Cruz Biotechnology	Cat# sc-53382; RRID: AB_2147138
Mouse monoclonal anti-Ku (p70) Ab-4	Thermo Fisher Scientific	Cat# MS-329-P1; RRID: AB_61461
Rabbit polyclonal anti-SLX4	Bethyl Laboratories	Cat# A302-270A; RRID: AB_1850156
Rabbit polyclonal anti-TFIIH p89 (S-19)	Santa Cruz Biotechnology	Cat# sc-293; RRID: AB_2262177
Rabbit polyclonal anti-GFP	Abcam	Cat# ab290; RRID: AB_2313768
Rabbit polyclonal anti-RAD51	Santa Cruz Biotechnology	Cat# sc-8349; RRID: AB_2253533
Rabbit polyclonal anti-RECQ5	P. Janscak Laboratory	Urban et al., 2016
Rabbit polyclonal anti-RECQ1	Novus Biologicals	Cat# NB100-618; RRID: AB_2178427
Rabbit polyclonal anti-53BP1	Santa Cruz Biotechnology	Cat# sc-22760; RRID: AB_2256326
Mouse monoclonal anti-α-Tubulin (DM1A)	Santa Cruz Biotechnology	Cat# sc-32293; RRID: AB_628412
Mouse monoclonal anti-GAPDH (0411)	Santa Cruz Biotechnology	Cat# sc-47724; RRID: AB_627678
Mouse monoclonal anti-Cyclin A (B-8)	Santa Cruz Biotechnology	Cat# sc-271682; RRID: AB_10709300
Rabbit polyclonal anti-FANCD2	Novus Biologicals	Cat# NB100-182; RRID: AB_100002867
Mouse monoclonal anti-LIG4 (D-8)	Santa Cruz Biotechnology	Cat# sc-271299; RRID: AB_10610371
Mouse monoclonal anti-XRCC4 (C-4)	Santa Cruz Biotechnology	Cat# sc-271087; RRID: AB_10612396
Mouse monoclonal anti-LIG3 (E-7)	Santa Cruz Biotechnology	Cat# sc-390922
Mouse monoclonal anti-BRCA2 (Ab-1)	EMD Millipore	Cat# OP-95; RRID: AB_2067762
Rabbit polyclonal anti-RAD52 (H300)	Santa Cruz Biotechnology	Cat# sc-8350; RRID: AB_2284949
Mouse monoclonal anti-POLD3 (M01) clone (3E2)	Abnova	Cat# H00010714-M01; RRID: AB_606803
Rabbit polyclonal anti-ZRANB3	Proteintech	Cat# 23111-1-AP; RRID: AB_2744527
Mouse monoclonal anti-EME1 (MTA31 7h2/1)	Santa Cruz Biotechnology	Cat# sc-53275; RRID: AB_2278026
Mouse monoclonal anti-ELL (B-4)	Santa Cruz Biotechnology	Cat# sc-398959
Rabbit polyclonal anti-PCNA	Abcam	Cat# ab18197; RRID: AB_444313
Mouse monoclonal anti-DNA-RNA Hybrid (S9.6)	Kerafast	Cat# ENH001; RRID: AB_2687463
Rabbit polyclonal anti-Nucleolin	Abcam	Cat# ab22758; RRID: AB_776878
Mouse monoclonal anti-RNA polymerase II (CTD4H8)	Millipore	Cat# 05-623; RRID: AB_309852
Mouse monoclonal anti-RNA polymerase II (H5)	BioLegend	Cat# 920204; RRID: AB_2616695
Rat monoclonal anti-BrdU/CldU [BU1/75 (ICR1)]	Abcam	Cat# ab6326; RRID: AB_305426
Mouse monoclonal anti-BrdU/IdU (B44)	BD Biosciences	Cat# 347580; RRID: AB_10015219
Cy™3 AffiniPure F(ab')₂ Fragment Donkey Anti-Rat IgG (H+L)	Jackson ImmunoResearch	Cat# 712-166-153; RRID: AB_2340669
Alexa Fluor 488 Goat Anti-Rabbit IgG (H+L)	Thermo Fisher Scientific	Cat# A-11008: RRID: AB_143165
Alexa Fluor 594 Goat Anti-Rabbit IgG (H+L)	Thermo Fisher Scientific	Cat# A-11012: RRID: AB_141359
Alexa Fluor 488 Goat Anti-Mouse IgG (H+L)	Thermo Fisher Scientific	Cat# A-11001: RRID: AB_2534069
Alexa Fluor 594 Goat Anti-Mouse IgG (H+L)	Thermo Fisher Scientific	Cat# A-11005: RRID: AB_141372
Goat anti-rabbit IgG-HRP	Sigma-Aldrich	Cat# A0545; RRID: AB_257896
Goat anti-mouse IgG-HRP	Sigma-Aldrich	Cat# A4416; RRID: AB_258167
Chemicals, Peptides, and Recombinant Proteins		
Phenylmethanesulfonyl fluoride (PMSF)	AppliChem	Cat# A0999
cOmplete, EDTA-free Protease Inhibitor Cocktail	Sigma-Aldrich	Cat# 11873580001
Phosphatase inhibitor cocktail tablets (PhosSTOP)	Roche	Cat# 04906837001

Continued

REAGENT or RESOURCE	SOURCE	IDENTIFIER
Lipofectamine RNAiMAX Transfection Reagent	Thermo Fisher Scientific	Cat# 13778150
Doxycycline	Takara Bio	Cat# 631311
Nocodazole	Sigma-Aldrich	Cat# M-1404
KaryoMAX® Colcemid Solution in HBSS	Thermo Fisher Scientific	Cat# 15210040
Aphidicolin	Sigma-Aldrich	Cat# A-0781
RO-3306	Sigma-Aldrich	Cat# SML0569
Cytochalasin B	Sigma-Aldrich	Cat# C6762
5-ethynyl-2′-deoxyuridine (EdU)	Thermo Fisher Scientific	Cat# A10044
5-ethynyl-2′-uridine (EU)	Thermo Fisher Scientific	Cat# E10345
Proteinase K	Roche	Cat# 03115852001
PvuII-HF	New England Biolabs	Cat# R3151S
RNase A (Type I-AS)	Sigma-Aldrich	Cat# R5503
5-Chloro-2′-deoxyuridine	Sigma-Aldrich	Cat# C6891
5-Iodo-2′-deoxyuridine	Sigma-Aldrich	Cat# I7125
Camptothecin	Sigma-Aldrich	Cat# C9911
Cordycepin	Sigma-Aldrich	Cat# C3394
5,6-Dichlorobenzimidazole 1-β-D-ribofuranoside (DRB)	Sigma-Aldrich	Cat# D1916
Pyridostatin pentahydrochloride (PDS)	Tocris Biosciences	Cat# 4763
Olaparib (AZD2281, Ku-0059436)	Selleckchem	Cat# S1060
Hydroxyurea	Sigma-Aldrich	Cat# H8627
B02 (RAD51 inhibitor)	Sigma-Aldrich	Cat# SML0364
AICAR (RAD52 inhibitor)	Sigma-Aldrich	Cat# A9978
Mirin (MRE11 inhibitor)	Sigma-Aldrich	Cat# M9948
Acrylamide/Bis solution (37.5:1) 30% w/v, 2.6% C	Serva	Cat# 10688.01
PAGE ruler plus prestained protein ladder	Thermo Fisher Scientific	Cat# 26619
Amicon Ultra-0.5ml centrifugal filters	Merc	Cat# UFC510096
DMEM (1X)	GIBCO	Cat# 41966-029
FBS (Lot # 42F1367K)	GIBCO	Cat# 10270-106
FBS, Qualified (Lot # 42A1081K) (Tet system approved)	GIBCO	Cat# 10270-106
Penicillin-Streptomycin	Sigma-Aldrich	Cat# P0781
Puromycin	InvivoGen	Cat# ant-pr-1
Hygromycin B Gold	InvivoGen	Cat# ant-hg-1
G 418 disulfate salt	Sigma-Aldrich	Cat# A1720
ECL Advance Blocking Reagent	GE Healthcare	Cat# RPN418V
Vectashield Antifade Mounting Medium	Vector Laboratories	Cat# H-1000
DAPI	Sigma-Aldrich	Cat# D9542
ProLong Gold Antifade Mountant	Thermo Fisher Scientific	Cat# P36930
Fluoromount-G	Thermo Fisher Scientific	Cat# 00-4958-02
BSA, HS, Reagent grade	Europa Bioproducts Ltd	Cat# EQBAH64-1000
Pulsed Field Certified™ Agarose	Bio-Rad	Cat# 1620137
SeaPlaque™ GTG™ Agarose	Lonza	Cat# 50111
Formaldehyde solution	Sigma-Aldrich	Cat# F8775
Acetic acid	Honeywell/Fluka	Cat# 695092
Hydrochloric acid 32%	Merc	Cat# 1.00319.1000
Methanol	Merc	Cat# 1.06009.2500
Ethanol absolute	VWR Chemicals	Cat# 2081.321
Tween 20	Sigma-Aldrich	Cat# P1379
Triton X-100	Sigma-Aldrich	Cat# T9284

(Continued on next page)

Continued

REAGENT or RESOURCE	SOURCE	IDENTIFIER
Sodium deoxycholate	Sigma-Aldrich	Cat# D6750
N-Lauroylsarcosine sodium salt	Sigma-Aldrich	Cat# L9150
Amersham Protran 0.2 μm NC (Nitrocellulose Blotting Membrane)	GE Healthcare Life Sciences	Cat# 10600001
1,4-Dithiothreitol (DTT)	Sigma-Aldrich	Cat# 11583786001
Microscope slides	Thermo Fisher Scientific	Cat# ISO 8037/I
Sodium dodecyl sulfate (SDS)	Sigma-Aldrich	Cat# L4509
Countess Cell Counting Chamber Slides	Thermo Fisher Scientific	Cat# C10228
50-Well Disposable Plug Molds (used for PFGE)	Bio-Rad	Cat# 1703713
Ethidium bromide	Sigma-Aldrich	Cat# E8751
Cresyl Violet acetate	Sigma-Aldrich	Cat# C5042
Critical Commercial Assays		
Click-iT Plus EdU Alexa Fluor 488 Imaging Kit	Thermo Fisher Scientific	Cat# C10637
Click-iT RNA Alexa Fluor 488 Imaging Kit	Thermo Fisher Scientific	*Cat# C10329*
Plasmid Mini Kit (100) (used for DNA isolation for EM)	QIAGEN	Cat# 12125
Pierce[R] ECL Wetsern Blotting Substrate	Thermo Scientific	Cat# 32106
SuperSignal[R] West Femto Maximum Sensitivity Substrate	Thermo Scientific	Cat# 34095
Duolink *In Situ* PLA Probe Anti Rabbit PLUS	Sigma-Aldrich	Cat# DUO92002
Duolink *In Situ* PLA Probe Anti Mouse MINUS	Sigma-Aldrich	Cat# DUO92004
Duolink *In Situ* Detection Reagents Green	Sigma-Aldrich	Cat# DUO92014
Deposited Data		
Original imaging data	This study	https://doi.org/10.17632/ydkd56y7rr.1
Experimental Models: Cell Lines		
U-2 OS	ATCC	ATCC® HTB-96
HeLa	ATCC	ATCC® CCL-2
HeLa Kyoto	Cancer Research UK	CVCL_1922
MRC5 (SV40 transformed)	ATCC	ATCC® CCL-171
VA13 (SV40 transformed)	ATCC	ATCC® CCL-75.1
T-REx™-U2OS	Thermo Fisher Scientific	Cat# R712-07
RA3331/E6E7/hTERT (SLX4 null)	Kim et al., 2013	N/A
RA3331/E6E7/hTERT complemented with wild-type *SLX4* cDNA	Kim et al., 2013	N/A
RA3331/E6E7/hTERT complemented with *SLX4 ΔSAP* cDNA	Kim et al., 2013	N/A
1BR	Cottarel et al., 2013	N/A
411BR	Cottarel et al., 2013	N/A
MUS81 WT U2OS	Minocherhomji et al., 2015	N/A
MUS81 (D338A/D339A) U2OS	Minocherhomji et al., 2015	N/A
POLD3 WT *U2OS*	Minocherhomji et al., 2015	N/A
U2OS T-REx GFP-RNaseH1 WT	Teloni et al., 2019	N/A
U2OS T-REx GFP-RNaseH1 D210N	Teloni et al., 2019	N/A
HeLa Kyoto MUS81 knockout (clone 167)	This study	N/A
Oligonucleotides		
Control siRNA (siLUC): CGUACGCGGAAUACUUCGA dTdT	Microsynth	N/A
RECQ5 siRNA_1: CAGGUUUGUCGCCCAUUGGAA dTdT	Microsynth	N/A
RECQ5 siRNA_2: GGAGAGUGCGACCAUGGCU dTdT	Microsynth	N/A
RECQ1 siRNA: GCAAGGAGAUUUACUCGAA dTdT	Microsynth	N/A
EME1 siRNA: GCUAAGCAGUGAAAGUGAA dTdT	Microsynth	N/A
MUS81 siRNA: CAGCCCUGGUGGAUCGAUA dTdT	Microsynth	N/A
MUS81 siRNA_(siMUS81[UTR]): GCCAUAUGUGUCAUGUAGA dTdT	Ambion	Cat# 130845

(Continued on next page)

Continued

REAGENT or RESOURCE	SOURCE	IDENTIFIER
SLX4 siRNA: AAACGUGAAUGAAGCAGAAUU dTdT	Microsynth	N/A
RAD52 siRNA_1: AAGGAUGGUUCAUAUCAUGAA dTdT	Microsynth	N/A
RAD52 siRNA_2:	Thermo Fisher Scientific	s1176 (Cat# 4392420)
ZRANB3 siRNA: D-010025-03-0005	Dharmacon	Cat# 84083
RAD51 siRNA: AAGGGAAUUAGUGAAGCCAAA dTdT	Microsynth	N/A
BRCA2 siRNA: CAGGACACAAUUACAACUAAA dTdT	Microsynth	N/A
siBRCA1 siRNA: CAGGAAAUGGCUGAACUAGAA dTdT	Microsynth	N/A
POLD3 siRNA: CAACAAGGCACCAGGGAAA dTdT	Microsynth	N/A
POLD3 SMARTpool siRNA	Dharmacon	Cat# L- 026692-01-0010
LIG3 siRNA: CAGAUAACCCAGCACAUUG dTdT	Microsynth	N/A
LIG4 siRNA_1: GCUAGAUGGUGAACGUAUG dTdT	Microsynth	N/A
LIG4 siRNA_2: AAGCCAGACAAAAGAGGUGAA dTdT	Microsynth	N/A
XRCC4 siRNA: AUAUGUUGGUGAACUGAGA dTdT	Microsynth	N/A
KU70 siRNA: NM_001469	QIAGEN	Cat# SI03033884
ELL siRNA	Santa Cruz Biotechnology	Cat# sc-38041
Hs_ELL_10 FlexiTube siRNA (siELL^{UTR}): CAGGCCUGCCCUGCUAUUUCA dTdT	QIAGEN	Cat# SI05016788
Recombinant DNA		
pSpCas9(BB)-2A-GFP	a gift from Feng Zhang	Addgene # 48138
pSpCas9(BB)-2A-GFP [MUS81-sgRNA-A]	This study	N/A
pSpCas9(BB)-2A-GFP [MUS81-sgRNA-B]	This study	N/A
pSpCas9(BB)-2A-GFP [MUS81-sgRNA-C]	This study	N/A
Software and Algorithms		
ImageJ (used for analysis of immunofluorescence microscopy images)	ImageJ Software	https://imagej.nih.gov/ij
GraphPad Prism 8 for Mac OS X	GraphPad Software	https://www.graphpad.com
DigitalMicrograph version 1.83.842	Gatan, Inc.	http://www.gatan.com

LEAD CONTACT AND MATERIALS AVAILABILITY

Further information and requests for resources and reagents should be directed to and will be fulfilled by the Lead Contact, Pavel Janscak (pjanscak@imcr.uzh.ch). All unique/stable reagents generated in this study are available from the Lead Contact without restriction.

EXPERIMENTAL MODEL AND SUBJECT DETAILS

Source of cell lines used in the study is reported in the Key Resources Table.

METHOD DETAILS

Cell culture

U2OS, HeLa, MRC5 and VA13 cells were grown in Dulbecco's Modified Eagle Medium (DMEM; Thermo Fisher Scientific), supplemented with 10% fetal calf serum (FCS; Thermo Fisher Scientific) and streptomycin/penicillin (100 U/ml), at 37°C in a humidified incubator containing 5% CO_2. U2OS T-REx cell lines carrying pAIO-based vectors for conditional expression of GFP-tagged wild-type RNase H1 or RNase H1 D210N (RNase H1 ORF fused C-terminally to GFP) were cultivated in DMEM supplemented with 10% FBS (Tet-free approved), streptomycin/penicillin (100 U/ml), 50 μg/ml hygromycin B and 1 μg/ml puromycin (Teloni et al., 2019). RNase H1-GFP expression was induced by addition of doxycycline to a concentration of 1 ng/ml. U2OS T-REx stable cell lines carrying pAIO-based vectors for expression of Flag-tagged versions of wild-type RECQ5, RECQ5F666A and RECQ5K58R were described previously (Urban et al., 2016). To induce expression of RECQ5 variants, doxycycline was added to a concentration of 0.4 ng/ml. Expression level of exogenous RECQ5 was tuned to be comparable with the level of endogenous RECQ5 by adjusting doxycycline concentration. The *MUS81* WT, *MUS81 (D338A/D339A)* and *POLD3* WT stable U2OS cell lines were grown in the presence of

neomycin (G418) (1 mg/ml) (Minocherhomji et al., 2015). Human FA complementation group P (FA-P; SLX4 deficiency) fibroblast cell line, RA3331, transformed using HPV6 and E7 proteins and immortalized with a human catalytic subunit of telomerase hTERT (RA3331/E6E7/hTERT), and its derivatives expressing HA-tagged wild-type SLX4 or SLX4 ΔSAP were grown in DMEM supplemented with 15% FBS, 2 μg/ml puromycin and streptomycin/penicilllin (100 U/ml) (Kim et al., 2013). Human telomerase reverse transcriptase-immortalized human fibroblasts 1BR (control) and 411BR (isolated from a LIG4 syndrome patient) were grown in DMEM supplemented with 15% FBS and streptomycin/penicillin (100 U/ml) (Cottarel et al., 2013).

CRISPR/Cas9-mediated generation of MUS81 knockout cells

The HeLa Kyoto *MUS81* mutant cell lines were generated as follows: sgRNA target sequences were cloned into the pSpCas9(BB)-2A-GFP vector (PX458, a gift from Feng Zhang; Addgene plasmid # 48138) and verified by sequencing; MUS81-sgRNA-A (AGCCCCGCAGGGGCGACTTG); MUS81-sgRNA-B (TACTGGCCAGCTCGGCACTC), MUS81-sgRNA-C (TGGTCACCACTTCTTA ACCA). HeLa Kyoto cells were co-transfected with MUS81-sgRNA-A and MUS81-sgRNA-B, or MUS81-sgRNA-A and MUS81-sgRNA-C, using Lipofectamine 2000. Transfection efficiency was verified by GFP fluorescence. Clonal cell lines were isolated by limiting dilution in 96-well plates. Total extracts of single clones were prepared and analyzed by western blotting, using mouse monoclonal anti-MUS81 antibody (Abcam). The mutant clones selected carried large deletions in the *MUS81* gene, verified by Sanger sequencing of PCR-amplified genomic fragments, and showed no detectable MUS81 protein by western blotting. A mutant clone generated using A+B gRNA combination (clone 167) was used in this study.

Small-interfering RNA transfections

Transfections of siRNAs (a final concentration of 40 nM) were done at 30%–40% confluency using Lipofectamine RNAiMAX (Invitrogen) according to the manufacturer's instructions. 24 hr after siRNA transfection, the medium was exchanged with fresh medium. The sequences of the sense strand of siRNA duplexes are listed in Key Resources Table. For ectopic expression of RECQ5 variants in stable U2OS T-REx cell lines, endogenous RECQ5 was depleted by transfection of RECQ5 siRNA_2 for a total time of 72 hr. 24 hr after siRNA transfection, doxycycline (0.4 ng/ml) was added to induce expression of RECQ5 variants for a further 48 hr. Where siRECQ5, siRAD52 and siLIG4 are indicated, cells were transfected with RECQ5 siRNA_1, RAD52 siRNA_1 and LIG4 siRNA_1, respectively. For experiment in Figure 5F, RAD52 siRNA_2 was used.

Clonogenic assay

24 hr after siRNA transfection, cells were re-plated in triplicates in 6-well plates (150 cells/well). After 24 hr, cells were treated with indicated concentrations of the PARP inhibitor olaparib (Selleckchem), CPT and PDS, respectively for additional 24 hr. Where required, 2 μM olaparib was added together with CPT or PDS. After drug treatment, cells were washed twice with 1x PBS and cultured for additional 10 days in fresh medium without the drug. Subsequently, colonies were stained with 0.5% (w/v) crystal violet in 20% (v/v) ethanol for 30 min in dark. After staining, plates were washed with water and air-dried. Visible colonies were counted to calculate percentage of survival relative to untreated cells. To assess clonogenic survival upon ectopic overexpression of RNase H1 in U2OS T-REx/RNH1-GFP cells, doxycycline (1.0 ng/ml) was added after replating siRNA-transfected cells in 6-well plates.

Preparation cell extracts and western blot analysis

Cells were suspended in lysis buffer [50 mM Tris-HCl buffer (pH 7.5), 120 mM NaCl, 20 mM NaF, 1 mM EDTA, 6 mM EGTA, 15 mM Na-Pyrophosphate and 0.5% (v/v) NP-40] supplemented with 1 mM benzamidine, 0.2 mM PMSF, 0.5 mM sodium orthovanadate and protease inhibitor cocktail (Complete, EDTA-free; Sigma-Aldrich), and sonicated for 7 min with a Diagenode sonicator. Cellular debris was separated from soluble fraction by centrifugation at 12,000 rpm for 30 min at 4°C and protein concentration was measured by Bradford assay. 30-60 μg of total protein from cell lysates were loaded onto 8%–10% SDS-PAGE gels. After electrophoresis, separated proteins were transferred from gel onto a nitrocellulose membrane in a wet-transfer apparatus (Bio-rad) with buffer containing 10% ethanol and 90% 1x transfer buffer (transfer buffer 10x: 25 mM tris, 192 mM glycine, 10% methanol) at 100 V for 2 hr in cold room at 4°C. The membrane was blocked with 2% ECL blocking solution in TBS-T [20 mM Tris-HCl (pH 7.4), 150 mM NaCl, 0.1% (v/v) Tween-20] for 30 min. Afterward, the membranes were incubated with the primary antibodies in 4% ECL blocking solution at 4°C O/N. The membranes were then washed 3 times in TBS-T and incubated with appropriate horseradish peroxidase-coupled (HRP) secondary antibody in 2% ECL blocking solution for 60 min at RT. Afterward, the membranes were washed three times with TBS-T and protein bands were detected by luminol-based reaction using a chemiluminescence reagent (Pierce). The primary antibodies used for western blotting: FLAG mouse monoclonal (F1804, Sigma-Aldrich; 1:500 dilution), BRCA1 (D-9) mouse monoclonal (sc-6954, Santa Cruz Biotechnology; 1:1000 dilution), MUS81 (Clone MTA30 2G10/3) mouse monoclonal (M1445, Sigma-Aldrich; 1:1000 dilution), Ku p70 (Ab-4) mouse monoclonal (MS329-P1, Thermo Fisher Scientific; 1:1000 dilution), SLX4 rabbit polyclonal (A302-270A, Bethyl Laboratories; 1:1000 dilution), TFIIH p89 (S-19) rabbit polyclonal (sc-293, Santa Cruz Biotechnology; 1:1000 dilution), GFP rabbit polyclonal (ab290, Abcam; 1:1000 dilution), RAD51 rabbit polyclonal (sc-8349; Santa Cruz Biotechnology; 1:1000 dilution), RECQ5 rabbit polyclonal (Janscak lab; 1:1000 dilution), RECQ1 rabbit polyclonal (NB100-182, Novus Biological; 1:1000 dilution), LIG4 (D-8) mouse monoclonal (sc-271299, Santa Cruz Biotechnology; 1:500 dilution), XRCC4 (C-4) mouse monoclonal (sc-271087, Santa Cruz Biotechnology; 1:500 dilution), LIG3 (E-7) mouse monoclonal (sc-390922, Santa Cruz Biotechnology; 1:500 dilution), BRCA2 (Ab-1) mouse monoclonal (OP-95, EMD Millipore; 1:1000 dilution), RAD52 (H300) rabbit polyclonal (sc-8350, Santa Cruz Biotechnology; 1:500

dilution), POLD3 (M01, clone 3E2) mouse monoclonal (H00010714-M01, Abnova; 1:1000 dilution), ZRANB3 rabbit polyclonal (23111-1-AP, Proteintech; 1:1000 dilution), EME1 (MTA31 7h2/1) mouse monoclonal (sc-53275, Santa Cruz Biotechnology; 1:1000 dilution), GAPDH (0411) mouse monoclonal (sc-47724, Santa Cruz Biotechnology; 1:1000 dilution), ELL (B-4) mouse monoclonal (sc-398959, Santa Cruz Biotechnology; 1:500 dilution). Secondary antibodies used for western blotting: goat anti-rabbit IgG-HRP (A5050, Sigma-Aldrich; 1:1000 dilution), goat anti-mouse IgG HRP (A4416, Sigma-Aldrich; 1:2000 dilution).

Immunofluorescence assays

Cells grown on autoclaved coverslips were transfected with siRNA and/or treated with drugs. After the treatment, cells were washed two times with 1x PBS and pre-extracted for 15 min with ice cold 1x PBS containing 0.5% (v/v) Triton X-100. Then the cells were washed three times with 1xPBS and fixed with 4% formaldehyde for 10 min at RT. After three washes with 1x PBS, fixed cells were permeabilized in 1x PBS containing 0.2% (v/v) Triton X-100 for 10 min at RT. Cells were then washed with PBS and blocked in 5% BSA/1x PBS solution for 45 min. Coverslips were then incubated O/N at 4°C with appropriate primary antibodies diluted in 5% BSA/1x PBS. The following day, coverslips were washed three times with 1x PBS and incubated for 60 min at RT with secondary antibodies diluted in 5% BSA/1x PBS. After three washes with 1x PBS, coverslips were incubated with 1 μg/ml DAPI/1x PBS for 15 min in dark at RT. Then the coverslips were washed twice with 1x PBS and mounted with Vectashield antifade medium. The mounted slides were left to dry at RT for 30 min and then sealed with nail polish. Images were acquired with a Leica DM6B upright fluorescent microscope (63x/1.40 Oil immersion) and analyzed with the tools of ImageJ. The DAPI signal was used for generation of an intensity threshold-based mask to identify individual nuclei. This mask was applied to measure nuclear foci number or mean fluorescence intensity in different channel for each nucleus by using speckle inspector tool in BioVoxxel Toolbox plugin and mean intensity measurement tool, respectively. At least 300 cells were scored for each condition in three different experiments. The primary antibodies used for the immunofluorescence staining: MUS81 (MTA30 2G103) mouse monoclonal (sc-53382, Santa Cruz Biotechnology; 1:500 dilution), 53BP1 rabbit polyclonal (sc-22760, Santa Cruz Biotechnology; 1:500 dilution), Cyclin A (B-8) mouse monoclonal (sc-271682, Santa Cruz Biotechnology; 1:50 dilution), FANCD2 rabbit polyclonal (NB100-182, Novus Biologicals; 1:500 dilution). Secondary antibodies used for immunofluorescence staining: Alexa Fluor 488 Goat Anti-Rabbit IgG (A110334, Thermo Fisher Scientific; 1:300 dilution), Alexa Fluor 594 Goat Anti-Rabbit IgG (A11037, Thermo Fisher Scientific; 1:300 dilution), Alexa Fluor 488 Goat Anti-Mouse IgG (A11001, Thermo Fisher Scientific; 1:300 dilution), Alexa Fluor 594 Goat Anti-Mouse IgG (A11005, Thermo Fisher Scientific; 1:300 dilution).

Detection of RNA:DNA hybrids with S9.6 antibody

Staining RNA:DNA hybrids with S9.6 antibody was performed using a previously published protocol (De Magis et al., 2019). Briefly, cells grown on coverslips were fixed with ice-cold methanol for 10 min at RT. After a brief wash with 1x PBS, cells were permeabilized with acetone for 1 min on ice, washed three times with 1x PBS and blocked in 3% BSA/0.1% Tween-20/4x SSC for 1 hr at RT. After a brief wash with 4X SSC, coverslips were incubated with mouse monoclonal anti-RNA:DNA hybrid (S9.6) antibody (Kerafast, ENH001; 1:200) and rabbit polyclonal anti-Nucleolin antibody (Abcam, ab22758; 1:1000) diluted in 3% BSA/0.1% Tween-20/4x SSC for 1 hr (in dark, RT). After the incubation, coverslips were washed with 4X SSC and incubated with Alexa Fluor 488 Goat Anti-Mouse IgG (Life Technologies, A11034; 1:400) and Alexa Fluor 647 Goat Anti-Rabbit IgG (Invitrogen, A21235; 1:400) diluted in 3% BSA/0.1% Tween-20/4x SSC for 30 min (in dark, RT). Then the coverslips were washed three times with 4x SSC, counterstained with 1 μg/ml DAPI in distilled water and mounted using Fluoromount-G (Invitrogen). The representative images were acquired with a Leica DM6B fluorescent microscope. For the analysis of S9.6 signal, the automated image acquisition was performed on an IX83 microscope (Olympus) equipped with ScanR imaging platform using 40x/0.9 NA objective. The analysis of acquired images was performed using ScanR Analysis software. At least 1000 nuclei were analyzed per condition. The nuclei were identified based on DAPI signal and the intensity of S9.6 signal was measured for each nuclear object. For the analysis of nucleoplasmic S9.6 signal excluding the nucleolar signal, nucleoli were identified based on the staining with anti-Nucleolin antibody and the nucleolar S9.6 signal was subtracted using analysis module of ScanR software.

In situ proximity ligation assay

U2OS cells were grown on autoclaved coverslips and treated with drugs as indicated in Figure legends. After treatment, cells were washed twice with 1x PBS and pre-extracted for 10 min with ice-cold 1x PBS containing 0.5% (v/v) Triton X-100 and protease inhibitor cocktail (Complete, EDTA-free; Sigma-Aldrich). Then, the cells were washed twice with 1xPBS and fixed with 4% (v/v) formaldehyde for 10 min at RT. After two washes with 1x PBS, fixed cells were incubated with 1x PBS containing 0.2% (v/v) Triton X-100 for 10 min at RT. Cells were then washed twice with 1xPBS and blocked in 5% BSA/1x PBS solution for 45 min. Coverslips were then incubated O/N at 4°C with appropriate primary antibodies diluted in 5% BSA/1x PBS. The following day, coverslips were washed twice with 1x PBS and proximity ligation assay (PLA) was performed using Duolink PLA technology (Sigma-Aldrich) according to the manufacturer's instructions. Briefly, coverslips were incubated with anti-Mouse MINUS and anti-Rabbit PLUS PLA probes (Sigma-Aldrich) for 1 hr at 37°C. After two wash steps in Wash Buffer A (0.01 M Tris, 0.15 M NaCl and 0.05% Tween 20, pH 7.4) for 5 min, PLA probes were ligated for 30 min at 37°C. Coverslips were then washed two times for 5 min in Wash Buffer A. Amplification using the 'Duolink *In Situ* Detection Reagents Green' (Sigma-Aldrich) was performed at 37°C for 100 min. After amplification, coverslips were washed twice in Wash Buffer B (0.2 M Tris and 0.1 M NaCl, pH 7.5) for 10 min. Then coverslips were incubated with

1 μg/ml DAPI/1x PBS for 15 min in dark at RT and subsequently washed twice with 1x PBS. Finally, coverslips were mounted using ProLong Gold antifade mounting medium. Images were acquired with a Leica DM6B upright fluorescent microscope (63x/1.40 Oil immersion) and analyzed using ImageJ. The following primary antibodies were used: rabbit polyclonal anti-PCNA (Abcam, ab18197), rabbit polyclonal anti-FANCD2 (Novus Biologicals, NB100-182), mouse monoclonal anti-RNA polymerase II, CTD4H8 (Millipore, 05-623), mouse monoclonal anti-RNA polymerase II, H5 (BioLegend, 920204).

Analysis of metaphase chromosome spreads and MiDAS assay

Cells seeded in 10-cm dishes were treated with 9 μM RO-3306 in combination with 0.4 μM aphidicolin for 16 hr. Cells were subsequently washed three times with 1x PBS for 5 min and then released in fresh medium (pre-warmed to 37°C) containing 0.1 μg/ml Colcemid for 60 min. In the case of MiDAS analysis, cells were released to medium containing 20 μM 5-ethynyl-2′-deoxyuridine (EdU) and 0.1 μg/ml Colcemid for 60 min. Metaphase cells were collected by shake-off and centrifugation at 1200 rpm for 5 min. After one wash with 1x PBS, cells were swollen by incubation in 75 mM KCl (pre-warmed to 37°C) for 20 min at 37°C. Swollen mitotic cells were collected at 1200 rpm for 5 min, fixed using methanol:acetic acid (3:1), and dropped onto pre-hydrated glass slides and aged for up to 24 hr. Chromosome spreads were mounted with Vectashield mounting medium containing DAPI. Images were acquired using a Leica DM6B upright fluorescent microscope at (63x/1.40 Oil immersion). For MiDAS analysis, metaphase spread slides were aged for 24 hr followed by EdU detection using Click-iT Plus EdU Alexa fluor 488 Imaging Kit (Thermo Fisher Scientific) and chromosomes stained with Vectashield mounting medium containing DAPI. Images were captured using a Leica SP8 upright confocal laser-scanning microscope (63x/1.40 Oil immersion). Quantifications of DAPI-negative gaps and EdU incorporation events (twin foci and complex foci were counted as one event) on metaphase chromosome spreads was done manually with help of ImageJ.

DNA fiber spreading assay

Cells were labeled with 30 μM 5-chloro-2′-deoxyuridine (CldU) for 30 min, washed three times with 1x PBS, and then labeled with 250 μM 5-iodo-2′-deoxyuridine (IdU) for 30 min. After labeling, cells were washed three times with 1x PBS, quickly trypsinized and re-suspended in 1x PBS to a concentration of 250,000 cells per ml. The labeled cells were diluted 1:3 with unlabeled cells, and 2.5 μL of this cell suspension were mixed with 7.5 μL of lysis buffer [200 mM Tris-HCl (pH 7.5), 50 mM EDTA, 0.5% (w/v) SDS] on a glass slide by gently stirring with a pipette tip. After 9-min incubation at RT, the slides were tilted at 30°-40°, the surface tension of the drops was disrupted by a tip and the drops were allowed to run down the slides slowly. The DNA spreads were air-dried and fixed in methanol/acetic acid (3:1) at 4°C overnight. DNA fibers were denatured with 2.5 M HCl for 1 hr at RT, washed four times with 1x PBS and blocked with 2% BSA in 1x PBS for 40 min. After blocking, slides were incubated for 2.5 hr in the dark at RT with rat monoclonal anti-BrdU antibody (ab6326, Abcam; 1:500 dilution) to detect CldU and mouse monoclonal anti-BrdU antibody (347580, BD Biosciences; 1:100 dilution) to detect IdU. Slides were then washed four times with 1x PBST (PBS supplemented with 0.2% Tween-20) and incubated with secondary antibodies, donkey anti-rat Cy3 (712-166-153, Jackson ImmunoResearch; 1:150 dilution) and goat anti-mouse Alexa 488 (A110334, Thermo Fisher Scientific; 1:300 dilution), for 2 hr in the dark at RT. After washing four times with 1x PBST, the slides were air-dried in the dark for 40 min at RT and mounted with ProLong Gold antifade mounting medium (25 μL per coverslip 24x50 mm). Images were acquired with a Leica DM6B upright fluorescent microscope (63x/1.40 Oil immersion). CldU and IdU tract lengths (μm) were measured by using segmented line tool of ImageJ.

Quantification of nascent RNA production by 5-ethynyl uridine labeling

After or during the mentioned treatment, cells grown on coverslips were pulsed with 1 mM 5-ethynyl uridine EU for 30 min. Following three washes with 1x PBS, cells were fixed and permeabilized for 20 min in PTEMF buffer (20 mM PIPES pH 6.8, 10 mM EGTA, 0.3% Triton X-100, 1 mM MgCl2 and 4% formaldehyde) at room temperature on a motion-waving shaker with low speed. After three washes with 1x PBS, EU incorporation was detected with Click-iT EU Alexa fluor 488 Imaging Kit (Thermo Fisher Scientific). Then, coverslips were incubated with 1 μg/ml DAPI/1x PBS for 15 min in dark at RT and subsequently washed twice with 1x PBS. Finally, coverslips were mounted using Fluoromount-G (Invitrogen). Images were acquired with a Leica DM6B upright fluorescent microscope (20x objective). The nuclei were identified based on DAPI staining and the mean EU fluorescence intensity per nucleus was measured using ImageJ software.

Electron microscopy

Electron microscopy analysis was performed as described (Zellweger et al., 2015), with minor modifications. Briefly, cells were collected, washed once with and re-suspended in 1x PBS. *In vivo* psoralene cross-linking of the DNA was achieved by repetitive (twice) cross-linking with 4,5′, 8-trimethylpsoralen (10 μg /ml final concentration) in the dark for 5 min, followed by irradiation pulses with UV 365 nm monochromatic light (UV Stratalinker 1800) for 3 min. For DNA extraction, cells were lysed in lysis buffer [40 mM Tris-HCl (pH 7.5), 1.28 M sucrose, 20 mM MgCl₂, and 4% (v/v) Triton X-100] and digested with digestion buffer [800 mM guanidine-HCl, 30 mM Tris-HCl (pH 8.0), 30 mM EDTA (pH 8.0), 5% (v/v) Tween-20, and 0.5% (v/v) Triton X-100] at 50 °C for 2 hr in presence of 1 mg/ml proteinase K. The DNA was purified by phase separation method using chloroform/isoamylalcohol (24:1) with centrifugation at 8000 rpm for 20 min using a Sorvall LYNX 600 centrifuge. DNA was precipitated by adding equal volume of isopropanol to the upper phase collected in the previous step. Finally, the DNA was washed with 70% Ethanol and disolved in 200 μl TE (Tris-EDTA) buffer. 100 U of the restriction enzyme PvuII were used to digest 12 μg of the isolated genomic DNA in 250 μL of 1x CutSmart buffer

(New England Biolabs) for 5 hr, and to eliminate RNA contamination, 6 µL of 10 mg/ml RNase A was added during the last 3 hr. Replication intermediate enrichment was obtained using QIAGEN Plasmid Mini Kit (100) columns. The surface tension of QIAGEN-tip 20 columns was reduced by applying 1 ml QBT buffer. Columns were then washed with 10 mM Tris-HCl (pH 8.0), 1 M NaCl and equilibrated with 10 mM Tris-HCl (pH 8.0), 300 mM NaCl. After loading of DNA, columns were washed with 10 mM Tris-HCl (pH 8.0) containing 900 mM NaCl. DNA was eluted with caffeine solution [10 mM Tris-HCl (pH 8.0), 1 M NaCl and 1.8% (w/v) caffeine]. To purify and concentrate DNA, an Amicon size-exclusion column was used. DNA was then resuspended in TE buffer. The benzyldimethylalkylammonium chloride (BAC) method was used to spread the DNA on water surface and then to load it on carbon-coated 400-mesh copper grids. Subsequently, DNA was coated with platinum using a high vacuum evaporator MED 020 (BalTec). Microscopy was performed with a transmission electron microscope (Tecnai G2 Spirit; FEI; LaB6 filament; high tension $\leq$ 120 kV) equipped with a side mount charge-coupled device camera (2600 × 4000 pixels; Orius 1000; Gatan, Inc.). Images were processed and analyzed with DigitalMicrograph version 1.83.842 (Gatan, Inc.) and ImageJ (National Institutes of Health), respectively.

Pulsed-field gel electrophoresis
Cells were harvested by trypsinization, washed once with 1x PBS and resuspended in 1x PBS (1.0×10^6 cells/50 µl). Agarose plugs of 1.0×10^6 cells were prepared in a disposable plug mold (Bio-Rad Laboratories) by mixing (1:1) of 2% (w/v) SeaPlaque GTG agarose in 1xPBS and cells suspended in 1xPBS. Plugs were incubated in lysis buffer [100 mM EDTA, 1% (w/v) sodium lauroyl sarcosinate, 0.2% (w/v) sodium deoxycholate, and 0.5 mg/ml proteinase K] at 37 °C for 72 hr and then washed four times in 20 mM Tris-HCl (pH 8.0) buffer containing 50 mM EDTA for 5 min each time on shaker before loading onto 0.9% (w/v) Pulsed Field Certified agarose (Bio-Rad) prepared in Tris-borate/EDTA buffer. Electrophoresis was performed in a pulsed-field gel electrophoresis apparatus, CHEF DR III variable angle system (Bio-Rad), run in Tris-borate/EDTA buffer for 21 hr at 14 °C according to the following protocol (block I: 9 hr, 120° included angle, 5.5 V cm^{-1}, 30–18 s switch; block II: 6 hr, 117° included angle, 4.5 V cm^{-1}, 18–9 s switch; block III: 6 hr, 112° included angle, 4.0 V cm^{-1}, 9–5 s switch). Gels were stained with ethidium bromide and gel images were acquired by an AlphaImager™ system (Alpha Innotech Corporation). DNA bands were quantified using ImageJ. For each lane, the mean intensity of the band corresponding to broken DNA was divided by the mean intensity of the band corresponding to intact DNA. The resulting values were normalized to the value obtained for control condition (taken as 100%).

QUANTIFICATION AND STATISTICAL ANALYSIS

Statistical analysis was performed with GraphPad Prism 8 software using paired or unpaired t test or Mann-Whitney test, where appropriate. Statistical details of experiments can be found in the figure legends.

DATA AND CODE AVAILABILITY

Original imaging data have been deposited to Mendeley Data and are available at https://doi.org/10.17632/ydkd56y7rr.1

Supplemental Information

Fork Cleavage-Religation Cycle and Active

Transcription Mediate Replication Restart

after Fork Stalling at Co-transcriptional R-Loops

Nagaraja Chappidi, Zuzana Nascakova, Barbora Boleslavska, Ralph Zellweger, Esin Isik, Martin Andrs, Shruti Menon, Jana Dobrovolna, Chiara Balbo Pogliano, Joao Matos, Antonio Porro, Massimo Lopes, and Pavel Janscak
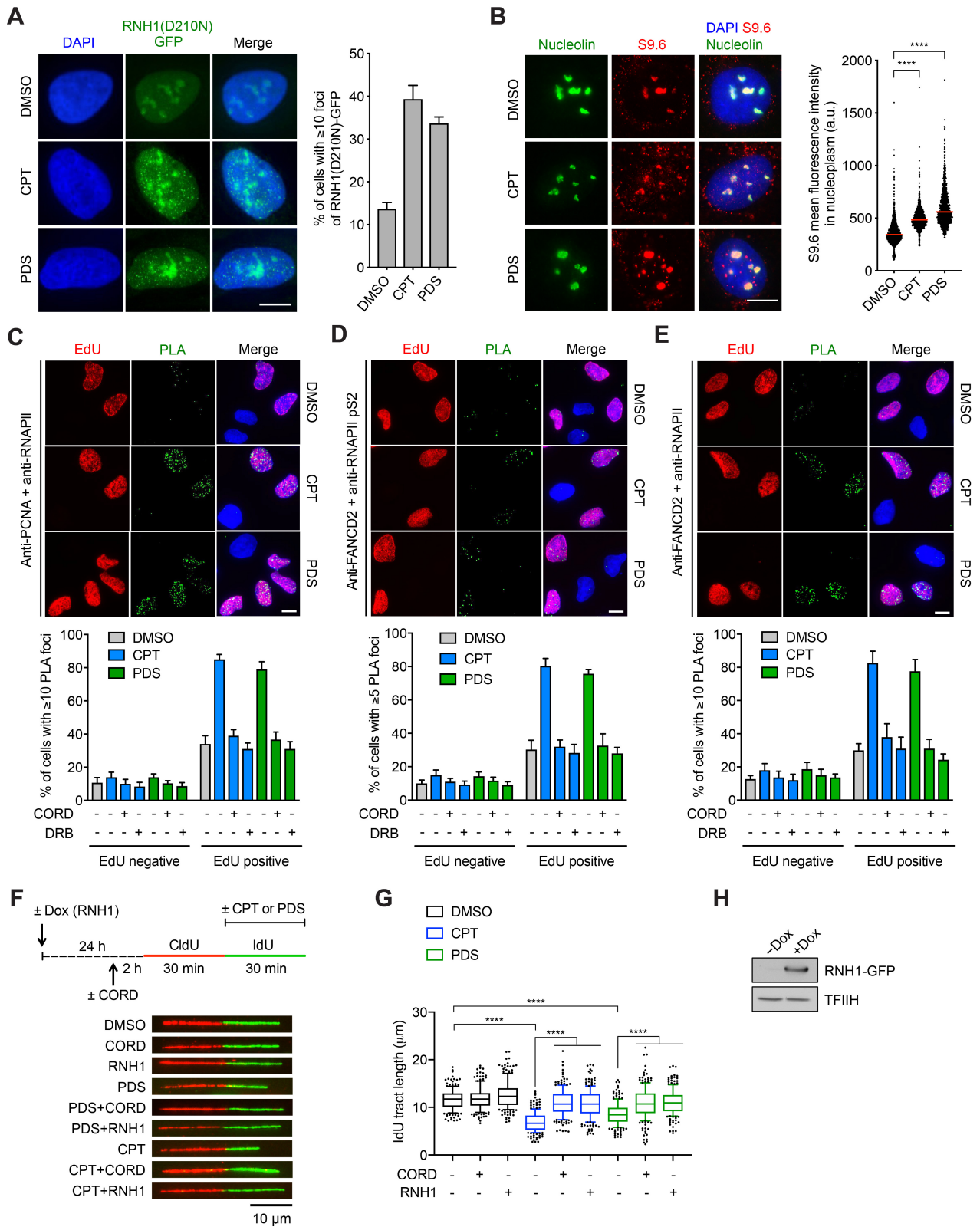
Figure S1

Figure S1, related to Figure 1. Camptothecin and pyridostatin induce transcription-replication interference

(A) Formation of nuclear foci of catalytically-inactive form of RNase H1 in cells treated with camptothecin (CPT) or pyridostatin (PDS). *Left panel*: Representative images of U2OS T-REx/RNH1(D210N)-GFP cells induced with doxycycline (1 ng/ml) for 24 hr and treated with DMSO, pyridostatin (PDS; 10 μM) and camptothecin (CPT; 100 nM), respectively for the last 30 min. Cells were pre-extracted before fixation. Nuclei were stained with DAPI. RNH1(D210N)-GFP foci indicate sites of R-loop formation. In mock-treated cells, R-loops form predominantly in rDNA localized in nucleoli. Scale bar, 10 μm. *Right panel*: Quantification of images represented in the left panel. Data are the mean ± S.D., n=3. At least 300 nuclei were analyzed for each condition. (B) CPT and PDS induce formation of RNA:DNA hybrids. *Left panel*: Representative immunofluorescence images of U2OS cells treated with 100 nM CPT or 10 uM PDS for 30 min and 10 min, respectively. RNA:DNA hybrids are stained with S9.6 antibody (red). Nucleolin staining identifies nucleolar compartment (green). *Right panel*: Quantification of nucleoplasmic S9.6 signal in cell images represented in the left panel. S9.6 fluorescence intensity of the nucleoplasmic compartment was calculated by subtracting the nucleolar S9.6 signal from the total nuclear S9.6 intensity. Horizontal lines represent median (n > 1000). ****$P < 0.0001$ (Mann-Whitney test). Scale bar, 10 μm. (C) Co-localization of PCNA and RNA polymerase II (RNAPII) in S-phase nuclei of U2OS cells upon treatment with CPT or PDS as determined by proximity ligation assay (PLA) and EdU-pulse labeling. Antibody against total RNAPII was used for PLA. (D and E) Co-localization of FANCD2 and RNAPII in S-phase nuclei of U2OS cells upon treatment with CPT or PDS as determined by PLA assay using antibodies against elongating RNAPII (D) or total RNAPII (E). (C-E) Representative images (*top panel*) and quantification of the percentage (*bottom panel*) of EdU-positive and EdU-negative cells with PLA foci. Cells were treated with 100 nM CPT or 10 μM PDS for 1 hr. EdU (10 μM) was added 10 min prior to

CPT/PDS. Where indicated, cordycepin (CORD; 50 µM) or 5,6-dichloro-benzimidazole 1-β-D-ribofuranoside (DRB; 100 µM) were added 2 hr prior to CPT/PDS treatment. Data represent the mean ± S.D., n=3. At least 100 nuclei were scored in each experiment. Scale bar, 10 µm. (F) Effect of RNase H1 (RNH1) overexpression and transcription inhibition on replication fork slowing induced by CPT (100 nM) or PDS (10 µM) in U2OS T-REx/RNH1-GFP cells. *Top panel*: Experimental workflow of DNA fiber assays. *Bottom panel*: Representative images of replication tracts detected on DNA fibers of cells treated as indicated. Quantification is shown in Figure 1B. (G) Box plot of IdU tract lengths for Figure 1B. (H) A western blot showing expression of RNH1-GFP in U2OS T-REx/RNH1-GFP cells upon induction with doxycycline (Dox) for 24 hr.
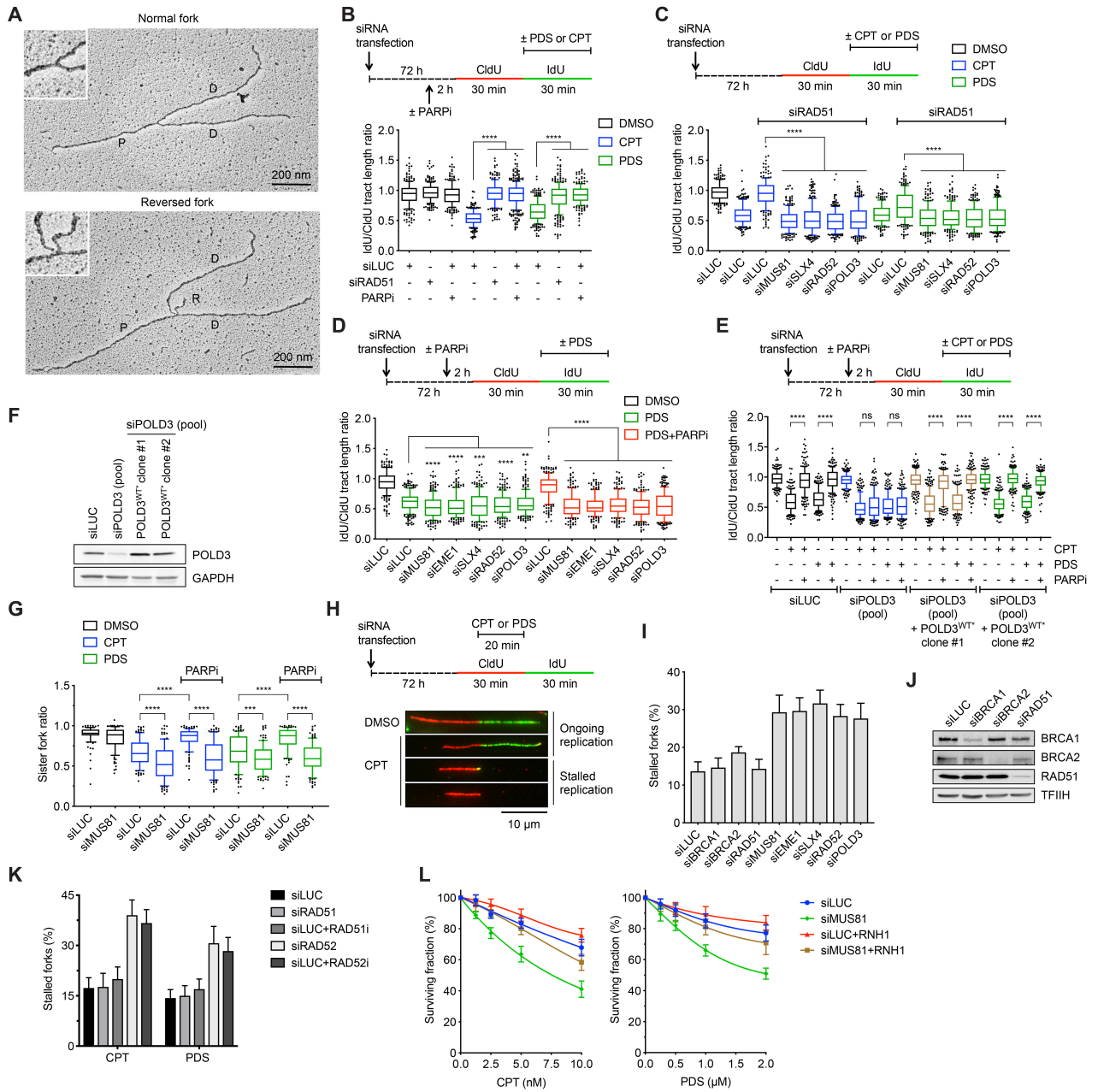
Figure S2

Figure S2, related to Figure 1. MUS81, EME1, SLX4, RAD52 and POLD3 are required for restart of replication forks stalled by R-loops

(A) Representative electron micrographs of normal (*top panel*) and reversed (*bottom panel*) replication forks observed on genomic DNA of U2OS T-REx/RNH1-GFP cells after treatment with 100 nM CPT for 1h. P, parental duplex; D, daughter duplex; R, regressed arm. (B) Effects of CPT (100 nM) and PDS (10 μM) on replication fork progression in U2OS cells upon PARP inhibition or RAD51 depletion. *Top panel*: Experimental workflow of DNA fiber assays. PARP activity was blocked by addition of the PARP inhibitor (PARPi) olaparib (10 μM) at 2 hr prior to DNA fiber labeling. *Bottom panel*: Box plot of values of IdU/CldU tract length ratio obtained for indicated conditions (n ≥ 200, whiskers: 10-90 percentiles). ns, not significant; ****P < 0.0001 (Mann-Whitney test). (C) Effect of depletion of MUS81, EME1, SLX4, RAD52 or POLD3 on the rescue of CPT- and PDS-induced replication fork slowing in U2OS cells by RAD51 depletion. *Top panel*: Experimental workflow of DNA fiber assays. *Bottom panel*: Box plot of values of IdU/CldU tract length ratio obtained for indicated conditions (n ≥ 200, whiskers: 10-90 percentiles). ns, not significant; ****P < 0.0001 (Mann-Whitney test). (D) Effect of depletion of MUS81, EME1, SLX4, RAD52 or POLD3 on the replication fork velocity in U2OS cells upon treatment with 10 μM PDS, and on the rescue of PDS-induced replication fork slowing by PARP inhibition with 10 μM olaparib. *Top panel*: Experimental workflow of DNA fiber assays. *Bottom panel*: Box plot of values of IdU/CldU tract length ratio obtained for indicated conditions (n ≥ 200, whiskers: 10-90 percentiles). ns, not significant; *P = 0.0252, **P = 0.0022, ***P = 0.0004, ****P < 0.0001 (Mann-Whitney test). (E) POLD3 is required for the rescue of replication fork slowing in CPT- and PDS-treated cells by PARP inhibition. *Top panel*: Experimental workflow of DNA fiber assays with U2OS cells and their derivatives stably transfected with an siRNA-resistant POLD3 construct (POLD3^{WT*}). *Bottom panel*: Box plot of values of IdU/CldU tract length ratio obtained for indicated conditions (n ≥ 200, whiskers: 10-90 percentiles). ns, not

significant; ****P < 0.0001 (Mann-Whitney test). (F) Western blot analysis of extract of cells in

(E). (G) Effect of MUS81 depletion and PARP inhibition on replication fork asymmetry in U2OS

cells treated with CPT or PDS. Images of DNA fibers from experiments in Figure 1F and S2D

were analyzed. Ratio of lengths of IdU tracts of sister forks is plotted for indicated conditions (n ≥

100, whiskers: 10-90 percentiles). ***P < 0.001; ****P < 0.0001 (Mann-Whitney test). (H)

Experimental workflow of replication restart assays and images of replication tracts detected on

DNA fibers of mock-treated (DMSO) and CPT-treated U2OS cells. Cells were labeled

sequentially with CldU and IdU for 30 min each. Where indicated, CPT (100 nM), PDS (10 μM)

or DMSO (mock treatment) were added during the last 20 min of the CldU pulse. Any fibres

showing incorporation of IdU (green) into replication tracts adjacent to CldU (red) tracts define

replication forks that could adequately resume DNA replication following the removal of CPT or

PDS. Irreversibly arrested forks would fail to incorporate IdU, and appear only as red tracts. (I)

Effect of depletion of the indicated proteins on replication restart following treatment of U2OS

cells with 10 μM PDS as measured by DNA fiber assays depicted in (H). The data represent the

percentage of active replicons (CldU-labeled) that fail to resume DNA synthesis (not IdU-labeled)

30 min after the removal of PDS. Data are the mean ± S.D., n = 3. (J) Western blot analysis of

extracts of U2OS cells transfected with indicated siRNAs. (K) Quantification of replication fork

stalling events in U2OS cells recovering from CPT or PDS treatment in the presence of RAD51 or

RAD52 inhibitors. DNA replication restart assay was performed as depicted in (H), with RAD51i

(B02; 50 μM) or RAD52i (AICAR; 40 μM) being added during IdU labeling. The data are

represented as in (I). (L) RNH1 overexpression rescues hypersensitivity of MUS81-depleted

U2OS T-REx/RNH1-GFP cells to CPT and PDS. At 48 hr after siRNA transfection, cells were

treated with different concentrations of CPT or PDS for 24 hr and then subjected to clonogenic

assay. Dox was added 24 hr before CPT/PDS treatment to induce RNH1-GFP expression. Data are

the mean ± S.D., n=3.
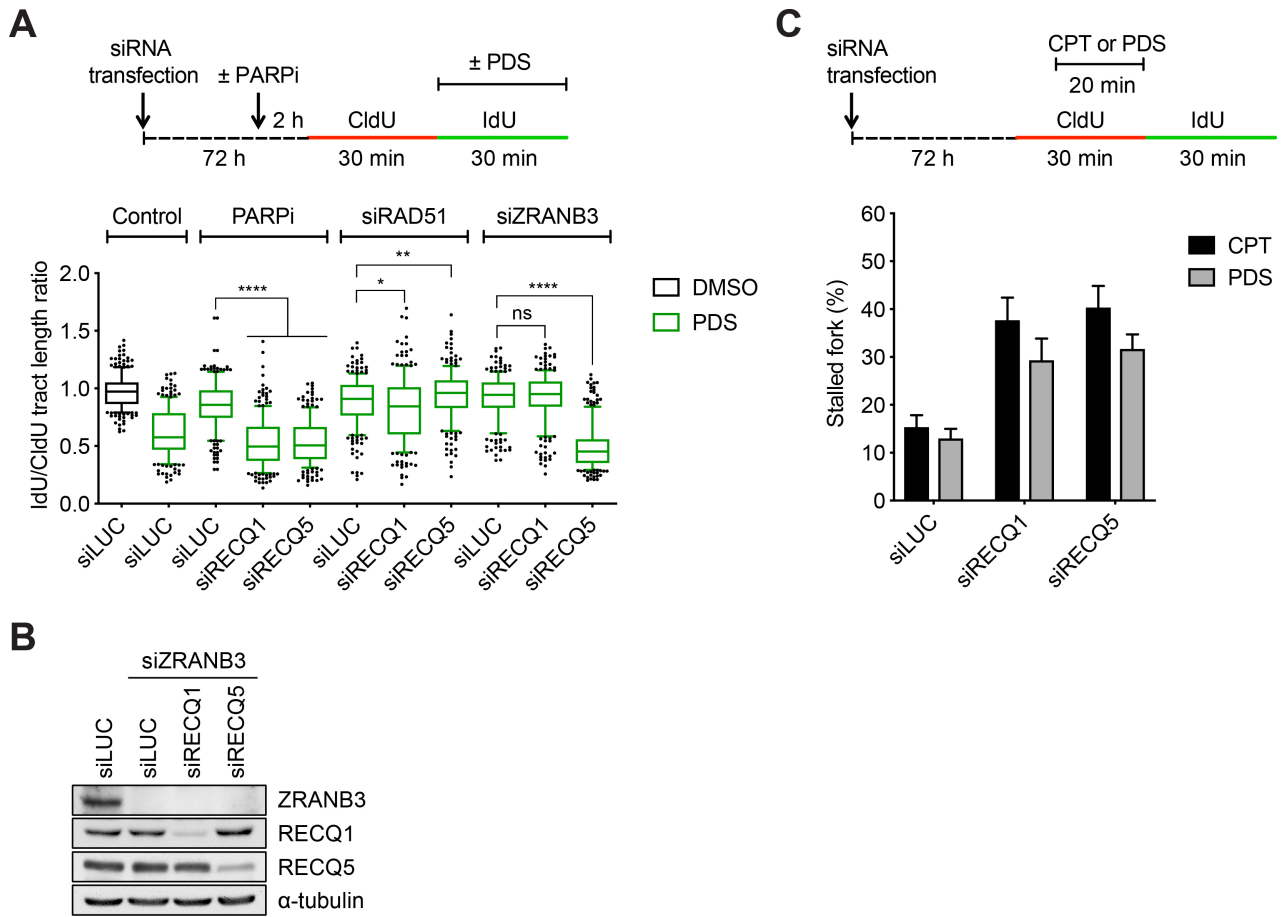
Figure S3

A

B

C

Figure S3, related to Figure 2. RECQ5 helicase mediates the switch from fork stalling to replication restart by disrupting RAD51 filaments

(A) Effects of depletion of RECQ1 or RECQ5 on the rescue of PDS-induced replication fork slowing in U2OS cells by PARP inhibition (PARPi) and RAD51 or ZRANB3 depletion, respectively. *Top panel*: Experimental workflow of DNA fiber assays. *Bottom panel*: Box plot of values of IdU/CldU tract length ratio obtained for indicated conditions in three independent experiments ($n \geq 200$, whiskers: 10-90 percentiles). ns, not significant; *P = 0.0119; ****P < 0.0001 (Mann-Whitney test). (B) Western blot analysis of extracts of U2OS cells transfected with indicated siRNAs. Cells were harvested 72 hr post siRNA transfection. (C) Replication restart following exposure to CPT or PDS is defective in U2OS cells depleted of RECQ1 or RECQ5. *Top panel*: Experimental workflow of replication restart assays. Cells were labeled sequentially with CldU and IdU for 30 min each. Where indicated, CPT (100 nM) or PDS (10 μM) were added during the last 20 min of the CldU pulse. *Bottom panel*: Quantification of replication fork stalling events. The data represent the percentage of active replicons (CldU-labeled) that fail to resume DNA synthesis (not IdU-labeled) 30 min after the removal of CPT. Data are the mean ± S.D., n = 3.
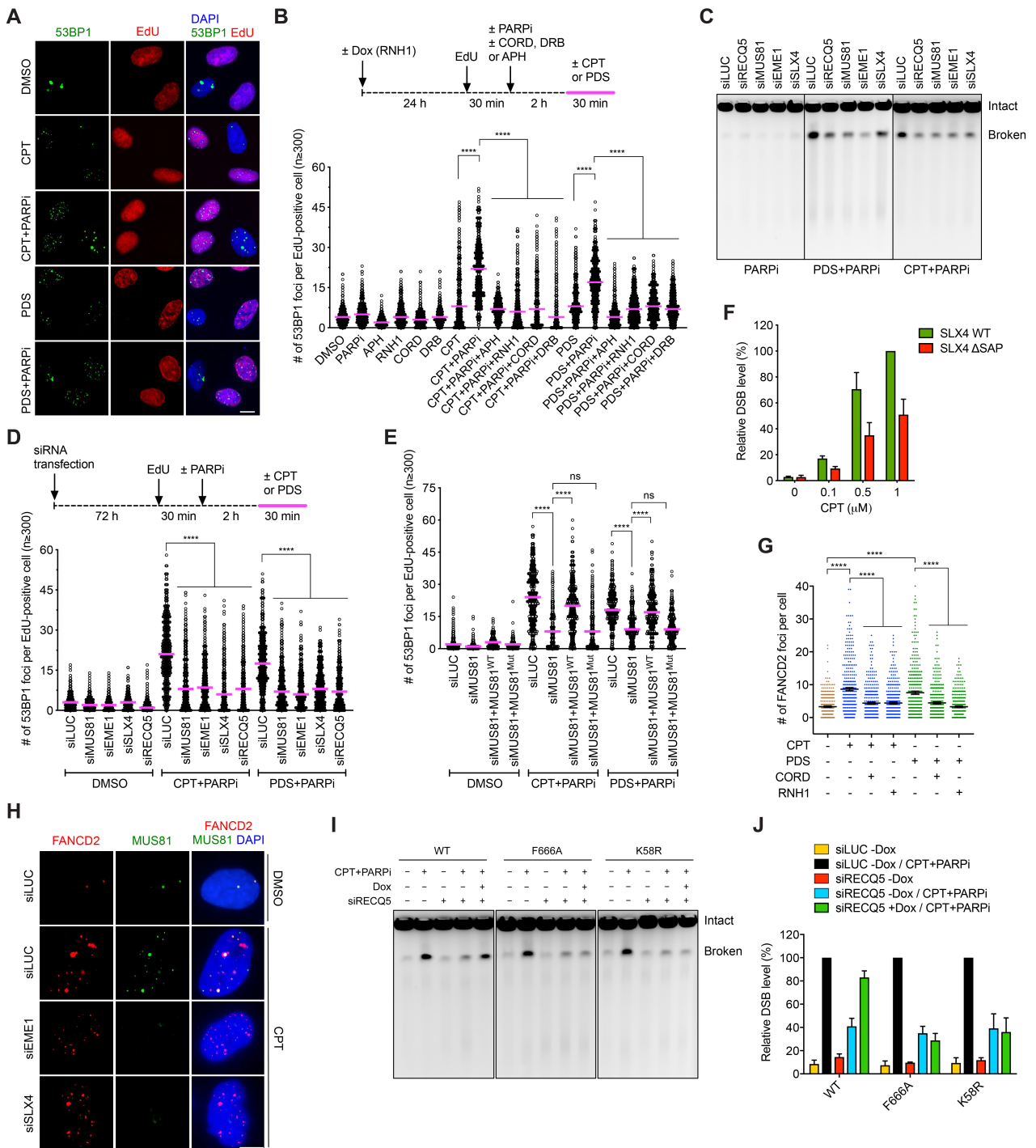
Figure S4

Figure S4, related to Figure 3. MUS81-mediated cleavage of R-loop-stalled forks requires disruption of RAD51 filaments by RECQ5

(A) Representative immunofluorescence images showing formation of 53BP1 foci (green) in nuclei of S-phase (EdU-positive, red) U2OS cells following a 30-min exposure to CPT (100 nM) or PDS (10 μM) in combination with PARP inhibitor (10 μM, PARPi). PARPi was added 2 hr before the start of CPT/PDS treatment. EdU-pulse labeling was carried out for 30 min ending 2 hr before addition of CPT/PDS. Scale bar, 10 μm. (B) 53BP1 nuclear focus formation stimulated by PARPi in CPT- and PDS-treated U2OS T-REx/RNH1-GFP cells depends on DNA replication, transcription and R-loop formation. *Top panel*: Experimental workflow. The drugs were present at the following concentrations: 100 nM CPT, 10 μM PDS, 10 μM PARPi, 50 μM cordycepin (CORD), 100 μM DRB and 5 μM aphidicolin (APH). *Bottom panel*: Quantification of 53BP1 foci in EdU-positive cells for indicated conditions. Horizontal lines represent median (n ≥ 300). (C) Pulsed-field gel electrophoresis analysis (PFGE) analysis of genomic DNA of U2OS cells treated with PARPi (*left panel*), PARPi + PDS (*middle panel*) and PARPi + CPT (*right panel*) at 48 hr following transfection of the indicated siRNAs. PARPi (10 μM) was added 2 hr before addition of CPT (1 μM) or PDS (20 μM). CPT and PDS were present for 5 hr. Quantification of DNA breakage is shown in Figure 3B. (D) Effect of depletion of the indicated proteins on the formation 53BP1 foci in S-phase (EdU positive) U2OS cells treated with CPT or PDS in the presence of PARPi. *Top panel*: Experimental workflow. *Bottom panel*: Quantification of 53BP1 foci in EdU-positive cells for indicated conditions. Horizontal lines represent median (n ≥ 300). (E) Formation of 53BP1 foci in CPT- and PDS-treated U2OS cells requires MUS81 endonuclease activity. U2OS cells stably transfected with wild-type (WT) *MUS81* or *MUS81(D338A/D339A)* (MUS81[Mut]) cDNA constructs were treated and analyzed as in (D). Parental U2OS cell line was used as control. Endogenous MUS81 was depleted with siRNA targeting MUS81 3'-UTR (siMUS81[UTR]). (F) The level of DNA breakage in RA3331/E6E7/hTERT fibroblasts, complemented with either

SLX4 wild type (WT) or SLX4 ΔSAP cDNAs, upon treatment with indicated concentrations of CPT. Genomic DNA was analyzed as in Figure 3A. Data represent the mean ± S.D., n = 4. (G) Effects of RNase H1 (RNH1) overexpression and transcription inhibition (CORD) on the formation of FANCD2 foci in U2OS T-REx/RNH1-GFP cells treated with CPT (100 nM) or PDS (10 μM) for 1 hr. RNH1-GFP expression was induced 24 hr prior to CPT/PDS treatment. CORD (50 μM) was added 2 hr prior to addition of CPT or PDS. Horizontal lines represent the mean ± S.E.M (n ≥ 300). (B,D,E,G) ns, not significant; ****P < 0.0001 (Mann-Whitney test). (H) Representative immunofluorescence images of mock- (siLUC), SLX4- and EME1-depleted U2OS cells after treatment with CPT (100 nM) or DMSO for 1 hr. Cells were stained for MUS81 (green) and FANCD2 (red). Nuclei were stained with DAPI (blue). Scale bar, 10 μm. (I) The level of chromosomal DNA breakage in cells in Figure 2C grown under indicated conditions. Where indicated, cells were treated with CPT (1 μM) and PARPi (10 μM) for 5 hr. Genomic DNA was analyzed by PFGE. (J) Quantification of gels represented in (I). DNA bands were quantified using Image-J software. Data were normalized and represent the mean ± S.D., n = 3.

Figure S5

A + APH
+ RO3306
16 h → G2 phase arrest → + EdU
+ Colcemid
1 h release → Metaphase spread 'click' reaction

B VA-13

C MRC5

D HeLa

E VA-13

F ± Dox (RNH1)
24 h → + APH
+ RO3306
16 h → G2 phase arrest → + EdU
+ Colcemid
1 h release → Metaphase spread 'click' reaction

G APH

H

I siRNA transfection → PARPi / ± PDS / ± HU
48 h / CldU 30 min / IdU 30 min / 5 h

J HU arrest after restart of semi-conservative replication

No fork reversal (siRAD51) — Nascent strand degradation −

Fork reversal (siBRCA2) — +

HU arrest after restart of conservative replication

Stable D-loop (siRAD51) — Nascent strand degradation −

Stable D-loop (siBRCA2) — −

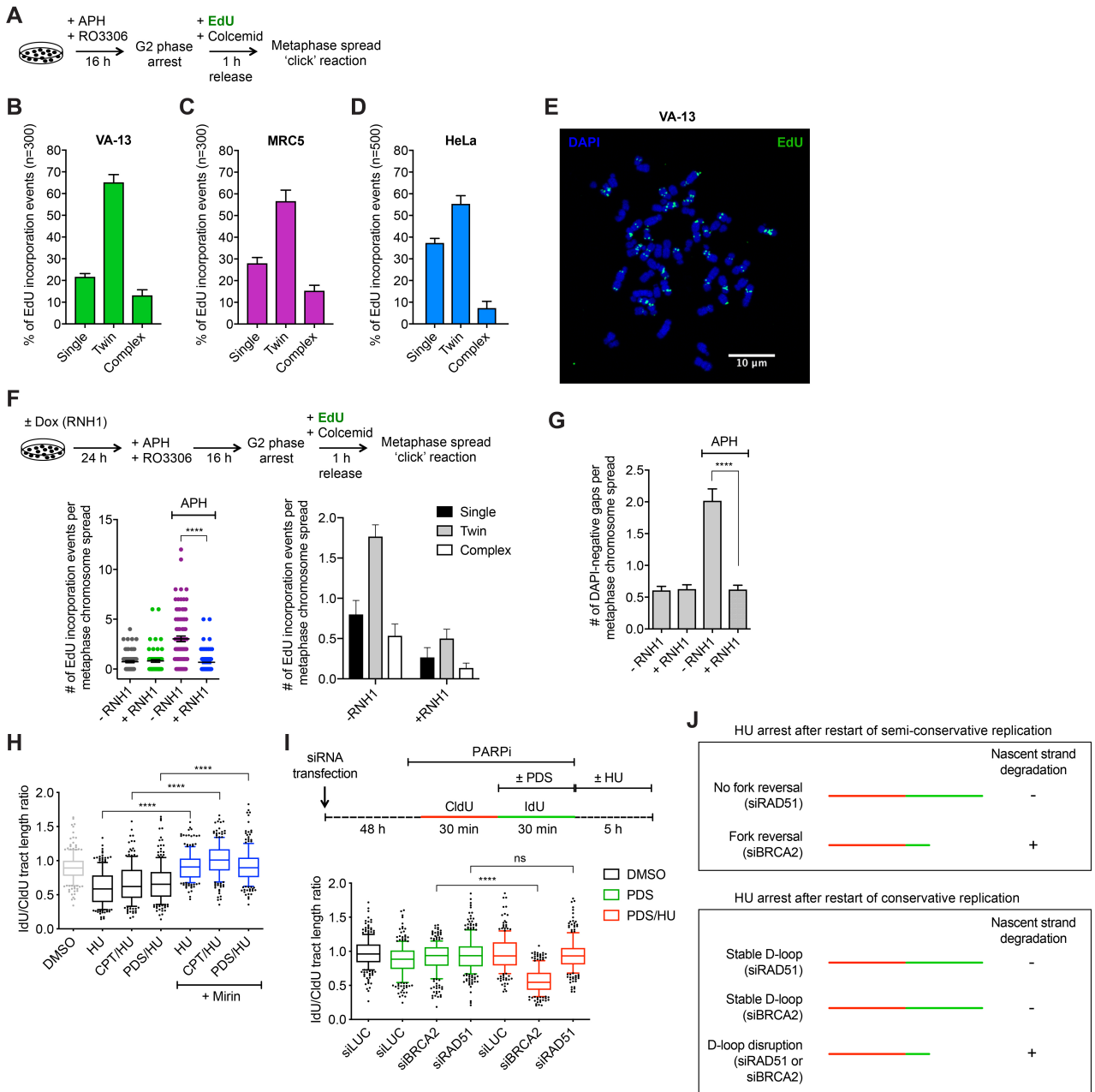D-loop disruption (siRAD51 or siBRCA2) — +

Figure S5, related to Figure 4. Restart of semiconservative DNA replication following R-loop-mediated fork stalling

(A-D) Experimental work flow (A) and quantification of EdU incorporation on metaphase chromosome spreads of VA-13 (B), MRC5 (C) and HeLa (D) cells following replication stress induced by low-dose of aphidicolin (+APH; 0.4 μM). Twin EdU foci (one on each sister chromatid) indicate semiconservative DNA replication. RO3306 was present at a concentration of 9 μM. (E) Representative image of EdU foci on metaphase chromosome spread of VA-13 cells treated as depicted in (A). (F) APH-induced mitotic DNA synthesis depends on R-loop formation. *Top panel:* Experimental workflow. U2OS T-REx/RNH1-GFP cells were treated with 0.4 μM APH and 9 μM RO-3306 for 16 hr (late G2 arrest), and then released into fresh medium containing EdU (20 μM) and colcemid (0.1 μg/ml) for a further 1 hr. Where required, doxycycline (Dox; 1 ng/ml) was added to induce RNH1-GFP expression. *Bottom left panel:* Quantification of EdU incorporation events on metaphase chromosomes of cells grown under indicated conditions. For each condition, at least 150 metaphases from three independent experiments were analyzed. The graph is scatter dot plot with black lines at mean. Error bars show S.E.M. ****P < 0.0001 (Mann-Whitney test). *Bottom right panel:* Quantification of single, twin and complex EdU foci. Data are mean ± S.E.M., n=3. (G) Quantification of DAPI-negative gaps on metaphase chromosomes of U2OS T-REx/RNH1-GFP cells grown under indicated conditions. At least 110 metaphase spreads from three independent experiments were scored for each condition. Data are mean ± S.E.M. ****P < 0.0001 (Mann-Whitney test). (H) HU-induced degradation of nascent DNA strands synthesized in BRCA2-depleted U2OS cells in the presence of CPT/PDS and PARPi depends on MRE11. DNA fiber labeling and drug treatments were performed as in Figure 4D and S5I. The MRE11 inhibitor Mirin (50 μM) was present during HU treatment. (I) Nascent DNA strands generated in the presence of PDS and PARPi are degraded upon replication arrest by hydroxyurea (HU) in BRCA2-depleted U2OS cells, indicative of semiconservative DNA

synthesis. *Top panel*: Experimental workflow of DNA fiber assays. Cells were cultured in the presence of olaparib (PARPi; 10 μM) during DNA fiber labeling. Where indicated, cells were treated with 10 μM PDS during IdU labeling, and/or with 4 mM HU for 5 hr after IdU labeling. *Bottom panel*: Box plot of values of IdU/CldU tract length ratio for mock (siLUC)-, BRCA2- and RAD51-depleted cells treated as indicated (n ≥ 200, whiskers: 10-90 percentiles). ns, not significant; ****P < 0.0001 (Mann-Whitney test). (J) Hypothetical outcomes of HU-induced arrest of semiconservative and conservative DNA replication in cells lacking BRCA2 or RAD51.
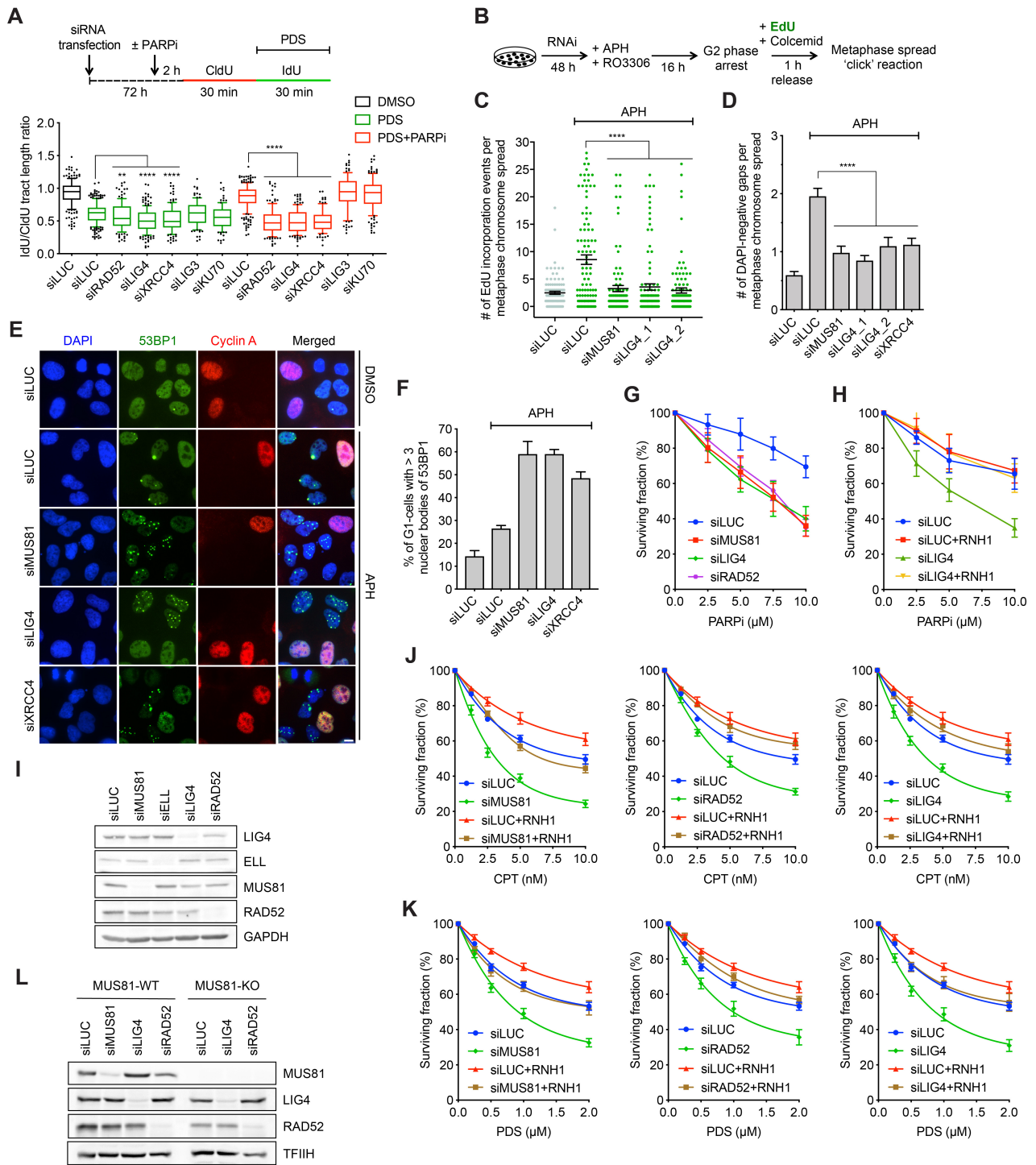
Figure S6

Figure S6, related to Figure 5. RAD52 and LIG4/XRCC4 mediate restart of R-loop-stalled forks

(A) Effect of depletion of indicated proteins on the replication fork velocity in U2OS cells upon treatment with 10 μM PDS, and on the rescue of PDS-induced replication fork slowing by PARP inhibition with 10 μM olaparib (PARPi). *Top panel*: Experimental workflow of DNA fiber assays. *Bottom panel*: Box plot of values of IdU/CldU tract length ratio obtained for indicated conditions in three independent experiments (n ≥ 200, whiskers: 10-90 percentiles). **P = 0.0022; ***P = 0.001; ****P < 0.0001 (Mann-Whitney test). (B) Experimental workflow of mitotic DNA synthesis (MiDAS) assay. 48 hr after siRNA transfection, cells were treated with APH (0.4 μM) and RO-3306 (9 μM) for 16 hr (late G2 arrest), and then released into fresh medium containing EdU (20 μM) and colcemid (0.1 μg/ml) for a further 1 hr. Metaphase chromosome spreads we subjected to click reaction to visualize the sites of EdU incorporation. (C) LIG4/XRCC4 is required for MiDAS induced by low-dose of aphidicolin (APH) in SV40-immortalized MRC5 fibroblasts. Graph shows quantification of EdU foci on metaphase spreads for cells transfected with indicated siRNAs. Twin or complex EdU foci were counted as one event. Horizontal lines represent the mean ± S.E.M. At least 100 metaphases were analyzed for each condition in three independent experiments. ****P < 0.0001 (Mann-Whitney test). (D) Quantification of DAPI-negative gaps on metaphase chromosome spreads of U2OS cells depleted for indicated proteins. Where indicated, cells were treated with 0.4 μM APH for 16 hr. Data represent the mean ± S.E.M. At least 100 metaphases were scored for each condition in three independent experiments. ns, not significant; ****P < 0.0001 (Mann-Whitney test). (E) Examples of G1 phase U2OS cells (cyclin A (red)-negative) containing 53BP1 nuclear bodies (green). Where indicated, cells were depleted of MUS81, LIG4 or XRCC4, and treated with 0.4 μM APH for 16 hr. Scale bar, 10 μm. (F) Quantification of G1-specific 53BP1 nuclear bodies in U2OS cells depleted for indicated proteins. Where indicated cells were treated with 0.4 μM APH for 16 hr. Data represent the mean ± S.D., n

=3. (G) Effect of depletion of LIG4 and RAD52 on sensitivity of U2OS cells to PARP inhibition. At 48 hr after siRNA transfection, cells were treated with different concentrations of olaparib (PARPi) for 24 hr and then subjected to clonogenic assay. (H) RNase H1 overexpression rescues hypersensitivity of LIG4-depleted U2OS T-REx/RNH1-GFP cells to PARP inhibition. Cell were treated and analyzed as in (G). RNH1-GFP expression was induced 24 hr before olaparib treatment. (I) Western blot analysis of extracts from U2OS T-REx/RNH1-GFP cells transfected with indicated siRNAs. (J and K) Depletion of MUS81, RAD52 or LIG4 in U2OS T-REx/RNH1-GFP cells combined with PARP inhibition confers hypersensitivity to CPT (J) and PDS (K), which can be rescued by RNase H1 (RNH1) overexpression. At 48 hr after siRNA transfection, cells were treated for 24 hr with 2 μM olaparib and different concentrations of CPT or PDS and then subjected to clonogenic assay. RNH1-GFP expression was induced 24 hr before treatment. (G,H,J,K) Data represent the mean ± S.D., n=3. (L) Western blot analysis of extracts from wild-type (MUS81-WT) and MUS81 knockout (MUS81-KO) HeLa Kyoto cells transfected with indicated siRNAs.
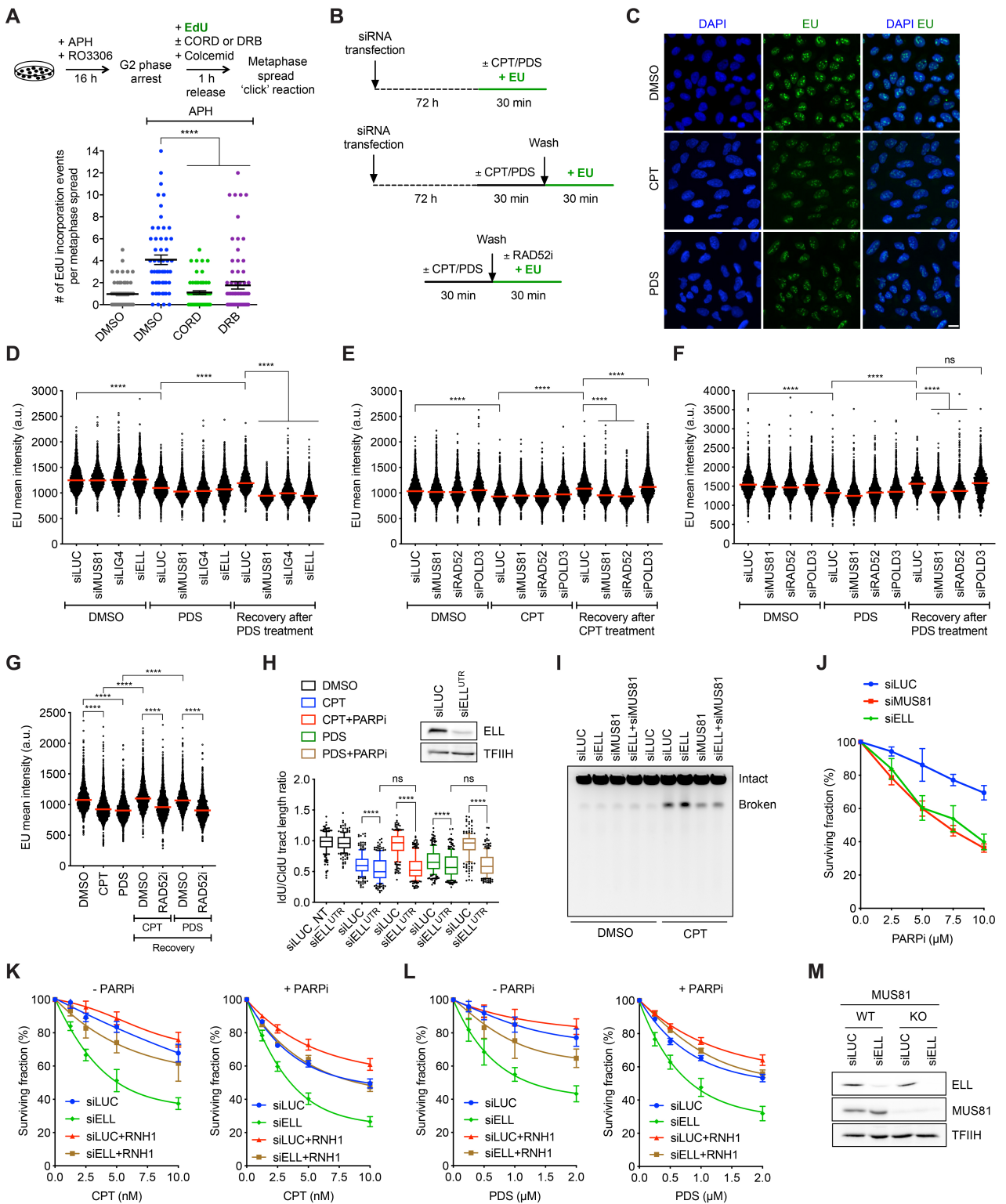
Figure S7

Figure S7, related to Figure 6. Restart of R-loop-stalled forks requires reactivation of transcription

(A) Effect of DRB (100 μM) and cordycepin (CORD, 50 μM) on EdU incorporation in U2OS cells released from G2 arrest following exposure to 0.4 μM aphidicolin (APH). Experimental workflow of MiDAS assay is depicted on the top. Data represent the mean ± S.E.M. At least 60 metaphases were analyzed for each condition in two independent experiments. ns, not significant; ****P < 0.0001 (Mann-Whitney test). (B) Experimental workflow of nascent RNA synthesis assays performed in this study. Nascent RNA strand production was quantified using 5-ethynyl uridine (EU; 1 mM) labelling. CPT and PDS were present at a concentration of 100 nM and 10 μM, respectively. (C) EU (green) incorporation into nuclei (DAPI, blue) of U2OS cells treated with DMSO, CPT or PDS. Experimental workflow is shown in (B, *top panel*). Cells were transfected with control siRNA (siLUC). Scale bar, 20 μm. (D) Depletion of MUS81, LIG4 and ELL, respectively, impairs resumption of transcription following exposure of U2OS cells to PDS. Experimental workflow is shown in (B, *top and middle panel*). (E and F). Depletion of RAD52, but not POLD3, impairs resumption of transcription following exposure of U2OS cells to CPT (E) or PDS (F). (G) Resumption of RNA synthesis following exposure of U2OS cells to CPT or PDS is impaired by RAD52 inhibitor (RAD52i; 40 μM). (D-G) Data represent the mean intensity of the EU signal in the nucleus. Horizontal lines represent median (n > 1800). ns, not significant; ****P < 0.0001 (Mann-Whitney test). (H) Effect of ELL depletion on replication fork progression in U2OS cells upon treatment with 100 nM CPT or 10 μM PDS, and on the rescue of CPT- or PDS-induced replication fork slowing by PARP inhibition with 10 μM olaparib (PARPi). DNA fiber assays were performed as in Figure 6D. ELL was depleted using siRNA targeting its 3'-UTR (siELL^UTR). *Top panel:* Western blot showing efficiency of ELL depletion. (I) Pulsed-field gel electrophoresis analysis of genomic DNA of U2OS cells treated with DMSO or CPT (1 μM) for 5 hr following depletion of the indicated proteins. (J) ELL depletion confers hypersensitivity to

PARP inhibition in U2OS cells. At 48 hr after siRNA transfection, cells were treated with different concentrations of olaparib (PARPi) for 24 hr and then subjected to clonogenic assay. (K and L) RNase H1 (RNH1) overexpression rescues hypersensitivy of ELL-depleted U2OS T-REx/RNH1-GFP to CPT and PDS. Where indicated, cells were co-treated with 2 μM olaparib (PARPi). (J-K) Data represent the mean ± S.D., n=3. (M) Western blot analysis of extracts from wild-type (WT) and MUS81 knockout (KO) HeLa Kyoto cells transfected with indicated siRNAs.

Table S1, related to Figure 1 and 2. Electron microscopy data for experiments in Figure 1D, 2B and 2D. (A and B) Percentage of observed reversed forks (% RF) in three (A) or two (B and C) independent experiments (Exp_1, Exp_2, Exp_3) for samples in Figure 1D (A), 2B (B) and 2D (C). Numbers of analyzed DNA molecules in brackets. NT, non-treated.

A

U2OS	NT	PDS			CPT		
T-REx	DMSO	DMSO	+CORD	+RNase H1	DMSO	+CORD	+RNase H1
% RF Exp_1	5 (99)	15 (94)	6 (99)	7 (90)	27 (94)	10 (94)	12 (94)
% RF Exp_2	7 (72)	18 (71)	11 (71)	10 (74)	28 (67)	12 (72)	14 (74)
% RF Exp_3	8 (72)	26 (81)	14 (76)	14 (89)	33 (74)	16 (73)	17 (90)

B

U2OS	siLUC		siMUS81		siSLX4		siRECQ5	
CPT	-	+	-	+	-	+	-	+
% RF Exp_1	5 (70)	27 (81)	16 (84)	39 (82)	20 (77)	37 (93)	20 (74)	39 (77)
% RF Exp_2	6 (71)	26 (80)	17 (74)	38 (75)	16 (80)	36 (77)	16 (70)	42 (70)

C

U2OS T-REx	WT			F666A			K58R		
siRECQ5	-	+	+	-	+	+	-	+	+
Dox	-	-	+	-	-	+	-	-	+
% RF Exp_1	7 (100)	16 (100)	9 (100)	8 (100)	17 (101)	18 (100)	8 (100)	16 (101)	17 (97)
% RF Exp_2	8 (71)	20 (60)	10 (71)	8 (71)	18 (60)	18 (70)	9 (70)	17 (71)	19 (67)

Research paper #3

Cancer-Cell-Intrinsic cGAS Expression Mediates Tumor Immunogenicity

Graphical Abstract
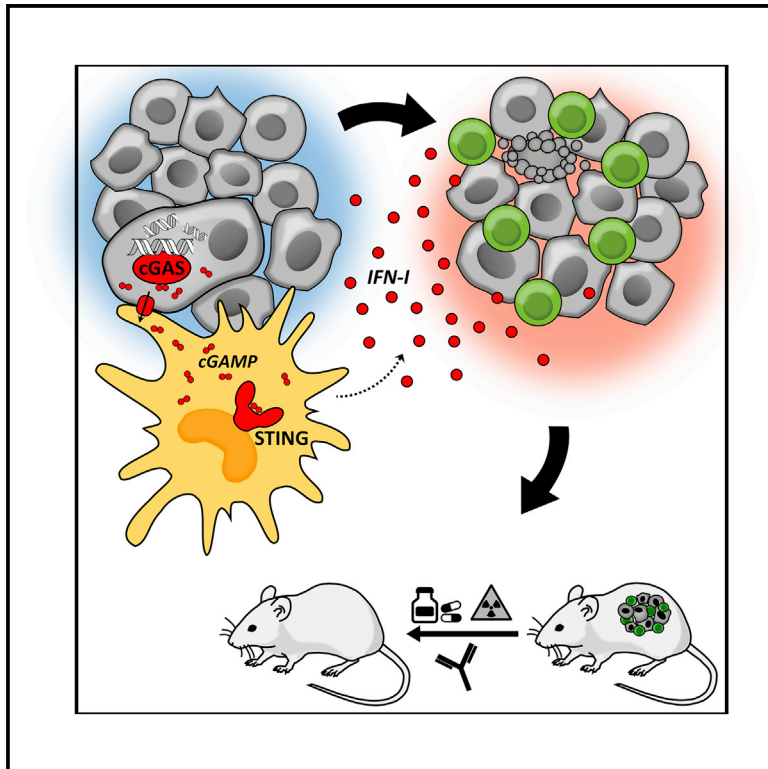
Authors

Linda Schadt, Colin Sparano,
Nicole Angelika Schweiger, ...,
Zuzana Nascakova, Winfried Barchet,
Maries van den Broek

Correspondence

vandenbroek@immunology.uzh.ch

In Brief

Schadt et al. show that cancer-cell-derived cGAMP is transferred to tumor-associated myeloid cells. Here, cGAMP activates STING and induces production of type I interferon. This promotes infiltration of protective CD8^{+} T cells and improves survival as well as response to therapy.

Highlights

- cGAS in cancer and STING in host cells are minimal requirements to activate CD8^{+} T cells

- Cancer cells transfer cGAMP to myeloid cells in the TME that make STING-dependent IFN-I

- Cancer-cell-intrinsic cGAS improves tumor immunogenicity and response to therapy

Cancer-Cell-Intrinsic cGAS Expression Mediates Tumor Immunogenicity

Linda Schadt,[1] Colin Sparano,[1] Nicole Angelika Schweiger,[1] Karina Silina,[1] Virginia Cecconi,[1] Giulia Lucchiari,[1] Hideo Yagita,[2] Emilien Guggisberg,[1] Sascha Saba,[1] Zuzana Nascakova,[3] Winfried Barchet,[4] and Maries van den Broek[1,5,*]

[1]Institute of Experimental Immunology, University of Zurich, Winterthurerstrasse 190, 8057 Zurich, Switzerland
[2]Department of Immunology, Juntendo University School of Medicine, Tokyo 113-8421, Japan
[3]Institute of Molecular Genetics of the ASCR, v. v. i., Videnska 1083, 142 20 Prague, Czech Republic
[4]Institute of Clinical Chemistry and Clinical Pharmacology, University Hospital and University of Bonn, Sigmund-Freud-Strasse 25, 35127 Bonn, Germany
[5]Lead Contact
*Correspondence: vandenbroek@immunology.uzh.ch
https://doi.org/10.1016/j.celrep.2019.09.065

SUMMARY

Sensing of cytoplasmic DNA by cyclic guanosine monophosphate-adenosine monophosphate (cGAMP) synthase (cGAS) results in production of the dinucleotide cGAMP and consecutive activation of stimulator of interferon genes (STING) followed by production of type I interferon (IFN). Although cancer cells contain supra-normal concentrations of cytoplasmic DNA, they rarely produce type I IFN spontaneously. This suggests that defects in the DNA-sensing pathway may serve as an immune escape mechanism. We find that cancer cells produce cGAMP that is transferred via gap junctions to tumor-associated dendritic cells (DCs) and macrophages, which respond by producing type I IFN *in situ*. Cancer-cell-intrinsic expression of cGAS, but not STING, promotes infiltration by effector CD8+ T cells and consequently results in prolonged survival. Furthermore, cGAS-expressing cancers respond better to genotoxic treatments and immunotherapy. Thus, cancer-cell-derived cGAMP is crucial to protective anti-tumor CD8+ T cell immunity. Consequently, cancer-cell-intrinsic expression of cGAS determines tumor immunogenicity and makes tumors hot. These findings are relevant for genotoxic and immune therapies for cancer.

INTRODUCTION

Cancer develops in the face of immune surveillance and thus needs to evade immune control to progress. The tumor microenvironment (TME) influences not only tumor progression but also the response to immune and standard therapies (Binnewies et al., 2018). Immunogenic or hot tumors contain more infiltrating T cells than cold tumors and are associated with favorable prognosis and better response to immune checkpoint inhibition (Galon et al., 2006; Van Allen et al., 2015). In contrast, cold tumors

can be T cell excluded or T cell ignorant (Chen and Mellman, 2017; van der Woude et al., 2017), suggesting that multiple mechanisms may contribute to a tumor being cold. Besides the presence of infiltrating T cells, hot tumors are characterized by a type I interferon (IFN) signature (Gajewski et al., 2013). Indeed, type I IFN is essential for the generation of protective anti-tumor immunity, and tumor-infiltrating dendritic cells (DCs) are essential for both production of and response to type I IFN in the TME (Diamond et al., 2011; Fuertes et al., 2011; Dai et al., 2017; Dunn et al., 2006).

The production of type I IFN is downstream of the sensing of cytoplasmic double-stranded DNA (dsDNA) (Stetson and Medzhitov, 2006; Vanpouille-Box et al., 2018), which is normally absent from eukaryotic cells. However, substantial amounts of cytoplasmic dsDNA are found under pathological conditions, including viral infection, genomic instability, and DNA damage (Fenech et al., 2011; Harding et al., 2017; Ishikawa et al., 2009; Li and Chen, 2018; Mackenzie et al., 2017). Consistent with these findings, radiotherapy (Burnette et al., 2011; Deng et al., 2014) and chemotherapy (Ahn et al., 2014; Sistigu et al., 2014) induce type I IFN. Upon binding of dsDNA, cyclic guanosine monophosphate-adenosine monophosphate (cGAMP) synthase (cGAS) catalyzes the formation of the second messenger cGAMP. Subsequently, cGAMP binds to stimulator of interferon genes (STING), resulting in phosphorylation of interferon regulatory factor 3 (IRF3) and production of type I IFN (Ablasser et al., 2013a; Ishikawa and Barber, 2008; Li and Chen, 2018; Sun et al., 2013; Wu et al., 2013; Gao et al., 2013; recently reviewed in Ablasser and Chen, 2019).

Cancer cells often constitutively contain a high concentration of cytoplasmic dsDNA, which further increases upon DNA-damaging therapies such as radio- or chemotherapy (Shen et al., 2015). Given the important role of type I IFN in priming of protective T cell immunity (Diamond et al., 2011; Dunn et al., 2006; Fuertes et al., 2011), the presence of cytoplasmic dsDNA in cancer cells may contribute to their immunogenicity. Downregulation of the cGAS/STING pathway correlates with poor prognosis in human cancer (Song et al., 2017; Xia et al., 2016; Yang et al., 2017). Together, this suggests that the absence of cytoplasmic dsDNA sensing contributes to immune evasion of cancer cells.

It was proposed recently that cancer-cell-derived cytoplasmic dsDNA is transferred to tumor-associated DCs, resulting in cGAS/STING-dependent production of type I IFN by these DCs, priming of protective CD8$^+$ T cells, and tumor control (Woo et al., 2014). How cytoplasmic dsDNA is transferred from cancer cells to DCs, however, is largely unclear, although transfer via exosomes has been suggested (Kitai et al., 2017). In viral infections and carcinoma-astrocyte interactions, it was shown that cGAMP is transferred to neighboring cells via gap junctions, resulting in the activation of STING in cGAMP-receiving cells (Ablasser et al., 2013b; Chen et al., 2016).

Inspired by these observations, we proposed that cGAMP instead of cytoplasmic dsDNA is transferred from cancer cells to DCs, thus enabling the production of type I IFN and priming of protective immunity, even in situations where cancer cells have a compromised STING pathway. We show here that CD8$^+$ T-cell-mediated control of cancer depends on cancer-cell-derived cGAMP. This is in line with the recent observation that natural killer (NK)-cell-mediated control of tumor cells requires expression of STING by host cells and cGAS by cancer cells (Marcus et al., 2018), thus supporting our hypothesis. Furthermore, we show that cancer-cell-intrinsic cGAS makes tumors more sensitive to chemo-, radio-, and immunotherapy.

Thus, we propose that expression of cGAS by cancer cells determines tumor immunogenicity as well as its response to genotoxic and immune checkpoint inhibition therapies.

RESULTS

Production of Type I IFN in Co-cultures of DCs and Cancer Cells Requires Expression of cGAS by Cancer Cells and STING by DCs

To select an experimental system for testing whether cancer-cell-intrinsic cGAS expression contributes to tumor immunogenicity, we probed the cGAS/STING pathway in different murine tumor cell lines. Most cell lines expressed cGAS and/or STING, albeit different amounts (Figures 1A and S1A). To measure whether the cGAS/STING pathway is functional, we transfected the cell lines with DNA and quantified secreted type I IFN using a reporter cell line. All but two cell lines spontaneously produced very low amounts of type I IFN, which increased upon transfection with DNA (Figure 1B). In the CT26 cell line that is considered immunogenic, we next established CT26 mutants deficient for cGAS (CT26$^{\Delta Mb21d1}$) or STING (CT26$^{\Delta Tmem173}$) using CRISPR/Cas9 technology and validated the absence of cGAS or STING by western blot (Figure 1C). CT26 cells modified with an empty vector (CT26^{ctrl}) were used as control. In addition, we engineered cGAS-negative Lewis lung carcinoma (LLC; ATCC CRL-1642) cells (Figure 1A) to express cGAS (LLC^{Mb21d1}) and confirmed the expression of cGAS by western blot (Figure 1D).

As the STING pathway is frequently compromised in cancer cells (Song et al., 2017; Xia et al., 2016; Yang et al., 2017), they rely on other cell types for the production of immune-stimulating type I IFN. It has been suggested that tumor-associated DCs fulfill this role after uptake of cancer-cell-derived dsDNA (Klarquist et al., 2014; Woo et al., 2014). To study whether cancer cells can induce the production of type I IFN in DCs, we measured the amount of type I IFN in co-cultures (Figures

1E–1G and S1B–S1D). We observed a strong induction of type I IFN in co-cultures of CT26^{ctrl} cells with wild-type bone-marrow-derived DCs (BMDCs) compared to cancer cells or BMDCs alone (Figures 1F and S1B). Type I IFN was absent from co-cultures of cGAS-deficient CT26$^{\Delta Mb21d1}$ cells with wild-type BMDCs (Figure 1F) but present in co-cultures of STING-deficient CT26$^{\Delta Tmem173}$ cells with BMDCs (Figure S1C). These data suggest that the production of type I IFN depends on cancer-cell-intrinsic expression of cGAS, but not STING. Co-cultures using cGAS-deficient BMDCs gave similar results to those using wild-type BMDCs, suggesting that expression of cGAS in BMDCs is dispensable for the production of type I IFN. Type I IFN was not detectable in co-cultures of any CT26 cell line with STING-deficient BMDCs (Figure 1F). This suggests that expression of STING in DCs is essential for the production type I IFN in co-cultures cGAS-expressing cancer cells. In line with the abovementioned findings, we observed that cGAS-overexpressing LLC^{Mb21d1} cells induce type I IFN secretion in co-cultured BMDCs, while the parental LLC cells do not (Figure 1G).

Intercellular transfer of cGAMP has been reported to depend on gap junctions (Ablasser et al., 2013b; Chen et al., 2016). To investigate whether cell-cell contact is indeed required for cGAMP transfer from cancer cells to DCs, we used a transwell system and found that the production of type I IFN was abrogated (Figure S1D). This excludes transfer of soluble or exosome-associated cGAMP.

To identify whether cGAMP is transferred from tumor cells to DCs over gap junctions, we generated connexin-43 (CX43)-deficient CT26 cells (CT26$^{\Delta Gja1}$) (Figure 1C). To assess the exchange of cytoplasm between cells, we used the calcein AM transfer assay (Figure S1E) (Ablasser et al., 2013b; Saccheri et al., 2010). CT26$^{\Delta Gja1}$ cells transferred significantly less calcein AM to co-cultured BMDCs than CT26^{ctrl} cells (Figures S1F and S1G), suggesting that deleting Gja1 is sufficient to reduce cytoplasmic exchange. We then co-cultured CX43-deficient CT26$^{\Delta Gja1}$ cells with BMDCs and found that the production of type IFN I was abolished (Figure 1F).

Thus, we showed that minimal requirements for production of type I IFN in cancer cell/BMDC co-cultures are the expression of cGAS in cancer cells and STING in BMDCs, suggesting transfer of cGAMP and not dsDNA from cancer cells to BMDCs. Furthermore, we showed that cGAMP is transferred via gap junctions *in vitro*.

Cancer-Cell-Intrinsic cGAS Deficiency Promotes Tumor Progression and Makes Tumors Cold

After having established that cancer-cell-intrinsic cGAS is essential for production of type I IFN by neighboring DCs *in vitro*, we investigated the contribution of cancer-cell-derived cGAMP on immune surveillance. Therefore, we injected CT26^{ctrl}, CT26$^{\Delta Mb21d1}$, or CT26$^{\Delta Tmem173}$ cells subcutaneously (s.c.) in BALB/c mice and monitored tumor growth and survival (Figure 2A). We found that cGAS-deficient, but not STING-deficient, CT26 tumors grow faster than control CT26 tumors (Figure 2B), resulting in significantly reduced survival (Figure 2C).

To exclude that the increased tumor growth of CT26$^{\Delta Mb21d1}$ cells is due to cell-intrinsic features, we measured the growth
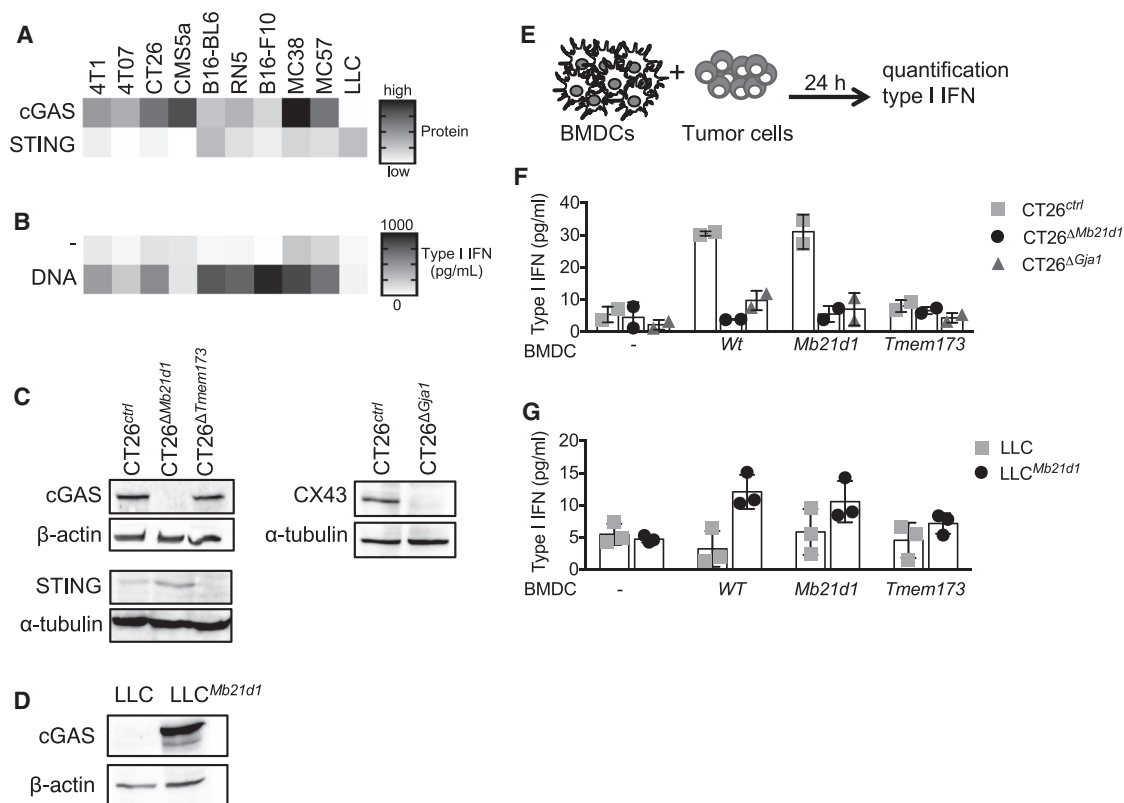
Figure 1. Production of Type I IFN in Co-cultures of DCs and Cancer Cells Requires Expression of cGAS by Cancer Cells and STING by DCs

(A) Expression of cGAS and STING protein in murine tumor cell lines *in vitro*. Expression was measured by western blot, and data are represented as relative protein expression in arbitrary units (cGAS/β-actin and STING/α-tubulin). The heatmap shows the range between low (white) to high (black) expression. Plots show pooled results from three independent experiments.

(B) *In vitro* production of type I IFN by murine tumor cell lines over 24 h. The upper row shows spontaneous production, and the lower row shows production of cells transfected with 1 μg genomic dsDNA. The heatmap shows the range between 0 pg/mL (white) and 1,000 pg/mL (black). Plots show pooled results from three independent experiments.

(C) Confirmation of deficiency of cGAS, STING, and connexin-43 (CX43) by western blot in CT26$^{\Delta Mb21d1}$, CT26$^{\Delta Tmem173}$, and CT26$^{\Delta Gja1}$ cells, respectively.

(D) Confirmation of cGAS overexpression in LLC^{Mb21d1} by western blot.

(E) Experimental design for (F) and (G). Cancer cells (0.15 x 10^6) were co-cultured with 0.5 × 10^6 bone marrow derived dendritic cells (BMDCs) from wild-type (WT), cGAS-deficient (*Mb21d1*) or STING-deficient (*Tmem173*) mice. After 24 h, type I IFN was measured in the supernatant with the reporter cell line LL171. Every symbol represents one biological replicate. Bars represent mean ± SD. Results are representative of 2 independent experiments each.

(F) CT26^{ctrl}, CT26$^{\Delta Mb21d1}$, and CT26$^{\Delta Gja1}$ cancer cells.

(G) LLC and LLC^{Mb21d1} cancer cells.

See also Figure S1.

---

of CT26^{ctrl}, CT26$^{\Delta Mb21d1}$, or CT26$^{\Delta Tmem173}$ cancer cells *in vitro* and found no significant difference (Figure S2A). Next, we injected CT26^{ctrl}, CT26$^{\Delta Mb21d1}$, or CT26$^{\Delta Tmem173}$ cells in NOD.Cg-*Prkdc^{scid} Il2rg^{tm1Wjl}* (NSG) mice that lack T, B, and NK cells (Figure S2B). All three CT26 cell lines showed similar growth and survival characteristics (Figures S2C and S2D), suggesting that the increased growth of cGAS-deficient CT26 tumors is due to compromised immune surveillance.

To further support the role of cancer-cell-derived cGAMP in immune control of tumors, we analyzed the immune infiltrates associated with CT26^{ctrl}, CT26$^{\Delta Mb21d1}$, and CT26$^{\Delta Tmem173}$ tumors in BALB/c mice 22 d after tumor cell injection (Figure 2D). Within the CD45$^+$ leukocyte population, the proportions of CD3$^+$, CD8$^+$, and CD8$^+$ IFN-γ$^+$ T cells were significantly lower in cGAS-deficient tumors than control or STING-deficient tumors

(Figures 2E and S2E). To address whether the tumor-specific CD8$^+$ T cell population is influenced by the absence of cGAS in cancer cells, we analyzed IFN-γ production by tumor-associated CD8$^+$ T cells after *in vitro* stimulation with a cancer-cell-specific peptide, AH-1 (Huang et al., 1996) (Figure 2F, left panel, and Figure S2F). In addition, we saw that cGAS-expressing tumors contained a higher proportion of CD39$^+$ cells within the CD8$^+$ population (Figure 2F, right panel, and Figure S2F), suggesting an increase in tumor-specific CD8$^+$ T cells (Simoni et al., 2018). Our observation that cGAS-proficient tumors contain higher concentrations of the T-cell-derived effector cytokines IFN-γ and tumor necrosis factor alpha (TNF-α) further substantiates that cGAS-expressing tumors are hot (Figure 2G). The proportion of other immune cells like CD4$^+$ and FoxP3$^+$ CD4$^+$ T cells as well as myeloid cells were comparable in the different tumors
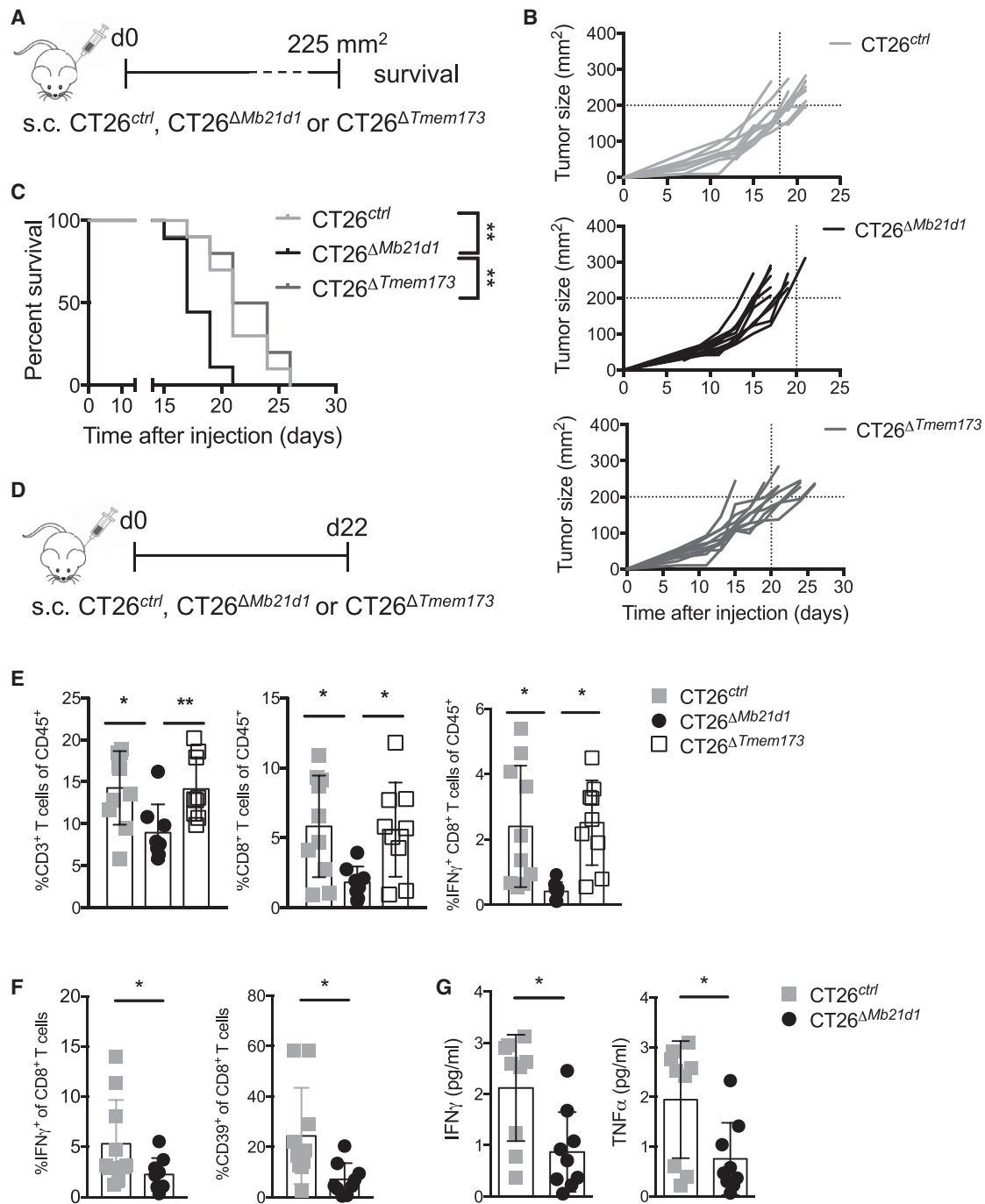
Figure 2. Cancer-Cell-Intrinsic cGAS Expression Makes Tumors Hot and Promotes Immune Surveillance

(A) Experimental design for (B) and (C). CT26^{ctrl}, CT26$^{\Delta Mb21d1}$, or CT26$^{\Delta Tmem173}$ cells were injected subcutaneously into BALB/c mice (n = 10 mice per group).

(B) Tumor size was measured with a caliper. Every line represents an individual mouse. Results are representative of four independent experiments.

(C) Survival curve. Death event is defined as tumor size >225 mm^2. Statistics were calculated using the log-rank (Mantel-Cox) test. Results are representative of four independent experiments. **p < 0.01.

(D) Experimental design for (E)–(G). CT26^{ctrl}, CT26$^{\Delta Mb21d1}$, or CT26$^{\Delta Tmem173}$ cells were injected subcutaneously into BALB/c mice (n = 9–10 mice per group).

(E) Percentage of immune cells in tumors analyzed by flow cytometry at the endpoint (day 22). Percentage of IFN-γ^+ CD8$^+$ T cells in tumors was determined after *in vitro* stimulation with phorbol 12-myristate 13-acetate (PMA)/ionomycin in the presence of brefeldin A. Every symbol represents an individual mouse. Bars represent mean ± SD. Statistics were calculated using one-way ANOVA with Tukey's multiple comparison correction. Gating strategies are shown in Figure S2E. Results are representative of three independent experiments.

(legend continued on next page)

(Figure S2G; data not shown). Moreover, we found no differences in the proportion of NK cells in the different tumors (Figure S2H). For gating strategies, see Figures S2I and S2J, respectively.

Depletion of CD8$^+$ T cells promoted the growth of CT26^{ctrl}, but not CT26^{ΔMb21d1}, tumors (Figure S2K). This underscores the relevance of CD8$^+$ T cells for controlling CT26 tumor growth as well as the importance of cancer-cell-intrinsic cGAS for recruiting those T cells (Figure 2E).

To substantiate our findings, we monitored tumor growth and survival of C57BL/6 mice that were injected with LLC or LLC^{Mb21d1} cells (Figure S3A). We found that the overexpression of cGAS in LLC cells resulted in slower tumor growth (Figure S3B), prolonged survival (Figure S3C), and an infiltrate reminiscent of hot tumors (Figures S3D and S3E). To strengthen the concept that type I production in the TME depends on the transfer of cGAMP, but not DNA, from cancer to host cells, we injected LLC or LLC^{Mb21d1} in wild-type C57BL/6 or cGAS-deficient B6(C)-$Cgas^{tm1d(EUCOMM)Hmgu}$/J (cGAS$^{-/-}$ B6) mice (Figure S3F). As shown above, LLC^{Mb21d1} tumors contained more effector CD8$^+$ T cells than LLC tumors, independently of the mouse genotype (Figures S3G and S3H). These data suggest that the DNA-sensing capacity of the host is insignificant for the generation of antitumor immunity.

Thus, cancer-cell-intrinsic cGAS expression promotes infiltration by effector CD8$^+$ T cells that control tumor growth.

Cancer-Cell-Derived cGAMP Induces Production of Type I IFN by Tumor-Associated DCs

Using co-cultures of cancer cells and BMDCs, we showed that cancer-cell-derived cGAMP is transferred to DCs, which produce type I IFN in turn. To investigate whether this process is operative in tumors *in vivo*, we isolated established CT26^{ctrl} and CT26^{ΔMb21d1} tumors from BALB/c mice (Figure 3A). From half of the tumors, we prepared a lysate; the other half was processed for single-cell analysis by flow cytometry. The lysate of cGAS-deficient CT26 tumors contained significantly less IFN-β than that of control CT26 tumors (Figure 3B). To identify the cell type that produces type I IFN in CT26 tumors, which we consider a proxy for uptake of cancer-cell-derived cGAMP, we used PrimeFlow. We applied this flow-cytometry-based method to detect transcripts in single cells, because intracellular staining for type I IFN using antibodies is not sufficiently sensitive or reliable (Lienenklaus et al., 2009; Scheu et al., 2008). We stained CT26^{ctrl} and CT26^{ΔMb21d1} tumors for different lineage markers as well as *Ifnb1* transcripts. We detected the *Ifnb1* signal almost exclusively in the CD45$^+$ leukocyte fraction (Figure 3C). We found a significantly higher percentage of *Ifnb1*$^+$ cells within the leukocyte fraction of CT26^{ctrl} tumors than in cGAS-deficient CT26^{ΔMb21d1} tumors (Figure 3D). Moreover, the majority of

Ifnb1$^+$ cells in CT26^{ctrl} tumors were DCs and macrophages, of which both were reduced in cGAS-deficient CT26^{ΔMb21d1} tumors (Figures 3E and S4A). Conventional DC1s (cDC1s) and cDC2s differ concerning their capacity to activate T cells and can be discriminated by surface expression of CD11b or CD103 (Broz et al., 2014). We saw that both cDC1s and cDC2s expressed significantly higher amounts of *Ifnb1* transcripts in CT26^{ctrl} tumors than in cGAS-deficient CT26^{ΔMb21d1} tumors (Figures S4B and S4C). Comparison of the *Ifnb1* signal in tumor-associated, major histocompatibility complex class II (MHCII)$^+$ cells to that in MHCII$^+$ naive spleen cells (negative control) or MHCII$^+$ spleen cells stimulated *in vitro* with a STING agonist (positive control) technically validated this readout (Figure S4D).

Thus, DCs and macrophages associated with cGAS-expressing tumors produce type I IFN *in situ*, whereas their ability to do so is compromised in cGAS-deficient tumors. This suggests that cancer-cell-derived cGAMP indeed is transferred to neighboring myeloid cells.

The Efficacy of DNA-Damaging Cancer Therapies Depends on Cancer-Cell-Intrinsic Expression of cGAS

In response to DNA damage, genomic instability, or viral infection, the amount of cytoplasmic dsDNA is increased in eukaryotic cells (Fenech et al., 2011; Harding et al., 2017; Ishikawa et al., 2009; Mackenzie et al., 2017). Since cytoplasmic dsDNA is the substrate for cGAS, we investigated the effect of genotoxic treatments on immune-mediated control of cGAS-deficient and control CT26 tumors. First, we confirmed that the amount of cytoplasmic dsDNA in untreated CT26 cancer cells is indeed higher compared to untransformed cells by ~100-fold (Figure S5A). We then applied genotoxic stress to CT26 cells *in vitro* to validate an increase of the cytoplasmic dsDNA concentration. Different genotoxic treatments including radiation with 8 Gy or 20 Gy as well as exposure to 15 μM cisplatin increased the amount of cytoplasmic DNA significantly (Figure S5A).

Second, we investigated whether cGAS-deficient cancer cells have a decreased sensitivity to genotoxic treatments per se and determined the survival of CT26^{ctrl} or CT26^{ΔMb21d1} cancer cells after treatment with radiation or cisplatin (Figure S5B). We found that both cell lines showed a similar decrease in the surviving fraction upon increasing doses of radiotherapy and cisplatin (Figure S5B). In addition, we observed similar radiation-induced DNA damage in CT26^{ctrl} or CT26^{ΔMb21d1} cells as measured by gamma-H2AX staining (Figure S5C and S5D). This suggests that the sensitivity toward genotoxic treatments is not influenced by the absence of cGAS in CT26 cancer cells.

Third, we analyzed the immune-stimulating effect of radiotherapy in mice bearing cGAS-deficient or control CT26 tumors. Therefore, we subjected BALB/c mice bearing established

---

(F) Percentage of IFN-γ$^+$ (left panel) and CD39$^+$ (right panel) cells within the CD8$^+$ T cell population in the tumor analyzed by flow cytometry at the endpoint (day 17) after *in vitro* stimulation with AH-1 peptide in the presence of brefeldin A. Every symbol represents an individual mouse. Bars represent mean ± SD. Statistics were calculated using the Mann-Whitney *U* test. Gating strategies are shown in Figure S2F. Results are representative of two independent experiments.

(G) Concentration of IFN-γ and TNF-α in tumor lysate normalized to total protein concentration measured at the endpoint (day 22). Every symbol represents an individual mouse. Bars represent mean ± SD. Statistics were calculated using unpaired two-tailed Student's t test. *p < 0.05, **p < 0.01. Results are representative of two independent experiments.
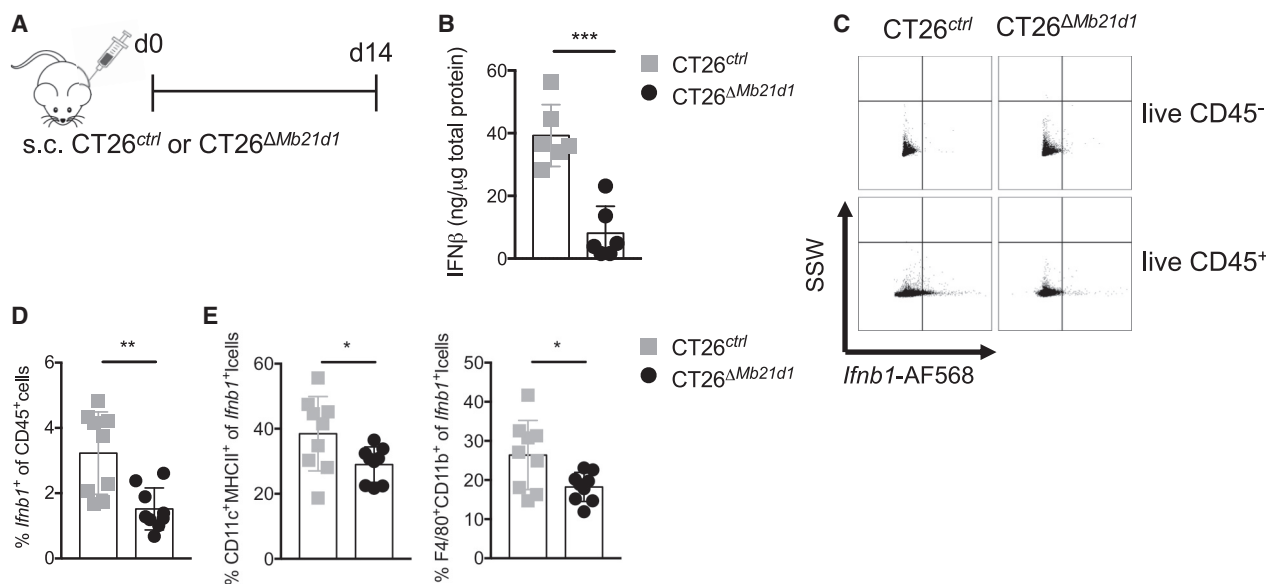
See also Figures S2 and S3.

Figure 3. Cancer-Cell-Derived cGAMP Induces the Production of IFN-β by Tumor-Associated DCs

(A) Experimental design. CT26^{ctrl} or CT26^{ΔMb21d1} cells were injected subcutaneously into BALB/c mice (n = 10 mice per group).

(B) IFN-β concentration in tumor lysate normalized to total protein concentration measured at the endpoint (day 14). Every symbol represents an individual mouse.

(C) Representative plots for measurement of Ifnb1 mRNA by flow cytometry in CT26^{ctrl} and CT26^{ΔMb21d1} tumors. The upper panels are gated on live, CD45$^-$ cells. The lower panels are gated on live, single CD45$^+$ cells.

(D) Percentage of Ifnb1$^+$ cells in the CD45$^+$ population at the endpoint (d 14).

(E) Percentage of DCs and macrophages of all live, single Ifnb1$^+$ cells. DCs were gated as CD45$^+$CD11c$^+$MHCII$^+$ and macrophages as CD45$^+$CD11b$^+$F4/80$^+$ cells. Every symbol represents an individual mouse. Bars represent mean ± SD. Statistics were calculated using unpaired two-tailed Student's t test. *p < 0.05, **p < 0.01, ***p < 0.005. Gating strategies are shown in Figure S4A. Results are representative of two independent experiments.

See also Figure S4.

CT26^{ctrl} or CT26^{ΔMb21d1} tumors to radiotherapy given as a single dose of 20 Gy (Surace et al., 2015) (Figure 4A). As shown above, untreated CT26^{ΔMb21d1} tumors grew faster than untreated CT26^{ctrl} tumors (Figure 4B), which resulted in a shorter survival (Figure 4C). Although both tumors responded to radiotherapy, therapy-induced growth retardation and increase in survival was only marginal in mice bearing cGAS-deficient tumors. In contrast, the clinical response of mice bearing CT26^{ctrl} tumors was very pronounced and resulted in tumor clearance in 3 out of 10 mice (Figures 4B and 4C). Radiotherapy supports CD8$^+$ T-cell-mediated immunity (Gupta et al., 2012; Surace et al., 2015; Galluzzi et al., 2017); therefore, we characterized immune infiltrates in irradiated and untreated tumors. We found that numbers of CD3$^+$ and CD8$^+$ T cells were increased upon radiotherapy in CT26^{ctrl} tumors, but not cGAS-deficient CT26^{ΔMb21d1} tumors (Figure S5E).

We used a similar experimental setup to compare the sensitivity of CT26^{ctrl} or CT26^{ΔMb21d1} tumors to another genotoxic treatment, cisplatin (Figure 4D). Cisplatin significantly retarded tumor growth and prolonged survival of mice bearing CT26^{ctrl} tumors (Figures 4E and 4F). In contrast, cisplatin had no effect on the growth of cGAS-deficient CT26^{ΔMb21d1} tumors (Figure 4E), nor did it increase survival (Figure 4F).

Thus, although radiotherapy and cisplatin have a different mode of action, both induce higher concentrations of cytoplasmic dsDNA. This explains why both genotoxic therapies show only limited or even no clinical efficacy when tumors lack

the expression of cGAS and consequently cannot process the dsDNA into immune-stimulating cGAMP.

cGAS-Expressing Tumors Respond Better to Immune Checkpoint Inhibition

Several reports described that hot tumors respond better to immune checkpoint inhibition (Ayers et al., 2017; Van Allen et al., 2015). Since cGAS-expressing tumors have a hot phenotype, we hypothesized that treatment with anti-PD1 plus anti-CTLA4 is more efficacious in such tumors. To test this, we treated mice bearing CT26^{ctrl} or CT26^{ΔMb21d1} tumors with anti-PD1 plus anti-CTLA monoclonal antibodies and monitored tumor growth and survival (Figure 5A). As shown in Figures 2 and 4, untreated CT26^{ΔMb21d1} tumors grew faster than untreated CT26^{ctrl} tumors, which resulted in a shorter survival (Figures 5B and 5D). Although both tumors responded to the checkpoint inhibitor treatment, CT26^{ctrl} tumors responded significantly better than cGAS-deficient CT26^{ΔMb21d1} concerning the survival of these mice (Figure 5D). We observed complete tumor rejection in 8 out of 20 mice with CT26^{ctrl} tumors but only 2 out of 20 mice with CT26^{ΔMb21d1} tumors (Figure 5C).

Cancer-Cell-Intrinsic Expression of cGAS Correlates with Infiltration of CD8$^+$ T Cells in Human Microsatellite-Stable Colorectal Cancer

To determine the clinical relevance of our findings, we analyzed colorectal adenocarcinoma resection specimens from 25
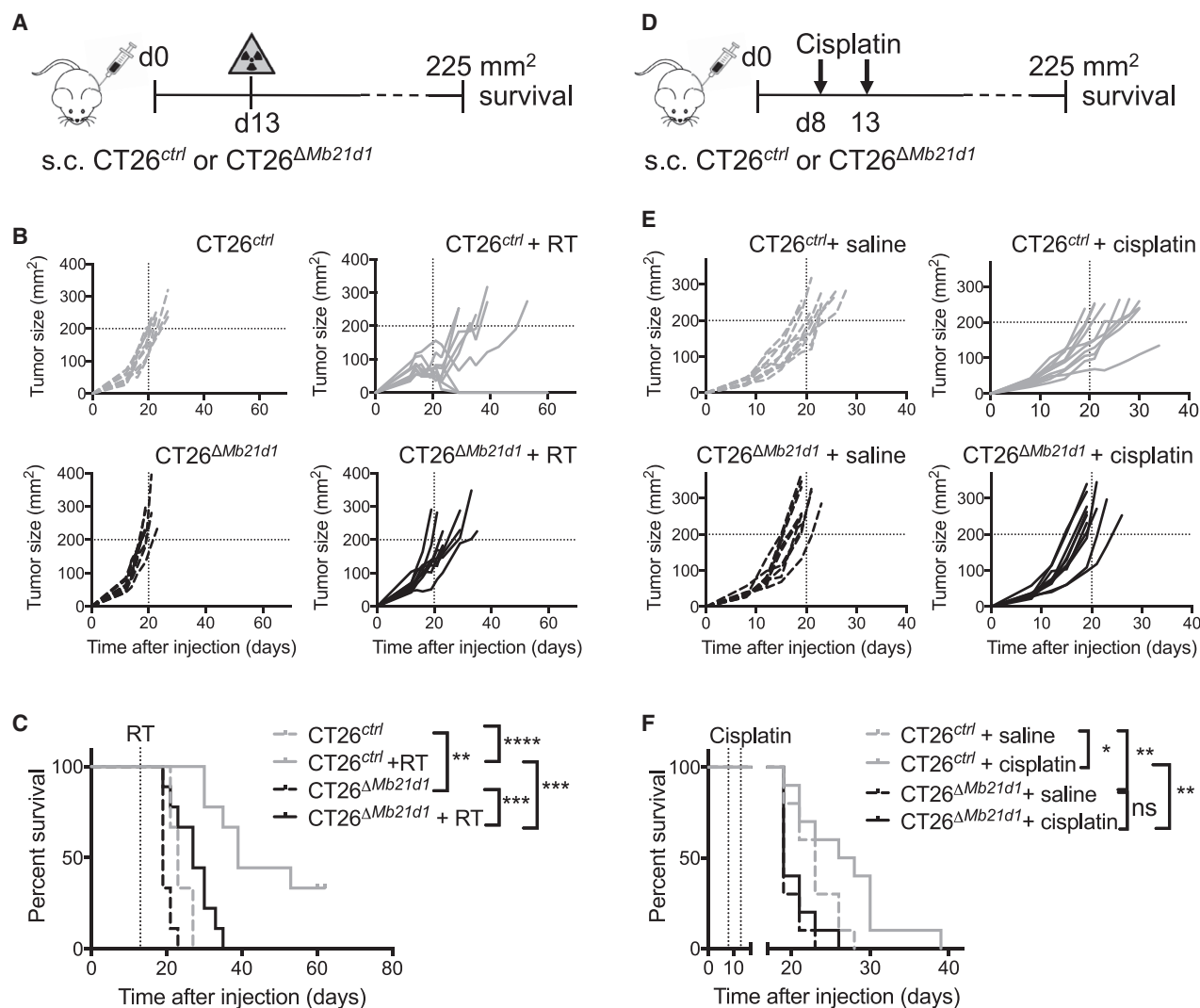
Figure 4. The Efficacy of DNA-Damaging Cancer Therapies Depends on Cancer-Cell-Intrinsic Expression of cGAS

(A) Experimental design for (B) and (C). CT26^{ctrl} or CT26$^{\Delta Mb21d1}$ cells were injected subcutaneously into BALB/c mice (n = 10 mice per group). Radiotherapy (RT; 1× 20 Gy) was applied to the tumor on day 13.

(B) Tumor size was measured with a caliper. Every line represents an individual mouse.

(C) Survival curve. Death event is defined as tumor size >225 mm^2. Statistics were calculated using the log-rank (Mantel-Cox) test. **p < 0.01, ***p < 0.005, ****p < 0.001.

(D) Experimental design for (E) and (F). CT26^{ctrl} or CT26$^{\Delta Mb21d1}$ cells were injected subcutaneously into BALB/c mice (n = 10 mice per group). Mice were treated with cisplatin (3 mg/kg) or saline on days 8 and 13.

(E) Tumor size was measured with a caliper. Every line represents an individual mouse.

(F) Survival curve. Death event is defined as tumor size >225 mm^2. Statistics were calculated using the log-rank (Mantel-Cox) test. *p < 0.05, **p < 0.01.

See also Figure S5.

patients. Using four-color multiplex immunofluorescence, we stained for cGAS, pan-cytokeratin (PanCK; epithelial cells), and CD8 (CD8$^+$ T cells) (Figure 6A). Our abovementioned data suggest that cancer-cell-intrinsic expression of cGAS characterizes hot tumors. Therefore, we specifically analyzed cGAS expression by tumor cells. We first applied an algorithm to segment the tissue in tumor and stroma based on expression of PanCK and morphology (Figure 6B). We then determined which proportion of cancer cells expressed cGAS (Figure 6C) and quantified the number of CD8$^+$ T cells per image (Figure 6D). We found that

only 15 out of 151 tumor images contained >10% cGAS$^+$ cancer cells (Figure 6E), whereas cGAS expression was detectable in all patients in the tumor-adjacent non-diseased tissue (Figure S6). We found a significant correlation between the percentage of cancer cells that express cGAS and the density of tumor-infiltrating CD8$^+$ T cells (Figure 6E). In one patient with heterogeneous expression of cancer-cell-intrinsic cGAS, we saw that CD8$^+$ T cells were mainly present in areas with cGAS expression (Figure 6F). This underscores the concept that cancer-cell-intrinsic cGAS directly drives the infiltration of CD8$^+$ T cells.
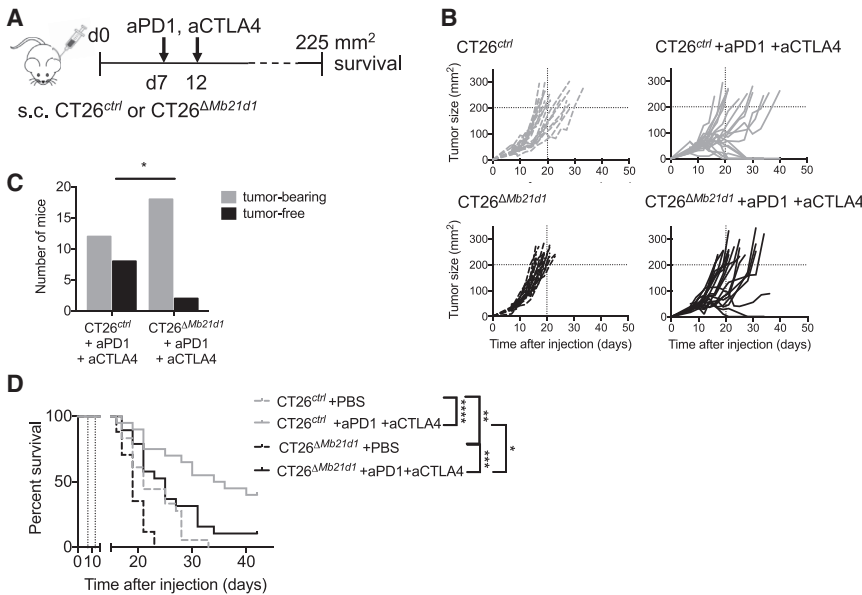
Figure 5. cGAS-Expressing Tumors Respond Better to Immune Checkpoint Inhibition

(A) Experimental design for (B)–(D). CT26^{ctrl} or CT26$^{\Delta Mb21d1}$ cells were injected subcutaneously into BALB/c mice (n = 10 mice per group). On days 7 and 12, mice were injected intraperitoneally (i.p.) with 250 μg anti-PD1 (RMP1-14) and 250 μg anti-CTLA4 (9H10) antibodies or PBS.

(B–D) Pooled data from two identical experiments. (B) Tumor size was measured with a caliper. Every line represents an individual mouse. (C) Number of tumor-bearing and tumor-free mice in CT26^{ctrl} or CT26$^{\Delta Mb21d1}$ after treatment with anti-PD1 and anti-CTLA4. Bars represent the total number of mice per group. Statistics were calculated using the chi-square test. (D) Survival curve. Death event is defined as tumor size >225 mm^2. Statistics were calculated using the log-rank (Mantel-Cox) test. *p < 0.05, **p < 0.01, ***p < 0.005, ****p < 0.001.

Thus, also in humans, cancer-cell-intrinsic cGAS expression positively correlates with T cell infiltration.

DISCUSSION

In this study, we have shown that cGAS expression in cancer cells is critical for tumor control by CD8$^+$ T cells. Cancer cells have plenty of substrate for cGAS because of their unusually high concentration of cytoplasmic dsDNA (Li and Chen, 2018). Consequently, cancer cells can produce substantial amounts of cGAMP. We uncovered that *in vitro* cGAMP is transferred via gap junctions from cancer cells to DCs, where it induces the production of type I IFN in a STING-dependent fashion. This is in line with the observations that intra-tumoral or even systemic application of STING agonists (Corrales et al., 2015; Dai et al., 2017; Li et al., 2016; Ramanjulu et al., 2018) or induction of gap junctions between cancer cells and DCs (Saccheri et al., 2010) improves immune surveillance. Furthermore, we found that cancer-cell-intrinsic cGAS is critical for the efficacy of genotoxic treatments such as radio-, chemo-, and immunotherapy.

Although initially known for antiviral activity, type I IFN influences immunity via direct action on innate and adaptive lymphocytes. For example, type I IFN activates NK cells to execute potent antiviral (Biron et al., 1999) and anti-tumor defense (Swann et al., 2007). In addition, type I IFN is essential for rejection of tumors by CD8$^+$ T cells (Diamond et al., 2011; Dunn et al., 2006; Fuertes et al., 2011). The connection between type I IFN and the cGAS/STING pathway has been appreciated for some time (Stetson and Medzhitov, 2006), and the importance of this pathway for control of cancer has recently received increasing attention (reviewed in Van-pouille-Box et al., 2018). According to the current view, cancer-cell-derived DNA obtains access to the cytoplasm of host cells via an unknown mechanism (Woo et al., 2014) or

exosomes (Kitai et al., 2017), resulting in STING-dependent production of type I IFN by the latter. This view is challenged by our results and work recently reported by Marcus et al. (2018) showing that cGAMP, and not dsDNA, is transferred from cancer cells to DCs.

The pivotal role of STING-dependent production of type I IFN by tumor-infiltrating myeloid cells (DCs and macrophages) concerning the generation of protective anti-tumor immunity was shown in several studies (Corrales et al., 2015; Marcus et al., 2018; Woo et al., 2014). However, which upstream events induce STING signaling in tumor-infiltrating DCs was not completely understood. We identified cancer-cell-derived cGAMP as the molecule that induces STING-dependent type I IFN production by DCs and macrophages, suggesting that host cGAS is dispensable for this response. Indeed, it has been shown in different tumor models that cGAS deficiency in the host does not influence tumor growth (Marcus et al., 2018; Wang et al., 2017). Along these lines, our *in vivo* data show that the immune infiltration of tumors from wild-type and cGAS-deficient mice is comparable for both hot and cold tumors. Additionally, we confirmed *in vitro* that the production of type I IFNs required cGAS expression in cancer cells and STING expression in DCs. Our data, together with previously published work, indicate that cGAMP, and not dsDNA, induces STING-activation in myeloid cells, including DCs and macrophages, and the consequent activation of the adaptive immune system. How cGAMP is transferred *in vivo* from cancer to immune cells has not been determined yet.

We showed that cancer-cell-intrinsic expression of cGAS and consequent production of cGAMP promotes tumor control by CD8$^+$ T cells, mainly by driving their differentiation into effectors. The same mechanism accounts for control of tumors that are recognized by NK cells rather than CD8$^+$ T cells (Marcus et al., 2018). Both studies together make a strong cause for the importance of cancer-cell-intrinsic expression of cGAS in the defense against cancer by innate as well as adaptive immune cells. Being equally important for innate and adaptive
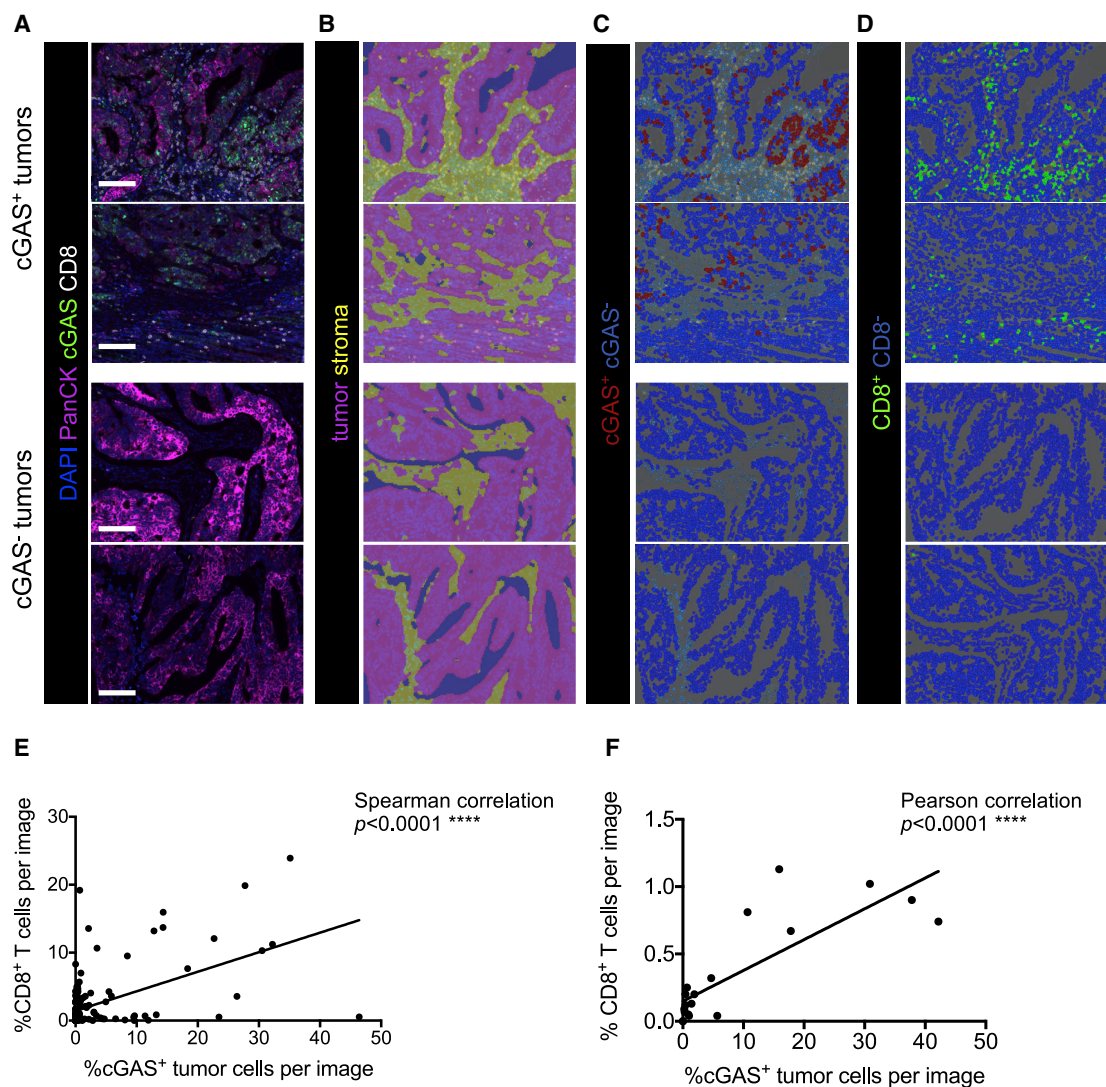
Figure 6. Cancer-Cell-Intrinsic Expression of cGAS Correlates with Infiltration of CD8^{+} T Cells in Human Microsatellite-Stable Colorectal Cancer

(A) Representative images of four-color multiplex immunofluorescence on resection specimens from four colorectal adenocarcinoma patients. Staining shows cGAS (green), epithelial cells (PanCK, magenta), CD8^{+} T cells (CD8, white), and nuclear staining (DAPI, blue). Scale bar represents 100 μm.

(B) Representative images of the applied tissue segmentation algorithm to differentiate tumor (magenta) and stroma (yellow) based on morphology and PanCK expression.

(C) Representative images of the applied cell segmentation and scoring algorithm in the tumor area for cGAS-positive (red), and -negative (blue).

(D) Representative images of the applied cell segmentation and scoring algorithm in the tumor and stroma for CD8-positive (green) and -negative (blue) cells.

(E) Correlation of the percentage of cGAS^{+} tumor cells and the percentage of CD8^{+} T cells per image. Every symbol represents one image; in total, 151 images were analyzed from 25 patients. At least 6 images were analyzed per patient. Statistics were calculated using nonparametric Spearman correlation.

(F) Correlation of the percentage of cGAS^{+} tumor cells and the percentage of CD8^{+} T cells in one patient with a heterogeneous distribution of cGAS expression in the tumor. Every symbol represents one image; in total, 20 images were analyzed from patient 14. Correlation was calculated using a parametric Pearson test. Statistics were calculated using the Pearson correlation coefficient.

See also Figure S6.

immunity against cancer assigns a key role to cGAS among immune regulators.

We showed that cancer-cell-intrinsic expression of cGAS influences the quality of immune infiltration in human colorectal adenocarcinoma. Since CD8^{+} T cell infiltration correlates with increased survival of cancer patients in many disease entities, analysis of cGAS expression by cancer cells may be a potential biomarker for survival or response to (immune) therapies. We observed that tumor-adjacent non-diseased tissues in all patients expressed cGAS in epithelial and stromal cells, whereas cGAS expression was rare in carcinoma cells. This suggests that loss of cGAS is

an immune escape mechanism and goes in line with the observation that the loss of cGAS expression correlates with progression of colorectal cancer (Xia et al., 2016; Yang et al., 2017).

Although most cancer cells contain a substantial concentration of cytoplasmic dsDNA, this can further be increased by genotoxic stress (Harding et al., 2017; Härtlova et al., 2015; Sheng et al., 2018). This explains why immune stimulation by genotoxic treatment is cGAS/STING dependent and radiotherapy is less efficient in STING-deficient mice (Deng et al., 2014). Also, combining radiotherapy with a STING agonist improved therapeutic efficacy (Baird et al., 2016). Moreover, artificially enhancing the concentration of cytoplasmic DNA and cyclic dinucleotides in dying cancer cells enhanced STING signaling in cells that engulfed such dying cells, promoting immune activation (Ahn et al., 2018).

A recent report showed that the increase of cytoplasmic dsDNA upon radiotherapy depends on the dose of radiation used; doses >10–12 Gy induce expression of the DNA exonuclease TREX1, resulting in degradation of cytoplasmic dsDNA in three different cancer cell lines (TSA, MC38, and 4T1) and reduced immunogenicity (Vanpouille-Box et al., 2017). In contrast, we found a comparable increase of cytoplasmic dsDNA after irradiation with 8 or 20 Gy as well as exposition to 15 μM cisplatin in CT26. We currently lack an explanation for this discrepancy. Furthermore, we showed that therapeutic efficacy of radiotherapy given as a single dose of 20 Gy was decreased in cGAS-deficient CT26 tumors when compared to cGAS-proficient tumors.

We can offer at least two explanations for our observation that cGAS-expressing cancers respond better to genotoxic treatment. First, therapy-induced increase of cytoplasmic dsDNA may translate directly in production of more cGAMP and type I IFN, thus providing a stronger immune stimulus. However, untreated cancer cells already contain at least 10-fold more cytoplasmic dsDNA than untransformed cells, and we do not know whether a further 2- to 4-fold increase by genotoxic therapy significantly adds to immune stimulation. Second, genotoxic therapies, and perhaps all therapies that involve concomitant immune stimulation, may work better when tumors are hot at the start of therapy. Indeed, some studies show that immune checkpoint inhibitors work better if cancer cells contain substantial amounts of cytoplasmic dsDNA (Vanpouille-Box et al., 2017) or if they are combined with intratumoral application of STING agonists (Wang et al., 2017; Ager et al., 2017).

Tumor-infiltrating effector CD8+ T cells mediate the clinical response to immune checkpoint inhibitors. Therefore, hot tumors respond better to immune checkpoint inhibition (Ayers et al., 2017; Van Allen et al., 2015). cGAS-expressing tumors responded significantly better to anti-PD1 and anti-CTLA4 treatment than cGAS-deficient tumors, which is in line with our observation that cancer-cell-intrinsic cGAS promotes infiltration by effector CD8+ T cells that can be targeted by immune checkpoint inhibition.

Despite the wealth of evidence for cGAS/STING supporting anti-tumor immunity, there are reports showing a detrimental role of this pathway. First, STING was shown to promote the growth of poorly immunogenic tumors via indolamine 2,3 dioxygenase (IDO) activation (Lemos et al., 2016). This study used mostly LLC and EL-4 cancer cells, and we showed here that LLCs contain low amounts of cGAS, which may explain their low immunogenicity. The authors did not address, however, how STING drives IDO production and subsequent suppression of CD8+ T cells. Second, it was shown that chromosomal instability leads to micronuclei, increased amounts of cytoplasmic dsDNA, activation of the cGAS/STING pathway, and increased metastasis (Bakhoum et al., 2018). Most of the experiments used xenografted human cancer cells, thus precluding involvement of the immune system. Third, STING-deficient mice are resistant to inflammation-driven skin squamous cell carcinoma (Ahn et al., 2014), which may not be representative of most cancers. Fourth, metastatic cells in the brain establish gap junctions with astrocytes to transfer cGAMP. The resulting, STING-dependent production of pro-inflammatory cytokines supports proliferation of metastasized cells and makes them chemoresistant (Chen et al., 2016). Thus, in a particular context, the cGAS/STING pathway may promote cancer.

In summary, together with the recent report by Marcus et al. (2018), our results propose that cancer-cell-intrinsic cGAS is essential to tumor control by innate as well as adaptive immunity. Thus, cGAS expression makes tumors hot and may serve as a useful biomarker for immunogenicity and presumably also for responsiveness to (immune) therapy.

STAR★METHODS

Detailed methods are provided in the online version of this paper and include the following:

- KEY RESOURCES TABLE
- LEAD CONTACT AND MATERIALS AVAILABILITY
- EXPERIMENTAL MODEL AND SUBJECT DETAILS
  - Mouse strains
  - Cell lines
  - Colorectal adenocarcinoma paraffin sections
- METHOD DETAILS
  - Modification of cell lines
  - Measurement of cGAS and STING in tumor cell lines
  - Co-culture experiments
  - *In vivo* tumor experiments and treatments
  - Flow cytometry
  - Western blotting
  - Quantification of type I IFN
  - Quantification of cytoplasmic DNA
  - Quantification of cytokines in tumor lysates
  - Four-color immunofluorescence
  - Calcein AM transfer assay
  - Quantification of gamma-H2AX
  - Colony-forming assay
- QUANTIFICATION AND STATISTICAL ANALYSIS
  - Quantification of immunofluorescence data
  - Statistical analysis
- DATA AND CODE AVAILABILITY

REFERENCES

Ablasser, A., and Chen, Z.J. (2019).). CGAS in action: expanding roles in immunity and inflammation. Science 363, eaat8657.

Ablasser, A., Goldeck, M., Cavlar, T., Deimling, T., Witte, G., Röhl, I., Hopfner, K.P., Ludwig, J., and Hornung, V. (2013a). cGAS produces a 2′-5′-linked cyclic dinucleotide second messenger that activates STING. Nature 498, 380–384.

Ablasser, A., Schmid-Burgk, J.L., Hemmerling, I., Horvath, G.L., Schmidt, T., Latz, E., and Hornung, V. (2013b). Cell intrinsic immunity spreads to bystander cells via the intercellular transfer of cGAMP. Nature 503, 530–534.

Ager, C.R., Reilley, M.J., Nicholas, C., Bartkowiak, T., Jaiswal, A.R., and Curran, M.A. (2017). Intratumoral STING activation with T-cell checkpoint modulation generates systemic antitumor immunity. Cancer Immunol. Res. 5, 676–684.

Ahn, J., Xia, T., Konno, H., Konno, K., Ruiz, P., and Barber, G.N. (2014). Inflammation-driven carcinogenesis is mediated through STING. Nat. Commun. 5, 5166.

Ahn, J., Xia, T., Rabasa Capote, A., Betancourt, D., and Barber, G.N. (2018). Extrinsic phagocyte-dependent STING signaling dictates the immunogenicity of dying cells. Cancer Cell 33, 862–873.e5.

Ayers, M., Lunceford, J., Nebozhyn, M., Murphy, E., Loboda, A., Kaufman, D.R., Albright, A., Cheng, J.D., Kang, S.P., Shankaran, V., et al. (2017). IFN-γ-related mRNA profile predicts clinical response to PD-1 blockade. J. Clin. Invest. 127, 2930–2940.

Baird, J.R., Friedman, D., Cottam, B., Dubensky, T.W., Jr., Kanne, D.B., Bambina, S., Bahjat, K., Crittenden, M.R., and Gough, M.J. (2016). Radiotherapy combined with novel STING-targeting oligonucleotides results in regression of established tumors. Cancer Res. 76, 50–61.

Bakhoum, S.F., Ngo, B., Laughney, A.M., Cavallo, J.A., Murphy, C.J., Ly, P., Shah, P., Sriram, R.K., Watkins, T.B.K., Taunk, N.K., et al. (2018). Chromosomal instability drives metastasis through a cytosolic DNA response. Nature 553, 467–472.

Binnewies, M., Roberts, E.W., Kersten, K., Chan, V., Fearon, D.F., Merad, M., Coussens, L.M., Gabrilovich, D.I., Ostrand-Rosenberg, S., Hedrick, C.C., et al. (2018). Understanding the tumor immune microenvironment (TIME) for effective therapy. Nat. Med. 24, 541–550.

Biron, C.A., Nguyen, K.B., Pien, G.C., Cousens, L.P., and Salazar-Mather, T.P. (1999). Natural killer cells in antiviral defense: function and regulation by innate cytokines. Annu. Rev. Immunol. 17, 189–220.

Broz, M.L., Binnewies, M., Boldajipour, B., Nelson, A.E., Pollack, J.L., Erle, D.J., Barczak, A., Rosenblum, M.D., Daud, A., Barber, D.L., et al. (2014). Dissecting the tumor myeloid compartment reveals rare activating antigen-presenting cells critical for T cell immunity. Cancer Cell 26, 638–652.

Burnette, B.C., Liang, H., Lee, Y., Chlewicki, L., Khodarev, N.N., Weichselbaum, R.R., Fu, Y.X., and Auh, S.L. (2011). The efficacy of radiotherapy relies upon induction of type i interferon-dependent innate and adaptive immunity. Cancer Res. 71, 2488–2496.

Chen, D.S., and Mellman, I. (2017). Elements of cancer immunity and the cancer-immune set point. Nature 541, 321–330.

Chen, Q., Boire, A., Jin, X., Valiente, M., Er, E.E., Lopez-Soto, A., Jacob, L., Patwa, R., Shah, H., Xu, K., et al. (2016). Carcinoma-astrocyte gap junctions promote brain metastasis by cGAMP transfer. Nature 533, 493–498.

Corrales, L., Glickman, L.H., McWhirter, S.M., Kanne, D.B., Sivick, K.E., Katibah, G.E., Woo, S.R., Lemmens, E., Banda, T., Leong, J.J., et al. (2015). Direct activation of STING in the tumor microenvironment leads to potent and systemic tumor regression and immunity. Cell Rep. 11, 1018–1030.

Dai, P., Wang, W., Yang, N., Serna-Tamayo, C., Ricca, J.M., Zamarin, D., Shuman, S., Merghoub, T., Wolchok, J.D., and Deng, L. (2017). Intratumoral delivery of inactivated modified vaccinia virus Ankara (IMVA) induces systemic antitumor immunity via STING and Batf3-dependent dendritic cells. Sci. Immunol. 2, eaal1713.

Deng, L., Liang, H., Xu, M., Yang, X., Burnette, B., Arina, A., Li, X.D., Mauceri, H., Beckett, M., Darga, T., et al. (2014). STING-dependent cytosolic DNA sensing promotes radiation-induced type I interferon-dependent antitumor immunity in immunogenic tumors. Immunity 41, 843–852.

Diamond, M.S., Kinder, M., Matsushita, H., Mashayekhi, M., Dunn, G.P., Archambault, J.M., Lee, H., Arthur, C.D., White, J.M., Kalinke, U., et al. (2011). Type I interferon is selectively required by dendritic cells for immune rejection of tumors. J. Exp. Med. 208, 1989–2003.

Dunn, G.P., Koebel, C.M., and Schreiber, R.D. (2006). Interferons, immunity and cancer immunoediting. Nat. Rev. Immunol. 6, 836–848.

Fenech, M., Kirsch-Volders, M., Natarajan, A.T., Surralles, J., Crott, J.W., Parry, J., Norppa, H., Eastmond, D.A., Tucker, J.D., and Thomas, P. (2011). Molecular mechanisms of micronucleus, nucleoplasmic bridge and nuclear bud formation in mammalian and human cells. Mutagenesis 26, 125–132.

Franken, N.A., Rodermond, H.N., Stap, J., Haveman, J., and van Bree, C. (2006). Clonogenic assay of cells in vitro. Nat. Protoc. 1, 2315–2319.

Fuertes, M.B., Kacha, A.K., Kline, J., Woo, S.R., Kranz, D.M., Murphy, K.M., and Gajewski, T.F. (2011). Host type I IFN signals are required for antitumor CD8+ T cell responses through CD8alpha+ dendritic cells. J. Exp. Med. 208, 2005–2016.

Gajewski, T.F., Schreiber, H., and Fu, Y.X. (2013). Innate and adaptive immune cells in the tumor microenvironment. Nat. Immunol. 14, 1014–1022.

Galluzzi, L., Buqué, A., Kepp, O., Zitvogel, L., and Kroemer, G. (2017). Immunogenic cell death in cancer and infectious disease. Nat. Rev. Immunol. 17, 97–111.

Galon, J., Costes, A., Sanchez-Cabo, F., Kirilovsky, A., Mlecnik, B., Lagorce-Pagès, C., Tosolini, M., Camus, M., Berger, A., Wind, P., et al. (2006). Type, density, and location of immune cells within human colorectal tumors predict clinical outcome. Science 313, 1960–1964.

Gao, P., Ascano, M., Wu, Y., Barchet, W., Gaffney, B.L., Zillinger, T., Serganov, A.A., Liu, Y., Jones, R.A., Hartmann, G., et al. (2013). Cyclic [G(2′,5′)pA(3′,5′)p] is the metazoan second messenger produced by DNA-activated cyclic GMP-AMP synthase. Cell *153*, 1094–1107.

Gupta, A., Probst, H.C., Vuong, V., Landshammer, A., Muth, S., Yagita, H., Schwendener, R., Pruschy, M., Knuth, A., and van den Broek, M. (2012). Radiotherapy promotes tumor-specific effector CD8+ T cells via dendritic cell activation. J. Immunol. *189*, 558–566.

Harding, S.M., Benci, J.L., Irianto, J., Discher, D.E., Minn, A.J., and Greenberg, R.A. (2017). Mitotic progression following DNA damage enables pattern recognition within micronuclei. Nature *548*, 466–470.

Härtlova, A., Erttmann, S.F., Raffi, F.A., Schmalz, A.M., Resch, U., Anugula, S., Lienenklaus, S., Nilsson, L.M., Kröger, A., Nilsson, J.A., et al. (2015). DNA damage primes the type I interferon system via the cytosolic DNA sensor STING to promote anti-microbial innate immunity. Immunity *42*, 332–343.

Huang, A.Y., Gulden, P.H., Woods, A.S., Thomas, M.C., Tong, C.D., Wangt, W., Engelhardt, V.H., et al. (1996). The immunodominant major histocompatibility complex class I-restricted antigen of a murine colon tumor derives from an endogenous retroviral gene product. Proc. Natl. Acad. Sci. USA *93*, 9730–9735.

Inaba, K., Inaba, M., Romani, N., Aya, H., Deguchi, M., Ikehara, S., Muramatsu, S., and Steinman, R.M. (1992). Generation of large numbers of dendritic cells from mouse bone marrow cultures supplemented with granulocyte/macrophage colony-stimulating factor. J. Exp. Med. *176*, 1693–1702.

Ishikawa, H., and Barber, G.N. (2008). STING is an endoplasmic reticulum adaptor that facilitates innate immune signalling. Nature *455*, 674–678.

Ishikawa, H., Ma, Z., and Barber, G.N. (2009). STING regulates intracellular DNA-mediated, type I interferon-dependent innate immunity. Nature *461*, 788–792.

Kitai, Y., Kawasaki, T., Sueyoshi, T., Kobiyama, K., Ishii, K.J., Zou, J., Akira, S., Matsuda, T., and Kawai, T. (2017). DNA-containing exosomes derived from cancer cells treated with topotecan activate a STING-dependent pathway and reinforce antitumor immunity. J. Immunol. *198*, 1649–1659.

Klarquist, J., Hennies, C.M., Lehn, M.A., Reboulet, R.A., Feau, S., and Janssen, E.M. (2014). STING-mediated DNA sensing promotes antitumor and autoimmune responses to dying cells. J. Immunol. *193*, 6124–6134.

Lemos, H., Mohamed, E., Huang, L., Ou, R., Pacholczyk, G., Arbab, A.S., Munn, D., and Mellor, A.L. (2016). STING promotes the growth of tumors characterized by low antigenicity via IDO activation. Cancer Res. *76*, 2076–2081.

Li, T., and Chen, Z.J. (2018). The cGAS-cGAMP-STING pathway connects DNA damage to inflammation, senescence, and cancer. J. Exp. Med. *215*, 1287–1299.

Li, T., Cheng, H., Yuan, H., Xu, Q., Shu, C., Zhang, Y., Xu, P., Tan, J., Rui, Y., Li, P., and Tan, X. (2016). Antitumor activity of cGAMP via stimulation of cGAS-cGAMP-STING-IRF3 mediated innate immune response. Sci. Rep. *6*, 19049.

Lienenklaus, S., Cornitescu, M., Ziętara, N., Łyszkiewicz, M., Gekara, N., Jabłónska, J., Edenhofer, F., Rajewsky, K., Bruder, D., Hafner, M., et al. (2009). Novel reporter mouse reveals constitutive and inflammatory expression of IFN-β in vivo. J. Immunol. *183*, 3229–3236.

Mackenzie, K.J., Carroll, P., Martin, C.A., Murina, O., Fluteau, A., Simpson, D.J., Olova, N., Sutcliffe, H., Rainger, J.K., Leitch, A., et al. (2017). cGAS surveillance of micronuclei links genome instability to innate immunity. Nature *548*, 461–465.

Marcus, A., Mao, A.J., Lensink-Vasan, M., Wang, L., Vance, R.E., and Raulet, D.H. (2018). Tumor-derived cGAMP triggers a STING-mediated interferon response in non-tumor cells to activate the NK cell response. Immunity *49*, 754–763.e4.

Ramanjulu, J.M., Pesiridis, G.S., Yang, J., Concha, N., Singhaus, R., Zhang, S.Y., Tran, J.L., Moore, P., Lehmann, S., Eberl, H.C., et al. (2018). Design of amidobenzimidazole STING receptor agonists with systemic activity. Nature *564*, 439–443.

Saccheri, F., Pozzi, C., Avogadri, F., Barozzi, S., Faretta, M., Fusi, P., and Rescigno, M. (2010). Bacteria-induced gap junctions in tumors favor antigen cross-presentation and antitumor immunity. Sci. Transl. Med. *2*, 44ra57.

Scheu, S., Dresing, P., and Locksley, R.M. (2008). Visualization of IFNbeta production by plasmacytoid versus conventional dendritic cells under specific stimulation conditions in vivo. Proc. Natl. Acad. Sci. USA *105*, 20416–20421.

Shen, Y.J., Le Bert, N., Chitre, A.A., Koo, C.X., Nga, X.H., Ho, S.S., Khatoo, M., Tan, N.Y., Ishii, K.J., and Gasser, S. (2015). Genome-derived cytosolic DNA mediates type I interferon-dependent rejection of B cell lymphoma cells. Cell Rep. *11*, 460–473.

Sheng, W., LaFleur, M.W., Nguyen, T.H., Chen, S., Chakravarthy, A., Conway, J.R., Li, Y., Chen, H., Yang, H., Hsu, P.H., et al. (2018). LSD1 ablation stimulates anti-tumor immunity and enables checkpoint blockade. Cell *174*, 549–563.e19.

Siliņa, K., Burkhardt, C., Casanova, R., Solterman, A., and van den Broek, M. (2018a). A quantitative pathology approach to analyze the development of human cancer-associated tertiary lymphoid structures. Methods Mol. Biol. *1845*, 71–86.

Siliņa, K., Soltermann, A., Attar, F.M., Casanova, R., Uckeley, Z.M., Thut, H., Wandres, M., Isajevs, S., Cheng, P., Curioni-Fontecedro, A., et al. (2018b). Germinal centers determine the prognostic relevance of tertiary lymphoid structures and are impaired by corticosteroids in lung squamous cell carcinoma. Cancer Res. *78*, 1308–1320.

Simoni, Y., Becht, E., Fehlings, M., Loh, C.Y., Koo, S.L., Teng, K.W.W., Yeong, J.P.S., Nahar, R., Zhang, T., Kared, H., et al. (2018). Bystander CD8+ T cells are abundant and phenotypically distinct in human tumour infiltrates. Nature *557*, 575–579.

Sistigu, A., Yamazaki, T., Vacchelli, E., Chaba, K., Enot, D.P., Adam, J., Vitale, I., Goubar, A., Baracco, E.E., Remédios, C., et al. (2014). Cancer cell-autonomous contribution of type I interferon signaling to the efficacy of chemotherapy. Nat. Med. *20*, 1301–1309.

Song, S., Peng, P., Tang, Z., Zhao, J., Wu, W., Li, H., Shao, M., Li, L., Yang, C., Duan, F., et al. (2017). Decreased expression of STING predicts poor prognosis in patients with gastric cancer. Sci. Rep. *7*, 39858.

Stetson, D.B., and Medzhitov, R. (2006). Recognition of cytosolic DNA activates an IRF3-dependent innate immune response. Immunity *24*, 93–103.

Sun, L., Wu, J., Du, F., Chen, X., and Chen, Z.J. (2013). Cyclic GMP-AMP synthase is a cytosolic DNA sensor that activates the type I interferon pathway. Science *339*, 786–791.

Surace, L., Lysenko, V., Fontana, A.O., Cecconi, V., Janssen, H., Bicvic, A., Okoniewski, M., Pruschy, M., Dummer, R., Neefjes, J., et al. (2015). Complement is a central mediator of radiotherapy-induced tumor-specific immunity and clinical response. Immunity *42*, 767–777.

Swann, J.B., Hayakawa, Y., Zerafa, N., Sheehan, K.C.F., Scott, B., Schreiber, R.D., Hertzog, P., and Smyth, M.J. (2007). Type I IFN contributes to NK cell homeostasis, activation, and antitumor function. J. Immunol. *178*, 7540–7549.

Uzé, G., Di Marco, S., Mouchel-Vielh, E., Monneron, D., Bandu, M.T., Horisberger, M.A., Dorques, A., Lutfalla, G., and Mogensen, K.E. (1994). Domains of interaction between alpha interferon and its receptor components. J. Mol. Biol. *243*, 245–257.

Van Allen, E.M., Miao, D., Schilling, B., Shukla, S.A., Blank, C., Zimmer, L., Sucker, A., Hillen, U., Foppen, M.H.G., Goldinger, S.M., et al. (2015). Genomic correlates of response to CTLA-4 blockade in metastatic melanoma. Science *350*, 207–211.

van der Woude, L.L., Gorris, M.A.J., Halilovic, A., Figdor, C.G., and de Vries, I.J.M. (2017). Migrating into the tumor: a roadmap for T Cells. Trends Cancer *3*, 797–808.

Vanpouille-Box, C., Alard, A., Aryankalayil, M.J., Sarfraz, Y., Diamond, J.M., Schneider, R.J., Inghirami, G., Coleman, C.N., Formenti, S.C., and Demaria, S. (2017). DNA exonuclease Trex1 regulates radiotherapy-induced tumour immunogenicity. Nat. Commun. *8*, 15618.

Vanpouille-Box, C., Demaria, S., Formenti, S.C., and Galluzzi, L. (2018). Cytosolic DNA sensing in organismal tumor control. Cancer Cell *34*, 361–378.

Wang, H., Hu, S., Chen, X., Shi, H., Chen, C., Sun, L., and Chen, Z.J. (2017). cGAS is essential for the antitumor effect of immune checkpoint blockade. Proc. Natl. Acad. Sci. USA *114*, 1637–1642.

Woo, S.R., Fuertes, M.B., Corrales, L., Spranger, S., Furdyna, M.J., Leung, M.Y.K., Duggan, R., Wang, Y., Barber, G.N., Fitzgerald, K.A., et al. (2014). STING-dependent cytosolic DNA sensing mediates innate immune recognition of immunogenic tumors. Immunity *41*, 830–842.

Wu, J., Sun, L., Chen, X., Du, F., Shi, H., Chen, C., and Chen, Z.J. (2013). Cyclic GMP-AMP is an endogenous second messenger in innate immune signaling by cytosolic DNA. Science *339*, 826–830.

Xia, T., Konno, H., Ahn, J., and Barber, G.N. (2016). Deregulation of STING signaling in colorectal carcinoma constrains DNA damage responses and correlates with tumorigenesis. Cell Rep. *14*, 282–297.

Yang, C.A., Huang, H.Y., Chang, Y.S., Lin, C.L., Lai, I.L., and Chang, J.G. (2017). DNA-sensing and nuclease gene expressions as markers for colorectal cancer progression. Oncology *92*, 115–124.

STAR★METHODS

KEY RESOURCES TABLE

REAGENT or RESOURCE	SOURCE	IDENTIFIER
Antibodies		
STING	Cell Signaling Technology	Clone D2P2F; 13647S; RRID:AB_2732796
cGAS	Cell Signaling Technology	Clone D3O8O; 31659S; RRID:AB_2799008
CX43	Cell Signaling Technology	Clone 3512; 3512S; RRID:AB_2294590
Alpha-tubulin	Cell Signaling Technology	Clone DM1A; 3873S; RRID:AB_1904178
Beta-actin	Sigma	Clone AC-15; A5441; RRID:AB_476744
HRP-goat-anti-mouse IgG	BioLegend	Poly4053; RRID:AB_315009
HRP-goat-anti-rabbit IgG	Dianova	111-035-008; RRID:AB_2337937
cGAS	Cell Signaling Technology	Clone D1D3G; 15102S; RRID:AB_2732795
CD8	Bio-Rad	4B11; MCA1817T; RRID:AB_322868
Pan-Cytokeratin	Santa Cruz	Clone h-240; sc-15367; RRID:AB_2134438
HRP-donkey-anti-rabbit IgG	Jackson ImmunoResearch	711-035-152; RRID:AB_10015282
HRP-donkey-anti-rat IgG	Jackson ImmunoResearch	712-035-153; RRID:AB_2340639
AlexaFluor 568-goat-anti-mouse IgG	Life Technologies	A11031; RRID:AB_144696
gamma-H2AX	Millipore	05-636; RRID:AB_309864
CD11b – FITC	BioLegend	Clone M1/70; 101206; RRID:AB_213789
NK1.1 – FITC	BioLegend	Clone PK136; 108706; RRID:AB_313393
CD4 – PE	BioLegend	Clone GK1.5; 100408; RRID:AB_312693
CD45.2 – PerCP/Cy5.5	BioLegend	Clone 104; 109828; RRID:AB_893350
CD45.2 – APC	BioLegend	Clone 104; 109814; RRID:AB_389211
IFNgammma – PE/Cy7	BioLegend	Clone XMG1.2; 505826; RRID:AB_2295770
CD8a – BV605	BioLegend	Clone 53-6.7; 100744; RRID:AB_2562609
CD3e – APC	BioLegend	Clone 17A2; 100236; RRID:AB_2561456
FoxP3 – APC	eBioscience	Clone FJK-16 s; 17-5773-80; RRID:AB_469456
CD8a – APC	BioLegend	Clone 53-6.7; 100712; RRID:AB_312751
CD4 – APC/Cy7	BioLegend	Clone GK1.5; 100414; RRID:AB_312699
CD3e – APC/Cy7	BioLegend	Clone 17A2; 100222; RRID:AB_2242784
CD11c – BV650	BioLegend	Clone N418; 117339; RRID:AB_2562414
CD45.2 – BV605	BioLegend	Clone 104; 109841; RRID:AB_2563485
CD11b – BV510	BioLegend	Clone M1/70; 101245; RRID:AB_2561390
F4/80 – PB	BioLegend	Clone BM8; 123124; RRID:AB_893475
F4/80 – BV421	BioLegend	Clone BM8; 123132; RRID:AB_11203717
CD31 – FITC	BioLegend	Clone 390; 102406; RRID:AB_312901
MHC-II – PE/Cy7	BioLegend	Clone M5/114.15.2; 107630; RRID:AB_493528
CD122-PE	BioLegend	Clone TM-beta 1; 123210; RRID:AB_940617
NKp46-PerCP/eFluor 710	eBioscience	Clone 29A1.4; 46335182; RRID:AB_1834441
CD3- PE/Cy7	BioLegend	Clone 145-2C11; 100320; RRID:AB_312685
CD45-PB	BioLegend	Clone 104 Mouse; 109820; RRID:AB_492872
CD49b-APC	BioLegend	Clone DX5; 108910; RRID:AB_313415
CD39-PerCP/eFluor 710	eBioscience	Clone 24DMS1; 46039182; RRID:AB_10717953
CD103 PE	BioLegend	Clone 2E7; 121405; RRID:AB_535948
Zombie Violet Fixable Viability Kit	BioLegend	423114
Zombie NIR Fixable Viability Kit	BioLegend	423106

(Continued on next page)

Continued

REAGENT or RESOURCE	SOURCE	IDENTIFIER
Biological Samples		
Tissue microarray of 120 colorectal adenocarcinoma samples	Department of Pathology and Molecular Pathology, University Hospital Zurich, Switzerland	N/A
Paraffin sections of colorectal adenocarcinoma samples with determined MSI status	Triemli Hospital Zurich	N/A
Chemicals, Peptides, and Recombinant Proteins		
Recombinant mouse IFN-beta	Sigma-Aldrich	I9032-1VL
Polyethylenimine (PEI)	Polysciences	23966-1
Cisplatin	Sandoz	L01XA01
Matrigel	Corning	354234
Zombie-Violet fixable viability stain	BioLegend	423114
Zombie-NIR fixable viability stain	BioLegend	423106
PMA	Sigma	P1585-1MG
Ionomycin	Sigma	I0634-1MG
Brefeldin A	Sigma	B6542-25MG
AH-1 peptide (SPSYVYHQF)	PolyPeptide Laboratories	N/A
FoxP3/Transcription factor staining buffer set	eBioscience	00-5523-00
Opal 520	PerkinElmer	FP1487001KT
Opal 540	PerkinElmer	FP1494001KT
Opal 620	PerkinElmer	FP1495001KT
Opal 650	PerkinElmer	FP1496001KT
Opal 690	PerkinElmer	FP1497001KT
1X Plus Amplification Diluent	PerkinElmer	FP1498
Anti-PD1	Hideo Yagita, Tokyo, Japan	RMP1-14
Anti-CTLA4	Jim Allison, Texas, US	9H10
Calcein, AM, cell-permanent dye	Invitrogen	C3100MP
Poly-L-lysine (0.1%)	Sigma Aldrich	P8920
Critical Commercial Assays		
Prime Flow RNA assay	ThermoFisher	88-18005-210
Prime Flow IFNb1	ThermoFisher	PF210 (VB10-3282108-PF)
Mouse IFN-beta ELISA	PBL Assay Science	42410-1
Luciferase 1000 assay system	Promega	E4550
NE-PER Nuclear and cytoplasmic Extraction Reagents	ThermoFisher	78833
AccuClear Nano dsDNA Assay kit	Molecular Devices	R3650A
LEGENDplex Mouse Inflammation Panel	BioLegend	740150
Experimental Models: Cell Lines		
4T07	Gerhard Christofori, Basel, Switzerland	N/A
4T1	Burkhard Becher, Zurich, Switzerland	N/A
B16BL6	Lubor Borsig, Zurich, Switzerland	N/A
B16F10	ATCC	CRL-6475
CMS5a	Hiroyoshi Nishikawa, Osaka, Japan	N/A
CT26	ATCC	CRL-2638
LL171	Roman Spörri, ETHZ, Switzerland	N/A
LLC	ATCC	CRL-1642
MC38	Mark Smyth, Brisbane, Australia	N/A
MC57	Rolf Zinkernagel, Zurich, Switzerland	N/A

Continued

REAGENT or RESOURCE	SOURCE	IDENTIFIER
RN5	Emanuela Felley-Bosco, Zurich, Switzerland	N/A
CT26*ΔMb21d1*	This paper	N/A
CT26*ΔTmem173*	This paper	N/A
CT26*ΔGja1*	This paper	N/A
CT26*Ctrl*	This paper	N/A
LLC*Mb21d1*	This paper	N/A
X63-mGM-CSF	Manfred Kopf, Zurich, Switzerland	N/A
Experimental Models: Organisms/Strains		
BALB/cRj1	Janvier	N/A
C57BL/6NRj	Janvier	N/A
B6(C)-*Cgas*$^{tm1d(EUCOMM)Hmgu}$/J	The Jackson Laboratory	026554
NOD.Cg-*Prkdc*^{scid}*Il2rg*^{tm1Wjl}/SzJ	The Jackson Laboratory	013062
C57BL/6J-*Tmem173*^{Gt}/J	The Jackson Laboratory	017537
B6.129S2-*Ifnar1*^{tm1Agt}/Mmjax	The Jackson Laboratory	32045-JAX
Oligonucleotides		
Primers for CRISPR/Cas9 genomic editing, see Table S1	This paper	N/A
Recombinant DNA		
pSpCas9(BB)-2A-GFP	Addgene	PX458; 48138
pLenti-EF1α-Flag-mm-cGas	Winfried Barchet, Bonn, Germany	N/A
pMD2.G	Addgene	12259
pCMV-dR8.91	Christian Münz, Zurich, Switzerland	N/A
Software and Algorithms		
Prism	GraphPad Prism software	Version 7.0
FlowJo	Tree Star software	Version 10.1
inForm	PerkinElmer	CLS1355781
ImageJ	Fiji	N/A
Other		
Irradiation unit	RADSOURCE	RS2000
FastPrep tissue homogenizer	MPBiomedicals	N/A
Zirconium beads	Precellys	BER103BK
Multispectral microscopy system Vectra 3.0	PerkinElmer	N/A
SpectraMax i3	Molecular Devices	N/A
DM6 B fluorescent microscope	Leica Biosystems	N/A
IX83 microscope	Olympus	N/A
Scan R imaging platform	Olympus	N/A

LEAD CONTACT AND MATERIALS AVAILABILITY

Further information and requests for resources and reagents should be directed to and fulfilled by the Lead Contact, Dr. Maries van den Broek (vandenbroek@immunology.uzh.ch).

All unique/stable reagents generated in this study are available from the Lead Contact with a completed Materials Transfer Agreement.

EXPERIMENTAL MODEL AND SUBJECT DETAILS

Mouse strains

BALB/cRj1 and C57BL/6NRj mice were purchased from Janvier and cGAS-deficient (cGAS$^{-/-}$, B6(C)-*Cgas*$^{tm1d(EUCOMM)Hmgu}$/J) mice were purchased from Jackson Laboratory. NOD.Cg-*Prkdc*^{scid}*Il2rg*^{tm1Wjl}/SzJ (NSG) mice were originally obtained from the Jackson

Laboratory and provided by Christian Münz, University of Zurich, Switzerland. Femora and tibiae from STING-deficient (C57BL/6J-*Tmem173^Gt^*/J; T*mem173^Gt^*) mice were provided by Winfried Barchet, University of Bonn, Germany. All mice were kept and bred under pathogen-free conditions at the Laboratory Animal Services Center at the University of Zurich. All experiments were performed with 8-12-weeks-old female mice, unless stated otherwise. All animal experiments were approved by the Cantonal Veterinary Office Zurich under the license number 084/2015 and 140/2018 and performed according to cantonal and federal regulations.

Cell lines

CT26, LLC, 4T1, B16F10, B16BL6, MC38, MC57, CMS5a and 4T07 provided by were cultured in Dulbecco's modified Eagle's medium (DMEM, GIBCO) supplemented with 5% fetal calf serum (FCS, Thermo Fisher Scientific), 30 U/ml Penicillin, 30 μg/ml Streptomycin (antibiotics, Thermo Fisher Scientific) and 2 mM L-Glutamine (Thermo Fisher Scientific). RN5 cells were cultured in DMEM/F-12 (1:1) medium (Thermo Fisher Scientific) supplemented with 15% FCS, 0.1 mM 2-mercaptoethanol (Sigma Aldrich), 1% MEM non-essential amino acids (Thermo Fisher Scientific) and 100 mM sodium pyruvate (Thermo Fisher Scientific) and antibiotics. LL171 (Uzé et al., 1994) were cultured in Roswell Park Memorial Institute (RPMI) 1640 medium (GIBCO) supplemented with 10% FCS, L-Glutamine and antibiotics. CT26 *Mb21d1*-, *Tmem173*- or *Gja1*-deficient cells, and LLC *Mb21d1*-overexpressing cells were generated and cultured as described above.

All cell lines were tested negative for a number of pathogens including *Mycoplasma* ssp. by PCR.

Colorectal adenocarcinoma paraffin sections

Tumor tissues from patients with colorectal adenocarcinoma of the proximal colon were collected at the Triemli Hospital Zurich, Switzerland. Donors provided written, informed consent to tissue collection, analysis and data publication. Law abidance was reviewed and approved by the ethics commission of the Canton Zurich (KEK-ZH-2015-0068 and KEK-ZH-2013-0584). Samples were numerically coded to protect donors' rights to confidentiality and privacy. The microsatellite-instability (MSI) status was determined by immunohistochemical detection of MLH1 and MLH2. We analyzed 25 patients with MS-stable disease.

METHOD DETAILS

Modification of cell lines

Mb21d1 (cGAS), *Tmem173* (STING) or *Gja1* (CX43) genes were targeted in CT26 cells using CRISPR/Cas9. Per gene, three guide-RNAs (gRNAs) were designed (Table S1), of which two were paired per transfection. gRNAs were cloned into the pSpCas9(BB)-2A-GFP vector. CT26 cells were transfected with polyethyleneimine (PEI) and 2000 ng of two PX458-gRNA expression plasmids per target gene. GFP⁺ cells were FACS-sorted using a FACSARIA III (BD Biosciences) and cloned by limiting dilution. Absence of target gene was confirmed in cGAS-deficient CT26 (CT26^ΔMb21d1^), STING-deficient CT26 (CT26^ΔTmem173^) and CX43-deficient CT26 (CT26^ΔGja1^) by Western Blot. In order to avoid potential single-clone-dependent artifacts, oligoclonal cell lines were generated as follows. Five clones with determined deficiency of target gene were mixed in equal parts and used for experiments. The control CT26 cell line (CT26^ctrl^) was generated as described above using the empty PX458 vector.

To overexpress cGAS, we used the lentiviral plasmid pLenti-EF1α-Flag-mm-cGAS. Lentiviral particles were generated using a second-generation lentiviral packaging system consisting of pMD2.G and pCMV-dR8.91. LLC cells were transduced and subsequently cultured in DMEM supplemented with 2 μg/ml puromycin (Invitrogen, #A11138-03) to select transduced cells. cGAS overexpression was confirmed by Western Blot.

Measurement of cGAS and STING in tumor cell lines

Tumor cells (1.5×10^6) were seeded in T175 flasks, cultured for 24 h and expression of cGAS and STING was quantified by Western Blot.

To assess the function of cGAS and STING, 3×10^5 tumor cells/well were seeded in 24-well plates. Tumor cells were transfected with 1 μg genomic DNA extracted from CT26 cells using PEI. Cells were incubated overnight at 37°C and type I IFNs were quantified in the supernatant using the LL171 (Uzé et al., 1994) reporter cell line.

Co-culture experiments

Bone marrow-derived dendritic cells (BMDCs) were generated as described (Inaba et al., 1992). Briefly, bone marrow cells were cultured in RPMI 1640 medium containing 10% supernatant from X63-mGM-CSF cells for 7-9 days. At least 85% of the resulting cells expressed CD11c and MHC class II as determined by flow cytometry (not shown). Hundred-fifty-thousand tumor cells and 0.5×10^6 BMDCs were co-cultured in a well of a 24-well plate. After 24h, supernatant was collected and type I IFNs were quantified using the reporter cell line LL171. Alternatively, IFNβ was quantified by ELISA.

In vivo tumor experiments and treatments

Tumor cells were suspended at 2×10^6/ml in a 2:1 mix of PBS:Matrigel. Hundred μl of this suspension were injected subcutaneously (s.c.) into the right flank of mice. Tumor size was measured in two dimensions (length and width) every 2-4 days starting on day 7 using a caliper. Immediately before start of interventions, mice were assigned to different experimental groups in such way that the average

and variance of tumor size was similar for each group. Radiotherapy was applied locally on the tumor as a single dose of 1 × 20 Gy with 1.6 Gy/min on day 13 (Surace et al., 2015). Cisplatin (Sandoz) was injected i.p. at 3 mg/kg on day 8 and 13. Control mice were injected with 150 μL of 0.9% NaCl. For immune checkpoint inhibition, anti-PD1 (RMP1-14) and anti-CTLA4 (9H10) monoclonal antibodies were injected i.p. at 250 μg per dose on day 7 and 12. Control mice were injected with 200 μL PBS. CD8^{+} T cells were depleted on day 9 by i.p. injection of 250 μg of a CD8-depleting antibody (YTS169.4). Control mice were injected with 100 μL PBS. For survival studies, mice were euthanized when the tumor reached a size of 225 mm[2].

Flow cytometry

Excised tumors were collected in RPMI supplemented with 10% FCS and cut into small pieces. Tumor pieces were digested with 1 mg/ml collagenase IV (Bioconcept) at 37°C on a rotating device. After 45 min, 2.6 μg/ml DNaseI (ThermoFisher Scientific) was added and digestion continued for additional 15 min at 37°C. Cells were washed with 0.01 M EDTA in PBS by centrifugation at 350 g for 5 min. Red blood cells were lysed using RBC lysis buffer (17 mM Tris pH 7.2, 144 mM NH$_4$Cl) for 2 min. Cells were washed with PBS and filtered through a 70 μm filter to remove debris. Single cells were stained according to standard protocols. Briefly, cells were surface-stained in 50 μL antibody-mix in PBS. Dead cells were excluded using fixable viability stain according to the manufacturer's instructions. For intracellular cytokine staining, cells were stimulated with 50 ng/ml phorbol 12-myristate 13-acetate (PMA) plus 500 ng/ml ionomycin or with AH-1 peptide (Huang et al., 1996) (SPSYVYHQF, the H-2L^d-restricted epitope derived from endogenous retroviral gp70, which is expressed in CT26, 10^{-6} M) for 1 h at 37°C. Subsequently, brefeldin A (10 μg/ml) was added and cells were incubated for additional 3 h. Cells were stained for surface molecules as described above, washed with PBS, and fixed for 30 min on ice using IC Fixation Buffer from Foxp3/Transcription Factor Staining Buffer Set. Subsequently, cells were stained for intracellular IFNγ in 1X permeabilization buffer from the Foxp3/Transcription Factor Staining Buffer Set overnight at 4°C. After washing with 1X permeabilization buffer, samples were suspended in FACS buffer (PBS, 20 mM EDTA pH 8.0, 2% FCS) and acquired using a CyAn ADP9 flow cytometer (Beckman Coulter) or FACS LSRII Fortessa (BD Biosciences).

Due to lack of suitable antibodies for intracellular staining of type I IFN, we detected *Ifnb1* transcripts in single cells by flow cytometry using the PrimeFlow RNA Assay according to manufacturer's protocol. Briefly, single-cell suspensions were surface-stained as described above. Fixation and permeabilization was performed according to manufacturer's instructions. For mRNA detection, *in situ* hybridization with type I Alexa Fluor 568-labeled *Ifnb1* probe was performed for 2 h at 40°C. The signal was amplified by incubating samples for 2 h in PreAmplification reagent at 40°C and additional 2 h at 40°C in Amplification reagent. Samples were incubated with label probes at 40°C for 1 h, washed and acquired on a FACS LSRII Fortessa (BD Biosciences).

For quantitative analysis, CountBright absolute counting beads were used (ThermoFisher Scientific). In all staining, dead cells were excluded using Live/Dead fixable staining reagents (Invitrogen), and doublets were excluded by FSC-A versus FSC-H gating. Samples were analyzed using FlowJo v10 software (Tree Star Inc.). Analysis was performed on single, live cells.

Western blotting

To extract proteins, cells were suspended in RIPA buffer (ThermoFisher) supplemented with protease inhibitor (cOmplete, Mini Protease Inhibitor Cocktail, Roche) and subjected to two freeze-thaw cycles. The protein concentration was determined using the DC Protein Assay (Bio-Rad). For quantification of cGAS and Connexin 43 (CX43, GJA1), a total of 20 μg protein was loaded and for the determination of STING, 100 μg were loaded per lane of a 10% SDS-PAGE gel. Proteins were transferred onto a nitrocellulose membrane (GE Healthcare Life science) with 350 mA for 2 h at 4°C. The membrane was blocked in 5% non-fat milk powder in Tris-buffered saline containing 0.05% Tween-20 (TBS-T) for 1 h at room temperature (RT) or overnight at 4°C. Membranes were stained with the primary antibodies against cGAS (1:1'000), STING (1:1'000), CX43 (1:1'000), α-TUBULIN (1:5'000) or β-ACTIN (1:5'000). Membranes were incubated for 1 h at RT or overnight at 4°C with antibodies diluted in 5% non-fat milk powder in TBS-T. Membranes were washed three times for 10 min in TBS-T and incubated in with the secondary antibody: HRP-goat-anti-mouse IgG (1:10'000) or HRP-goat-anti-rabbit IgG (1:10'000) in 5% non-fat milk powder in TBS-T for 1 h at RT. Membranes were washed three times for 10 min in TBS-T and chemiluminescent reaction was started using the WesternBright ECL kit (Advansta). Protein bands were detected using a Fusion Solo S imager (Vilber). The Precision Plus Protein Dual Color Standard (Bio-Rad) was used to assess molecular weight of protein bands. Relative quantification of cGAS/β-ACTIN and STING/α-TUBULIN ratio was performed using ImageJ software.

Quantification of type I IFN

Type I IFNs were quantified using the reporter cell line LL171. Briefly, 3.5x10^4 LL171 cells were seeded per well in 96-well flat-bottom plates and incubated with samples for 24 h at 37°C in a CO$_2$-incubator. Reporter cells were lysed using the Luciferase Cell Culture Lysis 5X Reagent and transferred to a white 96-well LUMITRAC plate (Greiner Bio-One GmbH). Luciferase activity was measured using the Luciferase Assay System in a TECAN plate reader (Tecan). Standard curves were prepared using serial dilutions of recombinant murine IFNβ ranging from 0 to 1'000 pg/ml.

Quantification of cytoplasmic DNA

Tumor cells were seeded at 1x10^6 cells/well in a 6-well plate and exposed to DNA-damaging treatments. Specifically, cells were irradiated with 8 or 20 Gy using a RS2000 (Radsource) irradiation machine at 6.7 Gy/min or treated with 15 μM Cisplatin (Sandoz).

Cytoplasmic dsDNA was measured in live cells 24 h later. As a control, 1×10^6 fresh splenocytes were used. The cytoplasmic fraction was extracted using the NE-PER Nuclear and Cytoplasmic Extraction Reagents. Cytoplasmic dsDNA was quantified using the Ac-cuClear Nano dsDNA Assay Kit and a SpectraMax i3 (Molecular Devices) microplate reader as described (Vanpouille-Box et al., 2017).

Quantification of cytokines in tumor lysates

Pieces of excised tumors were snap-frozen in liquid nitrogen and stored at $-80°C$. To prepare a lysate, 2x weight in volume of PBS supplemented with protease inhibitor was added to frozen tumor pieces. Zirconium oxide beads were added, and samples were ho-mogenized for 30 s at 5 m^2/s^2 using a FastPrep® instrument using. Samples were centrifuged at $4°C$ at 14'000 g for 15 min. The su-pernatant was collected on ice and immediately used. Total protein concentration was measured using DC Protein Assay (Bio-Rad). Cytokines were quantified in lysates using the LEGENDplex Mouse Inflammation Panel according to manufacturer's instructions. Samples were acquired on CyAn ADP9 flow cytometer (Beckman Coulter). IFNβ was quantified by ELISA and read on a SpectraMax i3 (Molecular Devices) plate reader.

Four-color immunofluorescence

For antigen-retrieval, slides were heated for 2 h at $55°C$ and incubated in Trilogy pretreatment solution (CellMarque) in a pres-sure cooker for 15 min. After cooling for 15 min, slides were washed with milli-Q to remove remaining paraffin and treated with 3% H_2O_2 in H_2O for 15 min. Slides were washed with milli-Q water and incubated with 4% BSA/0.01% Triton X-100 in PBS for 15 min at $37°C$ to prevent unspecific binding of antibodies. Subsequently, slides were incubated overnight at $4°C$ or 3 h at RT with a primary antibody diluted in 1% BSA/0.01% Triton X-100 in PBS. Following primary antibodies were used: anti-cGAS (1:500), anti-Pan-Cytokeratin (1:2000) and anti-CD8 (1:1000). After incubation, slides were washed 3 times for 5 min with 0.01% Triton X-100 in PBS and incubated for 1 h at RT with following HRP-conjugated secondary antibodies: Donkey-anti-rabbit IgG (1:1'000) and donkey-anti-mouse IgG (1:1'000), diluted in 1% BSA in 0.01% Triton X-100 in PBS. The signal was amplified using 1:100-diluted fluorophore-conjugated tyramides Opal 520, Opal 540 and Opal 690 in amplification buffer (PerkinElmer) for 10 min at RT. Slides were washed subsequently and boiled for 12 min in 10 mM citric acid pH 6.0 to strip the bound antibodies. Blocking and incubation with the next primary and secondary antibody, tyramide amplification and strip-ping was repeated for different targets that were consecutively detected. Finally, slides were washed, incubated with 0.5 μg/ml 4′,6 diamidine-2-phenylindole (DAPI; Invitrogen) for 5 min, washed again and mounted with ProlongDiamond medium (Invitrogen).

Calcein AM transfer assay

Tumor cells were washed twice with PBS and labeled with Calcein AM dye (5 μg/ml in PBS) at $37°C$ for 30 min in the dark. Cells were washed twice with PBS and 0.5×10^6 cells were plated in complete RPMI in a well of a 12-well plate. Five-hundred-thousand BMDCs were added to the tumor cells and incubated at $37°C$ for 6 h. Cells were collected, washed with PBS and surface-stained with fluo-rescently-labeled antibodies. After washing with PBS, samples were acquired using a CyAn ADP9 flow cytometer (Beckman Coulter). Calcein AM was detected in the FITC-channel.

Quantification of gamma-H2AX

Four-chambered culture slides (BD Falcon) were treated with poly-L-lysine for 10 min and dried for 2 h at RT. Seventy-five thousand $CT26^{ctrl}$ and $CT26^{\Delta Mb21d1}$ were grown per chamber overnight. Cells were left untreated, irradiated with 1 Gy or 5 Gy and incubated for 1 h. Slides were briefly washed with PBS and incubated with the pre-extraction solution (25 mM HEPES pH 7.7, 50 mM NaCl, 1 mM EDTA, 3 mM $MgCl_2$, 300 mM sucrose, 0.5% Triton X-100) for 5 min on ice. After washing with PBS, cells were fixed with 4% para-formaldehyde in PBS for 15 min at RT. To prevent unspecific binding of antibodies, slides were incubated with 1% BSA in PBS for 15 min. Slides were incubated with anti-gamma-H2AX (1:200, Millipore) in 1% BSA in PBS for 90 min at RT. Slides were washed and incubated with the AlexaFluor568-coupled secondary antibody goat anti-mouse IgG (1:400, Life Technologies) in 1% BSA in PBS in the dark for 30 min at RT. Slides were washed three times with PBS and stained with 0.5 μg/ml 4′,6 diamidine-2-phenylindole (DAPI; Invitrogen) in deionized H_2O for 5 min, washed again and mounted with FluoroMount medium (Invitrogen). Immunofluorescent im-ages were captured on a DM6 B fluorescent microscope (Leica Biosystems) using an oil-immersion objective (63x/1.4 NA). The auto-mated image acquisition was performed on an IX83 microscope (Olympus) equipped with ScanR imaging platform and 40x/0.9 NA objective. Nuclei were identified based on DAPI signal, and the intensity of gamma-H2AX for each nuclear object were analyzed using the Analysis ScanR software. At least 500 nuclei were analyzed per sample.

Colony-forming assay

The colony-forming assay was performed according to the description in Franken et al. (2006). Briefly, 10, 50 and 100 $CT26^{ctrl}$ and $CT26^{\Delta Mb21d1}$ were seeded in one well of a 6-well plate in duplicates and incubated for 4 h at $37°C$. Cells were left untreated, irradiated with 2, 4, 5, 6 or 9 Gy or treated with Cisplatin (Sandoz) at concentrations of 1, 3, 15 or 30 μM. Cells were incubated for 6 days to form colonies. Colonies were washed with PBS, fixed and stained with 6% glutaraldehyde, 0.5% crystal violet in H_2O for 30 min. Fixation-staining solution was removed and wells were rinsed several times carefully with tap water. Plates were dried at RT and colonies

counted by eye. For the untreated control, the plating efficiency was calculated as followed: [# colonies ÷ # cells seeded] x 100%. For each treatment condition, the surviving fraction was calculated as follows: # colonies ÷ [# cells seeded x plating efficiency].

QUANTIFICATION AND STATISTICAL ANALYSIS

Quantification of immunofluorescence data

Stained slides were scanned using the automated multispectral microscopy system Vectra 3.0 (PerkinElmer). Six to 8 representative areas of tumor tissue were imaged at 200-fold magnification. Inform software (PerkinElmer) was used for spectral unmixing of individual fluorophores and autofluorescence, and to apply cell segmentation and quantification algorithm on the slide as described (Siliņa et al., 2018a, 2018b). Samples were excluded where the area was damaged, or the algorithm was not identifying properly.

Statistical analysis

Group sizes, number of replications, and explanation of the mean and error bars are provided in the figure legends. Statistical tests were performed with GraphPad Prism 7.0 (GraphPad Software). For comparison of two experimental groups, the unpaired two-tailed Student's t test was used, unless stated otherwise. When more than two groups were compared, the one-way ANOVA with Tukey's multiple comparison correction was used. Survival data were analyzed with a Log-rank (Mantel-Cox) test. $*p < 0.05$, $**p < 0.01$, $***p < 0.005$, $****p < 0.001$. Data are shown as mean ± SD unless specified otherwise.

DATA AND CODE AVAILABILITY

This study did not generate any unique datasets or code.

Supplemental Information

Cancer-Cell-Intrinsic cGAS Expression

Mediates Tumor Immunogenicity

Linda Schadt, Colin Sparano, Nicole Angelika Schweiger, Karina Silina, Virginia Cecconi, Giulia Lucchiari, Hideo Yagita, Emilien Guggisberg, Sascha Saba, Zuzana Nascakova, Winfried Barchet, and Maries van den Broek
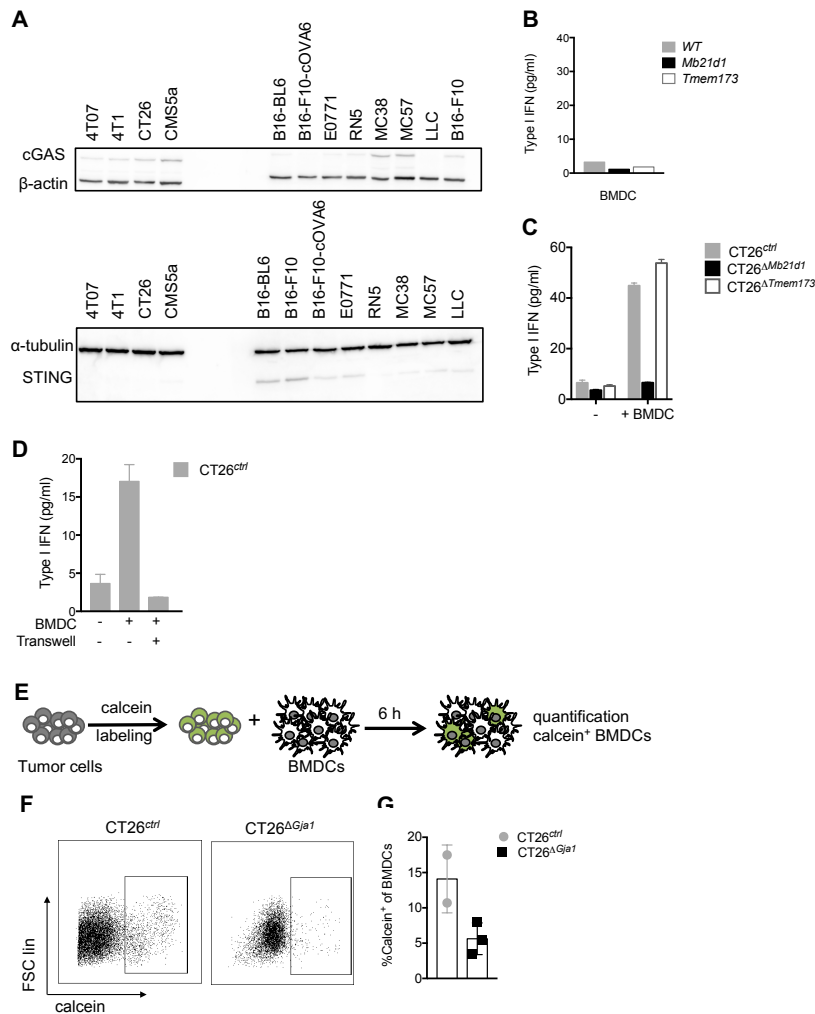
SUPPLEMENTAL INFORMATION

Fig. S1

Figure S1: cGAS and STING expression in murine tumor cell lines; controls for co-culture experiments. Related to Figure 1.

(A) Representative Western blot showing the expression of cGAS and STING protein in different murine tumor cell lines. (B-D) Concentration of type I IFN in the supernatant of various *in vitro* cultures after 24 h determined with the reporter cell line LL171. Results are representative of 2 independent experiments each. (B) Five hundred thousand bone marrow derived dendritic cells (BMDCs) from wild-type (*WT*), cGAS-deficient (*Mb21d1*) or STING-deficient (*Tmem173*) mice were cultured alone. Bars represent one biological replicate. (C) STING-deficient CT26 (CT26$^{\Delta Tmem173}$) resemble CT26^{ctrl} in co-cultures with BMDCs. CT26^{ctrl}, CT26$^{\Delta Mb21d1}$ *or* CT26$^{\Delta Tmem173}$ were cultured alone or co-cultured with BMDCs. Bars represent mean ± SD of three technical replicates. (D) Direct or trans-well co-cultures. Therefore, 0.25 x 10^5 CT26^{ctrl} were seeded per well or trans-well insert and 1 x 10^5 BMDCs were added to the wells. Every symbol represents one biological replicate. Bars represent mean ± SD. (E) Experimental design of calcein AM transfer assay of panels G and H: CT26^{ctrl} or CT26$^{\Delta Gja1}$ were labeled with calcein AM for 30 min at 37 °C. Labeled tumor cells were co-cultured in a 1:1 ratio with BMDC for 6 h, and the percentage of calcein$^+$ BMDCs was determined by flow cytometry. (F) Representative images of calcein$^+$ signal in BMDCs co-cultured with CT26^{ctrl} or CT26$^{\Delta Gja1}$ tumor cells. Cells were gated on live, CD45$^+$ cells. (G) Percentage of calcein$^+$ BMDCs upon co-culture with labeled CT26^{ctrl} or CT26$^{\Delta Gja1}$ tumor cells. Every symbol represents one biological replicate. Bars represent mean ± SD. Results are representative of 2 independent experiments.
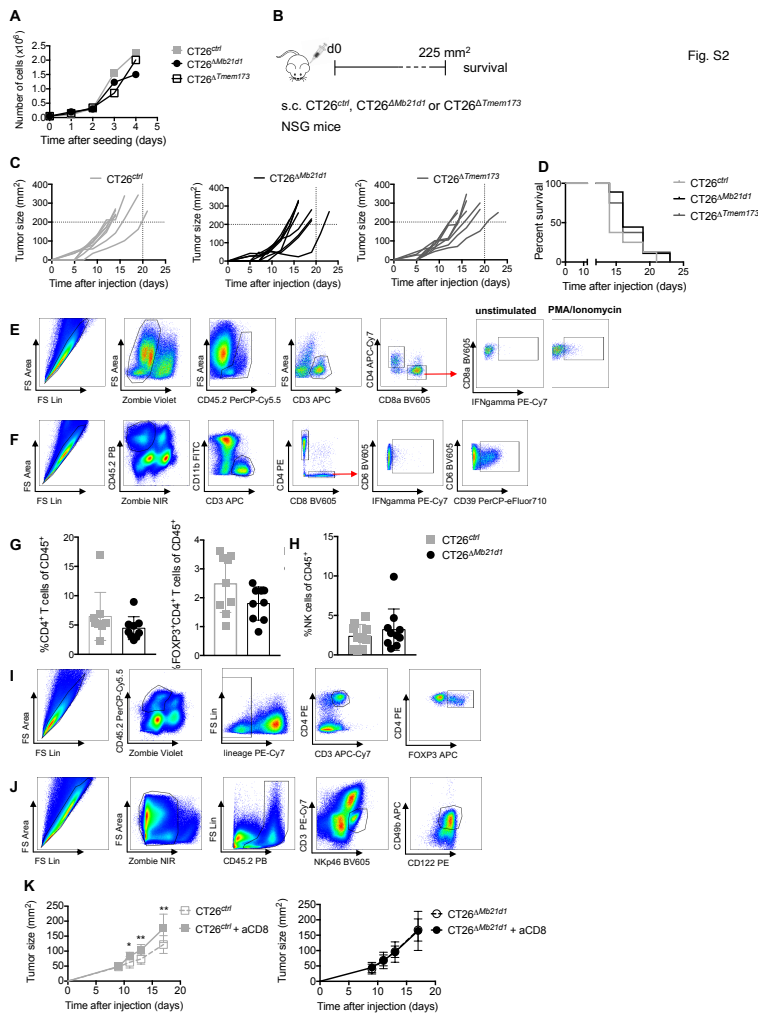
Figure S2: Cancer cell-intrinsic cGAS-expression has no effect on tumor growth in immunodeficient NOD.Cg-*Prkdc^scid Il2rg^tm1Wjl* (NSG) mice. Depletion of CD8$^+$ T-cells promotes tumor growth in cGAS-expressing tumors. Cancer cell-intrinsic cGAS expression does not influence the infiltration of CD4$^+$ T-cells, regulatory T-cells and NK cells. Related to Figure 2.

(A) *In vitro* growth curve of CT26^{ctrl}, CT26^{ΔMb21d1} or CT26^{ΔTmem173} cells. (B) Experimental design. CT26^{ctrl}, CT26^{ΔMb21d1} or CT26^{ΔTmem173} were injected subcutaneously into NSG mice (n=8-9 mice per group). (C) Tumor size was measured with a caliper. Every line represents an individual mouse. (D) Survival curve. Death event is defined as tumor size > 225 mm^2. (E) Gating strategy for T cells described in Figure 2E. (F) Gating strategy for CD8$^+$ T cells described in Figure 2F. (G and H) Percentage of CD4$^+$ T-cells, regulatory T-cells and NK cells in tumors analyzed by flow cytometry at the endpoint (d 17). T-cells were gated as CD45$^+$CD3$^+$ single, live cells, represented in Figure S2I. NK cells were gated as CD45$^+$CD3$^-$NKp46$^+$CD122$^+$CD49b$^+$ single, live cells, represented in Figure S2J. Every symbol represents an individual mouse. Bars represent mean ± SD. Statistics were calculated using the unpaired two-tailed Student's t-test. Results are representative of 2 independent experiments. (I) Gating strategy for CD4$^+$ and FOXP3$^+$CD4$^+$ T cells described in Figure S2G. (J) Gating strategy for NK cells described in Figure S2H. (K) Growth curve of CT26^{ctrl} or CT26^{Mb21d1} tumors in CD8$^+$ T-cell-depleted BALB/c mice. Two-hundred-thousand CT26^{ctrl} or CT26^{Mb21d1} were injected in BALB/c mice and injected i.p. with 250 µg of a CD8-depleting antibody (YTS169.4) on day 9 after tumor injection or with PBS (n=10 mice per group). Tumor growth was measured over time. Symbols represent the mean ± SD. Statistics were calculated on the individual days using the unpaired two-tailed Student's t-test. Results are representative of 2 independent experiments.
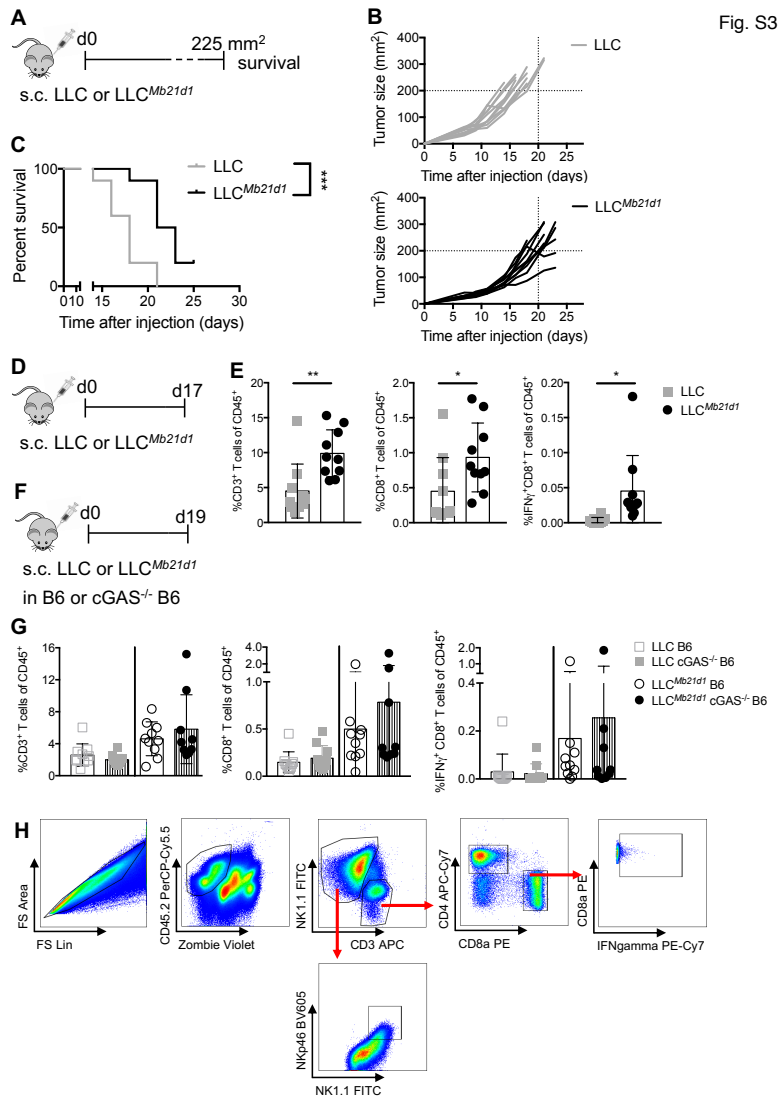
2

Figure S3: Overexpression of cGAS in LLC cells makes tumors hot and promotes immune surveillance. Related to Figure 2.

(A) Experimental design for panels B and C. LLC or LLC*Mb21d* were injected subcutaneously into C57BL/6 mice (n=10 mice per group). (B) Tumor size was measured with a caliper. Every line represents an individual mouse. (C) Survival curve. Death event is defined as tumor size >225 mm^2. (D) Experimental design for panel E. LLC or LLC*Mb21d1* were injected subcutaneously into C57BL/6 mice (n=10 mice per group). (E) Percentage of immune cells in tumors analyzed by flow cytometry at the endpoint (d 17). T cells were gated as CD45$^+$CD3$^+$ single, live cells, represented in panel F. Every symbol represents an individual mouse. Bars represent mean ± SD. Results in panel B, C and E are representative of 2 independent experiments. (F) Experimental design for panel G. LLC or LLC*Mb21d1* were injected subcutaneously into C57BL/6 (B6) or cGAS-deficient B6(C)-*Cgas^tm1d(EUCOMM)Hmgu*/J (cGAS$^{-/-}$ B6) mice (n=9-10 sex-matched mice per group). (G) Percentage of immune cells in tumors analyzed by flow cytometry at the endpoint (d 19). T cells were gated as CD45$^+$CD3$^+$ single, live cells, shown in panel H. Every symbol represents an individual mouse. Bars represent mean ± SD. (H) Gating strategy for T cells described in panel E and G.
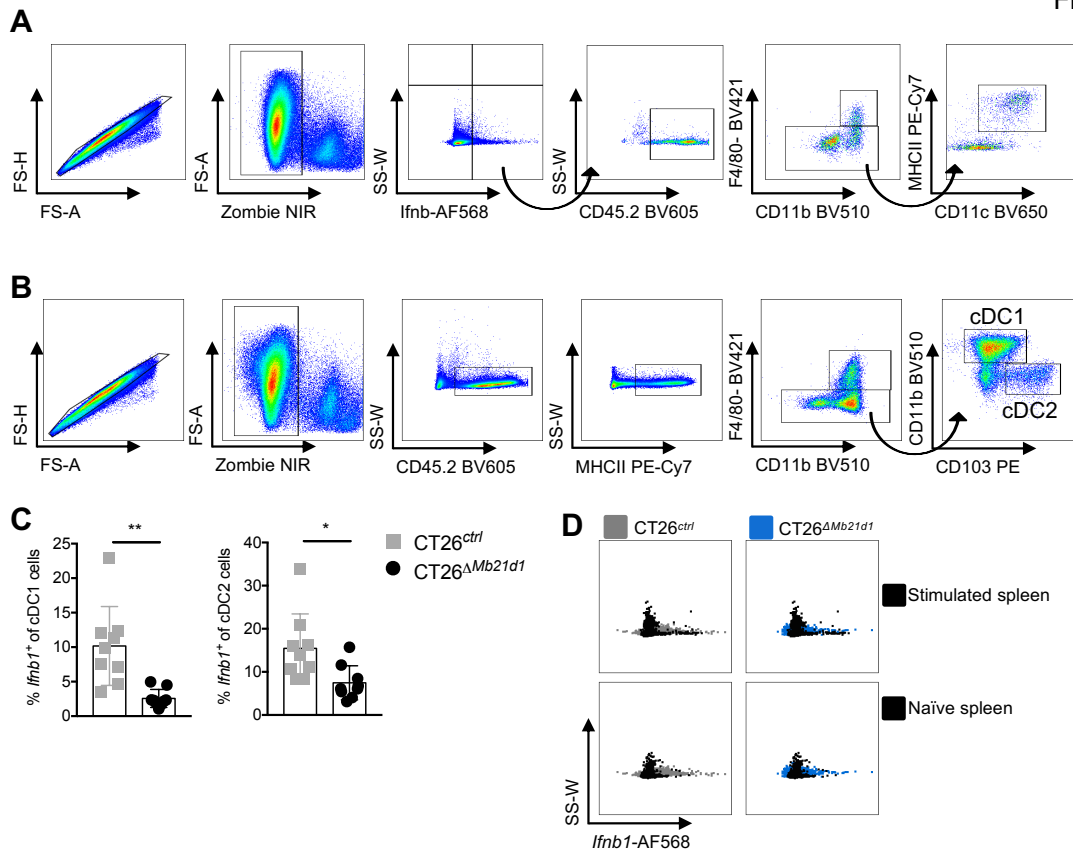
Figure S4: Detection of *Ifnb1* mRNA by flow cytometry in CT26 tumors. Related to Figure 3.
(A) Panels show the gating strategy for the analysis of the *Ifnb1* mRNA by flow cytometry data in Figure 3.
Ifnb1+ DCs were gated as CD45+CD11c+MHCII+F4/80- and macrophages as CD45+CD11b+F4/80+ single, live
cells. (B) Panels show the gating strategy for the analysis of the *Ifnb1* mRNA expression by cDC1s and cDC2s
shown in Figure S5C. cDC2s were gated as CD45+MHCII+F4/80-CD11b+ and cDC1s as CD45+MHCII+F4/80-
CD103+ single, live cells. (C) Percentage of *Ifnb1*+ cells in the cDC1 and cDC2 population at the endpoint (d
14). Every symbol represents an individual mouse. Bars represent mean ± SD. Statistics were calculated using
unpaired two-tailed Student's t-test. (D) Detection of *Ifnb1* mRNA by flow cytometry: Controls. As positive
control for *Ifnb1* transcripts, we used spleen cells that were stimulated *in vitro* with the STING agonist DMXAA
(50 µg/ml) for 3 h. As negative control, we used naïve, untreated spleen cells. Dot plots show MHCII+ live,
single cells from CT26 (grey) or CT26ΔMb21d1 (blue) tumors, overlaid with dot plots of stimulated (upper row,
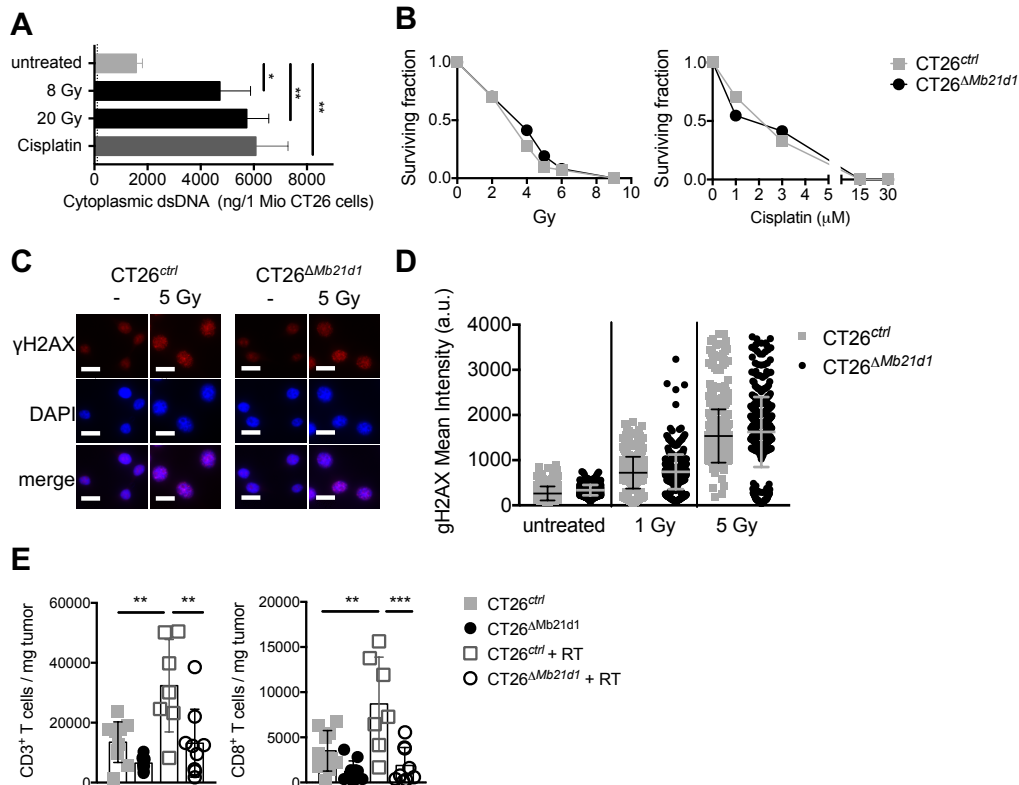black) or naïve spleen samples (lower row, black). All samples were gated on MHCII+ live, single cells.

Figure S5: CT26 *ctrl* **and CT26** *ΔMb21d1* **cells are equally sensitive to genotoxic treatment** *in vitro***. Related to Figure 4.**

(A) CT26 *ctrl* were irradiated *in vitro* with 8 Gy or 20 Gy, treated with 15 μM cisplatin or left untreated. Cytoplasmic DNA was quantified 24 h later. The data show the total amount of cytoplasmic double-stranded DNA (dsDNA) per one million live cells. The dotted line indicates the amount of cytoplasmic dsDNA of one million live splenocytes. Bars represent mean ± SD of 3 replicates. Statistics were calculated using the one-way ANOVA with Tukey's multiple comparison correction. Results are representative of 2 independent experiments. (B) Colony forming assay of CT26 *ctrl* and CT26 *ΔMb21d1* after exposition to different doses of radiation or to cisplatin. The surviving fraction was calculated as follows: # colonies ÷ [# cells seeded x plating efficiency]. Results are representative of 2 independent experiments. (C) Representative images of gamma-H2AX staining of untreated or irradiated (5 Gy) CT26 *ctrl* and CT26 *ΔMb21d1* cancer cells. The upper row shows staining for gamma-H2AX, the middle row shows the DAPI staining and the lower row shows merged images. Scale bar, 20 μm. (D) Quantification of C. Panel shows the mean intensity of gamma-H2AX per nucleus. Every symbol represents an individual nucleus. Results in panel C and D are representative of 2 independent experiments. (E) Percentage of immune cells in tumors analyzed by flow cytometry at the endpoint. Data show the number of live CD45^{+} CD3^{+} (left panel) or live CD45^{+} CD3^{+} CD8^{+} (right panel) per mg tumor. Every symbol represents an individual mouse. Bars represent mean ± SD. Statistics were calculated using the one-way ANOVA with Tukey's multiple comparison correction. Results are representative of 2 independent experiments.
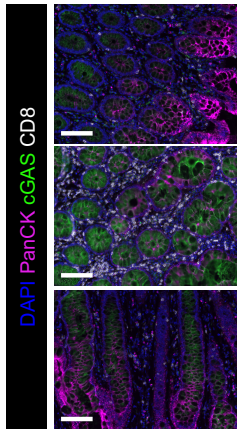
Figure S6: Epithelial and stromal cells in non-diseased, cancer-adjacent tissue express cGAS. Related to Figure 6.

(A) Representative images of 4-color multiplex immunofluorescence on non-diseased, cancer-adjacent areas from 3 colorectal adenocarcinoma patients. Staining shows cGAS (green), epithelial cells (PanCK, magenta), CD8+ T cells (CD8, white) and nuclear staining (DAPI, blue). Scale bar is 100 μm.

Table S1: Oligonucleotides for CRISPR/Cas9 genomic editing. Related to Star Methods (Key Resources Table, Oligonucleotides).

CRISPR gRNA ID	Target sequence 5'-3'
Mb21d1 #1	CGGGCCGCAGCTTTCCGCGT
Mb21d1 #2	GCGGACGGCTTCTTAGCGCG
Mb21d1 #3	CTTACGACTTTCCGCGCCTC
Tmem173 #1	GTCCAAGTTCGTGCGAGGCT
Tmem173 #2	AGCGGTGACCTCTGGGCCGT
Tmem173 #3	CAGTAGTCCAAGTTCGTGCG
Gja1 #1	CGTCAGGGAAATCAAACGGC
Gja1 #2	CGCTGATCCACGATAGCTAA
Gja1 #3	GGGCGTTAAGGATCGCGTGA